CRANFIELD UNIVERSITY

VENKATA RAJANIKANTH MACHAVARAM

MICRO-MACHINING TECHNIQUES FOR THE FABRICATION OF FIBRE FABRY-PEROT SENSORS

DEFENCE COLLEGE OF MANAGEMENT AND TECHNOLOGY

PHD THESIS

CRANFIELD UNIVERSITY

DEFENCE COLLEGE OF MANAGEMENT AND TECHNOLOGY

ENGINEERING SYSTEMS DEPARTMENT

PHD THESIS

ACADEMIC YEAR 2005-2006

Venkata Rajanikanth Machavaram

Micro-machining Techniques for the Fabrication of Fibre Fabry-Perot Sensors

Supervisors: Dr RA Badcock and Professor JG Hetherington

March 2006

Abstract

Fabry-Perot optical fibre sensors have been used extensively for measuring a variety of parameters such as strain, temperature, pressure and vibration. Conventional extrinsic fibre Fabry-Perot sensors are associated with problems such as calibration of the gauge length of each individual sensor, their relatively large size compared to the diameter of optical fibre and a manual manufacturing method that leads to poor reproducibility. Therefore, new designs and fabrication techniques for producing fibre Fabry-Perot sensors are required to address the problems of extrinsic fibre Fabry-Perot sensors.

This thesis investigates hydrofluoric acid etching and F_2-laser micro-machining of optical fibres to produce intrinsic Fabry-Perot cavities. Chemical etching of single mode fused silica fibres produced cavities across the core of the fibres due to preferential etching of the doped-region. Scanning electron microscope, interferometric surface profiler and CCD spectrometer studies showed that the optical quality of the etched cavities was adequate to produce Fabry-Perot interference. Controlled fusion splicing of etched fibres produced intrinsic Fabry-Perot cavities. These sensors were surface-mounted on composite coupons and their response to applied strain was studied using low coherence interferometry. These sensors showed linear and repeatable response with the strain measured by the electrical resistance strain gauges.

To carry out F_2-laser micro-machining of fused silica and sapphire substrates, a micro-machining station was designed and constructed. This involved the design of illumination optics for 157 nm laser beam delivery, the design and construction of beam delivery chamber, target alignment and monitoring systems. Ablation of fused silica and sapphire disks was carried out to determine ablation parameters suitable for micro-machining high aspect ratio microstructures that have adequate optical quality to produce Fabry-Perot interference. Cavities were micro-machined through the diameter of SMF 28 and SM 800 fibres at different energy densities. CCD interrogation of these intrinsic fibre cavities ablated at an energy density of 25×10^4 Jm^{-2} produced Fabry-Perot interference fringes.

The feasibility of micro-machining high aspect ratio cavities at the cleaved end-face of the fused silica fibres and through the diameter of sapphire fibres was demonstrated. A technique based on *in-situ* laser-induced fluorescence monitoring was developed to determine the alignment of optical fibres and ablation depth during ablation through the fibre diameter. Ablation of cavities through the diameter of fibre Bragg gratings showed that the heat-generated inside the cavity during ablation had no effect on the peak reflection and the integrity of core and cladding of the fibre. Finally, a pH-sensor, a chemical sensor based on multiple cavities ablated in multimode fibres and a feasible design for pressure sensor fabrication based on ablated cavity in a single mode fibre were demonstrated.

To my Parents

Acknowledgements

I am very grateful to Engineering Systems Department and Rolls-Royce Plc, for their financial support. I would like to thank Professor Gerard F Fernando, the initiator of this project, for giving me this opportunity, for his guidance, help and encouragement. I would also like to thank my academic supervisor Dr RA Badcock for his continuous help, training and support. I am very thankful to Professor JG Hetherington, head of Engineering Systems Department, for his support and encouragement. I am very grateful to Professor B Ralph for his advice and help throughout the period of my research.

The training and help of the LATE JR Tetlow is gratefully acknowledged. I am very grateful to Mike Teagle, Laboratory Manager of Sensors & Composites Group, for his immense help and encouragement. My special thanks goes to Maggie Keats for her patience, help and support. I am very grateful to Ros Gibson for her help and encouragement. I am very thankful to Dr B Degamber for his continuous help and encouragement during my difficult times and for many useful research discussions. I am very thankful to Sriram Krishnamurthy, my friend and colleague, for his help and encouragement. The help of Paula Bentley and Jo Nash is duly acknowledged. The help and encouragement of Dr J Rock is deeply acknowledged. I am thankful to Dr Francis Goodall, Dr G Kister, Dr J Talbot, Dr RongSheng, Dr C Tuck, Dr Moniruzamman, M Carpenter, R Hall, Dr J Painter and Dr P Geraldus for their help.

I am very thankful to my friends, Nagella Srikanth, Deniz Turan, Rahul Kharche, David Rulloda and B Ravikiran for their timely help and support.

I am very grateful to my mathematics teacher, M Ugandhar, for making me confident student of mathematics. I am extremely grateful to Professors KN Shrivastava, V Srinivasan, V Seshubai, PK Panigrahi, Ashok Chaterjee, Narayanarao, PK Pathak, Datta Gupta, SN Kaul and Dr Suneel Singh for their wonderful lectures in theoretical physics, which formed the driving force behind my research career.

I would like to thank my family, relatives and friends for their support, help and understanding during my research work.

Table of Contents

List of Figures

List of Tables

Glossary

CCD	Charge Coupled Device
DOF	Depth of Focus
EFFPI	Extrinsic Fibre Fabry-Perot Interferometer
ESR	Electron Spin Resonance
FBG	Fibre Bragg Grating
FP	Fabry-Perot
FTIR	Fourier Transform Infra-Red Spectrometer
FWHM	Full Width at Half Maximum
HAZ	Heat-Affected-Zone
HF	Hydrofluoric Acid
IFFPI	Intrinsic Fibre Fabry-Perot Interferometer
LIF	Laser-Induced-Fluorescence
LPG	Long Period Grating
MM	Multi-Mode
NA	Numerical Aperture
OSA	Optical Spectrum Analyser
PTFE	Polytetrafluroethylene
SEM	Scanning Electron Microscope
SLD	Super Luminescent Diode
SM	Single-Mode
UV	Ultra-Violet
Au	Arbitrary Units
Al_2O_3	Aluminium Oxide
Ar	Argon
ArF	Argon Fluoride
CaF_2	Calcium Fluoride
Cl	Chlorine
E′- Centre	Unpaired electron in a dangling sp^3 orbital of a three co-ordinated ‘Si’ atom.

eV	Electron Volt
F_2	Fluorine
F_{th}	Threshold Fluence
Ge	Germanium
GeO_2	Germanium Dioxide
GODC	Germanium Oxygen Deficiency Centre
H_2	Hydrogen
He	Helium
HNO_3	Nitric Acid
Kr	Krypton
KrF	Krypton Fluoride
LiF	Lithium Fluoride
MgF_2	Magnesium Fluoride
N_2	Nitrogen
NBOHC	Non-bridging Oxygen Hole Centre
$n_{cladding}$	Refractive Index of Fibre Cladding
n_{core}	Refractive Index of Fibre Core
Nd-YAG	Neodimium Yttrium Aluminium Garnet
Ne	Neon
O_2	Oxygen
ODC	Oxygen Deficiency Centre
POR	Peroxy-Radical
ppm	Particles Per Million
rms	Root Mean Square
Si	Silicon
SiF	Silicon Fluoride
SiO_2	Silicon Dioxide
SiOH	Silicon Hydroxide
TiC	Titanium Carbide
XeCl	Xenon Chloride

1 Introduction

The use of fibre optic sensors has been increasing rapidly for measuring a variety of parameters such as strain [1], temperature [2], pressure [3] and acoustic emission [4]. These sensors offer unique advantages when compared to conventional electrical sensors in many respects. For example, their dielectric material properties makes them immune to electrical interference and facilitates their use in harsh electrical environments; their small size makes them suitable for embedding inside materials and their chemical composition makes them inert to many chemicals. These sensors are used widely for structural health monitoring of advanced composite materials [5] and civil engineering structures [6].

Among a variety of optical fibre sensors, extrinsic Fabry-Perot (FP) and Bragg grating sensors are used widely due to their simple working principles, interrogation schemes and multiplexing capabilities. However, these sensors suffer from serious drawbacks in certain critical applications. For example, the use of fibre Bragg grating sensors in environments of dynamic strain and temperature changes requires compensation of one parameter for absolute measurement of the other parameter; in structural health monitoring of composite materials using embedded FP sensors, the physical dimensions of FP sensors (300 μm) are relatively much larger than reinforcing fibres (6-12 μm) and their discontinuity in geometric shape can lead to resin pocket and void formation, which not only reduces their reliability for sensing in embedded applications but could also deteriorate the mechanical properties of the host structure [7]. In addition to the problems posed by the geometric shape of the sensor, the manufacturing technique for FP sensors is a manual and laborious process, which makes it a low reproducible process with respect to the cavity length and gauge length, time-consuming and not cost effective.

A promising solution to the design and manufacturing problems of extrinsic fibre Fabry-Perot (EFFP) sensors could be the fabrication of FP cavities within the optical fibres [8]. These intrinsic cavities could reduce the size and the discontinuity in the shape of the

sensor. Hydrofluoric acid etching and laser micro-machining were identified as viable propositions for creating intrinsic FP cavities. A number of intrinsic FP cavity designs were proposed to develop sensors for a variety of sensing applications. The proof-of-concept of hydrofluoric acid etching of optical fibres as a possible alternative for extrinsic FP sensors was demonstrated. Argon fluoride (ArF) and Krypton fluoride (KrF) laser micro-machining of sapphire fibres has resulted in cavities of good optical reflectivity. However, the tapering of micro-machined cavities has been identified as a major obstacle in the path of realising the technique [8]. ArF and KrF excimer laser micro-machining of fused silica had yielded very rough optical surfaces, which are not suitable for FP cavity production. Industrial trials of F_2-laser micro-machining of fused silica and sapphire had produced cavities of well-defined shape. However, their suitability for FP interference and fabrication of intrinsic fibre FP cavities had not been demonstrated previously and hence is the topic of research interest in this project.

1.1 Aims and Objectives

The main aims of this PhD research are concerned with a novel approach to micro-machining Fabry-Perot etalons in fused silica optical fibres using F_2-laser ablation and hydrofluoric acid (HF) etching to fabricate intrinsic fibre Fabry-Perot sensors. The main objectives of this research are stated as follows:

(i) To fabricate intrinsic Fabry-Perot cavities in fused silica optical fibres using HF etching and investigate their response to applied strain.

(ii) To design and construct an F_2-laser micro-machining station, which is suitable for micro-machining high-aspect ratio cavities in fused silica and sapphire substrates.

(iii) To investigate the feasibility of micro-machining Fabry-Perot cavities through the diameter and at the cleaved end-face of fused silica optical fibres.

This PhD thesis reports on two techniques for producing intrinsic Fabry-Perot cavities in optical fibres. The first is hydrofluoric acid (HF) etching and the second is F_2-laser

micro-machining. HF etching of optical fibres to produce intrinsic cavities is possible because germanium doped-core of the optical fibre undergoes preferential etching compared to fibre cladding. SM 800 fibres were used for etching intrinsic cavities. The following aspects were researched and developed: (i) A study of the etch rate of the core and cladding; (ii) the geometry of cavities; (iii) the optical quality of etched cavities; (iv) the tapering of fibres; (v) techniques of fusion-splicing etched fibre end-faces; (vi) interrogation of intrinsic cavities produced from this technique; (vii) a comparison of sensor geometry with extrinsic FP sensors; (viii) and a review of the limitations of this technique. The sensors fabricated from this technique were deployed for measuring the strain in composite coupons and their response to fatigue (tension-tension fatigue) loading was studied. The data from the FP sensors were compared with the strain measured by surface-mounted electrical resistance foil strain gauges.

F_2-laser micro-machining of optical fibres to create FP cavities involved a number of stages. The use of a 157 nm excimer laser for materials processing requires a custom-designed micro-machining station. This involved the design and construction of a purge chamber to establish the beam transmission environment; the design of a beam delivery optical system suitable for micro-machining various geometries of Fabry-Perot micro-structures and the construction of a target alignment and monitoring system for aligning optical fibres in the image plane. Experimental work was carried out to build a suitable F_2-laser micro-machining station.

The next stage of the research was the evaluation of the micro-machining station. This involved: measurement of the transmission characteristics of the laser beam under various ambient conditions of purging, projection of mask features to the desired image dimensions and monitoring of the image plane with respect to the target surface.

Preliminary investigations of 157 nm laser ablation were carried out on fused silica and sapphire disks. These experiments were designed to identify suitable ablation parameters for producing Fabry-Perot micro-cavities. Fused silica and sapphire substrates were micro-machined at different energy densities and pulses. The morphology and optical

quality of ablated structures were studied under a scanning electron microscope (SEM) and an interferometric surface profiler (ISP) respectively. These investigations have formed a basis for further investigations of fibre ablation.

The next phase of the research work was concerned with the identification of suitable energy densities to produce FP cavities along the fibre diameter. Fibres were ablated along their diameter at different energy densities and the influence of energy density on cavity wall angle was studied. Ablation parameters suitable for producing microstructures of near-parallel wall surfaces were identified. The ability of the micro-machined cavity wall surfaces to act as FP etalons was investigated using a CCD (charge coupled device) spectrometer. Ablated microstructures in optical fibres were studied using a scanning electron microscope and an interferometric surface profiler. FP interference via micro-machined FP etalons through the fibre diameter was demonstrated in SM (Single-mode) 800 and SMF (Single-mode fibre) 28 fibres.

In order to obtain quantitative data on fibre ablation, the 157 nm laser-induced fluorescence was monitored *in-situ* at different energy densities and pulses. This was aimed at identifying the changes in fluorescence intensity with cavity ablation depth in fibres. An attempt was made to correlate fluorescence intensity with the ablation depth at a specified energy density. These investigations provided quantitative evidence for identifying cavity ablation depth in fibres during ablation of cavities through their diameter and improved the repeatability of micro-machining FP cavities in fibres.

Ablation of cleaved end faces of optical fibres was carried out to study the ablation characteristics along the germanium-doped core of optical fibres. The ablated structures were studied using an SEM to determine their morphology across the core. Problems associated with fibre alignment were identified as an obstacle in the path of realising this design of intrinsic fibre FP.

Sapphire optical fibres were ablated to demonstrate the fabrication of cavities through the fibre diameter. The optical response of cavities was studied using a CCD spectrometer.

The morphology and optical quality of microstructures in sapphire fibres were studied using an SEM and an interferometric surface profiler.

157 nm laser-induced effects on micro-machined cavities in fibres were studied by monitoring Bragg peak reflection during ablation of cavities through the diameter of fibre Bragg gratings. These experiments were aimed at investigating the effect of the heat generated during ablation on the core of the optical fibre. Cavities were micro-machined at different energy densities through the diameter of fibres on the grating region. The influence of 157 nm radiation on the photorefractive index was studied by irradiating fibre Bragg gratings with a 157 nm laser beam. The influence of 157 nm radiation on Bragg peak reflection was studied.

Finally, some applications of 157 nm laser micro-machined FP cavities were demonstrated. Multiple-cavities were micro-machined through the diameter of multi-mode optical fibres. The length of the fibre with micro-machined cavities was immersed in an acidified bromocresol dye solution. The pH of this solution was changed and the sensor was calibrated based on its transmitted output spectral intensity against the pH recorded by a pH meter. Multiple intrinsic cavities in multi-mode fibres were also used as transmission cells to detect amine in polyoxypropylenediamine to demonstrate chemical sensing. An attempt was made to demonstrate the feasibility of fabricating a pressure sensor in an SM 800 fibre via micro-machining a cavity through its diameter near the cleaved-end of the fibre.

1.2 Structure of the Thesis

This PhD thesis has been structured in the following manner:

Chapter 1: Introduction
A general overview of the issues covered in the thesis is presented in chapter one.

Chapter 2: Literature review

In chapter 2, a general introduction to interferometric optical fibre sensors is presented. Various techniques for the fabrication of FP sensors for different sensing applications are reviewed and the feasibility of laser micro-machining as a viable proposition for FP sensor fabrication is identified. Laser-material interactions during micro-machining and ablation of fused silica and sapphire substrates are reviewed to determine the feasibility of micro-machining FP cavities. The influence of various optical beam delivery systems on the quality of micro-machining is reviewed to identify the critical parameters of the optical beam delivery system for producing FP microstructures. Various critical issues involved in F_2-laser micro-machining are reviewed prior to building a micro-machining station. Chemical etching techniques for the production of optical fibre sensors are reviewed.

Chapter 3: Design and construction of F_2-laser micro-machining station

This chapter presents the design and construction of the purge chamber, the deployment of motorised translation stages for target alignment and a custom-designed target-monitoring system.

Chapter 4: Illumination design of optical beam delivery system

This chapter presents the design of illumination system for mask projection based on Köhler illumination. The degree of partial coherence of the imaging system is interpreted on the basis of Hopkin's partial coherence theory as presented in chapter 2.

Chapter 5: Experimental

This chapter gives a detailed account of experimental procedures that were used for conducting hydrofluoric acid etching of optical fibres, evaluation of F_2-laser micro-machining station, ablation of fused silica and sapphire disks, ablation of fused silica and sapphire optical fibres, *in-situ* monitoring of laser-induced fluorescence, ablation of fibre Bragg gratings and application of micro-machined optical fibres to demonstrate pH-sensing and chemical sensing of polyoxypropylenediamine. The experimental procedure

for demonstrating feasibility of fabricating pressure sensors using laser micro-machining is also presented.

Chapter 6 to 12: Results and discussion
These chapters present the results and discussion of chemical etching experiments, beam transmission experiments, ablation of fused silica and sapphire disks, ablation of optical fibres, *in-situ* monitoring of laser-induced fluorescence, F_2-laser radiation effects on fibre Bragg gratings and applications of laser micro-machined sensors respectively.

Chapter 13: Conclusions and suggestions for future work

1.3 Contributions of this Research

This PhD research has demonstrated two novel techniques for the fabrication of repeatable intrinsic Fabry-Perot cavities in fused silica optical fibres. These techniques have not only overcome the problems involved in the design and manual fabrication of extrinsic fibre Fabry-Perot sensors but also have the potential for the development of novel sensor systems. HF etching of optical fibres has been proved to be a low-cost technique for the fabrication of strain sensors. These sensors could be used for structural health monitoring of aerospace composite materials and civil engineering structures. F_2-laser micro-machining of fused silica optical fibres through their diameter has been found to be a feasible technique for fabricating intrinsic Fabry-Perot cavities. This is the first demonstration of a one-step fabrication process for producing intrinsic Fabry-Perot interferometers in optical fibres using laser ablation. These intrinsic cavities can be used as miniature transmission cells for monitoring chemical reactions through which a variety of chemical sensors can be developed. Based on the principle of measurement of changes in the cavity length via Fabry-Perot interference, these intrinsic fibre Fabry-Perot cavities could be used for developing strain, temperature and pressure sensors. The cavities micro-machined through the diameter of sapphire fibres could be filled with suitable materials and be used for high temperature sensing applications. The cavities in sapphire

fibres could also be used as transmission cells in high temperature environments for chemical process monitoring.

2 Literature Review

The advent of fibre optic sensing techniques based on interference of electromagnetic radiation has led to the development of sensors for measuring a variety of measurands such as strain, temperature and pressure. The basic working principle of interferometric sensors is measurand-induced optical path changes, which can be detected from the changes in the spectral interference. A variety of optical configurations and demodulation schemes have been developed for decoding the measurand. Optical fibre equivalents of the classical Fabry-Perot, Mach-Zehnder and Michelson interferometers and fibre Bragg gratings are the most common interferometric sensors. These sensors are used widely for structural health monitoring of advanced composite materials and civil engineering structures.

2.1 Single Mode and Multimode Fibres

Optical fibres are mainly classified into single-mode and multi-mode fibres. Single-mode fibres guide a single transverse mode, which is defined by two orthogonal polarization states [9]. A constant phase relationship exists between these two states as the mode propagates through the fibre and maintains the coherence of the guided beam. Therefore these fibres are suitable for phase modulation and used for making interferometric sensors. However in practice, due to deviations from circular symmetry of the refractive index distribution of the fibre core, a phase difference occurs between the polarisation states which leads to a reduction in the coherence of beam [10] . Typically, these fibres have a core diameter of 5 to 10 μm.

Multi-mode fibres guide a number of modes depending on the size of the fibre core. These multiple transverse modes have different phase constants and are essentially incoherent [11]. Therefore, these fibres are not suitable for phase modulation devices. These fibres are used widely for sensors based on intensity modulation. However, these sensors suffer from a lack of self-referencing intensity, which is due to intensity modulation caused by factors other than the measurand such as intensity fluctuations in the light source, perturbations along the fibre length and connectors. Typically,

these fibres have a core diameter of several tens of micrometres and carry much larger power of light than single mode fibres.

2.2 Mach-Zehnder and Michelson Interferometers

These interferometers have two single mode fibre paths of equal length: one arm is a reference signal carrier and the other arm is exposed to the measurand. In the Mach-Zehnder arrangement, the measurand-induced phase difference between the sensing and reference signals undergoes interference and produces fringes of superposition [12]. This arrangement is illustrated schematically in Figure 2-1.

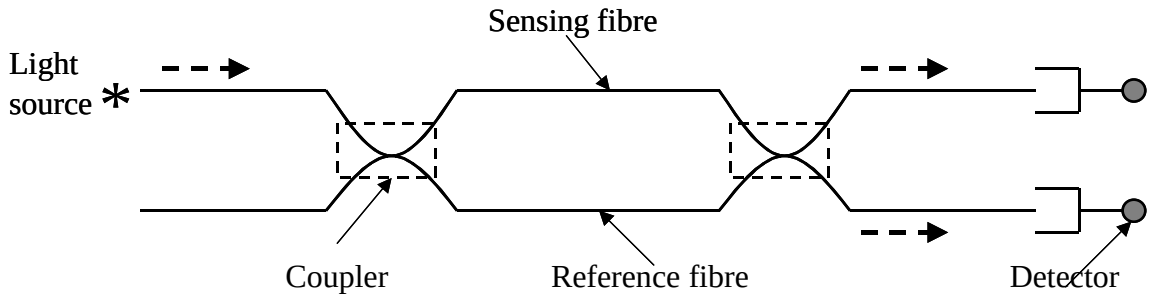

Figure 2-1: Schematic illustration of a Mach-Zehnder Interferometer.

In the Michelson interferometer, the sensing fibre is longer than the reference fibre and only one coupler is used to recombine the sensing and reference signals. Measurand-induced changes in the optical path difference between the two arms can be detected from the changes in the interference produced by the two signals. This arrangement is shown in Figure 2-2.

The essential criterion to be satisfied for producing interference of the reference and sensing signals in both these interferometers is that the difference between the optical path lengths of these two arms must be smaller than the temporal coherence length of the light source [13].

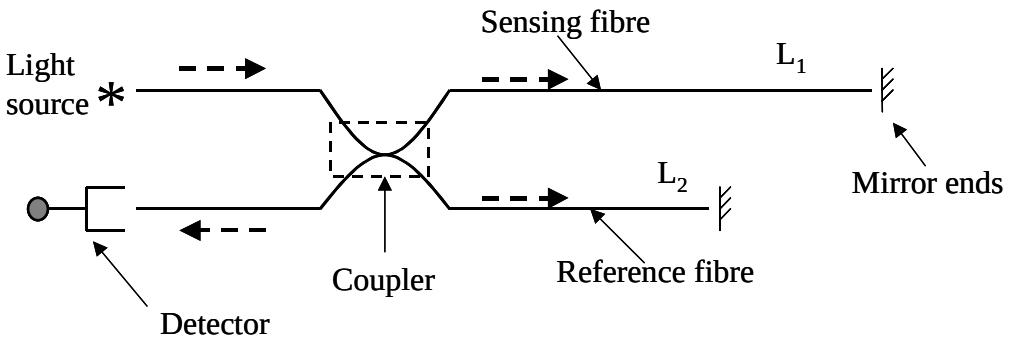

Figure 2-2: Schematic arrangement for a Michelson interferometer.

2.3 Extrinsic Fibre Fabry-Perot Interferometer

An extrinsic fibre Fabry-Perot interferometer (EFFPI) is constructed by using two single mode fibres, a single mode and a multimode reflector [14], two multimode fibres [15] and a precision bore glass capillary. The cleaved ends of the fibres are inserted into the capillary and separated by a distance ‘d’, the cavity length. The separation between the fusion points of the capillary and fibres is the gauge length of the sensor. The fibres are held inside the capillary by fusion splicing of the fused silica capillary and fibres or adhesive bonding. The typical internal diameter of the capillary is 128 μm with an external diameter of 300 μm. This design is shown in Figure 2-3 [16].

Light coupled into one of the optical fibres undergoes Fresnel reflection at the glass/air interface and the transmitted light undergoes Fresnel reflection at the air/glass interface of the cleaved ends of the optical fibres inside the silica capillary. Coherent light undergoing Fresnel reflections between the partially reflective parallel mirrors of the cavity produces optical interference. The optical path difference ‘2d’ between these two signals produces fringes of interference.

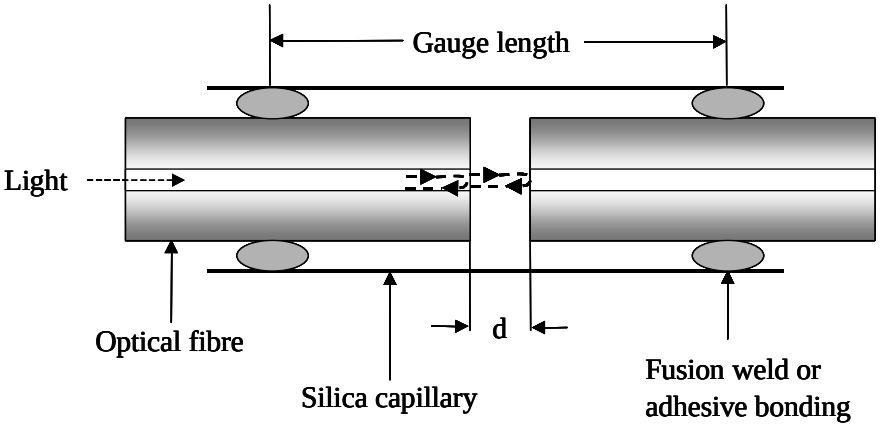

Figure 2-3: Schematic illustration of a fibre Fabry-Perot interferometer.

The phase 'φ' of the interference signal at a wavelength 'λ' can be expressed as [17]:

$$\varphi = \left(\frac{2\pi}{\lambda}\right) 2d \qquad \text{Equation 2-1}$$

where 'λ' is the design wavelength of the fibre.

The optical response of EFFPIs requires a suitable interrogation scheme to measure the changes in the interference pattern under the influence of the external parameters. The changes in the cavity length have to be measured from the changes in the interference pattern. The following section presents the interpretation of interference signal, calculation of cavity length and CCD interrogation of EFFPI sensor response.

2.3.1 Interrogation of Cavity Length

The sensing mechanism of Fabry-Perot (FP) sensors is a measurand-induced cavity length change, which can be detected from the interference fringe pattern. The absolute cavity length of the interferometer can be determined from the fringes of superposition using low coherence white light interferometry. A typical interference fringe pattern of the Fabry-Perot interferometer is presented in Figure 2-4. The optical path imbalance between the receiving and sensing interferometers produces cosine

fringes modulated by the transfer function of the light source. The cavity length can be determined from the FP interference as follows [18]: 'λ_1', 'λ_2' shown in Figure 2-4 are the two wavelength components of source that have a phase difference of integral multiples of 2π radians in the interference pattern. The phase difference at wavelength 'λ_1' between the two reflected beams, which has a path length difference of '2d' is expressed as:

$$\varphi_1 = \left(\frac{2\pi}{\lambda_1}\right)2d \qquad \text{Equation 2-2}$$

As the response at wavelength 'λ_1' is due to constructive interference, the phase difference is an integral multiple of 2π radians. At successive interference maxima, the phase difference will be $2\pi(N+1)$, $2\pi(N+2)$, $2\pi(N+3)$,…,$2\pi(N+n)$, where 'N' is an integer. Hence, the phase difference can be expressed as:

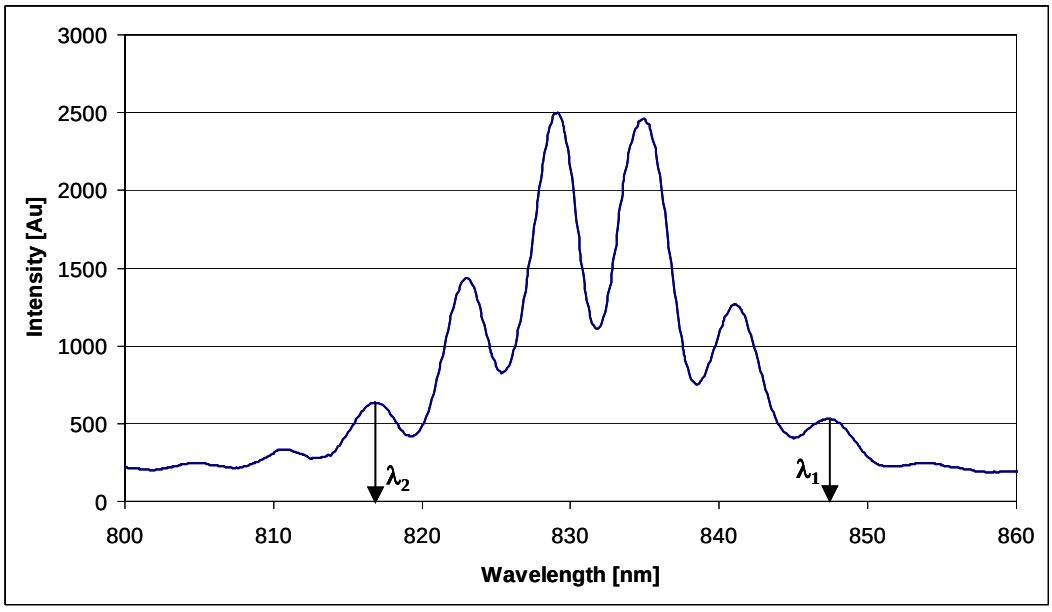

Figure 2-4: Spectral interference of a fibre Fabry-Perot sensor.

$$\varphi_1 = \left(\frac{2\pi}{\lambda_1}\right)2d = 2\pi N \qquad \text{Equation 2-3}$$

The phase difference at wavelength 'λ_2' can be expressed as:

$$\varphi_2 = \left(\frac{2\pi}{\lambda_2}\right)2d = 2\pi(N+n) \qquad \text{Equation 2-4}$$

where 'n' is the number of interference minima between the wavelengths 'λ_1' (nm) and 'λ_2' (nm).

The phase difference between the two interference maxima at wavelengths λ_1 and λ_2 can be expressed as:

$$\varphi_2 - \varphi_1 = \left(\frac{2\pi}{\lambda_2}\right)2d - \left(\frac{2\pi}{\lambda_1}\right)2d \qquad \text{Equation 2-5}$$

$$\Rightarrow 2\pi(N+n) - 2\pi N = 4\pi d\left[\left(\frac{1}{\lambda_2}\right) - \left(\frac{1}{\lambda_1}\right)\right]$$

$$\Rightarrow 2\pi n = 4\pi d\left(\frac{\lambda_1 - \lambda_2}{\lambda_1\lambda_2}\right)$$

$$\Rightarrow d = \frac{n\lambda_1\lambda_2}{2(\lambda_1 - \lambda_2)} \text{ nm} \qquad \text{Equation 2-6}$$

With reference to Figure 2-3, the absolute cavity length and the changes in the cavity length under the influence of the measurand can be determined from the interference fringe pattern. The change in the cavity length 'Δd' for a strain of 'ε' can be expressed as:

$$\varepsilon = \frac{\Delta d}{L} \qquad \text{Equation 2-7}$$

where 'L' is the gauge length of EFFPI sensor.

The basic interrogation scheme for detecting FP interference by using low coherence white light interferometry is illustrated in Figure 2-5. Light from a low coherence source is coupled into the EFFPI via a directional coupler. The light undergoing Fresnel reflections from the cleaved fibre ends is coupled via a coupler into a Fizeau interferometer and onto a CCD (charge coupled device) or a linear photodiode array [19]. The variable cavity length of the Fizeau interferometer matches with the cavity gap length of the EFFPI by recognising the maximum transmitted intensity position on the Fizeau wedge. This resonance position forms the reference and indicates the absolute EFFPI cavity gap length. The deviations from the reference position due to measurand-induced gap changes are measured.

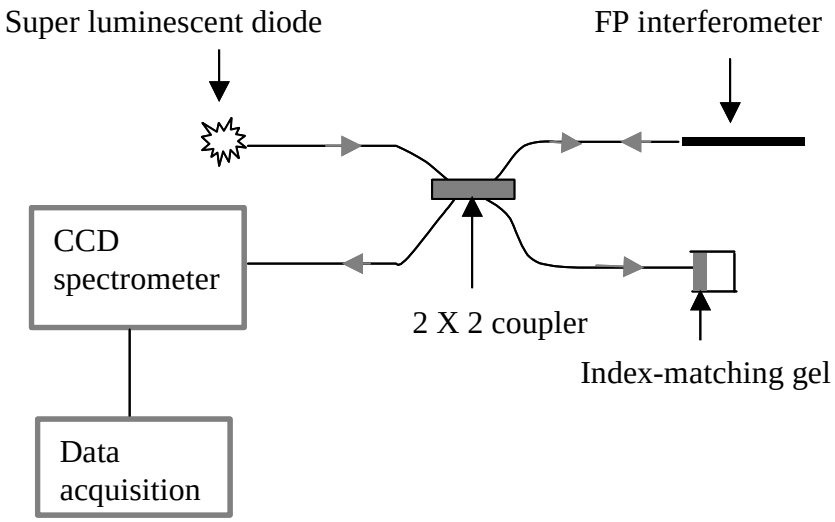

Figure 2-5: Interrogation scheme for measuring FP interference.

In white light low coherence interferometry, although the coherence length of the light source is smaller than the optical path length of the sensing interferometer, the interference fringes of superposition can be visualised under the condition that the difference in the optical path differences of sensing and reference interferometers is less than or equal to the coherence length of the light source [20].

EFFPIs are relatively compact, simple and involve less instrumentation for interrogation and have high multiplexing capability [21] than Michelson and Mach-Zehnder interferometers. However, the coupling efficiency of mono-mode EFFPI sensors is much smaller compared with multi-mode fibre FPs [15]. The problematic

issue of EFFPI sensors is that the manual fabrication method results in poor reproducibility of cavity length and gauge length. The following section gives an account of the problems involved in the manual fabrication method.

2.3.2 Manufacturing Problems Associated with EFFPI Sensors

Although EFFPIs are simple and easy to use, these sensors suffer from manual manufacturing techniques. The problems associated with manual fabrication can be stated as follows:

- Non-reproducible cavity length and gauge length of the sensor, which results in a need for independent calibration of each sensor;
- Difficulty of determining the exact gauge length;
- Accidental damage of cleaved ends during fibre insertion and airborne contamination, which deteriorates reflectivity;
- Misalignment of fibres during fusion splicing or adhesive bonding;
- Demands highly skilled labour and is a time consuming process; and
- Not suitable for industrial scale of production.

In order to avoid the problems involved in the manual fabrication of EFFPIs, new techniques for the fabrication of fibre Fabry-Perot sensors have been developed. The following section presents fabrication techniques involved in intrinsic and in-line fibre Fabry-Perot sensors for various applications.

2.4 Intrinsic and In-line Fabry-Perot Interferometers

Besides EFFPI, there are two types of fibre interferometers based on FP interference: intrinsic and in-line FP interferometers. In intrinsic FP interferometers, the partial reflectors are intrinsic to the fibre and are produced by creating reflecting interfaces along the fibre length. These reflectors are not separated by an air-gap. In-line FP interferometers are similar to EFFPI in the sense that the air gap exists only in between fibre end faces of cleaved fibres with no discontinuity of sensor geometry.

The literature review on intrinsic and in-line FP interferometers presents different fabrication techniques and associated problems.

Lee *et al.* [22] demonstrated intrinsic FP interferometers by producing multi-layer dielectric mirrors on fibre ends. Seven alternating layers of TiO_2/SiO_2 were deposited at the cleaved end of an optical fibre using a magnetron-sputtering system. The coated-end of the fibre was fusion spliced to an uncoated cleaved fibre by repeated and controlled splicing sequences in order to preserve the coating reflectivity. The other end of the uncoated fibre was spliced to the coated end of another fibre of the same reflectivity by repeating the same procedure to produce a Fabry-Perot cavity length of 9.5 mm between the two internal mirrors. The mirror reflectivity was reduced to 86% after fusion splicing from its initial reflectivity of 93%. A diode laser was used to illuminate the interferometer and the transmitted and reflected powers were measured when the interferometer was exposed to temperature changes in the linear regime of refractive index change of the fibre mode. Although the procedure for producing these two mirrors is the same, the measured transmitted and reflected powers during heating were smaller than powers calculated by assuming equal reflectivity of internal mirrors. The internal mirror finesse achieved by this technique was higher than the single layer coating of TiO_2 [23], [24] and better sensitivity was achieved. The problem with this technique is the poor repeatability of predetermined (or calculated) internal mirror reflectivities and mechanical strength of the splice.

Intrinsic FP configurations based on internal mirror coatings of TiO_2 were used for temperature measurements up to 800 °C [25]. A similar technique based on the thermal expansion of alternating layers of different refractive indices was used to measure temperatures up to 1100 °C [26]. A stack of one hundred and twenty layers of quarter wavelengths of highly temperature resistant silicon nitride and silicon-rich silicon nitride, which slightly differ in their refractive indices, were coated on the cleaved-end of the optical fibre. Constructive superposition of light reflected from the alternating layer stacks produced a strong peak reflection. The sensing mechanism is the shift in peak reflection due to the thermal expansion of these layers.

Kaddu *et al.* [27] used co-located or closely spaced Bragg gratings of different peak reflections to produce low coherence FP interference or near-sinusoidal transfer function. Three co-located Bragg gratings of nearly equal peak reflectivities and a FWHM of 0.6 nm at 827, 829, 831 nm were used. The peak reflections were chosen close to each other in order to use a single broadband light source. An SLD (super luminescent diode) at 830 nm with a FWHM of 9 nm was used for illumination. A bulk FP interferometer was used as a receiving interferometer. The combined effect, which is a beat envelope of FP fringes, is the superposition of outputs obtained at each reflection wavelength. The sensor was subjected to temperature changes from 20 to 60 °C and the centre of the fringe pattern was monitored to measure the changes in optical cavity length between the sensing and receiving interferometers. This technique has a relative ease in fabrication compared with the internal mirror splicing technique. However, sensors based on fibre Bragg gratings are not suitable for temperature measurements above 500 °C due to irreversible changes in refractive index modulation [6]. Recent studies of the use of Bragg gratings written on optical fibres with dopants such as B(Boran)-Ge(Germanium) and CCG (chemical composition grating), which were fabricated from hydrogen-loaded fluorine-doped germanosilicate fibres, had shown that these gratings can be used at temperatures well above 800 °C and up to 1100 °C respectively [28]. Bragg gratings were also used for measuring cryogenic temperatures (range: 300 K to 77 K) by sandwiching gratings in between Teflon substrates [29]. Teflon substrates, which have a high thermal expansion coefficient, were used to compensate the decreasing temperature sensitivity of Bragg gratings with decreasing temperature.

MacPherson *et al.* [30] used a fibre Bragg grating and a cleaved fibre end to form a low finesse intrinsic FP cavity. A Bragg grating was written on a single mode fibre at 784.89 nm with a peak reflectivity of 5.6% and a bandwidth of 3 nm. The fibre was cleaved at a distance of 3 mm from the Bragg grating. An FP cavity was produced when the sensing element was illuminated with the laser diode of a wavelength matching the Bragg reflection. The interference of Fresnel reflection from the cleaved end and the Bragg reflection produced FP interference. This intrinsic FP design was used to measure a transient heat flux. The sensor was operated in quadrature or the highest sensitivity condition to obtain the expected phase change of 2π. These

intrinsic FP designs based on Bragg gratings have the problem of cross sensitivity of strain and temperature.

Sirkis *et al.* [31] demonstrated an in-line FP cavity. This is similar to an EFFPI in the sense that an air cavity separates the cleaved ends of fibres. A hollow core fibre with an outer diameter the same as the optical fibres and an inner diameter of 70 μm was produced by drawing a silica tube of 3 mm inner diameter and 5 mm outer diameter. The hollow core fibre was cleaved to lengths ranging from 50-200 μm. Single mode optical fibres were fusion spliced to either end of the cleaved hollow fibre by controlling fusion splicing parameters. The bending strength of these fibres was found to be 17% less than the bending strength of stripped fibres. This design is more compact than an EFFPI and avoids geometric discontinuities. Unlike an EFFPI, the gauge length and the gap length of these sensors is the same. However, fabrication of these sensors involved tedious processes such as cleaving the hollow fibres to microscopic lengths and splicing them to fibres.

In comparison to EFFPIs, inline and intrinsic fibre Fabry-Perot interferometers avoid problems such as non-reproducibility of gauge length and cavity length. However, there are problems associated with intrinsic and inline Fabry-Perot sensors as well. For example, the dielectric internal mirror [22] technique suffers from poor reproducibility of internal mirror reflectivity and fusion joint; co-located Bragg gratings technique [27] suffers from cross-sensitivity of strain and temperature; hollow core fibre technique [31] is a complex fabrication technique as it involves cleaving of hollow fibres to microscopic lengths followed by fusion splicing. Therefore, there is a need for new manufacturing techniques of fibre Fabry-Perot sensors. In this research work, a couple of new techniques are explained in Sections 2.8 and 2.9 and developed further in this thesis.

Another type of fibre optics sensor that is widely used for sensing applications is the Bragg gratings sensor and its basic working principles are explained below.

2.5 Fibre Bragg Grating Sensors

A fibre Bragg grating (FBG) constitutes a periodic refractive index modulation on the photosensitive core of the optical fibre [6]. The widely used technique for producing FBGs is phase-mask writing. Phase mask suppresses all the orders of diffraction except ±1 orders. Spatially coherent ultraviolet laser sources are generally used for inducing refractive index changes. The near field interference pattern of +1 and –1 orders of diffraction is replicated as a modulation of refractive index along the germania-doped core of the fibre. When light is coupled through the fibre, it undergoes Fresnel reflections from various grating planes and these reflections constructively overlap to produce a narrow band reflection. This Bragg wavelength 'λ_B' can be expressed as:

$$\lambda_B = 2n_{eff}\Lambda \text{ nm} \qquad \text{Equation 2-8}$$

where, 'n_{eff}' is the effective refractive index of the fibre core and 'Λ' (nm) is the period of refractive index modulation, which will be half the period of phase mask. A schematic of a fibre Bragg grating sensor is shown in Figure 2-6.

When a FBG is subjected to strain and temperature, the modulated region experiences changes in refractive index and grating-spacing. This results in a shift of Bragg reflection. The effect of longitudinal strain 'ε' on Bragg wavelength can be expressed as [6]:

$$\Delta\lambda_B = \lambda_B(1 - P_e)\varepsilon \text{ nm} \qquad \text{Equation 2-9}$$

where, '$\Delta\lambda_B$' is the shift in Bragg wavelength and 'P_e' is the effective strain optic constant.

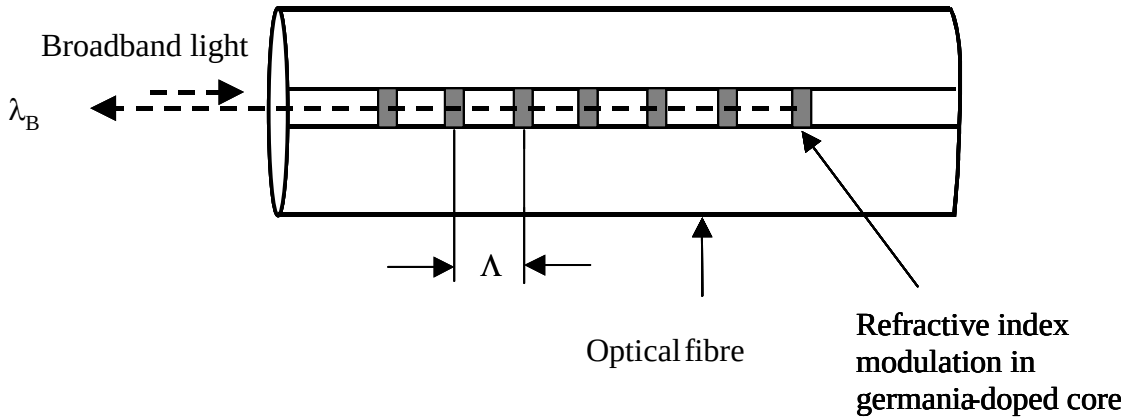

Figure 2-6: Schematic illustration of a fibre Bragg grating sensor.

The effect of a temperature change 'ΔT' (°C) on the Bragg wavelength can be expressed as:

$$\Delta\lambda_B = \lambda_B(\alpha_n + \alpha_\Lambda)\Delta T \qquad \text{Equation 2-10}$$

where 'α_n' ($°K^{-1}$) and α_Λ ($°K^{-1}$) are the thermo-optic coefficient of the germania-doped core and thermal expansion coefficient of the fibre respectively.

The cross-sensitivity of FBGs to strain and temperature is a major problem, which limits their application in environments of dynamic strain and temperature changes. Therefore, for absolute measurement of a measurand, an FBG must be isolated from the other measurands to which it is sensitive [32]. These sensors are simple, compact and mechanically robust and can be mass-produced. These sensors are used widely for structural health monitoring of advanced composite materials [2] and civil engineering structures [33]. EFFPI sensors are also used extensively for a variety of applications such as structural health monitoring, temperature, strain and pressure monitoring. The design of EFFPI sensors can be modified as per the requirements of the application. Numerous applications of EFFPI sensors are described in the next section.

2.6 Applications of EFFPI sensors

The main advantage of the basic design of the EFFPI sensors over the Bragg grating sensors is that the EFFPI sensors are insensitive to temperature and transverse strain.

The design and geometry can be modified to meet the requirements of the application. However, the geometry of EFFPI sensor causes problems in embedded applications. This section presents the applications of these sensors and problems associated with them.

2.6.1 Structural Health Monitoring

Fibre reinforced composite materials are replacing conventional engineering materials due to their high stiffness-to-weight ratio and strength-to-weight ratio. Their mechanical and thermal properties can be easily tailored to meet custom requirements. EFFPIs are used widely for studying various factors affecting the health of composite structures [5]. These sensors can be easily embedded or surface mounted due to their small size, compactness and durability in harsh environments. However, the use of EFFPIs for structural health monitoring is limited by the intrinsic factors of sensor design.

Lee *et al.* [7] investigated the effect of embedded sensors on mechanical properties of composite structures. The fatigue life of unidirectional and cross-ply specimens of glass/epoxy composites was significantly reduced with an increasing number of embedded optical fibre sensors. Cyclic fatigue tests of cross-ply composites have shown that most of the matrix cracks were initiated from the sites of embedded optical fibre sensors whereas the cracks were initiated from the edges of the specimen when no sensors were embedded. Finite element analysis (FEA) of these tests confirmed that stress and strain concentrations due to resin-rich regions around the sensor and the angular orientation of embedded fibres to the reinforcing fibres are responsible for degradation of fatigue life.

Levin and Jarlas [34] investigated the effect of low-energy impacts on embedded EFFPI sensors. The failure mechanisms in the ply groups of carbon fibre reinforced composites, where an EFFPI sensor was embedded, were studied. A piezo-transducer detected acoustic emission in the plates with embedded sensors. Microscopic examination revealed that de-bonding in the sensor and in the polyimide interface had occurred. The plate without a sensor resisted a load almost five times larger without

resulting in damage. The interaction of the sensor with the matrix is different at different depth positions and the vulnerability of the sensor was higher when embedded near surfaces. FEA showed that local stress concentrations leading to de-bonding of the sensor is the most critical failure mode.

The discontinuity in the geometry of EFFPIs is the cause of resin-rich regions and voids on both the sides of the sensors. The effect of these resin pockets is more pronounced when the sensors are at an angle to the adjacent plys. These resin pockets could be minimised by embedding the sensors parallel to the reinforcing fibres in-between parallel plies [5]. The size of the EFFPI sensing region is much larger than reinforcing fibres, which could lead to micro-bending of optical fibres [35] . Therefore, the performance and reliability of these sensors are severely affected by its dimensions and discontinuities in geometry.

2.6.2 Other Applications of EFFPI sensors

Fernando *et al.* [1] modified the design of EFFPI and demonstrated a variety of applications. A multimode EFFPI was embedded in a carbon fibre reinforced composite and was subjected to tensile and compressive strain. The sensor was interrogated in reflection mode to monitor cavity gap changes from FP interference and transmission mode for intensity-based measurements. The response of the sensor was found to be linear in both the interrogation schemes with the extensometer measurements. The design of the multimode EFFPI was modified by using a precision bore metal capillary in place of silica capillary for cure monitoring of epoxy resin. A slot was made on the surface of the metallic capillary to permit the ingress of uncured resin. The chemical kinetics of cure were verified by monitoring the transmission spectrum. However, the induction of a slot in the capillary was mechanical and produced deformation. Therefore, fibre alignment and repeatable gap lengths were not guaranteed through this technique. This cured specimen was immersed in distilled water and the ingress of moisture into the cured resin was periodically monitored from the transmission spectrum. The use of multimode EFFPIs is particularly useful for cure monitoring or moisture detection due to its high light-coupling efficiency. Although, an EFFPI itself is insensitive to temperature changes, the mismatch in

thermal expansion coefficients of sensor and matrix makes it sensitive to temperature. The design of an EFFPI was modified to discriminate between the dynamic effects of strain and temperature. A fibre Bragg grating was inserted into the quartz capillary with its cleaved distal end acting as a mirror and a multimode fibre as another mirror. The sensor was interrogated using low coherence interferometry. When this was embedded in composite material and subjected to dynamic strain and temperature changes, the response of the strain-isolated Bragg grating showed good linearity with thermocouple measurements and an FP showed good linearity with strain gauge measurements. An EFFPI was modified for vibration measurement. A multimode fibre was inserted into a precision-bore silica capillary and fusion welded to the capillary with its cleaved end, that acted as a cantilever fibre, projected out of the capillary. Another multimode fibre was inserted into the capillary with its cleaved end coinciding with one end of the capillary and fusion welded to it. These capillaries were supported in another silica capillary with a cavity gap in-between the two mirrors. These two smaller capillaries were bonded to the supporting tube at its ends using an adhesive. The working principle is that the vibrations produced by the electromagnetic shaker table change the light coupling efficiency into the cantilever fibre as it vibrates from its mean position. This was calibrated against a piezoelectric accelerometer at different applied frequencies and amplitudes. This work shows how the EFFPI sensor design could be modified for measuring a variety of measurands in transmission or reflection modes.

Yu *et al.* [36] modified an EFFPI design for detecting acoustic waves of partial discharges in power transformers. An optical fibre was inserted and fusion welded into a fused silica capillary such that the cleaved end coincided with one end of the capillary. This was again inserted and fusion welded into another fused silica capillary such that a small length separated the ends of both the capillaries. A fused silica diaphragm was fusion welded to the open end of the outer capillary to produce an FP cavity. Fused silica capillaries and the diaphragm were used to minimise the effects of temperature. The thickness of the diaphragm was 125 μm or 250μm with 10% reflective coatings. The acoustic waves generated during partial discharges deflect the diaphragm due to a difference in pressure on either side of the diaphragm. Membrane deflections modulate the cavity length and were measured using low coherence

interferometry. The difficulty in controlling the cavity length and loss of interference fringes due to cavity modulation caused by the hydrostatic pressure of the transformer oil, affected the repeatability of fabrication.

A similar design for detecting pressure was reported by Xu et al. [37]. A 1.5 mm diameter pit was mechanically drilled into the end-face of a 1.8 mm diameter fused silica ferrule. An optical fibre was introduced into the bore of the ferrule. A 125 μm silica diaphragm, which was coated with a thin reflective film, was welded to the end face of the ferrule using a CO_2 laser. The fibre was also welded to the ferrule using the CO_2 laser. An excellent linearity of cavity gap changes due to pressure changes in the range of 25-700 °C was achieved.

A modified EFFPI design was used for temperature sensing [38]. The insensitivity of an all-fused silica EFFPI had been overcome by using a borosilicate glass capillary, which has a thermal expansion coefficient 7 times larger than fused silica to obtain a thermal expansion mismatch. The sensitivity of this sensor was improved by using a soda-silicate reflector and fused silica capillary. The thermal expansion coefficient of soda-silicate reflector fibre was 17 times higher than fused silica. This thermal mismatch produced a sensitivity of 162 nmK^{-1} to an accuracy of ± 0.5 °C in the temperature range of 23 – 250 °C. The use of this sensor above 250 °C produced deformations in the fusion weld due to large thermal mismatch.

2.7 Conclusions on EFFPI Sensors

Although the use of EFFPI sensors for measuring a variety of measurands has been reported, the fundamental problems involved in manual manufacturing techniques were not sufficiently addressed in the literature. The problems of sensor size and discontinuity of geometry are major problematic issues in structural health monitoring. Although intrinsic FP designs, which replicate EFFPI design, are promising to some extent, the fabrication techniques are complex and not easily repeatable. The existing temperature sensors based on an EFFPI design are not suitable for use in high temperature environments above 1500 °C. The literature survey on EFFPI-based sensors shows a high requirement for low-cost novel

manufacturing techniques for the repeatable production of intrinsic Fabry-Perot sensors to address the needs of the aerospace composites industry and high temperature applications.

As mentioned in the introduction and aims of the research in Chapter 1, excimer laser-based fabrication of Fabry-Perot cavities is thought to be a viable proposition [8] for making fibre Fabry-Perot sensors. The technique of micro-machining high aspect ratio Fabry-Perot cavities in optical fibres via laser ablation is believed to yield intrinsic FP sensors which could over come the problems involved in the manual fabrication and design of EFFPI sensors. Before discussing the use of these lasers for manufacturing sensors, various aspects involved in excimer laser ablation of fused silica and sapphire substrates with reference to the fabrication of high aspect ratio Fabry-Perot cavities are presented.

2.8 Laser Micro-machining

Ultraviolet (UV) laser micro-machining has made a vital contribution to the development of micro and nano-technologies. UV-lasers such as frequency tripled (λ = 355 nm) and quadrupled (λ = 266 nm) Q-switched Nd-YAG lasers and excimer lasers such as XeCl (λ = 308 nm), KrF (λ = 248 nm), ArF (λ = 193 nm) and F_2 (λ = 157 nm) are being extensively used for materials processing. The use of excimer lasers for materials processing is better than other UV-lasers due to their short pulse duration and high photon energies that exceed the band-gap energy of many materials of interest for industrial and fundamental research.

Ablation is the spontaneous vaporization of a material when intense laser energy interacts with the solid or liquid phase of a material. Ablation of materials involves complex interactions such as electronic excitation, decomposition, heating, melting, expansion, plasma generation, condensation, solidification and sublimation. It is a combination of photo-chemical and photo-thermal processes. These interactions are governed by the physical and chemical properties of the material and the properties of interacting electro-magnetic radiation.

Ablation of a material at specified wavelengths is particularly governed by four factors: (i) the absorption of radiation by the material, (ii) the energy of the photon, (iii) the energy density of irradiation, and (iv) the duration of the laser pulse. The literature review on laser micro-machining presents ablation mechanisms for fused silica and sapphire at different excimer wavelengths and pulse durations. Ablation at other UV-wavelengths is also discussed along with the ablation at ultra short-pulsed visible wavelengths, optical beam delivery systems and recent technological advancements of laser micro-machining. The above mentioned aspects of the literature review will be discussed with reference to identifying and developing a suitable technology for laser micro-machining of intrinsic Fabry-Perot microstructures in optical fibres for a variety of sensing applications.

The following section presents ablation characteristics of fused silica and sapphire at various excimer wavelengths to identify the suitability of micro-machining FP cavities.

2.8.1 Ablation at Excimer wavelengths

Ihlemann [39] studied ablation of fused silica at 193, 248 and 308 nm wavelengths. Ablation of polished (arithmetic average roughness, R_a = 2 nm) and rough samples (R_a = 400 nm) of thickness 1-2 mm was carried out. The experimental results of ablation at these three wavelengths are presented in Table 2-1.

The photon energies of 4.03 eV (308 nm), 5 eV (248 nm), 6.43 eV (193 nm) were not sufficient to bridge the energy band gap of fused silica of ~8 eV. Therefore, bond breaking of Si-O occurs via two-photon absorption at sufficiently high energy densities [39]. Material ablation occurs by volume absorption of photon energy followed by bond- breaking, conversion to the molten state, then followed by material vaporization. The incubation period in polished samples is due to colour centre formation, which enhances absorption of light leading to clean ablation. The initial pulses of irradiation on a polished sample create imperfections on the surface, which act as light trapping centres. These imperfections enhance volume absorption of radiation and cause material ablation. After the incubation phase in polished samples,

the material ablation is the same as that of rough samples. In rough samples, the material ablation occurs from the first pulse in the form of explosive sputtering. The absence of an incubation phase in rough samples was attributed to direct volume absorption of radiation due to light trapping imperfections of the rough surface. These singularities are responsible for the lower ablation threshold (energy density below which material ablation is not possible) of the rough samples. The lower ablation threshold of polished samples at lower excimer wavelengths is due to stronger volume absorption or higher absorptivity.

Rear side ablation was explained by constructive interference of the incoming beam with the beam undergoing Fresnel reflection into the silica at the silica/air interface. There is no phase shift of incoming light and Fresnel reflection. This effect produces a higher effective intensity at the rear side and causes ablation. The ratio of effective intensities at the front 'I_{front}' and rear 'I_{rear}' surfaces can be expressed as:

$$\frac{I_{rear}}{I_{front}} = \frac{4n^2}{(n+1)^2} \qquad \text{Equation 2-11}$$

where 'n' is the refractive index of material at the wavelength of the ablating radiation. Due to the higher refractive index of fused silica at 193 nm, there is a significant difference between the ablation thresholds of the front and rear sides. The topography of rear side ablated structures was found to be cleaner and sharper due to the absence of plasma-mediation. Plasma-mediation hampers the efficiency of energy deposition in the material. Therefore, for a given absorbed energy, the material removal efficiency or ablation rate is higher on the rear side than the front side. Continuous nanosecond pulse ablation of structures at the front surface leads to the hindering of the plasma by the sidewalls, which in turn leads to heating, melting and resolidification of the ablated material [40]. This effect produces ablation debris on the sidewalls and around the crater in 193 nm ablation of the front side of the sample.

Table 2-1: Tabular illustration of ablation of fused silica at different excimer wavelengths [39].

Wavelength [nm]	**Sample surface**	**Ablation threshold [x 10^4 Jm^{-2}]**	**Incubation period [Pulses]**	**Ablation**	**General topography**
308 (ns pulses)	Polished	>19	5-20	Both front and Rear side ablation occurs	Micro-cracking of surface
	Rough	----------	No	----------	Rugged structures
248 (ns pulses)	Polished	10	20-50	Rear side ablation for first 10-20 pulses and then at front side	Clean and smooth structures
	Rough	5	No	No rear side ablation; 1.8 μm $pulse^{-1}$	Explosive ablation causing rugged structures
193 (ns pulses)	Polished	2.6	No	Rear side only	Sharp edges without cracks; slightly scaly and flaky craters
		3.2		Front side only	Cracking above ablation threshold
248 (fs pulses)	Polished	Similar to ns pulses of 248 nm	First few	No rear side ablation	Roughness increases with pulses

In general, rear side ablation is possible only in the case of weakly- absorbing materials. When the energy density is increased sufficiently, a higher volume absorption at the front surface prevents rear side ablation. This can be observed at 3.2 x 10^4 Jm^{-2} with 193 nm ablation. The intensity of irradiation at any energy density will be much higher for femtosecond pulses than nanosecond pulses due to the smaller pulse duration. Therefore, two-photon ablation occurs during the 248 nm femtosecond pulse ablation. The incubation effects are negligible during the

femtosecond pulse ablation. Plasma mediation is negligible in the case of femtosecond pulse ablation due to the very short duration of the pulse.

Although the morphology of structures [40] is clean and smooth, during the incubation pulses and in rear side ablation at 193 nm, the sidewall and crater roughness increases with the increasing number of pulses. No quantitative data on the surface roughness of craters and the sidewall angle was given.

Dyer *et al.* [41] studied ablation of soda lime glass, germania doped silica fibre preform and fused silica (Grade: Spectrosil B) at 248 and 193 nm. When these samples were irradiated at energy densities lower than their ablation thresholds, the incubation period was observed for several hundreds of pulses after which ablation of material was initiated. For example, the front side ablation threshold of Spectrosil B at 193 nm was 4.6 x 10^4 Jm^{-2}. However, ablation was observed at 2.3 x 10^4 Jm^{-2} after one thousand incubation pulses at 2.3 x 10^4 Jm^{-2}. This was attributed to the increase in the near surface absorption coefficient as a result of defect and colour centre formation and also due to surface roughening. This was also observed by Ihlemann [39] in polished samples of fused silica. Therefore the incubation period, which involves surface roughening and colour centre formation followed by ablation of material, is a common phenomenon in polished samples. These physical and chemical modifications gradually raise the energy density loading and surface temperature that leads to material ablation. The ablation threshold for strongly-absorbing materials is lower than weakly-absorbing material and the ablation threshold for a material is smaller at shorter wavelengths. For example, the effective absorption coefficient of soda lime glass at 248 nm is 5.3 x 10^6 m^{-1} and at 193 nm is 1.3 x 10^7 m^{-1}. The effective absorption coefficient 'α_{eff}' (nm^{-1}) and ablation rate 'd' are related by an empirical relation as [41]:

$$d = \left(\frac{1}{\alpha_{eff}}\right)\ln\left(\frac{F}{F_{th}}\right)\text{nm} \qquad \text{Equation 2-12}$$

where 'F_{th}' is the ablation threshold and 'F' is the applied fluence. The term 'α_{eff}^{-1}' is also called the effective optical energy penetration depth.

The ablation threshold of the doped region of a fibre preform at 193 nm is 1.7 x 10^4 Jm^{-2} and at 248 nm is 2.1 x 10^4 Jm^{-2}. Well-defined structures were obtained when the 20 mol% doped-region of preform was ablated at 193 nm. However, the ablation of the outer fused silica region produced fractures around the irradiated area. Doping would reduce the energy band-gap of the material, which in turn may be responsible for the well-defined ablation of microstructures.

Ihlemann and Wolff-Rottke [42] studied the ablation of fused silica and sapphire glass at 248 and 193 nm. The 248 nm ablation thresholds for fused silica and sapphire were found to be lower for femtosecond pulses than nanosecond pulses, whereas their ablation rates at the same energy density as at nanosecond pulses were higher. The rate of ablation of sapphire was found to be lower than fused silica in both the nanosecond and femtosecond ablation of 248 nm laser. This was true also for the nanosecond pulse ablation at 193 nm. The incubation period was observed during the ablation of sapphire at nanosecond pulses at 248 nm near the ablation threshold. In another publication by Ihlemann *et al.* [43], plume absorption studies revealed that at least 50% of the total pulse energy was absorbed or scattered in the ablation plume at a fluence of 20 x 10^4 Jm^{-2} during the 248 nm nanosecond pulse ablation of Al_2O_3, which has an energy band gap of 9.9 eV. The permanent increase in the absorption of the ablated surface was stronger at higher energy densities. During high intensity (due to high energy density) ablation of Al_2O_3, the initial photons of the pulse duration were absorbed by defects and in turn induced colour centres and seed electrons. The release of electrons led to an avalanche breakdown during the first nanoseconds. The remaining portion of the pulse generated and heated up the dense plasma, which caused explosive sputtering of material or thermally-induced ablation. This produced large heat-affected zones around the irradiated area causing collateral damage. The heat-affected zone (HAZ) during ablation can be expressed as[42]:

$$HAZ = (2Dt)^{0.5} \text{ nm} \qquad \text{Equation 2-13}$$

where 'D' (nm^2s^{-1}) is the thermal diffusivity and 't' (s) is the pulse duration. From this equation it can be understood that the HAZ for a material at specified wavelengths will be smaller for femtosecond pulses than nanosecond pulses. During a femtosecond pulse ablation of Al_2O_3 at 248 nm, the coupling of energy into a small volume of material is much higher than at the nanosecond due to the higher pulse intensity. There is no possibility for impact ionisation, which occurs over a time scale of 0.1 to 1 ns, due to much shorter pulse duration of femtosecond pulses. Therefore, ablation of the material is dominated by the two-photon (non-linear) absorption process at sufficiently high irradiance. The reason for the smaller ablation threshold of fused silica and sapphire at the femtosecond regime of ablation is due to a stronger coupling of photon energy into the material and the higher ablation rate is due to non-mediation of plasma.

Oliveira *et al.* [44] studied the ablation of alumina (66 wt%) – titanium carbide (34 wt|%) ceramics using a nanosecond KrF exicimer laser. At energy densities $\leq 30 \times 10^4$ Jm^{-2}, a cone or columnar-like topography was produced. Titanium carbide (TiC) has a higher absorption coefficient than alumina (Al_2O_3) at 248 nm and therefore attains its melting temperature much faster than alumina. Molten TiC protrudes above the surface and becomes small round globules due to surface tension. These globules coalesce and their mean diameter increases with the subsequent number of pulses. With a further increase in the number of pulses, the globules evolve into columns and become uniform across the irradiated area by the first 100-200 pulses of exposure. The tops of the columns are rich in TiC and the inter-column regions are rich in Al_2O_3. With subsequent irradiation, the difference in their concentrations decreases due to ablation and the columnar topography disappears. The columnar growth could be suppressed by using higher energy densities as higher energy densities cause a higher ablation rate, which reduces the concentration gradient of TiC and Al_2O_3 at the surface faster. This was achieved at energy densities about 30×10^4 Jm^{-2} [45].

Tuck [8] performed ablation of fused silica and sapphire with 248 and 193 nm nanosecond pulses to produce Fabry-Perot microstructures. Three aspects of ablation

were studied: the optical quality of craters, sidewalls and the wall-angle of microstructures. Optically smooth surfaces and parallel sidewalls were aimed to produce FP microstructures by imaging projected mask features. Ablation of flat samples of fused silica produced structures with severe undulations on the sidewalls and rugged craters dominated by ablation debris. Interferometric surface profile analysis showed poor optical quality of craters and sidewalls at 193 and 248 nm ablation. However, the optical quality of craters and sidewalls of sapphire microstructures produced from 248 nm laser ablation was found to be sufficient to produce Fabry-Perot interference. Sapphire optical fibres of 150 μm were ablated through the fibre diameter to a few tens of micrometres depth at 15×10^4 and 22×10^4 Jm^{-2}. The taper-angle of sidewalls was higher at lower energy density ablation and produced V-shaped groove structures. Industrial trials were carried out to identify the feasibility of using 157 nm lasers for production of FP microstructures. Well-defined and clean ablated structures were obtained in sapphire and silica. However, the optical beam delivery used for machining and optical quality of these structures was not mentioned because of commercial confidentiality. This work shows that the F_2-excimer laser emitting at 157 nm wavelength could be a possible choice for machining FP microstructures.

2.8.1.1 Summary of Ablation at Excimer Wavelengths

Ablation of fused silica at threshold energy densities has two phases of ablation: the first phase involves creation of defects and colour centres with a small ablation of material due to single photon absorption and the second phase is plasma-mediated ablation involving explosive sputtering. Nanosecond sapphire ablation is also a plasma-mediated process. Rear side ablation in fused silica at both 193 and 248 nm, produced structures with good wall definition and craters, which are relatively much cleaner than structures ablated at the front side. This is due to the absence of plasma mediation. Ablation of sapphire at 248 nm produced microstructures of optical quality sufficient for FP interference. However, tapering of sidewalls is a major obstacle to realising FP structures in optical fibres. Nanosecond ablation of sapphire and silica is plasma mediated and is a thermally-driven process resulting re-deposition of ablation debris and heat affected zones, which deteriorate the optical quality and resolution of

microstructures. Femtosecond pulse ablation is driven directly by two-photon absorption due to high coupling of pulse energy into the material. The plasma mediation is absent in femtosecond ablation. In general the poor optical quality of microstructures ablated in fused silica with nanosecond pulses of 193 and 248 nm is due to poor absorption and long pulse duration that initiates plasma-mediated thermal ablation. Therefore, 308 nm, 248 nm and 193 nm wavelength excimer lasers are not suitable for the fabrication of high aspect ratio FP micro-structures in fused silica and sapphire substrates. In addition to the poor absorption of fused silica and sapphire at these wavelengths there are other factors such as laser-induced plasmas and ambient surrounding the ablation site, which influence the ablation characteristics and optical quality of ablated structure as discussed below.

2.8.2 Effect of Laser-Induced Plasmas and Surrounding Ambient

The ablated material from the substrate surface attenuates the incoming laser pulse energy [46]. This is mainly explained by three mechanisms: inverse Bremsstrahlung effect (IB); photo-ionisation (PI); scattering and absorption (S & A). The ablation plume is composed of species such as neutral atomic or molecular species, ions, fragments of ablated material and free electrons. The free electrons absorb incoming photon energy and acquire additional kinetic energy. They undergo collisions with the other vapour species and cause further ionisation. This increases the electrical field of ions. Therefore, according to the IB effect, the probability of photon absorption due to electron-ion collision is much greater than electron-neutral species. Photo-ionisation of excited neutral species can occur during plume interaction with the photons. Electrons generated during photo-ionisation are not in thermal equilibrium with the ionised vapour and consequently undergo recombination. These photoelectrons contribute to the IB effect when their recombination time constant is comparable to the laser pulse duration. The ablation plume constitutes particle sizes ranging from a few nanometres to micrometres. The incoming radiation can be scattered or absorbed by these species that result in beam attenuation [46].

2.8.2.1 Influence of High-Aspect Ratio Cavities

Laser-induced plasmas have a significant influence on micro-machined cavities depending on their aspect ratio [47], [48]. The aspect ratio of the cavity is the ratio of depth of the cavity to diameter of entrance. The plasma temperature and electron number density are much lower on the surface than inside the cavity as it is free to expand. For cavities of different aspect ratios due to different entrance diameters (but the same depth as that used in these experiments), the plasma temperature and electron number density are highest for the highest aspect ratio due to the lateral confinement of cavity walls. The ablated material from each pulse interacts with the duration of pulse energy (directly and by multiple reflections from the sidewalls) by various processes such as IB, PI and S & A, which increase the electron number density and temperature. The plasma expands out of the cavity and cools rapidly by transferring its energy to the cavity walls by conduction, electron-ion recombination and condensation of vapour on the cavity walls. The plasma temperature generated inside the cavity will be higher at higher energy densities of ablation [49].

High-pressure plasmas expanding inside the ablated cavities can generate shock waves [50]. The summary [50] is presented as follows:

Shock waves generated inside the cavities are confined by their sidewalls. The fraction of plasma energy that drives the shock waves out of the cavity was smaller for cavities of higher aspect ratio. The energy of the plasma transferred to the cavity walls is higher in higher aspect ratio cavities due to higher confinement and hence the smaller the energy expended to drive the shock waves out of the cavities. The velocity of the shock wave expanding out of the cavity is higher for higher aspect ratio cavities due to higher pressure generated inside the cavity.

2.8.2.2 Effect of Surrounding Environment

Mendes and Vilar [46] studied the influence of the surrounding atmosphere and laser spot size on the ablation of Al_2O_3-TiC ceramics using a 248 nm excimer laser with a pulse duration of 30 ns FWHM. The ablation experiments were carried out under a

controlled atmosphere. Ablation rates were studied at different partial pressures of Ne, N_2, air, Ar and Kr. Their findings were summarised as follows:

1. The ablation rate was higher for smaller spot sizes than larger ones with energy density (range: 2.5 x 10^4 Jm^{-2} to 30 x 10^4 Jm^{-2}) and ambient pressure of 10^5 Pa surrounding the ablation site being constant. The spot size used in their experiments range from 50 μm to 430 μm. The ablation rate was independent of the spot size when the experiments were carried out in a vacuum.
2. The ablation rate at an energy density of 30 x 10^4 Jm^{-2} increased with decreasing ambient pressure (range: 10^5 Pa to 10^3 Pa). The ablation rate at this energy density and pressure range, increased for ambient gases as follows: Kr<Ar<Air<N_2<Ne<He. The rate of ablation was independent of ambient gas, when the ambient pressure was less than 10^3 Pa.
3. The redeposition of ablation debris was larger at higher ambient pressures; and it was smaller for 'He' than 'Kr' ambient at same pressure.

The lower ablation rate at higher ambient pressure and the lower ablation rate for higher molecular/atomic weight ambient were attributed to slower expansion of the ablation plume. The plume expansion was not hindered when the experiments were carried out in a vacuum. The increasing ablation rate with decreasing spot size was attributed to three-dimensional hemispherical expansion of the plume in the case of smaller spots and planar expansion in the case of larger spots. The particle density in the plume was smaller during hemispherical expansion than that of planar expansion. The plume-attenuation of pulse energy was explained by scattering and absorption. According to Mie scattering, the attenuation of radiation was predominantly due to absorption when $(2\pi a/\lambda)<<1$ and tends to attenuation due to scattering when $0.1<(2\pi a/\lambda)<1$, where 'a' and 'λ' are the size of the particle and wavelength of ablating radiation respectively. The size of redeposited ablation debris measured, when the ablation was carried out at 10^3 Pa ambient pressure, was found to be ~ 20 nm. The duration of the plume was found to be < 1μs. The size of the redeposited debris and duration of plume was higher (several microseconds) at higher ambient pressures. They attributed the larger debris at higher ambient pressures to cluster formation. The size of the clusters was determined by the collision cross-section and

duration of the plume, which were higher at higher ambient pressures. From this work, it can be understood that, the volume of debris deposition could be reduced either by ablating the material in a vacuum or by reducing the duration of pulse. These experiments were carried out for a few tens of pulses and therefore, did not investigate the effects of cavity walls and cavity aspect ratio on debris deposition. This factor is relevant because the cavities that are to be micro-machined in optical fibres are typically 125 μm in depth and debris deposition across the cavity walls could be detrimental to the optical quality of etalon surface.

Wolff-Rottke *et al.* [51] investigated the effects of laser-spot diameter on photo-ablation rates. The temporal shape of the excimer laser pulse was measured by using a photodiode at the rear-side of the sample. The FWHM and the intensity of the pulse were found to decrease with increasing energy density of ablation due to ablation plume attenuation. When different spot sizes were ablated, the ablation rate was found to increase with decreasing spot size. The ablation rate reached a higher saturation over a specified range of fluence with decreasing spot size. These results were analysed by using their mathematical modelling of ablation plume expansion. Their calculations showed that the number of particles of the expanding plume remaining in the beam during the pulse duration was lower for smaller spot sizes. Therefore, the plume-attenuation of pulse energy was lower and hence a higher ablation rate and higher saturation of the ablation rate for smaller spot diameters. The temporal pulse shape measurements showed that the expanding plume attenuated a significant duration of the pulse. During femtosecond pulse ablation, the ablation rate was found to be independent of spot diameter due to the absence of plasma mediation. The ablation rate was found to be higher, when the ablation experiments were conducted in a vacuum. This was in agreement with the findings of Mendes and Vilar [46]. From these results, it can be understood that during the ablation of two spot diameters at the same energy density, the fluence reaching the ablation surface after a specified ablation depth would be higher for a smaller spot diameter cavity and this therefore, influences the maximum achievable ablation depth. The spot-size dependence of attenuation of pulse energy was of great importance with reference to the fabrication of Fabry-Perot micro-cavities as the fluence reaching the target surface determines the geometry of the microstructure besides other factors such as the spatial

intensity distribution at the image plane and image defocusing, which will be discussed in the later sections of the literature review.

Burghardt *et al.* [52] observed severe tapering of ablated holes (array of holes) in polyimide using a 248 nm nanosecond pulsed laser. They ablated a series of holes along a line simultaneously using a uniform illumination of a mask and found that the taper angle of holes increased towards the centre hole from either end of the line. The holes at either end of the line have near-vertical cavity walls. Ablation plume studies had shown a cloud of ablated material, which was denser towards the central hole. Therefore, the plume attenuation could have a significant impact on the wall-angle of microstructure.

2.8.2.3 Summary of the Effect of Laser-Induced Plasmas and Surrounding Ambient

Laser-induced plasmas (LIPS) attenuate significantly the laser energy during nanosecond pulsed excimer laser ablation. This leads to a decreasing ablation rate, which in turn determines the shape of the microstructure. Due to the confinement of the plasma in high aspect ratio cavities, LIPS relax by transferring their energy to the cavity walls via various mechanisms. For example, condensation of vapour could lead to debris formation on the cavity walls deteriorating their optical quality. High molecular weight gases and high pressures also reduce the ablation rates. The dynamics of plume expansion determine the ablation rate of spot diameters. This implies that the geometry of the ablated microstructure could be different for different spot sizes at the same energy density of ablation. LIPS could have an influence on the tapering of cavity walls. Femtosecond laser ablation is uninfluenced by LIPS due to the short duration of the pulse. Therefore, the duration of pulse determines the ablation mechanisms and also influences ablation characteristics. The following section presents the differences between the ultra-short and nanosecond pulse ablation mechanisms and ultra-short pulse ablation of fused silica and sapphire substrates.

2.8.3 Ultra-short Pulse Ablation

The fundamental difference between nanosecond and ultra-short (picosecond and femtosecond) pulse ablation is the time scale over which pulse energy absorption occurs in the material [53]. With reference to nanosecond ablation, the energy absorption occurs on a time scale, which is much longer than electron-phonon relaxation (typically a few picoseconds) or lattice heating processes. Ablation of a material occurs when this volume absorption attains the necessary temperature for melting and vaporisation. On the other hand, for ultra-short pulses, the conduction band electrons generated by multi-photon absorption followed by avalanche ionisation are heated by laser energy much faster than the electron-phonon relaxation time. Multi-photon absorption provides 'seed' electrons for avalanche ionisation. Avalanche ionisation increases rapidly and increases the density of electrons in the conduction band and when the frequency of this plasma equals the laser frequency, strong absorption occurs in a small volume of material, thus heating the material very quickly past the liquid-to-vapour phase. The material vaporises from the surface after the duration of pulse and hence no plasma attenuation takes place. Due to the high intensity of ultra-short pulses, the ablation threshold for a material is smaller than the nanosecond pulse ablation. The ablation threshold for a material is directly proportional to the square root of the pulse duration at a specified wavelength.

During nanosecond pulse ablation, heat diffusion into the un-ablated surface could produce melt layers. However, the resulting melt layer thickness could be larger than that due to ultra-short pulse ablation. This is because most of the heated material reaches its vaporization temperature or most of the absorbed ultra-short pulse energy is converted into kinetic energy of the vapour phase. The heat penetration depth, as mentioned in Equation 2-13, approaches the optical energy penetration depth, as mentioned in Equation 2-12, with decreasing pulse duration [54].

In the nanosecond ablation process, seed electron generation occurs by bond breaking via absorption by defects in the lattice. At a specified energy density, the intensity of nanosecond pulses is smaller than that of ultra-short pulses due to their longer pulse duration. Increasing the energy density can increase the intensity of nanosecond

pulses. However, it is difficult to increase to the level of ultra-short pulses. At sufficiently high energy density ablation by nano-second pulses, optical breakdown of the material occurs. However, it does not proceed as avalanche ionisation in ultra-short pulses due to the lower pulse intensity. Ultra-short pulses do not rely on defect levels to generate seed electrons, rather they generate them by direct multi-photon ionisation due to high intensity. The electrons in the conduction band generated from defects undergo electron-phonon relaxation and heat up the material to its melting and vaporisation temperatures. The melt layer thickness in nanosecond pulse ablation is larger than that of ultra-short ablation due to liquid phase mediation and larger heat affected zones. The re-solidification of melt layers and droplet formation due to the recoil pressure of the ablated plume on the underlying melt could result in irregular shapes of ablated microstructures [55]. The combined thermal effects of the nanosecond pulse ablation associated with poor absorption (at 193 and 248 nm) often lead to a poor optical quality of ablated structures in fused silica and sapphire.

2.8.3.1 Ultrashort Pulse Ablation of Fused Silica and Sapphire

Fused silica and sapphire ablation at ultra-short pulse duration has been studied by a number of authors. The ablation threshold of fused silica at 300 fs pulses of 620 nm is 2.2 x 10^4 Jm^{-2} [56]. Surface ripples were observed after ten pulses. As the pulse number is increased, overall smoothing of the microstructure was observed. The dimensions of these ripple patterns were found to be much larger than that which could be produced from coherent interference of focussed light waves. The surface ripples were attributed to surface plastification and melting followed by relaxation of internal mechanical stress. These ripple patterns were not reported during nanosecond pulse ablation. Lenzner *et al.* [57] studied fused silica ablation at 780 nm in the ultra-short pulse domain. The topography of the microstructures and their geometry improved significantly by reducing the pulse duration from 3 ps to 5 fs. This was attributed to the higher rate of multi-photon ionisation during the shorter pulse duration. This could also be due to absence of plasma mediation during femto-second ablation

Wang *et al.* [58] studied the ablation of sapphire at 775 nm at a pulse duration of 150 fs. At 4.38 x 10^4 Jm^{-2}, the topography of the ablated microstructure remained rough and debris deposition was observed until 50 pulses. With successive irradiations, debris-free and clean structures with well-defined shapes, free of micro-cracks were produced. The ablation threshold of sapphire was found to decrease with increasing number of pulses on the same irradiated area and reached saturation after 50 pulses. This was attributed to colour centre formation with each pulse irradiation. This increased additional energy levels in between conduction and valence bands that lead to new excitation routes for the successive pulses. The taper angle of ablated holes was reduced by increasing the energy density. However, at energy densities as high as 9 x 10^4 Jm^{-2} micro-cracks were produced near the surface of the entrance. Sub-micrometre holes were observed during single shot ablation. This was attributed to the self-focussing effect. Schematic illustration of self-focussing is presented in Figure 2-7. During transmission of intense ultra-short laser beams through non-linear media such as air, the intensity-dependent induced-refractive index changes create wave-guide channels through the media.

As shown in Figure 2-7, the phase velocity decreases towards the axis of the Gaussian beam intensity (I) due to an increase of refractive index towards the beam axis. Different portions of the beam travel with different phase velocities depending on the beam intensity distribution and produce a lens effect that leads to different spots of much smaller size than the actual focussed spot size. Eventually, the phase fronts collapse to a point and converge the beam as if a lens focused them [59]. The influence of self-focussing on the craters of deeper holes was not mentioned [58].

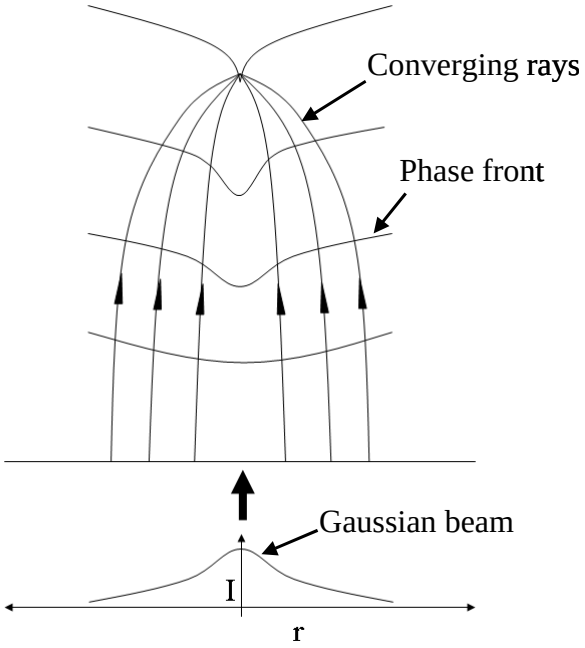

Figure 2-7: Schematic illustration of self-focussing of a Gaussian beam spatial intensity distribution [59].

2.8.3.2 Summary of Ultra-Short Pulse Ablation

Ultra-short pulse ablation is due to multi-photon absorption that leads to avalanche ionisation. Material ablation due to strong absorption occurs when the plasma frequency equals the incident radiation frequency. The thermal effects of ablation are much smaller compared to nanosecond ablation. There is no mediation of plasma during femtosecond ablation. Self-focussing effects during intense ultra-short pulse ablation could deteriorate the optical quality of microstructures.

As mentioned in the Section 2.8.1, colour centres form the main absorption channels during nano-second pulse ablation of fused silica and sapphire at 308 nm, 248 nm and 193 nm wavelength excimer lasers. Section 2.8.4 presents a brief overview of the concept of colour centres, their formation reactions in fused silica under the influence of UV excimer radiation and colour centres in germania-doped silica.

2.8.4 Colour Centres

Colour centres are defects in the lattice that produce new absorption bands in the visible or ultraviolet spectrum. These defects associated with the localised energy levels of the solid enable absorption of sub-band gap photon energies [60]. These are usually produced when chemical impurities are induced into the lattice or due to exposure to energetic radiations such as UV, γ-ray, neutrons and electrons [61].

As mentioned in the earlier Section 2.9.1 and 2.9.3.1, defects or colour centres play an important role in the ablation of fused silica. These defects are induced into the bulk of the material during industrial methods of preparation. These methods involve heat treatments and drawing that are aimed to avoid crystallization of silica [62]. Factors such as exposure to ionising electromagnetic and particle radiations and dopants also produce defects in fused silica. Fused silica has tetrahedral units of SiO_4 that lack long-range rotational and translational symmetries in the matrix. Four degenerate sp^3 hybridised-orbital of silicon are covalently bonded to four oxygen atoms to form a tetrahedral unit of SiO_4. The defects in the amorphous matrix of silica significantly affect its optical properties.

The optical transparency of fused silica up to the vacuum ultraviolet (200 nm – 10 nm) region of the electromagnetic spectrum is due to its large energy band gap of ~8-9 eV. Defects in the fused silica network introduce electronic states in between conduction and valence bands that give rise to new absorption bands. The literature review on colour centres gives a brief overview of defects in fused silica and defects induced due to germania-doped silica.

2.8.4.1 Colour Centres in Fused Silica

Defects in fused silica can be broadly classified into two types: intrinsic and extrinsic [63]. Intrinsic type defects are due to nonstoichiometry and radiation effects such as neutrons, ions, UV excimer lasers and γ-rays. Extrinsic defects are due to the induction of impurities such as germania, hydrogen and chlorine. The three main intrinsic defects are the E′-centre, non-bridging oxygen hole centre (NBOHC) and

peroxy radical (POR). These three are paramagnetic centres, characterised by an unbalanced spin, and are detected in electron spin resonance spectroscopy (ESR). Extrinsic defects also act as precursors for the formation of paramagnetic defects. Various paramagnetic centres and their formation reactions are presented in Table 2-2 [63]. E′-centre consists of an unpaired electron in a dangling sp^3 orbital of a three co-ordinated 'Si' atom. The symbol '≡' denotes three covalent bonds and '•' denotes an unpaired electron. The peroxy linkage ≡ Si – O – O – Si ≡ is formed when 'O_2' is introduced during the manufacturing process and reacts with E′-centres.

Ikuta *et al.* [68] studied colour centre generation in fused silica samples of different 'SiOH' concentrations and same concentrations of H_2 and SiF due to ArF and F_2-laser irradiations. The intensities of F_2- laser-induced ODC (oxygen deficiency centre) (7.6 eV) and E′ (5.8 eV) bands are higher in high 'SiOH' content silica indicating enhanced defect generation due to the presence of high 'SiOH' content. The growth of intensity of E′- band is linear with F_2-laser power density, indicating a one-photon-absorption process, while the intensity growth was proportional to the square of power density with the ArF laser, indicating a two-photon-absorption process of defect generation. Two-photon absorption-induced defect generation was not observed during F_2-laser irradiation. The proposed reactions of defect generation in fused silica with 157 and 193 nm lasers are presented in Table 2-3 and Table 2-4 respectively:

Table 2-2: Various paramagnetic defects and their formation reactions in fused silica.

Paramagnetic Defects	**Precursor**	**Reason for precursor**	**Proposed reaction**	**Reason for reaction**
≡ Si• (5.8 eV) [E′- Centre]	≡ Si – O – Si ≡	----------	≡ Si – O – Si ≡ (8.8 eV) → ≡ Si• + $^{+}$Si ≡ + O^{-}	γ - rays and UV lasers [63], F_2-excimer laser [64]
≡ Si• [E′- Centre]	≡ Si – Si ≡ [Flawed bond]	Oxygen deficient silica	≡ Si – Si ≡ (7.6 eV) → ≡ Si• + $^{+}$Si ≡ + e^{-}	X-rays or γ-irradiation (Imai *et al.* [65])
≡ Si• [E′- Centre]	≡ Si – H {≡ Si – O – Si ≡ + H_2 at high temperature → ≡ Si – OH + ≡ Si – H} [66]	Hydrogen introduced during manufacture	≡ Si – H (8.2 eV) → ≡ Si• + •H	----------
≡ Si• [E′- Centre]	≡ Si – Cl [63]	Chlorine introduced during manufacture	≡ Si – Cl → ≡ Si• + Cl^0 (atomic chlorine)	----------
≡ Si – O• (4.8 eV) [NBOHC]	≡ Si – O – O – Si ≡ [63]	Excess of oxygen in silica	≡ Si – O – O – Si ≡ (6.8 eV) → ≡ Si – O• + •O – Si ≡	Two photon excitation of KrF or ArF lasers [67]
≡ Si – O – O• [Peroxy radical]	≡ Si – O – O – Si ≡ [63]	Excess of oxygen in silica	≡ Si – O – O – Si ≡ (6.8 eV) → ≡ Si – O – O• + $^{+}$Si ≡ + e-	----------

Table 2-3: Defect generation reactions in fused silica during 157 nm (7.9 eV) exposure.

Reaction	Reaction products
≡ Si – O – Si ≡ (strained bond) + hν (7.9 eV)	≡ Si• (E′-centre) + •O – Si ≡ (NBOHC)
≡ Si• + •O – Si ≡ + H_2	≡ Si – H + HO – Si ≡
HO – Si ≡ + hν (7.9 eV)	H• + •O – Si ≡
H• + •O – Si ≡	HO – Si ≡ (hydrogen-bonded)
≡ Si – O – Si ≡ (strained bond) + hν (7.9 eV)	≡ Si – Si ≡ (ODC) + ½ O_2
≡ Si – Si ≡ + hν (7.9 eV)	2. ≡ Si• (E′-centre)
2. ≡ Si• + H_2	2. ≡ Si – H

Isolated ‘SiOH’ bonds were excited by F_2-photons and were relaxed partially into thermally stable hydrogen-bonded SiOH groups. The defect generation reactions in fused silica during 193 nm exposure is presented in Table 2-4:

Table 2-4: Defect generation reactions in fused silica during 193 nm (6.43 eV) exposure.

Reaction	Reaction products
≡ Si – O – Si ≡ (Unstrained) + 2hν	≡ Si• + •O – Si ≡
≡ Si• + •O – Si ≡ + H_2	≡ Si – H + HO – Si ≡ (isolated)
≡ Si – O – Si ≡ (Unstrained bond) + 2hν	≡ Si – Si ≡ (ODC) + ½ O_2
≡ Si – Si ≡ + 2hν	2. ≡ Si• (E′-centre)
2. ≡ Si• + H_2	2. ≡ Si – H

2.8.4.2 Colour Centres in Germania-Doped Silica

In germania (GeO) doped fused silica, germanium manifests itself as flawed bonds such as ≡ Si – Ge ≡ and ≡ Ge – Ge ≡. These oxygen deficiency centres act as precursors for GeE′ (≡ Ge•) centres. The formation reaction of GeE′ centres from oxygen deficiency centres using one photon excitation of ArF or KrF excimer laser can be expressed as [63]:

$\equiv Ge - Ge \equiv (\equiv Ge - Si \equiv)$ (5.06 eV) $\rightarrow \equiv Ge\bullet$ (6.3 eV) + $Ge^{+} \equiv (Si^{+} \equiv) + e^{-}$ Equation 2-14

Another two important paramagnetic defects in germania-doped silica are Ge (1) and Ge (2) centres [6]. In the Ge (1) (4.4 eV) centre, the 'Ge' atom with a trapped unpaired electron is co-ordinated to four O – Si next nearest neighbours. In the Ge (2) (5.8 eV) centre, the 'Ge' atom with a trapped unpaired electron is co-ordinated to one O – Ge (≡ Ge – O – Ge ≡) and three O – Si next nearest neighbours. Ge (1) and Ge (2) are termed germanium electron centres (GEC). The formation reaction of GEC from two photon absorption of KrF laser can be expressed as [6]:

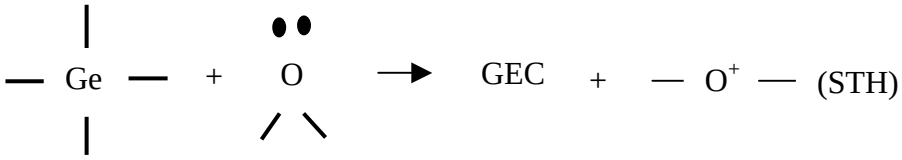

Equation 2-15

The lone pair of electrons on the oxygen atom is excited to the conduction band by two-photon absorption leaving behind a self-trapped hole (STH). The concentration of germanium oxygen deficiency centres (GODC) increase when germanosilicate glass is treated with hydrogen at high temperatures. This is due to the rupture of regular Ge – O bands. This formation reaction of GODC that increases absorption at 242 nm (5.1 eV) can be expressed as [69]:

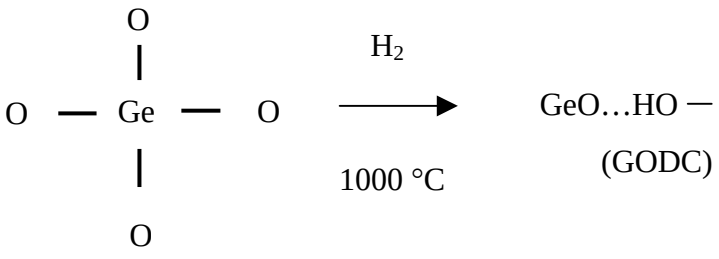

Equation 2-16

2.8.4.3 Photo-luminescence via Colour Centres

Some of these defect centres are optically active or undergo photo-luminescence when the corresponding defect bands are excited by UV-photons. The photo-luminescence emissions of various defects in fused silica and Ge-doped fused silica are presented in Table 2-5 [63], [70]:

Table 2-5: Photo-luminescence due to excitation of various defect centres.

Defect	**Photoluminescence**
≡ Si – Si ≡ (7.6 eV)	4.3-4.4 eV and 2.7 eV
≡ Si – O• (4.8 eV)	1.9 eV
O – Ge – O (6.8 eV)	4.2 eV (294 nm) and 3.1 eV (396 nm) [69]
≡ Si – OH ≡ Si – O• (NBOHC in high 'OH' content fused silica)	At 650 nm due to KrF laser irradiation [67] At 650 nm due to ArF laser irradiation [71]

In addition to colour centre formation, UV-laser irradiation also produces densification of fused silica or a compaction effect [72], [73]. Compaction of fused silica produces shrinkage and increases the refractive index of the irradiated zone. Densification is the ratio of the change in volume to the original volume of the irradiated zone. Laser-induced defects and structural rearrangements produce compaction that manifests as stress birefringence. Some of the effects of laser-induced densification of fused silica are: shortening of bond lengths of O – O, Si – Si, over co-ordination of 'Si' and 'O' atoms, decrease in the average bond angle of O – Si – O and Si – O – Si and increase in Young's and bulk modulus [74].

Ikuta *et al.* [75] studied the correlation between ODC formation and volume compaction in synthetic SiO_2 glass upon ArF and F_2 excimer-laser irradiation. A summary of their findings is presented as follows:

i. In samples of SiO_2 with ODC defects and no detectable H_2 and OH species, the refractive index (and density) of SiO_2 glass increased linearly with the concentration of thermally induced ODCs.

ii. In both H_2-impregnated samples of SiO_2 with and without 'OH', the concentration of E' and ODC centres linearly increased with irradiation dose of ArF and F_2-laser irradiation. The rate of increase of ODC concentration due to F_2-laser irradiation was three times higher than ArF-laser irradiation.

iii. In both H_2-free samples of SiO_2 with and without 'OH', the formation of ODCs was scarce. However, the concentration of E' and NBOHCs increased linearly with ArF and F_2-laser irradiation. In all these samples of SiO_2, a linear increase of refractive index change with the irradiation dose was observed.

iv. It was found that the laser-induced compaction in SiO_2 glass is not due to structural changes in the short range order that are due to point defect generation but is due to long-range structural changes of the Si – O – Si network.

v. In both H_2-impregnated samples of SiO_2 with and without 'OH', crack formation was observed due to ArF and F_2-laser irradiation. The explanation for the enhancement of crack propagation due to H_2-impregnation is that the 'OH' groups resulted from the interaction between H_2 and photo-induced defects causes stress corrosion that leads to crack formation.

2.8.4.4 Summary of Colour Centres

Excimer laser-induced colour centres produce a number of absorption channels through which laser energy can be effectively absorbed into the material. Flawed bonds produced during industrial processes of fused silica manufacture act as precursors for many paramagnetic defect centres. Germanium doping reduces the effective band gap of fused silica. Impurities in the silica matrix such as hydrogen and chlorine also act as precursors for defect generation. ArF and KrF-laser-induced colour centres in fused silica are due to two-photon absorption via normal '≡ Si – O – Si ≡' bonds and F_2-laser-induced colour centres are due to one-photon absorption via strained '≡ Si – O – Si ≡' bonds. Crack formation in SiO_2 glass due to stress corrosion of 'OH' could be a deleterious affect during micro-machining of Fabry-Perot

microstructures. As mentioned in earlier sections of the literature review on laser ablation, the cleanliness or topography of ablated structures depends on how strongly the interacting radiation is absorbed into the material, which in turn is governed by the generation and density of colour centres.

Besides laser-material interactions, the beam delivery optics in micro-machining applications determines the geometry and optical quality of ablated structures. Based on the requirements of the application, the laser beam characteristics such as the beam shape, spatial intensity distribution and beam divergence can be manipulated using suitable beam delivery optics. The following section presents the significance of various optical parameters of the beam delivery system in controlling the geometry of ablated structures.

2.8.5 Beam Delivery Optics

Besides laser-material interactions, the three dimensional geometry of the ablated microstructure is governed by the beam delivery optical systems. The features of the beam delivery system such as resolution, magnification and depth of focus can be controlled by changing optical parameters such as numerical aperture and partial coherence. However, the wavelength of light and diffraction set limitations on the features of the beam delivery system. The literature review on beam delivery optics discusses: the influence of various optical parameters on image formation and the need for beam homogenising optics in excimer laser micro-machining and their influence.

2.8.5.1 Mask Projection

A mask projection technique is extensively used in micro-machining and lithographic applications. In mask projection, the laser beam illuminates a converging lens at normal incidence [76]. Depending on the size of the field required to illuminate the mask features, the size of the beam can be altered by using suitable beam shaping telescopes. The mask can be placed towards the front or back focal plane of the

converging lens. If the mask is placed towards the front focal plane, then the finite aperture of the lens could limit the effective diffracted input from the mask feature [77]. This effect becomes significant when the input transparency of the mask has a high spatial frequency. Keeping the mask close to the lens can reduce this vignetting effect. The vignetting effect can be avoided by placing the mask towards the back focal plane of the lens. The mask input is placed close to the lens aperture so that the transparency is fully illuminated. The size of the Fourier transform at the focal plane of the lens, which is the Fresnel diffraction pattern of mask feature, can be made larger by reducing the distance between the mask and the lens. This arrangement has a specific advantage in micro-machining applications [8]. If a target (material to be ablated) surface is placed at the image plane of this lens, surface roughness around the boundary of the ablated structure can be observed. This is due to higher orders of diffraction that do not contribute much to the image formation. These unwanted effects can be filtered off by placing a physical stop of suitable diameter in the focal plane.

The converging wave-front from the positive lens couples light energy through the transparent features on the mask and projects them at the entrance pupil of the objective. The objective images the projected mask features at its focal plane according to its demagnification. The numerical aperture of the imaging system determines the resolution of spatial frequencies of the mask at the image plane. The higher the numerical aperture (NA), the lower the limit of resolution (R) of spatial frequency. If the spatial frequency of the object is zero, or the mask feature is a single transparency, then the use of higher NA objectives would include more diffraction orders in the imagery. Spatial resolution and NA are connected by Rayleigh's criterion as follows [78]:

$$R \sim \left(\frac{\lambda}{2NA} \right) \text{ nm} \qquad \text{Equation 2-17}$$

where 'λ' (nm) is the wavelength of light. The depth of focus (DOF) of an imaging system can be expressed as [78]:

$$DOF \sim \pm\left(\frac{\lambda}{2NA^2}\right) \text{ nm} \qquad \text{Equation 2-18}$$

where 'NA' is the numerical aperture of the imaging system. Therefore, the depth of focus of the imaging system varies inversely with the square of the numerical aperture. In high NA systems, the tolerance of error of defocusing is so small that the system imagery is no longer aberration-free for slight fluctuations from the focal plane. The contrast degradation of imagery due to the defocusing error is also high in high NA systems. The trade-off between resolution and DOF can be avoided by using shorter wavelength laser sources. This is the reason for the application of 157 nm excimer lasers in research towards the development of the next generation lithography.

DOF is a characteristic of the imaging system, which determines the distance over which the imagery does not undergo unacceptable loss of contrast and clarity. This feature of the imaging system could influence the depth of ablated structure over which the shape of the imaged mask feature remains in focus. This in turn could determine the geometry of the cavity. This is an important factor of the imaging system with reference to the fabrication of high aspect ratio FP cavities.

2.8.5.2 Partial Coherence

Another important factor, which determines the performance of imaging system, is the degree of partial coherence of the illumination. Fraunhofer and Fresnel diffractions do not take partial coherence between two points of an illuminated aperture into account while determining the diffraction of the imagery. Hopkins theory of partial coherence explains the degree of partial coherence between different points in the image plane [79]. The degree of partial coherence between any two points in a plane illuminated by an extended source of light is given by the phase-coherence factor 'γ_{12}', which can be expressed as:

$$\gamma_{12} = \frac{1}{\sqrt{I_1 I_2}} \int_{\Sigma} \frac{I(\xi,\eta)}{R_1 R_2} e^{ik(R_2 - R_1)} d\sigma \qquad \text{Equation 2-19}$$

where 'I_1', 'I_2' are the total intensities at these two points due to the whole extended source; $I(\xi,\eta)$ is the intensity of an arbitrary point of the source in the $\xi\eta$-plane; 'R_1', 'R_2' are the distances of the two illuminated points from the arbitrary point of the source and '$d\sigma$' is the element of the source corresponding to the location of an arbitrary source point. Here the source elements, although they emit coherent light, they are mutually incoherent. This means that the phasor amplitudes of the field at all points of the defined element, '$d\sigma$', of the source vary in unison and the phasor amplitudes of different source elements vary in a totally uncorrelated fashion. The points on the screen illuminated by a complete extended source will be fully-coherently illuminated when the modulus of 'γ_{12}', $|\gamma_{12}| = 1$. The modulus of the phase-coherence factor tends to approach unity, when the angular radius of the source tends to approach zero. As the angular size of the source increases, the coherence of the illumination of the points decreases. Therefore, the larger the angular size of the source, the smaller is the coherently illuminated area. In the case of aberration-free imaging systems, the degree of coherence in the exit pupil will be the same as that of the entrance pupil. Therefore, a high degree of coherence in the entrance pupil could produce a high degree of coherence at the image plane and hence a high contrast imagery.

If the object is illuminated using condenser optics, then the coherence of the illumination or partial coherence factor, 'σ', can be defined as the ratio of numerical aperture of the condenser to the numerical aperture of the imaging system. The coherence of the illumination is said to be highly coherent when this ratio approaches zero and highly incoherent when it approaches infinity [80]. The partial coherence factor reaches the limit of full coherence ($\sigma = 0$), when the effective illuminating source is a point source of light and reaches the limit of complete incoherence when the effective illuminating source is infinitely large [81]. Another way of defining the partial coherence is the ratio of effective size of the source at the entrance pupil to the diameter of the entrance pupil of the imaging system [82]. If the effective illuminating source is a point source, then this ratio becomes negligible and produces the highest

degree of coherence. In excimer laser micro-machining of Fabry-Perot devices in fused silica and sapphire [8], the contrast of images was very poor when the mask features were imaged without the use of a condenser. This is due to the poor spatial coherence of the excimer beam across the input transparency. The contrast was significantly improved, when Kohler-based illumination was used [8].

The effect of the degree of coherence on the resolution of an imaging system depends on the relative phase distribution associated with the object and cannot be generalised [77]. For example, there is no difference in the image intensity distribution of two points (pinholes) separated by the Rayleigh resolution limit, when the two points are incoherent point sources or two coherent point sources with a relative phase of $\pi/2$. However, in lithographic applications, the resolution and depth of focus for lines and spaces was found to be higher for less coherent illumination [83]. The influence of coherence of illumination on the geometry of high aspect ratio microstructures is not known. However, the contrast of images or the ablated structures can be improved by increasing the coherence of illumination.

2.8.5.3 Edge-Ringing and Speckle

Although high coherence of illumination produces high contrast images, two unwanted effects accompany. They are edge-ringing and speckle. When an input transparency with sharp edges is coherently imaged, the image intensity exhibits oscillations near the edges, which asymptotically approach unity of normalised intensity as the distance from the edge increases. It also produces a lateral shift of the image from its geometric position. This is due to the sharp cut-off of the pupil function of a unapodized optical system [84]. Edge-ringing in coherent imaging can be controlled by apodization of the exit pupil. Apodization of the exit pupil introduces an attenuating aperture around the diameter of the exit pupil, by which the oscillations near the edges may be suppressed. Edge-ringing could be avoided by using incoherent illumination. However, this results in a diminished contrast of images. A schematic illustration of the image intensity distribution of a sharp edge in coherent and incoherent imaging is presented in Figure 2-8 [77].

When the input transparency is coherently illuminated through the condenser optics, the presence of diffusing or light scattering particles on the surface of the condenser produces unwanted interference effects at the image plane [77]. This is known as the speckle effect. In micro-machining applications based on condenser optics, dust or other spurious particulate contamination on the condenser surface could produce speckle effects and deteriorate the optical quality of microstructures.

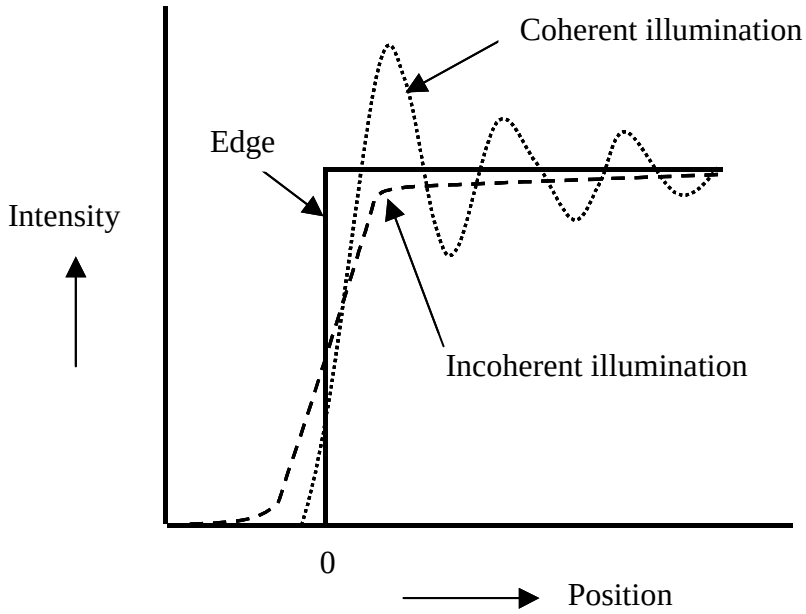

Figure 2-8: Schematic illustration of image intensity at different illumination coherences [77].

Tabat *et al.* [85] studied the diffraction intensity profile characteristics of a projected mask feature using a single converging lens. Polycarbonate was ablated using a KrF excimer laser. The XY-profile of the ablated structures showed a convexity of crater surface or a higher ablation rate at the perimeter of the structure. This feature of a crater surface obeyed the diffraction intensity profile of the mask feature and was found to be independent of the energy density of ablation and size of ablation spot. When the target surface was moved away from the image plane, the convexity of craters was reduced. This indicates that the ringing of diffraction intensity profile decreases from the image plane and the non-uniformity of ablation across the dimensions of the ablated feature decreases.

Another important factor that determines optical quality of excimer laser ablated microstructure is the spatial intensity profile at the image plane. The following section presents the typical raw beam characteristics of excimer lasers, the need for optical manipulation or modification of beam characteristics during micro-machining and the method of beam homogenization.

2.8.5.4 Optical Manipulation

The raw output beam of a stable excimer laser resonators is a complex superposition of a number of transverse modes [86], [87]. These higher order modes have the same wave-front curvature as a fundamental Gaussian profile, however, their large cross-sectional area reduces their irradiance at a given power level. Therefore, large output apertures are used in excimer lasers to increase the output power. These higher order transverse modes are very divergent and their multi-phased nature accounts for the poor spatial coherence of output beam. The complex superposition of output modes results in a Gaussian-like output with noisy fluctuations in spatial intensity distribution. The use of unstable excimer resonators reduces the poor spatial coherence, beam divergence and non-uniformity of output intensity. In unstable resonators, the central beam region is spread-out and the small path of the fundamental transverse coherent mode is spread across the aperture and higher order modes are significantly reduced [88]. However, the output power will be small compared to stable resonators due to mode volume loss.

These properties of excimer beams determine the extent of optical manipulation that has to be carried out during micro-machining applications. For example, the non-uniformities in spatial intensity of the output beam produces unwanted roughness and deteriorates the optical quality of ablated structures. Therefore, to produce a uniform illumination of mask features, the output excimer beams are homogenised by using diffractive optical elements. Fly's eye homogenisers are widely used for beam homogenising [89] . A fly's eye homogeniser constitutes an array of cylindrical lens-lets, which divide the beam into a number of beam-lets. These beam-lets are overlapped using a converging lens at its focal plane. The integration of these beam-lets averages the spatial intensity along both the dimensions of the excimer beam to

produce a top-hat intensity profile. An important design consideration of a homogeniser is that the aperture of the micro-lens should not be smaller than the coherence area of the partially coherent excimer beam in order to avoid unwanted speckle effects [90]. A homogenised beam improves the optical quality and edge definition of ablated structures [91].

Paterson *et al.* [92] studied the influence of energy density on the wall angle of ablated microstructures. A partially coherent and homogenised illumination was used for ablation. A dry film photo-resist was ablated by using the homogenised beam delivery of 193 nm excimer laser. The spatial intensity distribution of the image was calculated at different planes along the beam direction starting from the image plane. Factors such as illumination and projection optics, laser wavelength, fluence, number of pulses and material ablation characteristic at that wavelength were taken into account in the numerical model for the calculation of aerial image. It was found that the wall-angle profile of ablated structures at different energy densities obeyed the evolution of the aerial image at the corresponding energy densities with the ablation depth. Both positive and negative wall angles were produced by changing the energy density. However, perfectly vertical wall-angles were not achieved at all the applied energy densities of ablation. The wall angle measured for different numbers of pulses at all the energy densities was found to be increasing. For example, at an energy density of 1.5 Jm^{-2}, the wall angle obtained was ~ -10° for 200 pulses and ~ -5° for 800 pulses. A negative wall angle indicates that the trench narrows towards the bottom. Therefore, the wall angle is tending towards vertical during 800 pulses rather than 200 pulses.

2.8.5.5 Summary of Beam Delivery Optics

The quality of the ablated structures depends on the coherence of illumination. The degree of coherence at the exit pupil is the same as that in the entrance pupil in aberration-free imaging systems. The lowest achievable resolution (smallest achievable separation between two closely-spaced features) at a given numerical aperture of the imaging system at a wavelength is limited by diffraction. Partial coherence, divergence and spatial intensity of excimer beams determine the geometry

and optical quality of ablated structures. Edge-ringing and speckle are characteristic features of highly coherent imaging. Beam homogenising provides a uniform illumination of mask features. The wall angle of the ablated structures can be controlled by changing the energy density.

The ablation characteristics of fused silica and sapphire at 308 nm, 248 nm, 193 nm excimer lasers and ultra-fast lasers have been discussed in the earlier sections. The potential of ultra-fast lasers for machining high aspect ratio FP microstructures cannot be completely ruled out. The ablation studies by Tuck [8] at 193 nm and 248 nm excimer lasers proved that they are not suitable for machining FP microstructures. The industrial trails of 157 nm laser ablation of fused silica and sapphire carried out by Tuck [8] showed that these microstructures had better optical finish than the structures ablated at other excimer wavelengths. The following section presents F_2-laser ablation fused silica and other glasses and F_2-laser-induced photosensitivity carried out by other researchers.

2.8.6 F_2-Laser Micro-machining

Micro-machining of large band gap materials such as fused silica, sapphire and high density polymers such as polytetrafluoroethylene (PTFE) at 157 nm produced a higher optical finish and lower ablation debris than 193 and 248 nm micro-machining [93], [94], [95]. This is due to stronger absorption of 157 nm laser radiation. Fused silica has much stronger absorption than sapphire at 157 nm [96]. As mentioned in the review on colour centres in fused silica in Section 2.9.4.1, the strong interaction of 157 nm laser energy by single photon absorption is due to its high photon energy, which encroaches on the peak energy of various defect levels. The strong absorption of 157 nm radiation results in a short optical penetration depth. Therefore, the pulse energy is absorbed in a small thickness of material, which reduces the heat penetration depth. The excess energy during two-photon absorption of 193 and 248 nm laser radiation produces larger heat-affected zones, which in turn affect the quality of micro-machining. The strong absorption of 157 nm radiation also reduces the ablation threshold of materials. For example, the ablation threshold of fused silica at 193 nm is 3.2×10^4 Jm^{-2}, whereas for 157 nm radiation it is 1.1×10^4 Jm^{-2}. The optical

penetration depth of 193 nm in fused silica is 96 nm, whereas it is 59 nm at 157 nm. An incubation period was observed at energy densities lower than 1.1 x 10^4 Jm^{-2} [97]. The effective optical energy deposition in the surface of a material results in improved ablation depth resolution compared with the 193 and 248 nm lasers. For example [91], ablation of a 3% GeO_2-SiO_2 layer of 8 μm thickness grown over a 20 μm layer of SiO_2 using a 193 nm laser at an energy density of 3.6 x 10^4 Jm^{-2} for one pulse produced a 28 μm excision, leaving behind a rugged surface dominated by micro-cracks and melt zones, whereas the use of a 157 nm laser at an energy density of 3 x 10^4 Jm^{-2} for 100 pulses produced a 6 μm excision with a clean and smooth surface with a root mean square (RMS) roughness of less than 10 nm [91].

F_2-lasers are used widely for many micro-machining applications such as micro-optic, optoelectronic and microsystems fabrication [91], [98], [99], [100], [101]. Li *et al.* [102] machined microscope glass slides (Corning 2947) using homogenised F_2-laser radiation. Cavities of 30 μm width and 35 μm depth were produced at an energy density of 9 x 10^4 Jm^{-2}. These cavities were smooth and clean with vertical walls. V-shaped grooves were produced when microscope glass slides were machined at energy densities lower than 9 x 10^4 Jm^{-2}. Optical fibres were also cleaved at this energy density to produce a flat cleaved end with an RMS of 50 nm. A cylindrical micro-lens of dimensions 640 x 160 μm was machined on fused silica. Rough edges of the projection mask resulted in defects on the machined surface, which reduced the optical quality of the surface.

Obata *et al.* [103] studied the ablation of fused silica using multi-wavelength excitation. An F_2 and KrF laser pulses of energy densities of 0.4 x 10^4 and 2.9 x 10^4 Jm^{-2} were used to irradiate the fused silica sample without any time delay. F_2-laser photons excite the electrons to the defect levels. A fraction of these excited electrons are excited beyond the vacuum level by additional F_2-photons. Some of them are relaxed back to the valence band due to their short relaxation time (1.7 ns).

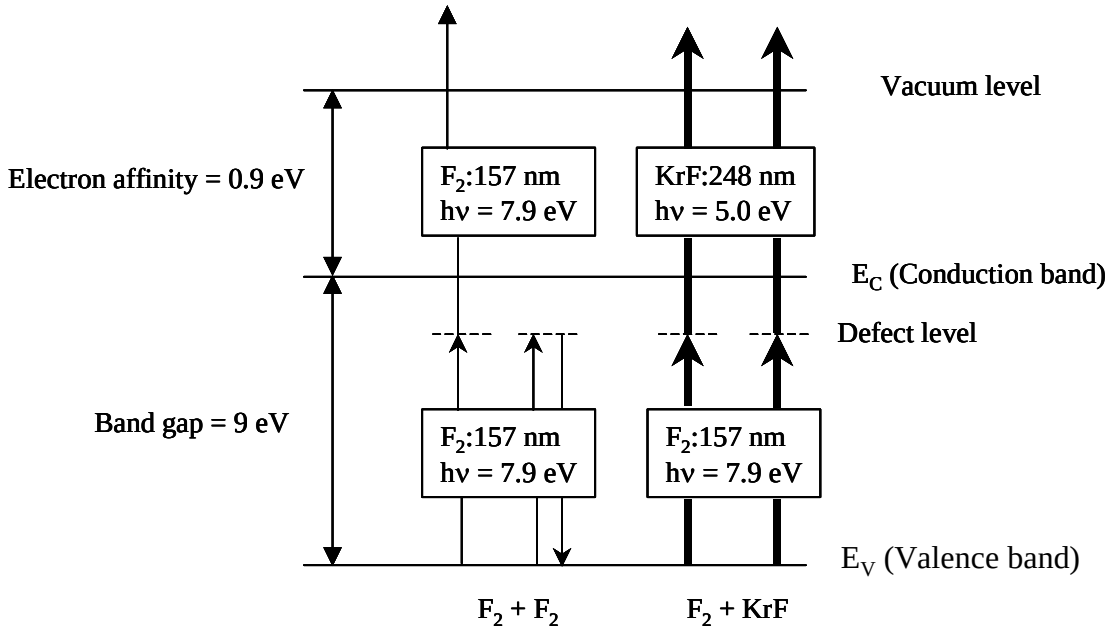

Figure 2-9: Schematic illustration of multi-wavelength excitation in fused silica [104].

However, during multi-wavelength excitation, the excited electrons of defect levels are excited to the vacuum level since the KrF-photons rely on defect level excitation. A schematic illustration of multi-wavelength excitation is presented in Figure 2-9. The defect levels are close to the bottom of the conduction band and the electron affinity of fused silica is 0.9 eV. KrF-photon energy is higher than the sum of these energies [104]. Therefore, the relaxation of electrons back to the valence band is avoided. Simultaneous multi-wavelength excitation produced more efficient photo-dissociation of the material resulting in smoother and cleaner structures than single wavelength excitation at either of these wavelengths. Single wavelength excitation cannot excite electrons from the valence to conduction band of fused silica as the band gap energy is ~9 eV.

Konovalov and Herman [105] reported 157 nm laser ablation-induced residual tensile stresses in fused silica (Corning 7940, UV grade). Samples were ablated at energy densities ranging from 1.9 - 4.7 x 10^4 Jm^{-2}. Interferometric surface profile analysis of the samples showed a convexity of craters at all the energy densities of ablation. This was attributed to material compaction and concomitant tensile stress immediately below the ablation surface. This compaction-induced convexity of the surface was also observed when samples were irradiated below the ablation threshold. Thermal

diffusion was found to be much higher than the optical penetration depth in this material. Wet chemical etching was carried out on ablated samples. Flattening of craters and stress relief was noted. Surface ripples, bulk compaction and tensile stresses were produced in deep laser-affected zones of silica-based materials during 157 nm ablation. These ablation-induced stresses could be detrimental to the fabrication of Fabry-Perot structures as this convexity of a surface or refractive index modification affects the optical reflectivity of the ablated surface.

2.8.6.1 F_2-Laser-Induced Photosensitivity

F_2-lasers are used widely for producing photo-refractive index changes in glasses [106], [107], [108]. These lasers produce refractive index changes in the range 10^{-4} to 10^{-3} in fused silica [106]. These photo-refractive index changes are much higher than those obtained by 193 and 248 nm irradiation. H_2 loaded OH-SiO_2 samples show a two-fold enhancement of 157-nm photosensitivity. This is due to the high reactivity of H_2 with OH groups under 157 nm irradiation to produce molecular H_2O, which has very strong absorption at 157 nm. These lasers were used for writing fibre Bragg gratings. Chen *et al.* [109] used 157 nm radiation for writing long period fibre gratings (LPG). The total exposure dose of 157 nm radiation was 250-fold smaller than 248 nm exposure to produce similar gratings in identical H_2-loaded fibres. This low exposure of 157 nm radiation also reduces thermal damage to the grating. The spectral shift and loss of grating reflectivity after annealing was also found to be much smaller on 157 nm written LPGs than 248 nm written LPGs. Therefore, 157 nm lasers induce stronger and faster refractive index changes than other excimer lasers.

Dyer *et al.*[110] studied F_2-laser heating of silica fibres. Bragg gratings were exposed to irradiance in the range 0-800 Wm^{-2}. The experiments were carried at an ambient pressure of $<10^{-2}$ Pa. Temporary shifts in Bragg peak reflection were observed due to laser-induced heating, in addition to permanent changes in refractive index. From the temperature calibration of a Bragg grating, the temporary shifts during exposure linearly increased with increasing irradiance and a maximum temperature rise of ~ 30 °C was observed at 800 Wm^{-2}. When the ambient pressure was increased from $<10^{-2}$ Pa to 10^2 Pa, the temporary shift during irradiance had fallen by an order of

magnitude. This was attributed to dissipation of heat by conduction to the ambient gas.

Chen *et al.* [111] studied F_2-laser-indued refractive index changes in fused silica fibres. When weak (low-reflectivity) Bragg gratings written on SMF-28 fibres using 248 nm laser were exposed to an accumulated 157 nm fluence of 25 x 10^4 kJm^{-2}, a saturated index change of 1.3 x 10^{-3} was observed. The amplitude of reflection was also increased with post 157 nm irradiation. However, the post 157 nm irradiation of strong (high-reflectivity) gratings made the gratings weaker. This was attributed to erasure of the strong grating index modulation formed by the KrF laser.

Unlike 248 nm and 193 nm excimer micro-machining stations, the 157 nm micro-machining requires beam transmission ambient, high purity lens materials and optical coatings to overcome transmission loses. The critical issues associated with 157 nm micro-machining beam delivery systems are presented in the next section. These aspects are significant as the author intends to develop a 157 nm laser micro-machining station.

2.8.6.2 Critical Issues Associated with 157 nm Lasers

Absorbing defects and colour centres in fused silica make it unsuitable for optical element manufacture at 157 nm. Crystalline fluorides such as lithium fluoride (LiF), magnesium fluoride (MgF_2) and calcium fluoride (CaF_2) are highly transmitting at this wavelength [112], [113], [114]. However, LiF and MgF_2 are not suitable for long-term use due to their hygroscopic nature and intrinsic birefringence respectively. CaF_2 is very suitable as a lens making material due to its high transmission, long-term durability, refractive index homogeneity, low stress birefringence and high thermal conductivity [115]. However, the costs involved in the manufacture of high purity CaF_2 are very high. Fluorine-doped low 'OH' content fused silica has also been proved to be a highly transmitting material at 157 nm [116]. 157 nm photons, although they cannot directly excite '≡ Si – O – Si ≡' bonds, interact with strained '≡ Si – O – Si ≡' bonds and produce colour centres. This is presented in Equation 2-16. Strained bonds are produced during densification of SiO_2 glass at high pressure.

Fluorine doping suppresses the formation of these colour centres via strained bonds by forming a '≡ Si-F' bond, which is stronger than 'Si – O'.

Conventional oxide optical coatings for anti-reflection, high reflection and partial reflection coatings are not suitable at 157 nm due to their high absorption. High-index layer materials such as lanthanum and gadolinium fluorides and low-index layer materials such as magnesium and aluminium fluorides are used in optical coatings of 157 nm optical elements [115].

The transmission of 157 nm is not possible in ordinary atmospheres due to strong absorption by oxygen, water vapour and hydrocarbon contamination [117]. Therefore 157 nm beam transmission conditions are established by evacuating the beam line to an ultra high vacuum or by purging with highly transmitting gases such as argon or dry N_2. Out-gassing from materials under the influence of high vacuum in the beam path also reduces transmission of the beam energy. Ambient transmission conditions used by various authors during the use of 157 nm laser were compared and are presented in Table 2-6.

Table 2-6: Transmission of 157 nm beam at various ambient conditions compiled from various sources.

Ambient conditions	**Transmission of 157 nm beam**
10 ppm of oxygen [112]	15% attenuation per metre
10 ppm of water vapour [112]	5% attenuation per metre
<11 ppm of oxygen [118]	50% transmission of pulse energy over 3 m long beam line
1 ppm of oxygen [117]	Attenuation of 1% per metre
10 ppm oxygen level obtained by purging dry N_2 at 10 litre minute^{-1} for 15 minutes [118]	50% transmission of pulse energy over 3 m long beam line
Oxygen less than 4 ppm and water vapour less than 3.5 ppm [102]	Attenuation <30% over 3 m long beam path length
Vacuum used for transmission is 0.01 Pa [108]	Transmission not specified

Purging is a low-cost technique for producing beam transmission conditions compared to ultra high vacuum methods. Purging reduces the partial pressure of contaminants. Purging a chamber to establish the desired partial pressure of contamination is determined by factors such as volume flow of purge gas per unit

time, diameter of the vent orifice and efflux velocity through the vent [119]. For example, infiltration of contamination through the vent orifice or through any other passage can be controlled by changing the flow rate of purge gas into the chamber. If the infiltration passage is very small, then the ratio of purge volume to flow rate of contamination into the purge volume through the passage (or vent) is very long. Under these conditions a low flow rate maintains clean conditions inside the chamber. When this ratio is very short, a higher flow rate is required to maintain the desired partial pressure of contaminant. If the effluent flow velocity through the vent is smaller than the incoming particle velocity then the particle can infiltrate into the chamber. Therefore, higher cross-sectional areas of the vent orifice require a higher purge gas flow rate to maintain the efflux velocity such that incoming particles cannot be infiltrated.

2.8.6.3 Summary of F_2-Laser Micro-machining

F_2- laser ablation offers an unprecedented control of geometry and optical quality of microstructures due to its high photon energy and strong absorption [91], [102]. The strong optical absorption of 157 nm laser radiation in sub-micrometre thicknesses of material enables a higher depth resolution and lower ablation threshold. These lasers are extensively used for surface micro-machining of fused silica. However, there are a number of aspects such as control of wall-angle and morphology of sidewalls and craters in high aspect ratio microstructures in large band gap materials, such as fused silica and sapphire, which need to be investigated. These investigations have not been previously reported and would provide valuable information for the fabrication of Fabry-Perot devices in optical fibres. These lasers induce stronger and faster photo-refractive index changes in fused silica and germania-doped silica. Although, an F_2-laser is an excellent tool for micro-machining applications, there are a number of critical issues such as lens materials, coatings and beam transmission, which ultimately determine the quality of micro-machining.

Besides laser ablation, hydrofluoric acid etching of optical fibres is another useful technique for producing repeatable Fabry-Perot etalons and sensors. The following section presents etching mechanisms of fused silica and germania-doped silica, a

review of HF etching of optical fibres for the fabrication of optical fibre probes and sensors for a variety of applications.

2.9 Chemical Etching of Optical Fibres

Hydrofluoric acid (HF) etching is extensively used in micro-sensors, micro-actuators and integrated circuit manufacturing [120]. It is also widely used for the manufacture of optical fibre probes for near-field optical microscopes. This literature review on the chemical etching of optical fibres is aimed at presenting various applications of HF etching of optical fibres such as optical fibre probes, strain and pressure sensors. The etching mechanisms of SiO_2 and germania-doped SiO_2 are also presented.

2.9.1 Etching Mechanisms of Fused Silica

Oku *et al.* [121] proposed a fused silica etching mechanism of HF. The proposed reaction is expressed as follows:

$$SiO_2 + 6HF \rightarrow 2H_3O^+ + SiF_6^{2-} \qquad \text{Equation 2-20}$$

The H-F in hydrofluoric acid solution attacks the strong Si–O bond of the tetrahedral silica network due to the high electronegativity of fluorine. Hydroxyl groups are formed at four oxygen atoms of the SiO_4 network. Then the fluoride ions attack the hydroxyl bonds of silicon and expand its co-ordination number from 4 to 6. Due to this reason, silicon can form 6 bonds with fluorine to form SiF_6^{2-}. The etch rate of germania-doped silica was higher than for pure silica. This is due to the lower bond energy of the doped core compared with the cladding. The average bond energy of Ge-O is 662 kJ mol^{-1} and Si-O is 799 kJ mol^{-1} [122]. The reaction between GeO_2 and HF can be expressed as [123]:

$$GeO_2 + 6HF \rightarrow 2H_3O^+ + GeF_6^{2-} \qquad \text{Equation 2-21}$$

2.9.2 Optical Fibre Probes via HF Etching

Optical fibre probes produced from HF acid etching of optical fibres are used in scanning near-field optical microscopy [124], [125], [126]. These fibre tips were more efficient than classical microscopy techniques due to their less-diffraction-limited imaging and high spatial resolution offered by their aperture size and fibre tip sample resolution. These probes are used in close proximity to the substrate surface to image the sample point-by-point. The basic technique of fabrication is by etching the cleaved end-face of the optical fibre until it reduces to a tip. However, the geometry and size of a fibre tip are very critical to achieve high transmission and mechanical robustness.

In the parallel-etching technique, the taper-angle at the tip was controlled by varying the number of parallel fibres etched in the stack (organic solvent-etchant) solution [125]. [127]. The meniscus height, which determines the taper- angle, is in turn governed by the separation between the fibres and the number of fibres etched. Taper-angles at the fibre tips ranging from 7° to 22° were achieved by this technique. Chaung *et al.* [126] reported fibre probes with a tip-apex angle of 90°. This is a two-step etching process by using buffered HF solution (HF + ammonium fluoride + distilled water). The first step of etching produces the desired tip size and taper along the cladding and the second step of etching at a higher concentration of ammonium fluoride produces the tip-apex angle. This large angle at the tip-apex reduced the evanescent losses and thereby increased the transmission efficiency. The surface smoothness of the fibre tips was improved by the HF impermeable tube etching technique, which was a perturbation-insensitive surface process [124]. Unlike stripped fibre etching, the tip formation starts at the end of the fibre and gradually shortens inside the tube. The tip formation was explained by the supply of HF from a larger volume to the circumference of the fibre rim than the central region. The protective polymer coating around the fibre facilitates the convection of HF to the upper regions of the fibre due to concentration gradients and gravitational removal of reaction products.

2.9.3 Cavity Production

Burrus and Standley [128] studied optical fibre etching with a 50% HF solution and the resulting cavity production due to preferential etching of dopant regions [128]. They observed a faster etching of fibre cores doped with Al_2O_3 and Nd_2O_3 than the un-doped fused silica cladding. Zhong and Inniss [129] studied the formation of cavities in GeO_2 doped cores of standard telecommunications fibres[129]. A preferential etching of doped cores was observed during etching with 1 vol% HF solution and a preferential etching of the cladding was observed during etching with buffered HF (3 parts ammonium fluoride {40%} + 1 part HF {49%} diluted by 50% in citric acid). This gave evidence that cavity production is possible due to preferential etching of the doped regions using hydrofluoric acid etching.

2.9.4 HF-Etched Fibre Sensors

A cavity production technique was utilised for the fabrication of optical fibre sensors. Murphy *et al.* [130] have produced cavities around the GeO_2 doped-core of 50/125 μm fibres, which were filled with a micro-porous sol-gel matrix containing an analyte-sensitive dye. The analyte response was due to the fluorescing nature of the dye upon irradiation at 850 nm. Quasi-distributed chemical sensing was achieved by using optical time domain reflectometry. Abeysinghe *et al.* [3] have fabricated pressure sensors based on cavity production in the core of large core borosilicate fibres followed by anodic bonding of a silicon diaphragm. The deflections produced in the diaphragm due to external pressure were interrogated by measuring the Fabry-Perot cavity length (formed between the cavity and diaphragm) changes. A positive photo-resist coating on the polished end face of a 200/400 μm fibre was irradiated with a focussed spot of a argon laser emitting at 457.9 nm followed by resist development and etching with a buffered HF solution. Silicon wafers of 4-10 μm thickness were positioned against wafers heated to 400 °C and a voltage of 1000 V was applied between them for 3 minutes to produce a bond. Borosilicate fibres were used for this fabrication due to the relatively large concentration of alkali ions, which provide better anodic bonding than the fused silica.

Zhu and Wang [131] made a miniature pressure sensor that was based on a cavity production by preferential etching of doped silica. A single mode fibre was fused to a 105/125 μm fibre with step-index un-doped core and fluorine-doped cladding. A 105/125 μm fibre was cleaved to a length of a few tens of micrometres. This end was spliced to a 62.5/125 μm fibre with graded index doped core. Then the 62.5/125 μm fibre was cleaved in the same fashion to a small length, which was etched in HF to produce a cavity. The un-doped core of the 105/125 μm fibre prevented etching of the SM fibre. This cavity was spliced to a 105/125 μm fibre by controlling the fusion current and again cleaved to a small length of 105/125 μm fibre. This end was again etched until the 105/125 μm fibre thickness was reduced to a diaphragm. The FP cavity was formed between the two un-doped surfaces of the 105/125 μm fibres. SM fibre served to couple light through the cavity. A schematic illustration of the fabrication steps is presented in Figure 2-10.

Unlike cavity creation, HF etching was also used for the production of periodically etched sections close to the fibre-core on the cladding of optical fibres [132]. Upon external loading along their length, the change in the mode volume at the etched sections due to photo-elastic effects caused a loss of output power as a function of strain in the fibre.

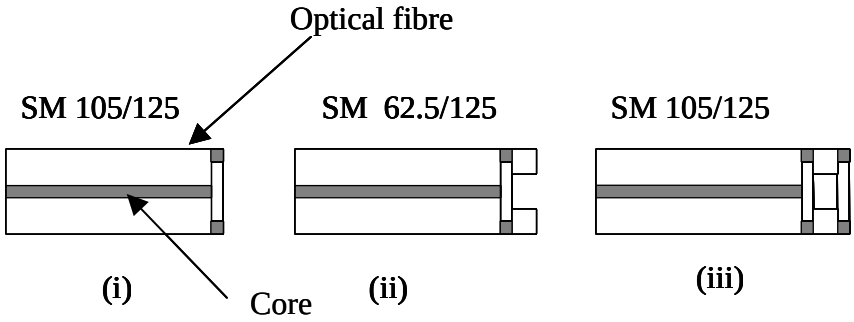

Figure 2-10: Sensor fabrication steps: (i) Etch barrier splicing/cleaving, (ii) Cavity splicing/cleaving/etching (iii) Diaphragm splicing/cleaving/etching [131].

Tuck and Fernando [133] demonstrated a strain sensor based on HF etching of SM 800 fibres. The underlying principle was preferential etching of the doped-core.

Fibres were etched using 48% HF at a temperature of 26 °C for different times to produce cavities of different etch depths. The etch rate of the core was found to be 1.8 μm minute^{-1}. Two etched fibres were spliced by controlling the fusion parameters to produce an intrinsic FP cavity. A sensor with a cavity length of 41 μm was surface-mounted on a steel coupon. The intrinsic FP sensor was interrogated using low coherence interferometry. The cavity gap changed with corresponding external load changes were observed. In another experiment by Tuck [8], a 54 μm sensor response was compared with the strain recorded by an electrical resistance strain gauge. The cavity length changes were linear with the response of the strain gauge. Higher cavity length changes were observed with sensors of larger cavity lengths. For a strain of 1000 με in the coupon, a cavity length change of 1.6 μm was observed in a sensor with a cavity length of 54 μm. This intrinsic FP fabrication technique offers a low cost fabrication route. However, this fabrication technique requires refinement for improved and repeatable cavity length production of intrinsic strain sensors. In addition to this, these sensors need to be evaluated for strain measurements in a harsh environment to assess their durability and reliability.

2.9.5 Summary of Chemical Etching of Optical Fibres

HF etching of optical fibres offers a low-cost fabrication of fibre probes that are widely used in near field microscopy. Faster etching of doped regions of fused silica produces cavities. The technique of cavity production in optical fibres can be used for measuring a variety of measurands. Intrinsic FP sensors via cavity production in optical fibres offer a low cost fabrication route for strain sensors. This manufacturing technique addresses various problems involved in EFFPI sensor fabrication.

2.10 Conclusions of the Literature Review

This literature review shows that addressing the various problems involved in the manufacturing and application of EFFPI sensors, could lead to the development of more efficient and low-cost sensor fabrication techniques. Laser micro-machining of

fused silica and sapphire substrates shows that fabrication of high optical quality microstructures is possible using F_2-lasers. However, with respect to the fabrication of FP cavities via F_2-laser micro-machining, there are a number of aspects such as the optical quality of microstructure wall surfaces, the optical quality of craters and the wall angle of cavities ablated through the diameter of optical fibres and through the cleaved end-face, which need to be investigated. To the best of the knowledge of the author, these aspects of high aspect ratio microstructure fabrication in fused silica and sapphire have not been investigated. The literature review also presented a number of factors of micro-machining, which influence the geometry and optical quality of ablated structures. Although HF etching of optical fibres for intrinsic FP sensor fabrication offers a low-cost route, this technique needs to be refined for more repeatable production and evaluation of sensors for use in harsh environments is required. Besides, FP structures, F_2-laser micro-machining could lead to the development of many other novel configurations of sensors for measuring a wide variety of measurands.

2.11 Proposed Fabry-Perot Configurations via F_2-Laser Micro-machining

Two types of Fabry-Perot configurations were proposed via laser micro-machining of fused silica optical fibres. They are schematically illustrated in Figure 2-11. The rationale of micro-machining through the fibre diameter is the production of cavities with parallel walls, which are perpendicular to the core of the optical fibre so as to produce intrinsic Fabry-Perot etalons. The rationale of micro-machining cavities at the cleaved end face of an optical fibre through its core is the production of a cavity crater surface of high optical quality, which produces FP interference when fused to the cleaved end of another fibre. Realization of these designs could significantly reduce the size of conventional EFFPI designs and open-up new possibilities for the production of sensors for measuring a variety of parameters.

In comparison to the manual fabrication of EFFPI and other techniques presented in the literature review, F_2-laser-based fabrication of intrinsic FP cavities in optical fibres has following advantages, namely:

1. Repeatability
2. Preset cavity length can be produced
3. Ease of manufacture
4. Mass production
5. Overcomes discontinuities in sensor geometry
6. Overcomes problems concerned with gauge length
7. Miniaturization of FP sensor

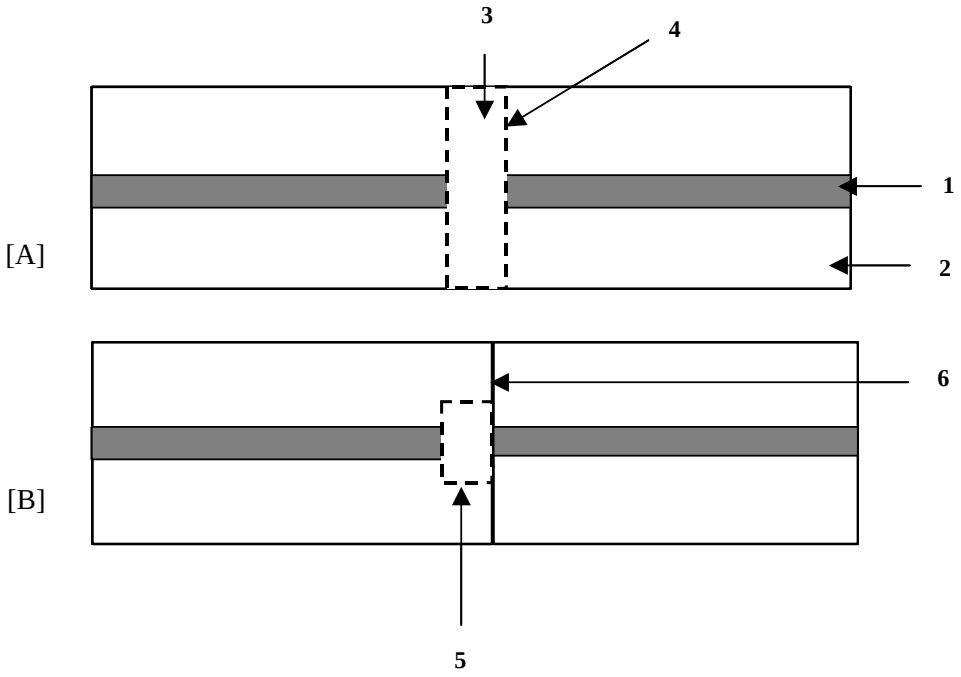

Figure 2-11: Schematic illustration of FP configurations for micro-machining optical fibres; [A] Cavity micro-machined through the diameter of the optical fibre, [B] Cavity micro-machined into the fibre core at the cleaved end of an optical fibre and fused to another optical fibre.

1. Core of the optical fibre
2. Cladding of the optical fibre
3. Cavity micro-machined through the diameter of the optical fibre
4. One of the vertical walls of the cavity micro-machined through the fibre diameter
5. Cavity micro-machined into cleaved end face through the core of the fibre
6. Cleaved end of another optical fibre fusion spliced to the micro-machined end face

3 Illumination Design of Optical Beam Delivery System

3.1 Overview

This chapter presents the design of the illumination system using a mask projection technique for micro-machining Fabry-Perot microstructures. The illumination design is based on conventional Kohler illumination. Illumination aspects such as degree of partial coherence, numerical aperture and demagnification of the image are designed to meet the criteria such as contrast in the image, depth of focus and resolution and dimensions of the microstructures. The significance of these factors with respect to micro-machining high aspect ratio cavities is discussed. The optical configuration of the imaging objective is presented. The optical elements of the beam delivery system were designed and constructed by Dr Francis Goodall, FG Optics, London, UK.

3.2 Beam Delivery Optical System

The beam delivery optical system used for these micro-machining experiments is based on conventional Kohler illumination. The reason for the Kohler illumination-based design was that the laser system was operated by a stable resonator, which has high conversion efficiency, high pulse-to-pulse energy stability, good quality beam profile. However, it suffers from high beam divergence and low spatial coherence. The influence of stable and unstable resonators on the coherence of output beam is presented in Section 2.8.5.4. Therefore, the intention of this design is to improve the coherence of the illumination, which in turn improves the contrast of images.

In Kohler illumination, the extended incoherent source is imaged at the back focal plane of the condenser lens. An aperture stop situated at the back focal plane controls the obliquity of the illumination. The diverging rays from each source points at the condenser stop position emerge as collimated pencils, which illuminate the object plane before entering the microscope objective. The irregularities in the brightness

distribution of the source do not cause irregularities in the illuminating field as the field of illumination is collimated. A schematic illustration of the central (for an on-axis source point) Kohler illumination arrangement is shown in Figure 3-1. However, the image of the source at the aperture stop will be extended when other off-axis points from the source are considered.

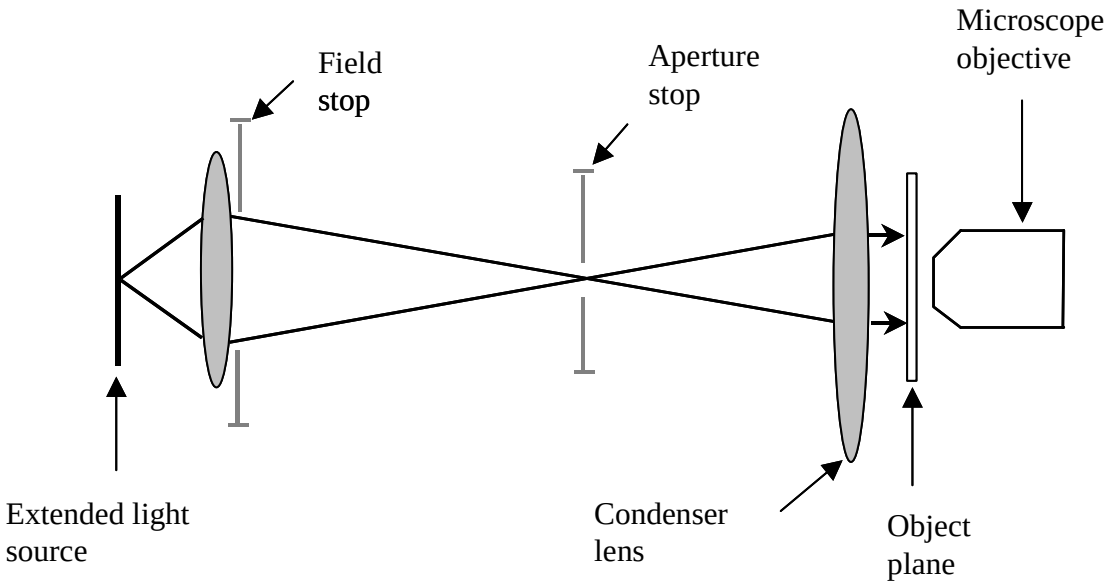

Figure 3-1: Schematic illustration of the central Kohler illumination arrangement.

The beam delivery optical system designed for micro-machining was a mask projection technique based on the above described illumination system. The raw beam from the 157 nm laser had dimensions of 23 x 7 mm. In this design it was assumed that the raw beam from the laser was a parallel beam. A plano-convex field lens was used to image the source at its focal plane. The entrance pupil of the imaging system or the stop-position coincides with the focal plane of the field lens. The imaging objective has a numerical aperture of 0.1 in the image space and has a demagnification ratio of 1:40. This demagnification is based on the size of the Fabry-Perot structures, which were designed to machine optical fibres of diameter of 125 μm. The reason for the choice of this demagnification ratio is that the size of the designed mask features is relatively smaller compared to the raw dimensions of the beam. Therefore, the mask feature can be illuminated by the peak intensity regions of the beam to reduce the inhomogenities in the spatial intensity distribution of quasi-Gaussian raw beam. The imaging system images the mask feature to +1 and –1 orders of diffraction at the image plane.

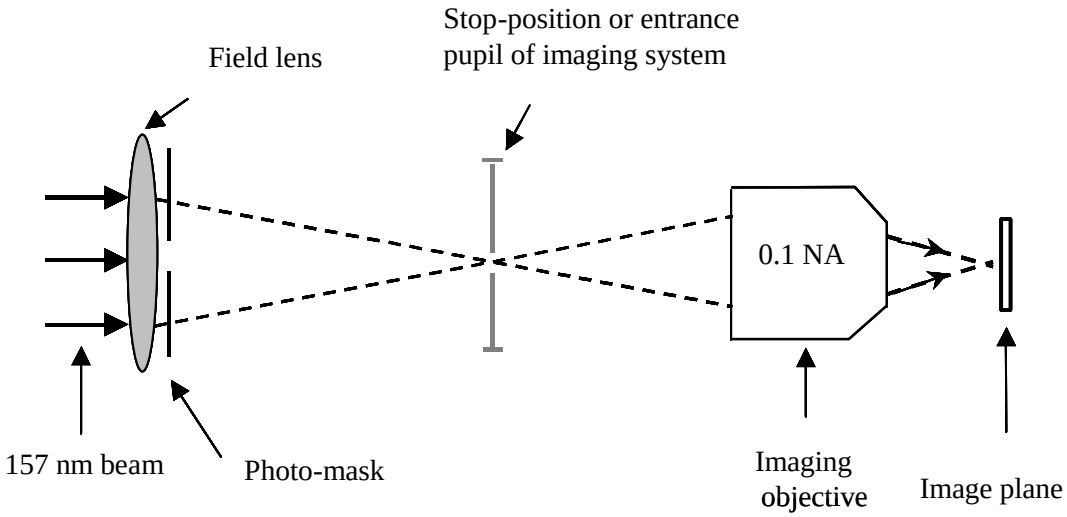

Figure 3-2: Schematic illustration of the illumination design of the optical system.

The choice of numerical aperture and demagnification was based on two important factors. The first one was that the mask features intended for imaging were simple transparencies such as squares, rectangles and circles, which were to be imaged one at a time. Unlike imaging of high spatial frequencies, which are to be resolved, this application does not demand high numerical aperture imaging systems. In addition to this, the depth of focus of imaging will be higher for lower numerical apertures. This feature of the imaging system had two advantages. The first one was that the alignment of the target surface in the image plane is relatively easy using the translation stages described earlier. The resolution of the motorised Z-stage used for these experiments was sufficient for keeping the depth of focus offered by the imaging system in view. The second reason was that the larger depth of focus preserves the image contrast to a higher depth while machining Fabry-Perot microstructures. This helped to control the shape of the micro-cavities to a greater depth. A schematic illustration of the illumination design is presented in Figure 3-2.

In the illumination design shown in Figure 3-2, the mask takes the position of the field stop as shown in Figure 3-1. The mask transparency was placed close to the centre of the field lens such that the beam, being close and parallel to the principal axis, could

be used for illumination. This arrangement is particularly useful for spatial filtering of inhomogenities of intensity in the raw beam profile. Therefore, the effective source is reduced to the dimensions of the mask feature.

The field from the mask is a spherical wave front converging towards the stop position to a point. Therefore, the effective source is imaged at the stop-position. According to a paraxial approximation, the image of the effective source can be considered as a virtual quasi-monochromatic point source. Therefore, the illuminated mask feature or the effective source, which is composed of coherent point sources that are mutually incoherent in the mask plane, is reduced to a point source at the stop-position. However, the obvious diffraction at the mask produces a spread, rather a patch of light source in the entrance pupil, which is much smaller than the mask feature. The objective images the stop at its working distance in the image space according to its demagnification. In the arrangement shown in Figure 3-1, the light from the effective source at the aperture stop position is collimated to illuminate the object plane. However, in Figure 3-2, the effective source or the mask feature itself is the object that is Fourier transformed at the entrance pupil to produce Fraunhofer diffraction.

Based on this illumination design, the distance between the mask and the field lens was 0.53 m, the distance between the stop and the imaging system was 0.1 m, the numerical aperture on the object side was 0.0025, diameter of the entrance pupil was 2.69 mm, the diameter of the exit pupil was 0.38 mm and it was located at a distance of 1.94 mm from the last lens element of the imaging system. The working distance of the imaging system was 0.04 m (data provided by FG Optics (UK), optics manufacturer). The 0.1 numerical aperture imaging system is a multi-lens element system, which produces a demagnification of 1:40 at the image plane. The demagnification can be defined as the ratio of numerical aperture in the object space to the numerical aperture in the image space. Based on this demagnification, the dimensions of the mask features are well within the dimensions of the raw excimer beam. For example, a 50 μm x 50 μm structure can be produced by imaging a 2 mm x 2 mm mask feature using a 1:40 demagnification imaging system. The dimensions of this mask feature are smaller than the dimensions of the raw beam that has rectangular

dimensions of 23 mm x 7 mm. Therefore, the mask transparencies can be illuminated by a near-uniform portion of the spatial intensity of the raw beam. The lens configuration of the imaging system provided by the manufacturer is presented in Figure 3-3.

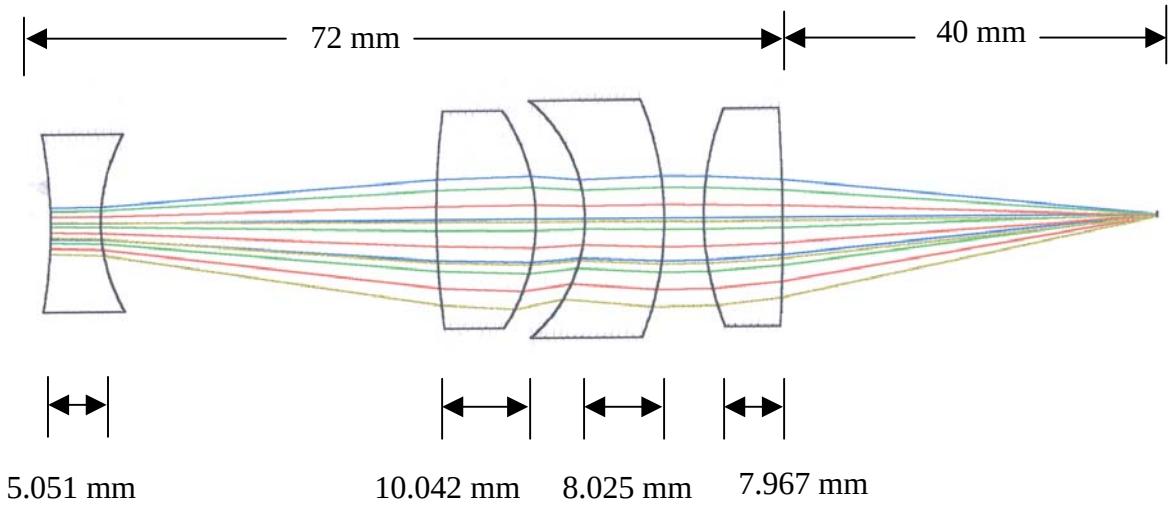

Figure 3-3: Schematic of ray paths (from left to right) through the multi-lens elements the of imaging system, thickness of each element and working distance.

This configuration is known as double Gauss configuration. Figure 3-3 illustrates the geometric optical path of the beam entering the imaging system from the stop position. This configuration provides a demagnification of 1:40 and a numerical aperture of 0.1 in the image space.

3.3 Coherence of Illumination Design

As presented in the literature review Section 2.8.5.2, the partial coherence of the illumination can be expressed as the ratio of the source to entrance pupil dimensions. In the illumination design used for micro-machining, the effective source is reduced to a point source at the entrance pupil. The diameter of the entrance pupil is 2.62 mm (manufacturer's data) and ratio of the point source size to the diameter of the entrance pupil tends to approach zero and therefore, the illumination design can be considered as highly coherent. It can also be observed from the value of numerical aperture on the object space, i.e., 0.0025, that the optical path difference between the pencils of

rays emitted from the entrance pupil is very small since the ray directions involved make very small angles with the optic axis. Assuming that the imaging system is free of aberrations and defect of focus, the contrast of image increases with coherence. The contrast of the imaged mask features determines the geometry of micro-machined structures. Therefore, the coherence of illumination plays an important role in micro-machining applications.

Since the illumination is considered coherent, the depth of focus and resolution of the imaging system can be approximated by the Raleigh criterion as [78]:

$$\text{Depth of focus} \sim \pm\left(\frac{\lambda}{2NA^2}\right) \qquad \text{Equation 3-1}$$

$$\Rightarrow \text{Depth of focus} \sim \pm\left(\frac{157\times10^{-9}}{2\times0.1^2}\right)$$

$$\Rightarrow \text{Depth of focus} \sim \pm 7.85\ \mu\text{m} \qquad \text{Equation 3-2}$$

The resolution of the imaging system can be expressed as:

$$\text{Resolution} \sim \frac{\lambda}{2NA} \qquad \text{Equation 3-3}$$

$$\Rightarrow \text{Resolution} \sim \left(\frac{157\times10^{-9}}{2\times0.1}\right)$$

$$\Rightarrow \text{Resolution} \sim 0.785\ \mu\text{m} \qquad \text{Equation 3-4}$$

3.3.1 Quantitative Assessment of the Coherence of Illumination Design

The following calculation gives a quantitative assessment of the coherence of illumination design. This calculation was developed according to the definition presented in Section 2.8.5.2 of the literature review. In Figure 3-4, 'AC' is the diameter of a mask feature or the effective source, 'α' is the angular radius of the effective source as seen from the centre of the entrance pupil and 'α′' is the angle

corresponding to the numerical aperture on the image side. The partial coherence factor, σ, can be expressed as:

$$\sigma = \frac{\sin\alpha}{\sin\alpha'} \qquad \text{Equation 3-5}$$

Suppose the diameter of the mask feature, AC = 1.5 mm. Then AB = 0.75 mm. The entrance pupil is at a distance of 530 mm (manufacturer's data) from the mask feature and from that it follows as:

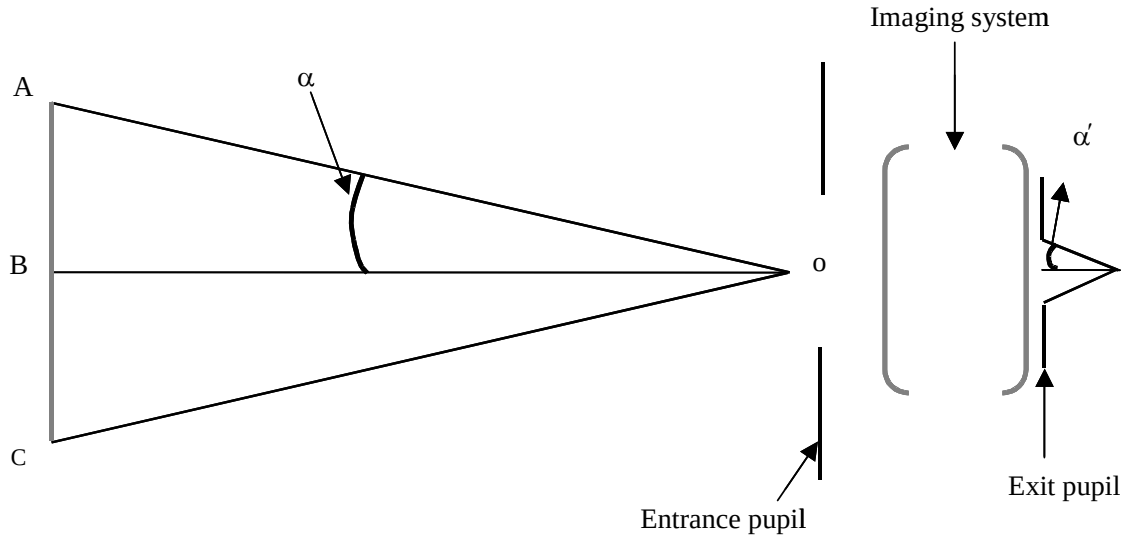

Figure 3-4: Schematic to assess the coherence of illumination.

$$\tan\alpha = \frac{0.75}{530} \qquad \text{Equation 3-6}$$

$$\Rightarrow \tan\alpha = 0.00141$$

$$\Rightarrow \alpha = 0.0807 \qquad \text{Equation 3-7}$$

$$\therefore \sin\alpha = 0.0014 \qquad \text{Equation 3-8}$$

We already know that sinα' = 0.1 and therefore the partial coherence of illumination is determined as:

$$\sigma = \frac{\sin\alpha}{\sin\alpha'} \qquad \text{Equation 3-9}$$

$$\Rightarrow \sigma = \frac{0.0014}{0.1}$$

$$\Rightarrow \sigma = 0.014 \qquad \text{Equation 3-10}$$

The illumination is almost coherent if $\sigma \to 0$ and incoherent if $\sigma \to \infty$. From Equation 3-10, the illumination can be considered as almost coherent since the value of 'σ' approaches zero. Therefore, this produces a high degree of coherence between the neighbouring points in the image plane and has to produce high contrast imagery. It does not imply that the coherence of the laser output is improved by the optical beam delivery system. However, the irradiance distribution at the image plane, which is an incoherent superposition of individual fringe patterns produced from the point sources of the extended incoherent source, comprises of higher visibility fringes. This is the result of illumination design.

3.4 Summary of Illumination Design

The illumination design of the beam delivery was based on conventional Kohler illumination. The effective size of the source was reduced to a point object at the stop position via the mask projection. As the angular radius of the source is reduced to a point, a high degree of coherence can be achieved. This ensures high contrast imagery. A low numerical aperture imaging system was used to improve the depth of focus. A larger depth of focus is particularly useful for micro-machining high aspect ratio cavities and eases alignment of target surfaces such as optical fibres. The demagnification of the imaging system can provide suitable dimensions of microstructures to be produced in optical fibres.

4 Design and Construction of F_2-laser Micro-machining Station

4.1 Overview

As explained in Section 2.8.6.2 of the literature review, a beam delivery chamber is required to establish a suitable transmitting environment along the path of 157 nm laser beam. This chapter presents the design and construction of two purge chambers and an ablation chamber, which are suitable for homogenised and un-homogenised beam delivery optical systems. It also presents the construction of a target alignment and monitoring system, which is suitable for controlled spatial motion of targets such as optical fibres during micro-machining.

Two beam delivery chambers were designed and constructed. A 3.3 m long beam delivery line to conduct the experiments on beam transmission and to align homogenised beam delivery optics; and a separate 460 mm long tunnel with an ablation chamber were constructed for un-homogenised beam delivery. The chambers were made of aluminium box sections of different lengths, which had a wall thickness of 3 mm. Aluminium was chosen due to its inertness to the purge gas and good corrosion resistance to atmospheric changes and air born contamination. The purge chamber was constructed by Mike Teagle, Laboratory manager, Sensors and Composites Group, Cranfield University.

4.2 Long-Beam Tunnel

Three aluminium box sections of lengths 0.9 m, 1m and 1.49 m were welded to produce a beam delivery chamber of 3.39 m. This is schematically shown in Figure 4-1. The box sections have cross-sectional dimensions of 0.15 m x 0.15 m. This cross-section was chosen to meet the requirements of the space needed to align the mounted optical elements. The dotted lines shown in Figure 4-1 are side openings of the tunnel, which were cut to suitable dimensions along the length and height of the chamber to induce and align the optical elements along the beam line.

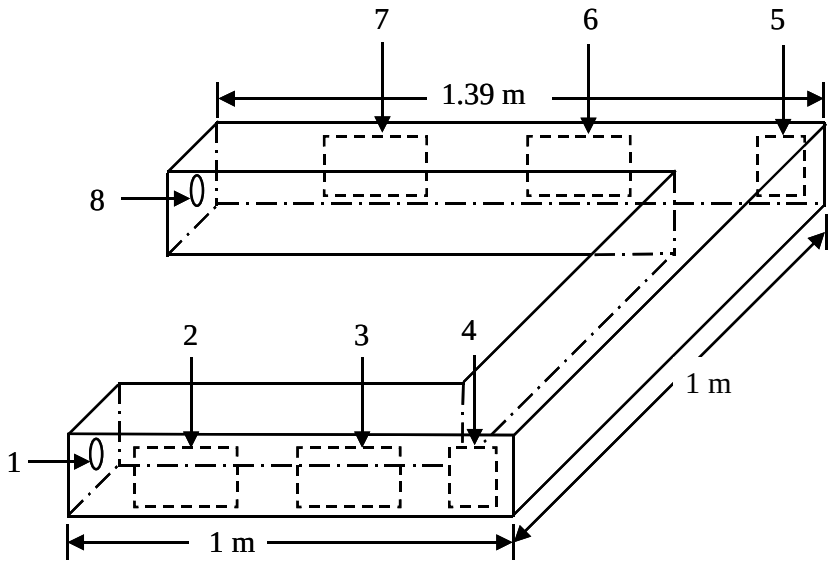

Figure 4-1: Schematic illustration of beam delivery chamber constructed for homogeniser optics.

1. 157 nm beam entry
2. Opening for aligning first beam shaping telescope
3. Opening for aligning second beam shaping telescope
4. Opening for aligning first high reflectivity mirror
5. Opening for aligning second high reflectivity mirror
6. Opening for beam homogenising optics
7. Opening for aligning for field lens and mask
8. Opening for coupling the long beam tunnel to ablation chamber

The exit point of the laser beam, (1) in Figure 4-1, was coupled to the centre of the tunnel using a vacuum flange. Holes were drilled 10 mm above the margin of the opening with a separation of 20 mm along the dimensions of the opening. Socket head screws with O-rings were sealed into the drilled holes using Studlock 270 (RS Components, UK) adhesive, such that the length of the screws was projected outside the chamber. This was done to avoid leaking of purge gas through the holes drilled in the chamber. Aluminium plates were used as side panels to close these openings. These openings are shown as (2), (3), (4), (5), (6) and (7) in Figure 4-1. The aluminium plates of the openings (2), (3), (6) and (7) had dimensions of 240 mm x 140 mm and those of (4) and (5) had dimensions of 140 mm x 140 mm. Holes were drilled in the aluminium plates such that a plate could be pushed into the outward

projected head screws of the chamber. A groove was machined along the dimensions of the plate in the interior border and O-ring nitrile rubber was sealed into the groove by using studlock 270 adhesive. The aluminium plate was pushed into the outward projected head screws of the chamber and locked using O-ring washers and wing nuts. The O-ring rubber along the groove pushes along the aluminium wall of the chamber and avoids leaking of the purge gas. All the openings of the chamber were constructed in this manner.

The beam was folded due to spatial constraints imposed by the dimensions of the pneumatic optical table. The weight of the tunnel was supported by steel I-sections laid beneath the tunnel along its length.

4.3 Short-Beam Tunnel

The short-beam tunnel has a length of 0.46 m from the beam exit point of the laser. The cross-sectional dimensions were the same as the long beam tunnel shown in Figure 4-1. It was same as the long-beam tunnel up to a length of 0.46 m with the exception of not having the second door at a distance of 0.35 m from the laser beam exit point. An aluminium frame of 30 mm width was welded along the outer margins of the tunnel and holes were drilled along the dimensions of the frame and socket head screws were fitted as explained in the construction of chamber doors. A nitrile rubber strip was cut to the same dimensions as the metallic frame and holes were made in it such that it fitted through the outward projected length of the socket head screws. This was designed to adapt to one of the 0.15 x 0.15 m openings of the ablation chamber such that a leak proof coupling between the tunnel and the ablation chamber could be maintained.

4.4 Ablation Chamber

Six aluminium plates were welded to make a cubical box of dimensions 0.55 x 0.4 x 0.4 m. These dimensions were chosen to meet the spatial requirements of motorised translation stages and optical mounts. Two opposite faces of dimensions 0.4 x 0.4 m

were cut to the dimensions of 0.15 x 0.15 m at their centres. The top face of dimensions 0.55 x 0.4 m was cut to dimensions of 0.15 x 0.15 m at a distance of 0.07 m from the edge near the coupling side. This is shown in Figure 4-2.

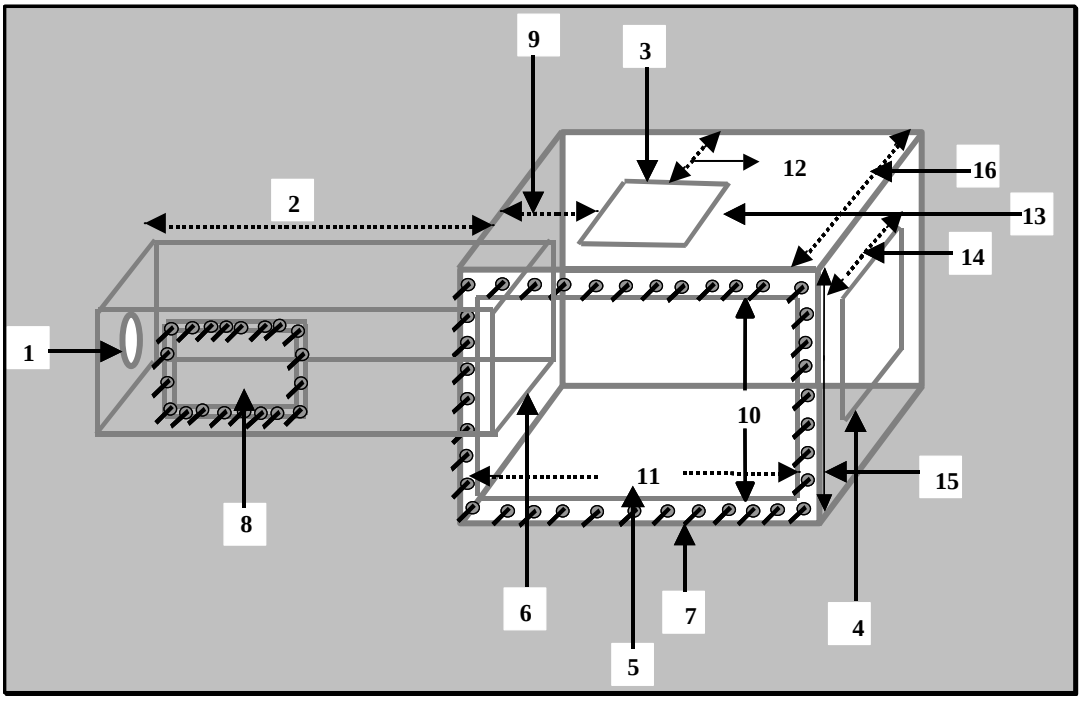

Figure 4-2: Schematic illustration of short beam tunnel coupled to the ablation chamber.

1. 157 nm beam entry
2. Length of the short tunnel = 0.46 m
3. Transparent glass window for on-axis CCD monitoring of target
4. Opening for the power supply leads
5. Main opening of the ablation chamber for accessing optical, opto-mechanical elements and electronic devices
6. Exit point of the short tunnel
7. Outward projected socket head screws
8. Opening of short tunnel for the alignment of field lens and mask
9. Separation between the ablation chamber edge and glass window = 0.07 m
10. Width of main opening of ablation chamber = 0.34 m
11. Length of main opening of ablation chamber = 0.49 m
12. Separation between the ablation chamber edge and glass window = 0.18 m
13. Dimensions transparent glass window = 0.15 m x 0.15 m
14. Dimensions of the opening for power supply leads = 0.15 m x 0.15 m

15. Height of the ablation chamber = 0.4 m
16. Width of the ablation chamber = 0.4 m
17. Vent orifice

The top opening was sealed with a 5 mm thick glass plate. This was made in the same procedure as the aluminium doors. This transparent door was used for alignment and monitoring the work piece during micro-machining. An aluminium plate of dimensions 0.55 x 0.4 m was made and was used to close the main door of the ablation chamber. This large opening was made to enable the alignment of the translation stages, optical mounts and work piece.

Holes were drilled above the margin of the opening for coupling such that the chamber could be pushed through the outward projected head screws of the frame at the end of the tunnel. O-ring rubber washers, wing nuts and Studlock 270 adhesive were used to seal the chamber to the tunnel. The nitrile rubber strip along the margin of the frame was pressed against the chamber wall to minimise leaking of purge gas.

An opening of 0.15 x 0.15 m was made in the main door of the chamber and 5 mm thick perspex sheet was used to seal this opening. The internal margin of the perspex window had a nitrile rubber lining to provide leak-proof sealing. This transparent window was made for monitoring the translation work piece visually, recording the energy from the display unit, which was positioned inside the chamber and for illuminating the work piece. A schematic illustration of the main door of the ablation chamber is shown in Figure 4-3. This door was used to seal the main opening of the ablation chamber shown in Figure 4-2.

An aluminium door was made for sealing the opening in the 0.4 x 0.4 m face of the chamber. The electrical connections between the motorised translation stages and the motion controller were made through this door. In order to achieve a leak-proof sealing of electrical leads through the door, four holes were made in this aluminium door. Plastic glands were introduced through these holes and sealed to the door around the outer margin by using a combination of epoxy resin and hardener.

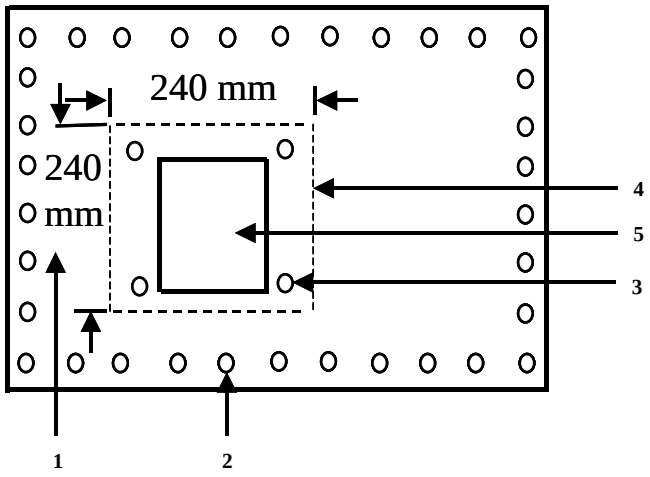

Figure 4-3: Schematic illustration of main door of the ablation chamber.

1. Main door of the ablation chamber
2. Holes drilled along the perimeter of the aluminium door
3. Holes drilled around the perimeter of 0.15 m x 0.15 m opening made in the main door from which the socket head screws are projected outward
4. Perspex window sealed to the main door using wing nuts
5. Opening made in the main door for housing perspex window

Electrical wires of suitable length were passed through the openings of the glands. Twenty-five wires were passed through each gland such that sufficient lengths of wire were available on either side of the door. Araldite adhesive (RS Components, UK), which was applied at the entrance of the opening of the gland formed a hard layer around the margins and held the wires close together. The rationale of this procedure was to make the opening of the glands leak-proof. It was allowed to cure and a combination of epoxy resin (diglycidyl ether of bisphenol A/bisphenol F) and hardener (polyoxypropylenediamine) was used to fill the gland from the other opening. The hard Araldite surface on the other side of the gland reduces the flow of resin around the margins and from spaces in between the wires. Small quantities of resin were filled and allowed to cure gradually at laboratory ambient conditions. Then the other end of the gland with Araldite was also filled with resin and allowed to cure. In summary, the epoxy resin was used to fill between the wires and to render the glands leak-proof. The same procedure was carried out for the other four glands.

Twenty-five pin D-connectors were soldered at the end of each set of wires on either sides of the door. A leak proof electrical communication was established between the motorised translation stages and the motion controller through the door of the chamber.

4.5 Target Alignment and Monitoring System

The work-piece was aligned into the image plane of the objective by using motorised translation stages. All the translation stages were supplied by Newport Ltd., UK. The Z-stage is a VM 12.7 CCE, which had a resolution of 0.001 μm and a travel range of 12 mm. The Y-stage is an UT50-20 PP, which had a resolution of 10 μm and a travel range of 50 mm. The X-stage was driven by an 850 G-actuator, which had a resolution of 0.035 μm and a travel range of 50 mm. These stages had sufficient resolution along the respective axes to align optical fibres of diameter of 125 μm.

The pyroelectric detector head was mounted on a metallic plate, which was clamped to a UR 80-PP rotation stage. The detector head was located in between the stop position and the imaging system. This stage has a resolution of 0.002° and a travel range of 360°. The detector head was mounted at the other end of the frame, such that it could be translated into the beam path by rotating the stage. The translation stages were mounted one above the other along the respective axes and clamped to each other. An L-shaped metallic frame was clamped to the assembly of translation stages such that the polished surface of its base lay near the working distance of the imaging system. This arrangement is shown in Figure 4-4. The surface of the base plate of the L-shaped metallic frame was polished such that it was horizontal.

A battery operated ‘Laser Star’, energy display unit was connected to the detector head and placed inside the ablation chamber. The display could be seen through the transparent perspex window of the main door of the ablation chamber. The work piece was illuminated using a 100 W white light source through the Perspex window.

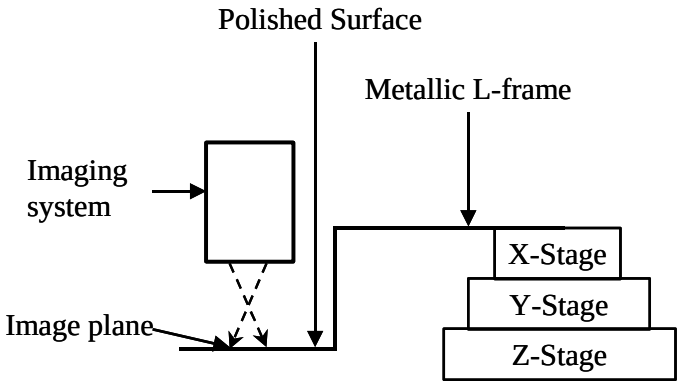

Figure 4-4: Schematic illustration of the target alignment system.

The target surface was translated into the focal plane of the imaging system by monitoring the focussed spot with a CCD camera. This was a STC - 725 black & white 0.5″ (12.7 mm) CCD camera (Alrad instruments Ltd., UK). This was a pixel size of 8.6 (horizontal) x 8.3 (vertical) μm and a horizontal resolution of 560 TVL. An imaging telescope (Fujinon, Japan) was used with the CCD camera. A pair of plano-concave lenses of focal lengths 50 and 25 mm were mounted in an extension tube with C-mount adapter rings. This lens combination along with the telescope expands the image plane and thereby increases the magnification of the object. A magnification of 160 X was achieved by using this lens combination. However, the target required a brighter illumination to preserve image contrast. Therefore during optical fibre micro-machining, the illuminating light source was moved closer to the target plane.

The camera was mounted above the transparent glass window of the chamber and was used to monitor the target along the axis of the imaging system, thereby reducing the refraction effects. The position of the camera was adjusted such that its working distance lay close to the target and was focussed at the target surface. When the target surface was gradually translated along the z-axis, the CCD camera captured the laser-induced fluorescence. A well-defined de-magnified fluorescence image of the projected mask feature could be observed as the stage was continued to translate in the same direction. This position of the target surface corresponds to image plane. The laser was operated at low pulse energy during target alignment so that the excess scatter of laser-induced fluorescence could be reduced and the de-magnified shape of the mask feature could be clearly seen. This helped to identify the image plane. This

procedure was implemented to align and monitor the surface of flat substrates and optical fibres. A schematic illustration of the on-axis monitoring of target is shown in Figure 4-5.

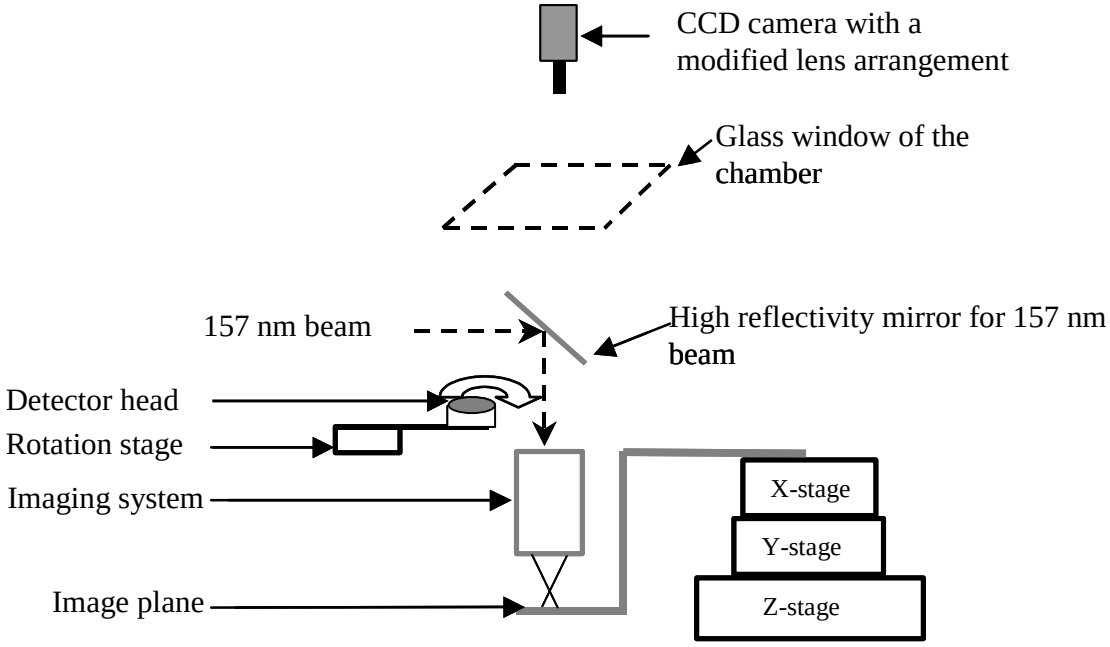

Figure 4-5: Schematic illustration of the arrangement of on-axis monitoring of the target.

4.6 Summary of the Beam Delivery Chamber

Two types of beam tunnels and an ablation chamber were designed and constructed. The short beam tunnel was designed for un-homogenised 157 nm beam delivery and the long tunnel for homogenised beam delivery. The ablation chamber was designed so that the work piece could be illuminated from outside the chamber and the target translation could be observed. Motorised translation stages had required resolution and this enables translation of targets such as optical fibres of 125 μm diameter. The imaging telescope of the CCD camera was modified using a pair of plano-concave lenses to enhance the magnification of work piece. Enhancement of the magnification of work piece and its illumination were critical aspects whilst aligning the optical fibres into the image plane of the objective during micro-machining. Evaluation of the purge chambers was carried out in a series of experiments to determine the transmission characteristics of 157 nm beam under specified gas (dry N_2) purging conditions. This is presented Chapter 7 and will be discussed at a later stage.

5 Experimental

This chapter presents the experimental techniques involved in chemical etching of optical fibres and F_2-laser micro-machining of fused silica and sapphire substrates. The results and discussion of results are presented from Chapter 6 onwards.

5.1 Materials

The details on the fused silica and sapphire optical fibres used in chemical etching and laser ablation experiments are presented in Table 5-1.

Table 5-1: Manufacturers' data on the fused silica and sapphire optical fibres.

Optical fibre	**Type**	**Manufacturer**	**Dopant Concentration of GeO_2 (mol%)**		**Core diameter (μm)**	**Cladding diameter (μm)**	**Numerical aperture**
			Core	**Cladding**			
SM800	Single-mode	Fibercore	2.67	-	5.6	125	0.13
SMF 28	Single-mode	Corning	1.6	-	9	125	0.11
MM 800	Multi-mode	Corning	8.47	-	50	125	0.21
Sapphire fibre	Multi-mode	----------	-	-	No core	150	-

- ‘OH’ and ‘Cl’ concentration in fused silica of SM 800 fibre are 0.2 ppm and 1500 ppm respectively.
- Softening temperature of SMF 28 fibre is 1600 °C.
- Thermal conductivity, specific heat and density of fused silica of SMF 28 fibres is 1.38 $Wm^{-1}K^{-1}$, 770 $Jkg^{-1}K^{-1}$ and 2200 kgm^{-3} respectively

The information about fused silica and sapphire disks is presented in Table 5-2.

Table 5-2: Manufacturers' data on the fused silica and sapphire disks.

Material	Type	Manufacturer	Diameter/Thickness	Purity	Transmission at 157 nm
Fused silica disks	Spectrosil® 2000	UQG Ltd	14.8 mm/2 ± 0.1 mm	99.9999%	----------
Sapphire disks	-	Edmund industrial optics Ltd	25.4 mm/2.3 ± 0.1 mm	99.99%	8% transmission through a thickness of 3 mm

- Softening temperature of Spectrosil fused silica is 1710 °C
- 'OH' and 'Cl' content of Spectrosil fused silica are 1000 ppm and <1 ppm respectively.
- Melting temperature of sapphire is 2047 °C.

5.2 Instrumentation

5.2.1 F_2-Excimer Laser

The F_2-laser (LPF 202) used for micro-machining experiments was supplied by Lambda Physik AG, Germany. The F_2-laser emits at a wavelength of 157 nm. It emits 50 mJ pulses at a maximum frequency of 20 Hz at an operating voltage of 26 kV. The pulse width of the laser is 17 ns FWHM. The raw beam has dimensions of 23 x 7 mm and a divergence of 3 x 1 mrad along the respective dimensions. The laser can be operated in constant energy mode or constant voltage mode. In constant voltage mode the operating voltage can be varied from 21 kV to 26 kV.

The spectrum of the LPF 202 consists of two emission lines centred at 157.63 nm and 157.52 nm. These lines have an intensity ratio of 10:1 respectively. The individual width of each emission line is 0.85×10^{-12} m. The photon energy of 157 nm radiation corresponds to 7.9 eV. The laser emits several percent of the radiation in the spectral range from 620 to 780 nm.

The 157 nm excimer laser has molecular fluorine as the active medium and helium as the buffer gas. The laser gases were supplied by Spectra gases Ltd., UK. During the execution of a new fill the laser cavity will be evacuated to a cavity pressure of 3000 Pa and the laser tube is filled with a mixture of 5% molecular fluorine (hydrogen fluoride free) and 95% helium (99.995%) to a partial pressure of 9000Pa. Then the tube will be filled with helium (99.995%) to a partial pressure of 301000 Pa. Then the total pressure of the tube is 313000 Pa. The laser system has a stable resonator and a rear mirror made of magnesium fluoride MgF_2, which is transparent to visible light.

5.2.2 KrF Excimer Laser

The Bragg star S-500 krypton fluoride (KrF) excimer laser used for writing fibre Bragg gratings was supplied by TuiLaser AG, Germany. This laser emits at a wavelength of 248 nm. It emits 18 mJ pulses at a maximum repetition rate of 500 Hz. The pulse duration, raw output beam dimensions and beam divergence are 10 ns (FWHM), 3 mm x 6 mm (FWHM) and < 1 mrad x 2 mrad (FWHM) respectively.

5.2.3 F_2-laser Beam Delivery Optical Elements

All the lens elements of the beam delivery system were manufactured by FG Optics, UK. The lens elements were made of projection grade crystalline calcium fluoride. This was supplied by Schott Lithotec AG, Germany. The typical internal transmittance of a 10 mm thick sample is greater than 99% (manufacturer's data). The exact transmittance data was not provided by the manufacturer. The material has a crystallographic structure of a cubic single crystal and a melting point of 1400 °C. All the lens elements were coated with anti-reflection coatings (Calcicoat, UK) to reduce the losses due to Fresnel reflections. The high reflectivity mirrors were supplied by Laseroptik GmbH, Germany. They have a reflectivity of 98% at an angle of incidence of 45°. These high reflectivity mirrors have dimensions of 60 mm x 35 mm x 2 mm.

5.2.4 Metal Stencil Mask

The mask used for these experiments was made on a stainless steel substrate of 2 mm thickness. Transparencies such as squares, rectangles and circles of dimensions ranging from 1 mm to 5 mm were cut on it by using Nd-YAG laser operating at 1064 nm. This was supplied by Metaq Precision, Germany.

5.2.5 Optical Mounts and Motorised Translation Stages

All the optical mounts were supplied by Newport Ltd., UK. The pneumatic optical table was supplied by Melles Griot, UK. The F_2-excimer laser and the purge chambers were mounted on the optical table. The technical information about the motorised translation stages was presented in Section 4.5.

5.2.6 Energy Detector

The PE50 pyroelectric detector head equipped with a vacuum flange was supplied by OPHIR electronics Ltd., UK. This detector can measure 157 nm power levels up to a maximum of 20 W, pulse durations down to a minimum of 0.3 ns and pulse repetition rates to a maximum of 200 Hz. The energy of the laser can be recorded from the laser star display unit (OPHIR electronics Ltd., UK).

5.3 Chemical Etching Experiments

The aim of this work is to investigate a technique for the production of intrinsic Fabry-Perot optical fibre sensors. This technique is based on hydrofluoric acid etching of fused silica optical fibres to create sensing-cavities around the fibre-core. A series of experiments were carried out to: (i) determine the etch rate of the cladding and germanium-doped core of single mode fibres; (ii) study the geometry of etched cavities and fibre-tapering profile; (iii) interrogate the optical reflectivity; (iv) deploy and fusion- splice etched fibre-ends; (v) interrogate the interference spectral response of the intrinsic cavity; and (vi) investigate the response of intrinsic Fabry-Perot sensors surface mounted on fibre-reinforced composite coupons and compare this with the response of electrical resistance strain gauges.

5.3.1 Optical Fibre Preparation

The buffer coating of the SM 800 optical fibres was chemically stripped using dichloromethane and cleaned with isopropyl alcohol using a lint-free tissue. The fibres were cleaved using a FITEL (323) optical fibre cleaver to a length of 0.015 m from the buffer coating. The cleaved fibres were inspected under the integral microscope of a BFS-60 single mode fusion splicer to ensure a flat cleaved end-face of the fibre.

5.3.2 Temperature Controlled Bath

A water bath was used for controlling the temperature of the acid during etching of the optical fibres. This was fabricated from an‘expanded-polystyrene’ container. The experimental set up is illustrated in Figure 5-1.

The expanded-polystyrene container used for protecting glass containers was cut to a suitable length above its closed bottom face. A glass plate was stuck to the cut-end

using silicon rubber adhesive. At the centre of the bottom face, a portion of the polystyrene was cut to the dimensions of the polyethylene beaker, which served as the hydrofluoric acid container during etching experiments. A small hole was made in the same surface of the polystyrene container to give an access for the temperature probe of the digital thermometer.

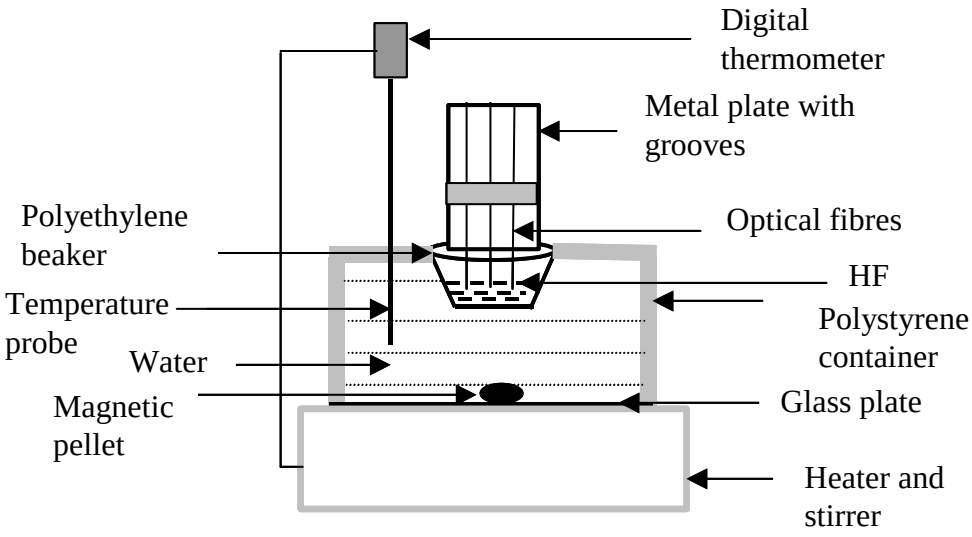

Figure 5-1: Schematic experimental set-up for hydrofluoric acid etching of optical fibres.

This entire vessel was filled with water to a suitable level such that the outer surface of the polyethylene vessel was surrounded by water. The glass-bottomed polystyrene water bath was placed on a hot plate equipped with a magnetic stirrer. The polystyrene wall surrounding the water serves as a heat insulator. A temperature control to ± 0.5 °C of the required temperature was achieved with the water bath.

5.3.3 Fibre Etching

Fibres were placed along the grooves in a metal plate such that the cleaned length of the fibres extended beyond the edge of the metal plate. Adjacent grooves in the metal plate were separated by 0.005 m. The fibres were supported along the grooves using an adhesive tape. The metal plate was held vertically above the polyethylene beaker such that the fibre end faces were positioned close to the bottom of the beaker. HF was introduced into the beaker such that the fibre ends were immersed in the acid. A

batch of 8 fibres was etched for 5, 12, 16, 22, 35 and 60 minutes to determine the etch rate of the fibre diameter and fibre core. The water bath temperature was set at 20 °C during the etching experiments.

The fibres were cleaned in distilled water after etching. They were then cleaned with isopropyl alcohol and observed under a Leica DC 200 (Germany) optical microscope to determine the rate of etching of fibres.

5.3.4 Study of Morphology with Electron Microscope

The morphology of etched fibre-ends was studied under a scanning electron microscope, LEO 435VP, LEO Electron Microscopy Ltd. (UK). The fibres that were etched for different times were cleaned with distilled water and then with isopropyl alcohol using a lint-free tissue. These fibres were gold-coated using a sputter coater to avoid the accumulation of charge on this dielectric surface, which deteriorates the quality of micrographs. A carbon pad was stuck to the surface of the stud and the gold-coated fibres were mounted on the pad using a silver paint.

To obtain quantitative data on the roughness of etched cavities, the cavities were studied using an interferometric surface profiler (AD Phaseshift, USA).

5.3.5 Optical Reflectivity of Etched Cavities

The etched cavities had to be optically smooth in order to produce Fabry-Perot interference fringes of high contrast. The optical reflectivity of these etched cavities was investigated before deploying them for manufacturing sensors. A charge coupled device spectrometer, HR 2000, (Ocean Optics Inc., USA) was used to interrogate the spectral interference response of these etched cavities. The etched-ends of the fibres were aligned against the cleaved end-face of another fibre. This alignment was carried out using manual rotary control of a BFS-60 (UK) single-mode fusion splicer equipped with an integral microscope at a magnification of 40 X. The etched fibre was butted against the cleaved end-face of another fibre and then translated away

from the cleaved end. The spectral interference response was recorded in both the butted and separated positions using Labview data acquisition software.

A broadband super-luminescent diode (SLD) light source was used to illuminate the etched fibres. The light undergoing Fresnel reflections from the etched cavity and cleaved fibre end was coupled to the CCD spectrometer using a 2x2 coupler. The free end of the cleaved fibre was immersed in an index-matching gel to avoid reflection from the other end-face. The interrogation scheme is schematically shown in Figure 5-2. The same interrogation scheme was used to observe the spectral interference response of the etched interferometers. In the case of etched interferometers, the spectral interference of light undergoing Fresnel reflections at the intrinsic cavity walls was interrogated.

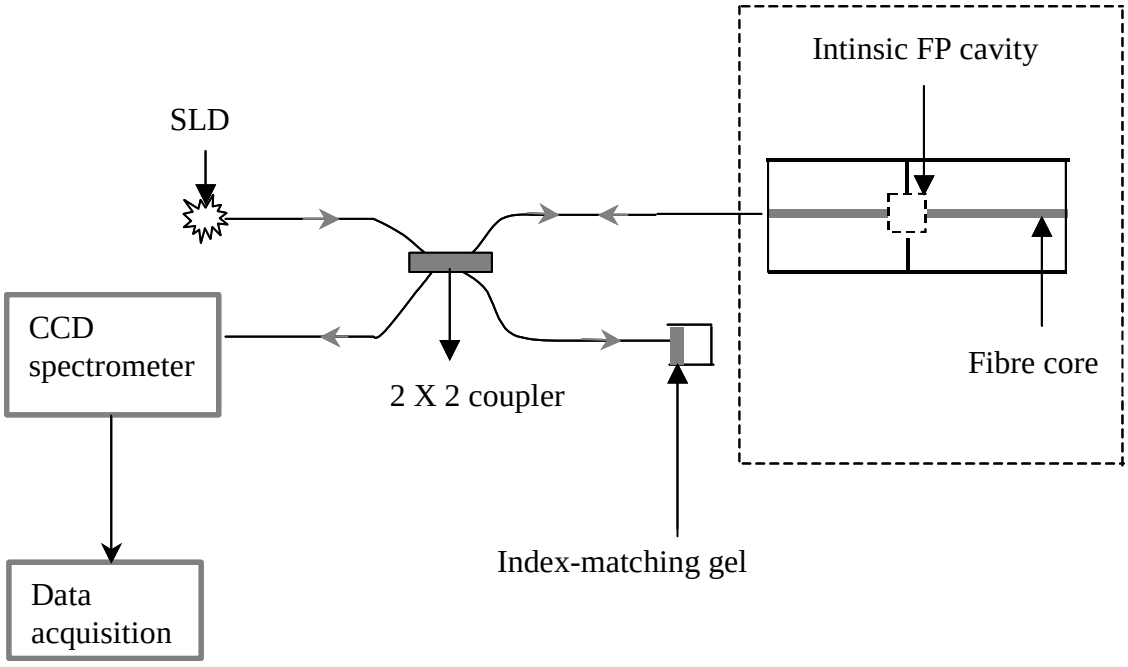

Figure 5-2: Schematic illustration of the CCD interrogation scheme for monitoring the spectral interference of HF etched optical fibres.

5.3.6 Fusion Splicing of Etched Fibres

The details of the fusion-splicing programme were as follows:

A BFS-60 single mode fusion splicer was used to fuse the etched fibres. The fibres were aligned along a line in two mutually perpendicular planes using the rotary control of the fusion splicer. The relative position of the fibres was viewed through the integral microscope. The etched end-faces of the two fibres were butted together before splicing. The initial parameters of the fusion programme were set to 14 μm and 10 mA. This means that the fibres would be backed off from their butted position by 7 μm and would be heated by a 10 mA electric arc current. The final parameters of the programme were set to 5 μm and 12 mA. This meant that the fibre ends would be brought together to a separation distance of 5 μm before they were butted again and heated up by a 12 mA current.

This programme was used to fusion splice the etched fibres etched for less than 20 minutes. To fusion splice fibres that were previously etched for 22 minutes, the initial arc current was reduced to 8 mA and the final arc current was reduced to 10 mA with the initial parameters unchanged.

5.3.7 Surface-Mounting of Etched Interferometers

Intrinsic fibre Fabry-Perot interferometers of different gap lengths were prepared to investigate their response to applied strain. These sensors were surface mounted on fibre reinforced composite coupons. Electrical resistance strain gauges, FLA-6-11 were mounted on the other side of coupon surfaces at their centres. The strain gauges were supplied by Tokyo Sokki Kenkyujo Co., Ltd. (Japan). These gauges had a gauge resistance of 120 ± 0.3 Ω and a gauge factor of 2.12. The sensors were mounted on separate composite coupons and the mounting procedure used was the same for all the composite coupons. The typical surface mounting procedure implemented on a glass fibre reinforced composite (GFRC) coupon is described as follows:

The surface of the composite coupon was abraded lightly using P400 grit paper (Turbat Durite, UK) to produce a roughened surface for mounting the intrinsic interferometer. The surface was degreased using CSM-1A degreaser spray, Measurement Group Ltd. (UK). The degreased surface was treated with M-PREP conditioner A (a water-based acidic surface cleaner) and wiped off with a lint-free tissue. Then the surface was treated with M-PREP neutralizer 5A (a water-based alkaline surface cleaner) and again wiped off with a lint-free tissue. This surface treatment procedure helps to produce a rigid bonding between the composite surface and glass fibre.

A schematic illustration of these markings along the axis of the coupon is shown in the following Figure 5-3. The etched sensor was laid along the length of the axis of the coupon, so that the spliced region of the sensor falls at the point 'O' shown in Figure 5-3. This was performed by observing the sensor using a magnifying eyepiece. Care was taken to ensure alignment along the axis. The fibre was held in tension along the axis of the coupon by using a soft tape at a distance of 0.015 m on either side of the point 'O', over the coating-stripped length of the sensor. The remaining length of the sensor was also taped to the coupon along the axis near the end-tabs. In order to obtain well-defined bonded points 0.01 m away from centre on either side along the axis, a high viscosity UV curing adhesive, Loctite 350 Adhesive, Henkel Loctite Adhesives Ltd. (UK), was taken on the tip of a hypodermic needle and gently laid on a point, so that it formed a small bead at that region. Then a high intensity UV light source, UVP spot cure, (USA), was closely exposed to the bead of the UV curing the epoxy for one minute to achieve a complete cure. According to the manufacturer, a thirty-second exposure was sufficient to produce a complete cure of this adhesive. The other end from the centre was also bonded to the coupon using the same procedure.

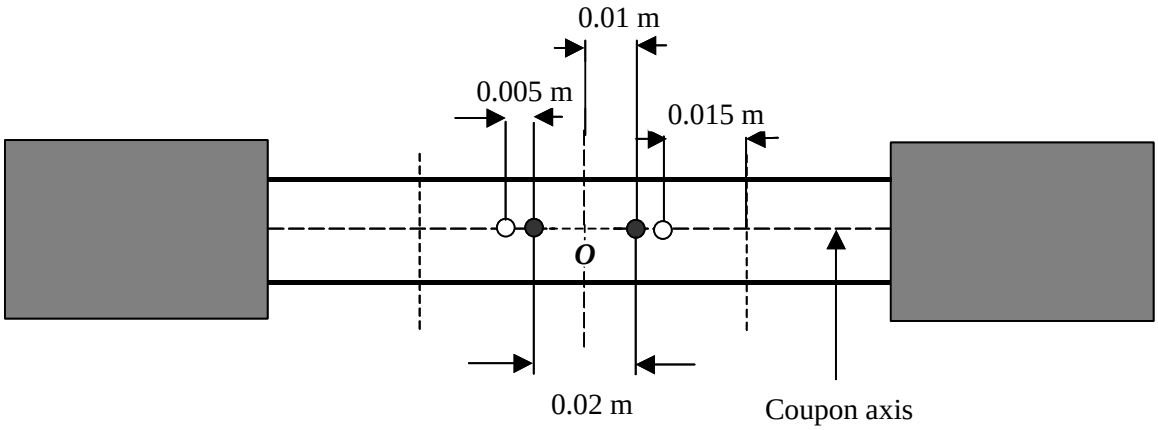

Figure 5-3: Schematic of a composite coupon with markings along the axis to mount the sensor.

A drop of cyanoacrylate adhesive, Permabond, (UK), was taken on the end of a hypodermic needle and introduced along a length of 0.005 m on the fibre from the UV-cured bead of the adhesive away from the centre. Then cyanoacrylate adhesive activator, RS Components, (UK), was sprayed over this region and allowed to evaporate. This activator increases the speed of bonding and reduces the spread of the low viscosity cyanoacrylate. Therefore, the bonded region of the sensor was located at a distance of 0.01 m from the centre of the axis on both the sides as show in Figure 5-3.

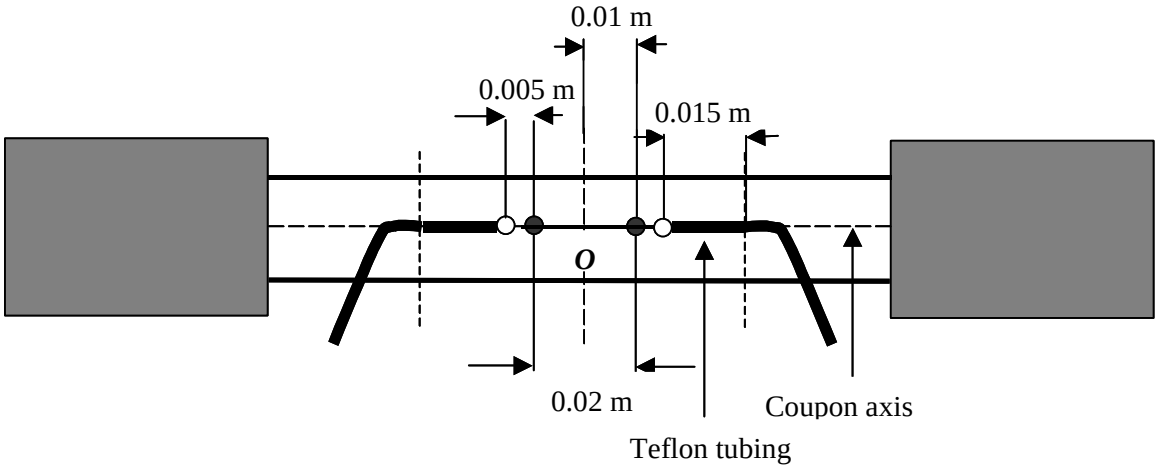

Figure 5-4: Schematic of surface mounted intrinsic Fabry-Perot interferometer.

The tape was taken off and a protective Teflon tube, 400 μm internal diameter was introduced over the remaining length of the fibre up to the cyanoacrylate bond. Then

the fibre was gently bent up to the 0.015 m marking from the end of cyanoacrylate bonding. The cyanoacrylate adhesive was introduced along this length on one end using hypodermic needle and adhesive activator was sprayed onto it. The other end was also bonded to the coupon in the same way. This is illustrated in the Figure 5-4. This fixed bend radius on either side induces the same loss of light intensity, irrespective of the light-coupling ends of the fibre and also reduces the effect of external physical perturbations on the set gauge length.

The two ends of the fibre outside the coupon were spliced to longer fibre lengths and were splice-protected. The long length of the fibre outside the coupon was also protected using Teflon tubing. The distance between the bonded points on the surface of the coupon was measured with an optical microscope.

5.3.8 Tensile Testing of Surface-Mounted Acid-Etched Sensors

The mounted Fabry-Perot interferometers were tested for their response to external strain. These tensile tests were carried out on an Instron 8501, tensile testing hydraulic machine. Three interferometers of different cavity lengths were used to study their response to strain in the composite coupons.

In order to investigate the response of intrinsic FP-sensors to tension-tension fatigue loading, a triangular waveform of tension-tension loading was applied to coupons mounted with intrinsic FPs. Two tests at two different frequencies were carried out. The first test was carried out at a frequency of 0.05 Hz, with a waveform of 1.5 kN (mean load) – 3 kN (maximum load) – 0 kN (minimum load). The second test was carried out at a frequency of 0.016 Hz, with the same waveform. The strain was recorded from the surface mounted electrical resistance strain gauges. The strain gauges were mounted on the other side of the coupons to measure strain in the coupons to the applied load.

5.4 F_2-Laser Beam Transmission Experiments

5.4.1 Alignment Laser

A 1 mW output laser pointer emitting at 630 nm was mounted behind the MgF_2 rear mirror of the excimer laser using a XY-Phi mount. The laser beam was made to pass through the laser cavity by adjusting the X and Y-translation and the tilt angle of the mount. The energy of the transmitted beam was measured at the exit point of the beam using a visible light energy detector-head and a Field Master energy display unit (Coherent Inc. Ltd., UK). The pointer was aligned such that a maximum energy was detected at the exit point of the beam. At this position, a card was placed around the aperture of the alignment laser to observe back reflections from the resonator optics. No oblique back reflections were observed at this position. When the alignment beam is reflected by smooth electrode surfaces, a loss of measured energy is observed.

Subsequent to the alignment of the laser mounts, the burn pattern of the raw excimer beam was taken on an ultraviolet detector paper, which was mounted close to the exit point of the beam. The location of the alignment laser spot was measured with respect to the burn pattern and where necessary, the alignment was fine tuned such that the spot from the alignment laser coincided with the centre of the burn pattern. The energy of the alignment laser beam was measured after fine-tuning and no change in detected energy was observed. This position of the alignment laser corresponded to the centre of the 157 nm beam. Then the burn pattern was taken at 100 and 200 mm away from the beam-exit point and the alignment spot location was compared with the respective burn patterns. Although the size of the raw beam increased with the distance from the beam exit due to divergence, the alignment laser spot was found to be at the centre of the burn patterns. This confirms that the alignment beam direction coincided with the central direction of the 157 nm laser beam. Therefore, the alignment beam coincided with the direction of the 157 nm laser beam.

5.4.2 Alignment of the High Reflectivity Mirrors

The high reflectivity mirrors were mounted on suitable optical mounts and were placed at positions 4 and 5 as shown in Figure 4-1. A card was mounted against the exit of the long beam tunnel at position 8 as shown in Figure 4-1 with its centre marked. The base of the mirror mounts was positioned at the centre of the tunnel base at their respective positions by using suitable spacers along the internal margins of the tunnel. The mirrors were positioned such that their coated side faces the 157 nm beam. This was done to reduce losses of 157 nm laser beam due to its path length in the mirror substrate. The mirror mount at position 4 of Figure 4-1 was adjusted such that the alignment laser beam illuminates the centre of the mirror. A schematic diagram of the ray path along the long beam tunnel via mirrors is presented in Figure 5-5. The angle on the mirror was adjusted to make the reflected portion of the alignment beam to illuminate approximately at the centre of the second mirror. Then the angle on the second mirror was adjusted such that the reflected portion from the second mirror approximately coincides with the centre of the exit of the tunnel marked on the card. As the alignment beam coincides with the central direction of the 157 nm laser beam, the mirror dimensions fully intercept the UV beam and direct it towards the centre of the exit of the tunnel.

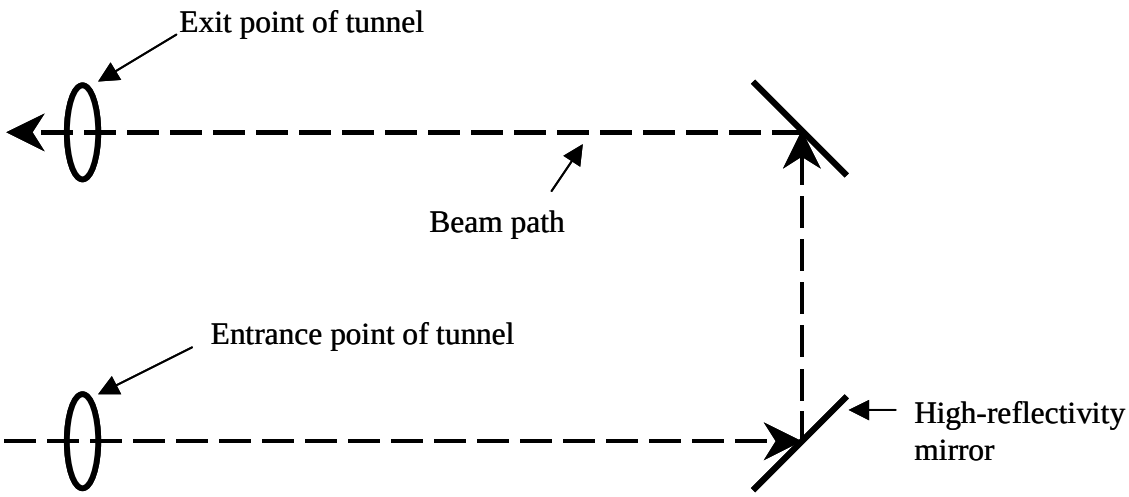

Figure 5-5: Schematic illustration of beam path in long tunnel.

5.4.3 Mounting the Detector-Head

The manufacturer (BFI Optilas, UK) of the energy detector head provided a protective holder for the head. The exit of the long beam tunnel was sealed using an aluminium plate or the end plate of the tunnel. The detector-head was sealed to the centre of the aluminium plate, such that it coincides with the centre of the tunnel. A schematic illustration of aluminium end plate and the detector head sealed to the exit point of the long beam tunnel is shown in Figure 5-6. With reference to Figure 5-6, [C] was positioned at the rear side of [B] such that the socket-head screws could be tightened into the holes drilled in the protective holder. The nitrile rubber in between the end-plate and the protective holder seals the detector-head to the plate. The holes shown in [A] were sealed with socket-head screws as explained in Section 4.2. Then the end-plate was placed against the exit opening of the tunnel. This is the same as placing face of [B] over face of [A], such that the projected socket head screws pass through the holes of [B]. Then the door is sealed to the exit by tightening with the wing nuts. The entrance of the tunnel was coupled to the exit point of the excimer laser by using a vacuum flange.

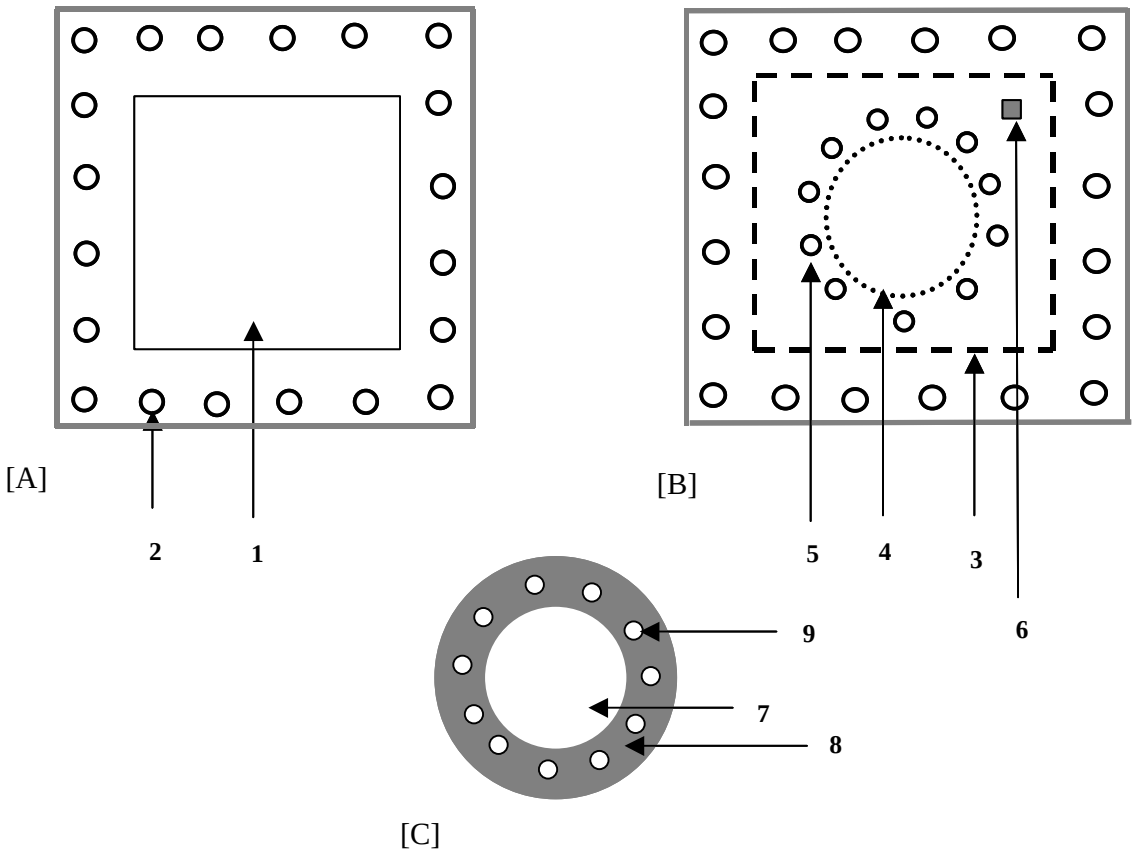

Figure 5-6: Schematic illustration of mounting detector head to the exit point of long tunnel; [A] End face of exit opening, [B] Aluminium door designed for mounting detector head, [C] Detector head surrounded by protective shielding.

1. Exit opening of tunnel
2. Holes drilled along the outer margin of the metallic frame
3. Nitrile rubber lining
4. Nitrile rubber lining on rear side to seal the detector head to the aluminium door
5. Holes drilled to seal socket head screws
6. Vent orifice
7. Detector head
8. Protective holder of the detector head
9. Holes drilled along the margin of the protective holder

5.4.4 Laser Safety Measures

F_2-excimer laser used in this study was a class-IV laser. All the optical elements and ablation target were enclosed in the purge chamber during experimentation. As the aluminium tunnel enclosed the entire beam line, there is no possibility of the beam entering outside the chamber. Therefore, the laser was reduced to a class-I laser. Laboratory coat, powder-free gloves and laser safety goggles of optical density six in the range of 190 nm to 1064 nm wavelength were used during laser operation. The excimer laser laboratory was equipped with interlocks, toxic gas (fluorine) detectors and exhaust, electrical safety, smoke and fire alarm facilities. The laser laboratory complied with the standard safety protocols of a class-IV laser laboratory according to the laser safety officer of the Defence Academy.

5.4.5 Purging the Long-Tunnel

The LPF 202 laser was supplied with an inlet for purge gas at its rear end for flushing the internal optics of the laser. The purge gas entered the coupled beam tunnel through the beam exit point of the laser. The purge gas used for these experiments was oxygen-free nitrogen (99.998%) and was supplied by BOC gases, UK. The flow rate of the purge gas was controlled using a flow meter (Preston Hydraulics, UK) connected to the nitrogen cylinder.

The internal surfaces of the purge chamber were degreased by using isopropyl alcohol and lint-free cloth prior to commencing the experiments. The total beam path length was 3.3 m. All the side doors of the chamber were sealed before purging.

In the first set of experiments, flow rates of 25 litre minute^{-1} and 35 litre minute^{-1} were applied and a 2.6 mm diameter circular vent orifice was used. A new gas fill was executed prior to each and every beam transmission experiment measurements to reduce the pulse-to-pulse energy fluctuations due to the decay of the quality of gas with time. The laser was operated in constant energy mode at 25 mJ output energy per pulse and at a frequency of 10 Hz. Energy was measured at every 3 minute intervals

after starting the purge gas flow. The energy display unit was set to display pulse energy averaged to every 3 seconds. The energy was measured after every 10 seconds for 60 seconds and all these values were averaged to obtain the transmitted energy after each three-minute interval and the transmitted percentage of energy was calculated. The purge flow was continued until the energy transmission stabilised.

To investigate the effect of reducing the flow rate after achieving a stabilised transmission, a flow rate of 35 litre minute^{-1} was applied and a 2.6 mm diameter circular vent orifice was used. The flow rate was continued until a 40% transmission was achieved and then the flow rate was reduced to 10 litre minute^{-1} and continued for 30 minutes to study the effect on energy transmission. The laser was operated in constant energy mode at 25 mJ output energy per pulse. The energy measurement was carried out in the same method as the first set of experiments.

5.4.6 Purging the Short-Tunnel

5.4.6.1 Alignment of Field Lens and Mask

These experiments were conducted to determine the energy densities that could be obtained through a 1.5 x 1.5 mm mask feature using the short beam tunnel. A schematic illustration of the short beam tunnel coupled to the ablation chamber was presented in Figure 4-2. The experimental set up for measuring the transmitted energy through the mask feature is shown schematically in Figure 5-7.

The plano-convex field lens and the metal stencil mask were mounted in suitable optical mounts. A pinhole was mounted against the exit point of the laser beam and the alignment laser was turned on. The alignment beam passed through the pinhole and illuminated the field lens. The tilt angle and the translation in X and Y directions was adjusted so that the alignment beam incidents normally at the centre of the field lens. This position of the field lens does not produce any oblique back reflections on the card with the pinhole mounted against the exit of the laser. The mask feature was positioned such that the alignment beam passed through the centre of the

transparency. The mask plane was at a distance of 10 mm from the field lens. This ensured that the central portion of the excimer beam illuminated the mask feature. This illumination also reduced the non-uniformity of the spatial intensity of excimer beam across the transparency. The detector head was mounted inside the ablation chamber at a distance of 720 mm from the mask such that the alignment beam illuminated the centre of the detector. This distance of the detector corresponded to the location of exit pupil of the imaging system.

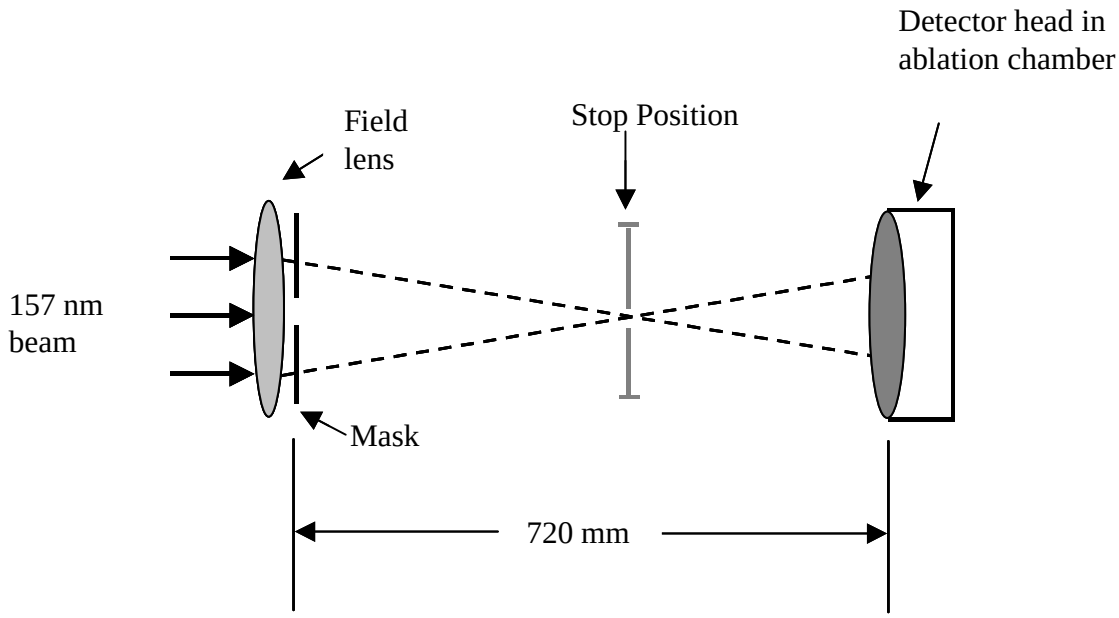

Figure 5-7: Schematic experimental set up for determining transmitted energy through a mask feature.

5.4.6.2 Purging Mask Projection Optics

All the side panels (or openings as mentioned in Figure 4-2) of the chamber are sealed prior to purging. A flow rate of 30 litre minute^{-1} was applied and the laser was operated in constant energy mode at 50 mJ pulse energy output at a frequency of 10 Hz. The vent orifice with a cross-sectional diameter of 5 mm was used. The energy was measured every 5 minutes after 60 minutes of purging up to 150 minutes.

5.5 Disk Ablation Experiments

The aims of this experimentation were as follows:

1. To evaluate the performance of the designed optical beam delivery system;
2. To characterise the morphology of microstructures ablated at different energy densities and numbers of pulses;
3. To determine the ablation rate of fused silica and sapphire substrates at different energy densities;
4. To gather quantitative information on the optical quality of structures ablated at different energy densities and numbers of pulses;
5. To identify feasible ablation parameters for micro-machining Fabry-Perot microstructures in optical fibres.

5.5.1 Beam Delivery Set-up

The beam delivery system used for micro-machining experiments was based on the illumination design presented in Chapter 4. This was an un-homogenised beam delivery system. The mask features were illuminated by the central portion of the beam, which corresponds to the peak intensity level of raw output beam. The use of the central portion of the raw beam for mask illumination reduces inhomogenities in the spatial intensity distribution of the output beam and it improves transmitted energy levels through the mask features.

The 0.1 numerical aperture imaging system produced a de-magnified image of the stop at a working distance of 40 mm. The lens configuration for the imaging system was presented in Section 3.2.

5.5.1.1 Gas-Purging of the Objective Lens Assembly

The imaging objective was provided with a pair of holes, which were diametrically opposite on the cylindrical metallic case, in between each successive pair of lens elements. This was done to purge the air gaps in between the lens elements of the

objective. A cylindrical PTFE (polytetrafluoroethylene) tube with three pairs of holes was built for purging the objective. A schematic illustration of purging the imaging objective is presented in Figure 5-8. Pairs of holes of suitable diameter were machined on the cylindrical surface of the PTFE tube at suitable distances so that they coincided with the locations of inlet and outlet holes on the cylindrical surface of the objective. The objective was inserted into the PTFE case. The internal diameter of the PTFE tube was approximately the same as the diameter of the objective so that the inserted objective was held rigidly inside the PTFE tube. A port was made through the wall of the ablation chamber and sealed using epoxy resin. This port carried dried nitrogen gas to purge the air gaps in between the lens elements of the objective. A gas flow divider was used to supply purge gas to three independent tubes, which were connected to the inlets of the PTFE case. The positive pressure of the purge gas was used to out purge air in between the lens elements and established a transmission medium for 157 nm laser beam. A low flow rate was applied to reduce the pressure of the purge gas on the surface of the calcium fluoride elements.

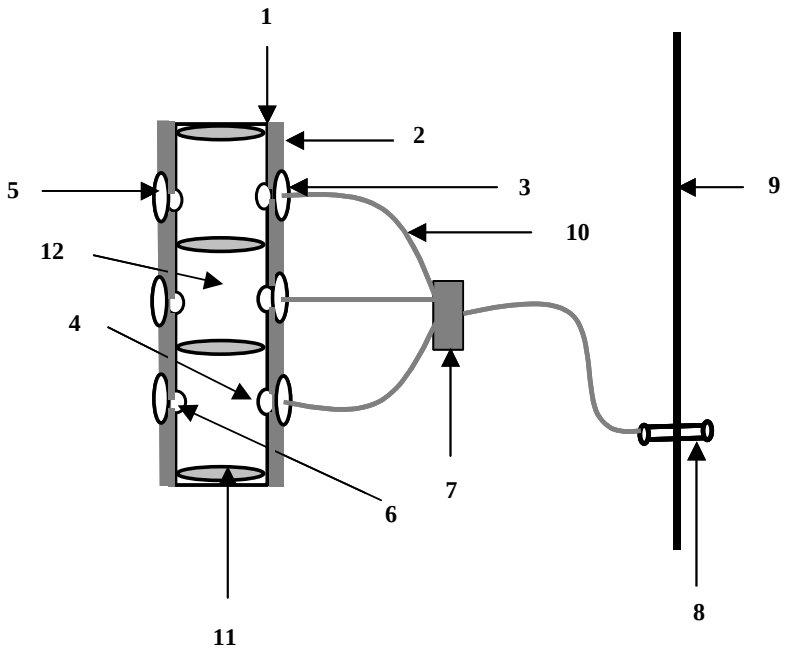

Figure 5-8: Schematic illustration of the PTFE fixture for purging the objective with N_2.

1. Imaging Objective
2. PTFE case which rigidly holds the objective
3. Inlet hole machined on the cylindrical surface of PTFE case
4.Inlet hole in the metallic surface of the objective
5. Outlet hole machined diametrically opposite to the inlet hole
6. Outlet hole diametrically opposite to the inlet hole of objective
7. Purge gas divider
8. A port sealed into the hole made in ablation chamber wall
9. Ablation chamber wall
10. Tube carrying dry nitrogen gas
11. Lens element of the objective
12. Air-gap in between the lens elements

5.5.1.2 Alignment of the Objective

The entrance and exit apertures of the objective were provided with circular lens protection caps. Holes of 0.5 mm diameter were drilled at the centre of these caps. Therefore, the axis of the objective passed through the pinholes in the caps. The

objective was mounted on a separate XY-manual translation stage. The tilt angle on the high reflectivity mirror, which was mounted on a separate mirror mount, was adjusted such that the alignment beam from the mask feature passes through the pinhole caps of the objective via reflection from the mirror. The alignment beam passes through the pinholes only when the mirror makes an angle of 45° with the alignment beam. A schematic illustration of the beam delivery set-up for micro-machining experiments is presented in Figure 5-9.

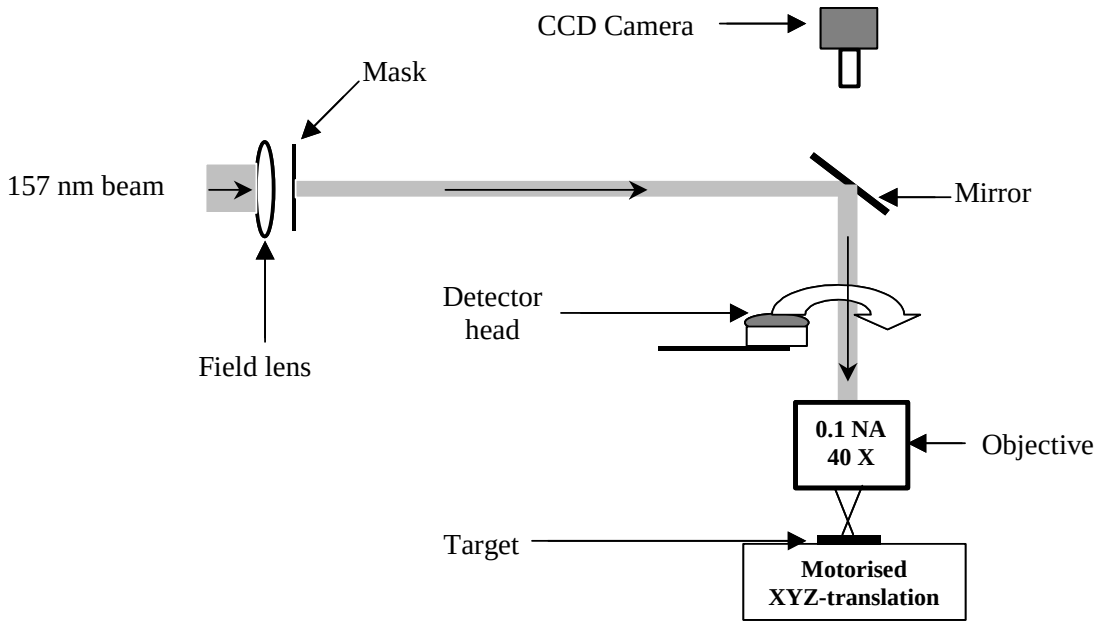

Figure 5-9: Schematic illustration of the beam delivery set-up for micro-machining applications.

5.5.1.3 Calculation for Estimating the Energy Density at the Target

A schematic illustration of beam delivery is presented in Figure 5-9. The detector-head was mounted above the objective. The surface of the detector head was separated by 20 mm from the objective. The transmitted energy from the mask feature was measured before ablation operation and the energy density at the work piece was calculated. The distance from the detector head to the work piece was 132 mm. While calculating the energy density at the work piece, the attenuation due to calcium fluoride elements of the objective and the beam path length through the nitrogen

atmosphere was considered. The attenuation per unit path length of the beam was measured from the beam transmission experiments.

5.5.2 Preparation of the Substrate

The fused silica and sapphire disks were cleaned with isopropyl alcohol and a lint-free optical cloth. The disks were placed on the polished base plate of the L-shaped metallic frame as shown in Figure 4-5. The surface of the disk was aligned into the image plane by using the CCD camera as described in Section 4.5. The disks were cleaned with isopropyl alcohol after ablation and secured from dust and other particulate contamination in a closed container.

5.5.3 Ablation Parameters

The disks were ablated by projecting a mask feature of dimensions 1.5 x 1.5 mm. The pulse energy was measured using an energy meter prior to ablation of every feature and the energy density at the image plane was calculated. A flow rate of 20 litre minute^{-1} was used to flush the short beam tunnel and the ablation chamber throughout the duration of experiments. The air-gaps between the lens elements of the imaging system were flushed continuously through the inlet and outlet holes of the objective throughout the duration of the experiment.

The discs were ablated at energy densities ranging from 7 x 10^4 Jm^{-4} to 26 x 10^4 Jm^{-4} at different pulse frequencies for varying numbers of pulses. The pulse energy was controlled by changing the operating voltage of the laser from 21 kV to 26 kV.

5.5.4 SEM, Surface profiler and Optical Microscope Studies

The morphology of the micro-machined structures on fused silica and sapphire discs was studied under a scanning electron microscope, LEO 435VP, LEO Electron Microscopy Ltd. (UK). A Microxam surface mapping microscope (AD Phaseshift,

USA) was used to measure the ablation depth of cavities and 3-dimensional profiles. The cavities were also studied under a Leica DC 200 optical microscope (Leica Microsystems Wetzlar GmbH, Germany).

5.6 Ablation of Optical Fibres

The aims of this experimentation were as follows:

1. To develop alignment techniques for micro-machining various Fabry-Perot configurations in fused silica optical fibres.
2. To verify the suitability of ablation parameters identified in fused silica disk ablation for micro-machining high aspect ratio cavities in optical fibres.
3. To study the effects of ablation at different energy densities on the wall angle of micro-cavities.
4. To interrogate the ablated cavities for Fabry-Perot interference.
5. To study the morphology of cavity wall surfaces using SEM.
6. To obtain quantitative information on the roughness and flatness of cavity walls using the surface profiler.
7. To verify the suitability of ablation parameters identified in sapphire disk ablation for micro-machining sapphire fibres.

5.6.1 Preparation of the Optical Fibres for Ablation

The optical fibres used for micro-machining experiments were described in Section 5.1. SMF 28, SM 800, MM 800 and sapphire fibres were used in these experiments. The acrylic coating of the optical fibres was stripped using dichloromethane and then cleaned with isopropyl alcohol and a lint free cloth.

5.6.2 Ablation of Optical Fibres Through the Diameter

5.6.2.1 Aligning Fibres in the Grooves

Parallel grooves were scribed on the surface of microscope glass slides over a length of 10 mm along the length of the glass slide, starting from the edge towards the centre of the glass slide. The glass slide was cleaned with isopropyl alcohol prior to each experiment. A steel plate of 5 mm thickness was clamped at its corners to the optical table. All the faces of the steel plate were polished to yield a smooth surface. The flatness of the polished surface was confirmed using a spirit level. The glass slide with scribed grooves was aligned such that its length coincided with the length the steel plate. The glass slide was clamped to the steel plate using two magnets along the margins of the length of the glass slide. This is schematically illustrated in [B] of Figure 5-10.

Two steel plates of 6 mm thickness were aligned on the optical table along the length of the steel plate with scribed glass slide on it. These steel plates were clamped to the optical table. Then each stripped fibre was aligned along the grooves of the glass slide such that the stripped length of the fibres lay in between the grooves. This was carried out using a suitable illumination and magnifying glass. The two ends of the each fibre were secured using an adhesive tape to the steel plates on either side of the central steel plate. Care was taken to avoid fibre bending along the grooves. This is illustrated in [A] of Figure 5-10. After aligning four fibres along the grooves of the glass slide, two magnets were gently placed over the grooves so that the glass slide with fibres in its grooves had been clamped via the magnet to the steel plate. This is shown in [B] of Figure 5-10. Then the ends of the fibres were un-taped and the central steel plate unclamped from the optical table. The magnets along the length of the steel plate were also removed. The magnetic clamping over the grooves kept the position of the glass slide with respect to the bottom steel plate and fibres along the grooves unchanged.

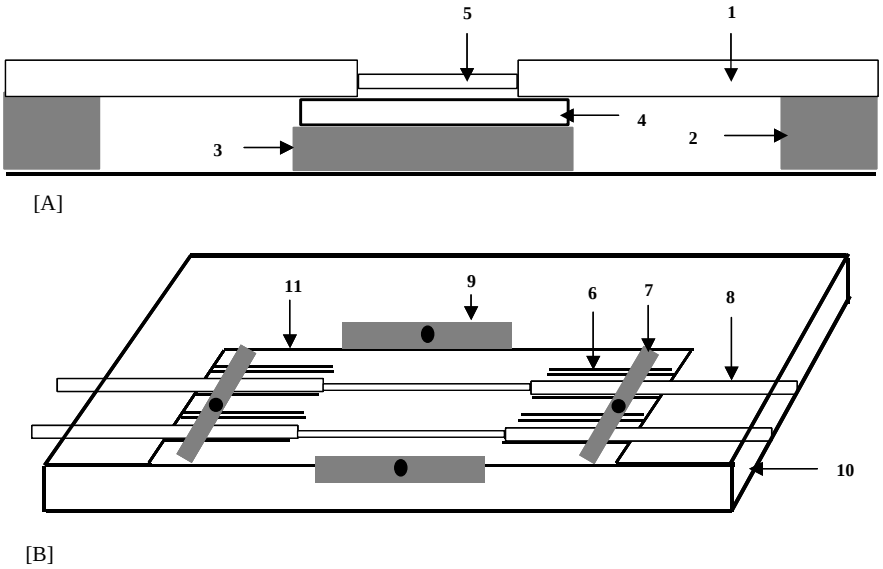

Figure 5-10: Schematic illustration of the fibre alignment for micro-machining through the diameter; [A] Schematic illustration of the alignment of the fibres on the grooves inscribed on the glass slide, [B] Schematic illustration of the magnetic clamping arrangement for securing the optical fibres.

1. Optical fibre
2. Steel plate to which the fibre end was secured using adhesive tape
3. Steel plate on which glass plate was mounted
4. Glass slide with scribed grooves
5. Stripped region of the fibre
6. Scribed groove on the glass slide
7. Magnetic clamping of the fibres
8. Optical fibre
9. Magnetic clamp used to align and secure the length of the glass slide along the steel plate
10. Steel plate
11. Magnetic clamp used to secure the glass slide

5.6.2.2 Positioning the Steel Plate

The steel plate on which the optical fibres were clamped was placed on the base plate of the L-shaped metallic frame of the motorised translation system. A description of the L-shaped frame was given in Section 4.5. An aluminium spacer was placed along

the length of the steel plate and positioned such that one edge of the aluminium spacer was parallel to the edge of the spacer and the other edge parallel to the edge of the base plate. Another aluminium spacer was placed against the edge of the base plate and the wall of the ablation chamber. This procedure made the dimensions of the steel plate parallel to the dimensions of the base plate. This is illustrated in Figure 5-11. The aluminium spacer between the wall of the ablation chamber and the steel plate was removed carefully after positioning the steel plate. This procedure was very important as it reduced the errors in positioning the fibre into the image plane. This was done to ensure that the etalon forming dimensions of the ablated structure was perpendicular to the core of the optical fibre. Mask features of dimensions 1.5 mm x 1.5 mm and 2 mm x 2 mm were imaged to ablate the optical fibres.

5.6.2.3 Aligning Fibres in the Image Plane

The alignment laser spot on the glass slide was taken as the reference to get an estimation of the location of the UV spot. The work piece was translated such that the alignment spot lay on the glass slide. Then the Z-stage was translated by 6 mm, which was approximately the height of the steel plate and the glass slide. The procedure for identifying the image plane was already presented in the disk ablation experiments of Section 5.5. After finding the image plane, the Z-stage was again translated by 200 micrometres in the negative Z-direction to bring the surface of the optical fibres into the image plane. The laser was operated at a frequency of 5 Hz at the lowest operating voltage, whilst translating the fibres into the image plane, to reduce excessive ablation. The fibres were illuminated through the perspex window of the main door using a light source placed outside the chamber. The translation of fibres into the image plane was monitored via the CCD camera. The fibres were aligned such that the laser-induced fluorescence fell at the centre of the fibre along its width. The same alignment procedure was carried out during the ablation of sapphire fibres.

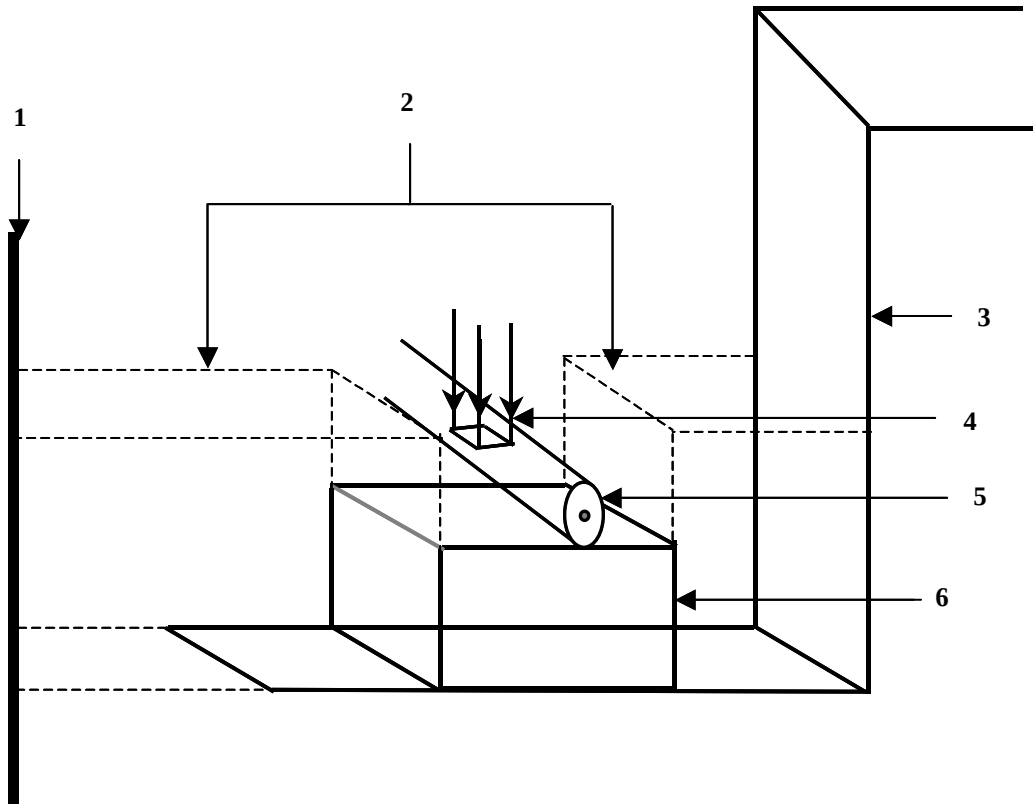

Figure 5-11: Schematic illustration of positioning of the optical fibres for the ablation experiments.

1. Wall of the ablation chamber
2. Aluminium spacers
3. L-Shaped aluminium frame
4. Imaging forming beam
5. Optical fibre (Viewing the ablation process through the diameter of the optical fibre)
6. Steel plate on which fibres were clamped using magnets

5.6.3 Alignment of Fibres for Micro-machining Cleaved End

Samples of cleaved SM 800 ribbon fibre cables were procured from Fujikura Ltd., UK. Each ribbon cable comprised twelve fibres. The width of the cable was 3 mm. The reason for using these ribbon cables was that the stripped and cleaved ends of the fibres of the cable could be aligned easier than aligning individual fibres.

An L-shaped steel plate of thickness 5 mm was polished on all its faces. Two lines with a separation of 3 mm were scribed perpendicular to the edge of the steel plate as shown in Figure 5-12. The surface of the steel plate was degreased with isopropyl alcohol and a microscope glass slide was bonded using cyanoacrylate adhesive to its surface such that its edge coincided with the edge of the L-shaped steel plate. The cleaved ends of the fibres of the ribbon cable were positioned such that they coincided with the edge of the glass slide and the ribbon cable was clamped via magnets to the steel plate. This positioning was carried with the aid of a binocular microscope. Then the L-shaped steel plate was positioned such that its edge coincided with the edge of the base plate of the L-shaped aluminium frame. This arrangement is shown in Figure 5-12.

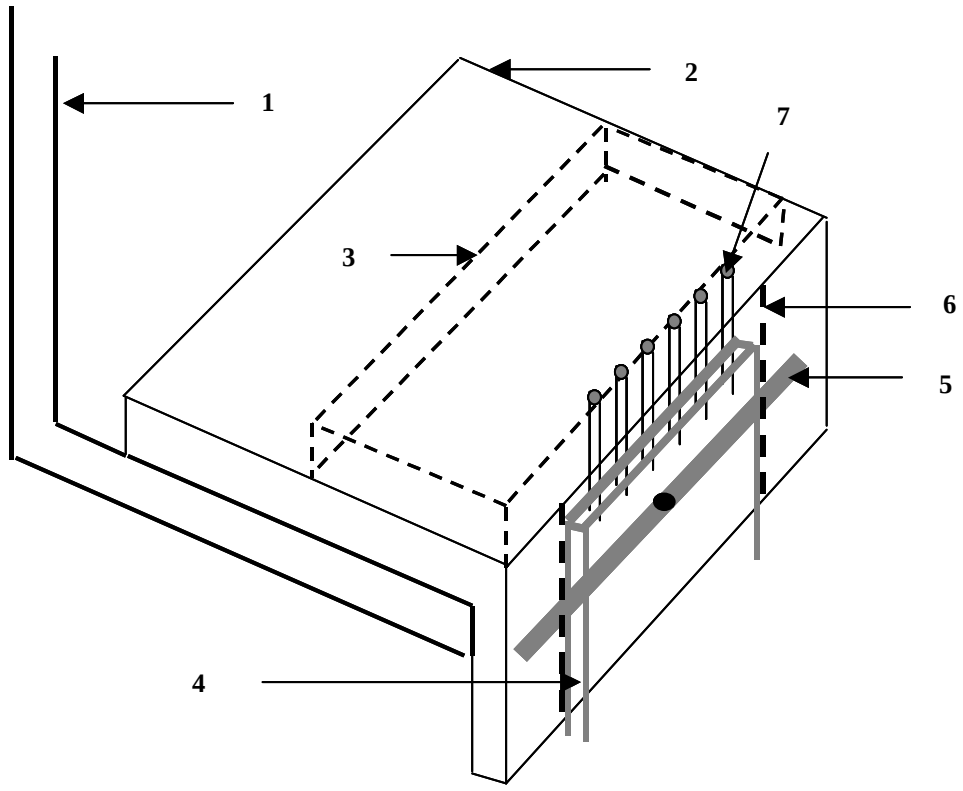

Figure 5-12: Schematic illustration showing the set up for aligning cleaved fibre ends of ribbon cable.

1. L-shaped aluminium frame
2. L-shaped steel frame
3. Microscope glass slide bonded to the surface of the steel plate
4. Ribbon cable
5. Magnetic clamp

6. Line scribed perpendicular to the edge of the steel plate
7. Cleaved end of the fibre of the cable

5.6.4 Ablation Parameters

In the ablation experiments, energy densities ranged from 7 x 10^4 Jm^{-4} to 27 x 10^4 Jm^{-4} at different pulse repetition rates ranging from 1 to 20 Hz were used. Purging of the beam line was carried out using the procedures described in Section 5.5.3. Microstructures of dimensions of 38, 50 and 75 μm were ablated in these experiments.

5.6.5 Characterisation of the Ablated Structures

The optical fibres that were micro-machined at different energy densities were interrogated using the CCD interrogation scheme presented in Figure 2-5. The assessment criteria were the ability of the ablated structures to show Fabry-Perot interference. Micro-machined cavities in sapphire fibres were interrogated by coupling light from a multimode fibre, MM 800. The cleaved end of the sapphire was butted to the cleaved end of the multimode fibre by aligning them under a BFS-60 fusion splicer. A study of the morphology of ablated structures was carried out using SEM and 3D profiling of ablated structures using surface profiler. The cavity wall tapering of ablated structures was studied under optical microscope.

5.7 *In-situ* Monitoring of Laser-Induced Fluorescence

The aim of this section was to develop a methodology for improving the repeatability of micro-machining Fabry-Perot cavities through the diameter of an optical fibre. In order to achieve this, the following aspects were investigated:

1. To monitor laser-induced fluorescence *in-situ* during ablation and study the evolution of fluorescence spectra with the number of pulses.

2. To express the peak intensities of fluorescence spectra as a function of ablation depth at a specified energy density.
3. To verify the validity of the relation deduced by comparing the calculated ablation depth with the measured ablation depth.

5.7.1 *In-situ* Laser-Induced Fluorescence Monitoring During Micro-machining

SMF 28 fibres were used in these experiments. Alignment of fibres was carried out according to the procedure presented in Section 5.6.2. A schematic illustration of monitoring laser-induced fluorescence during ablation is presented in Figure 5-13. The cavities were ablated at energy densities ranging from 7 x 10^4 Jm^{-4} to 26 x 10^4 Jm^{-4} at a pulse repetition rate of 20 Hz. The cavities were micro-machined from left to right in order to avoid loss of transmitted fluorescence intensity due to the preceding cavities. Cavities of different ablation depths were micro-machined along the length of the fibre and laser-induced fluorescence spectra were recorded using a CCD spectrometer (S2000, Ocean Optics Inc., UK) and data acquisition software (Labview). The ablation depth of the micro-machined cavities was measured using an optical microscope.

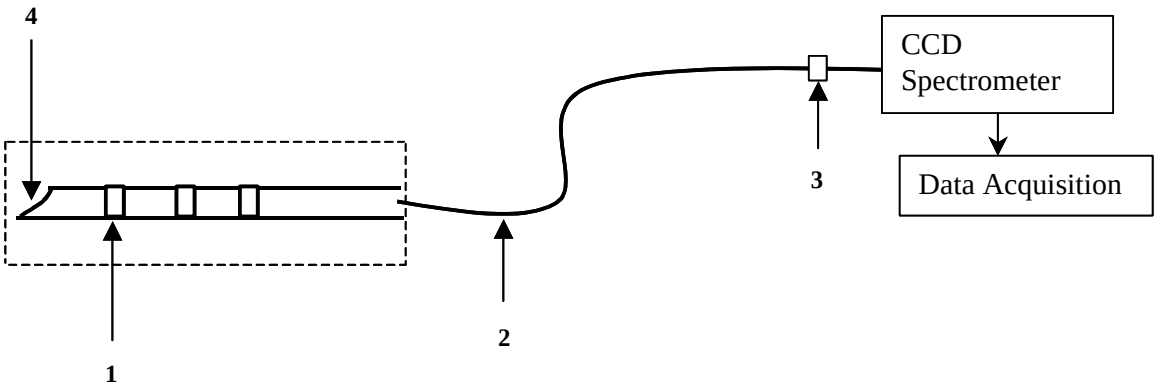

Figure 5-13: Schematic illustration of *in-situ* fluorescence monitoring during ablation.

1. Ablated cavity (Cavities drilled from left to right along the length of the fibre)
2. SMF 28 optical fibre
3. Vent orifice of ablation chamber
4. Broken end of the fibre

5.7.2 Monitoring Laser-Induced Fluorescence Spectral Changes

The evolution of intensity and fluorescence emission was studied from the fluorescence spectra recorded during the ablation through the fibre diameter at different energy densities. The influence of misalignment of an optical fibre during micro-machining on the evolution of intensity of fluorescence spectra was studied by ablating a cavity away from the diameter of the fibre.

5.7.3 Correlating Ablation Depth and Fluorescence Intensity

The peak intensities of fluorescence spectra recorded during ablation of a fibre through its diameter at an energy density of 23 x 10^4 Jm^{-2} were expressed as a function of ablation depth. Then the ablation depth of another two different cavities ablated at this energy density was determined using the function deduced and an optical microscope independently. Then these two ablation depths were compared.

5.8 Ablation of Fibre Bragg Gratings

The aim of these experiments was to investigate the radiation effects of the 157 nm laser beam on the refractive index of fused optical fibres. These investigations were important because they determine whether the radiation effects were deleterious to the fabrication of Fabry-Perot cavities. In order to investigate the radiation effects, the aims of the experiments conducted were as follows:

1. To investigate the effect on the refractive index of fibre Bragg gratings when they were exposed to the laser beam.
2. To investigate the effect of heat generated on the refractive index of the fibre Bragg grating during ablation of a cavity through the diameter of the optical fibre.

5.8.1 Inscribing Bragg Gratings

The Bragg gratings used in these experiments were written on SMF 28 fibres using a KrF excimer laser. The coating on the fibres was stripped to a length of 15 mm and cleaned with isopropyl alcohol. Gratings were written via a phase mask technique. The phase grating used for writing Bragg gratings had a grating period of 1059.8 nm. It had dimensions of 10 mm x 3 mm. The KrF laser was operated to emit pulse energy of 17 mJ at a repetition rate of 200 Hz for 5 minutes to a write strong grating on each fibre. The gratings written in this procedure were used for 157 nm laser beam exposure experiments. Bragg gratings used for ablation experiments were also written using the same procedure, however, the gratings were written in between two markings separated by 10 mm on the stripped length of the fibre. Therefore, the exact location of the gratings on the fibres (used for ablation experiments) was known.

5.8.2 Exposure of Bragg Gratings

The Bragg reflection peaks were measured using an optical spectrum analyser (MS9710B, Anritsu Ltd., UK) equipped with a broadband light source (LPB-1550-D). The detector can detect radiation in the wavelength range of 0.6 to 1.75 μm. The spectra were recorded at a centre wavelength of 1534 .1 nm, a span of 0.6 nm, a total sampling points of 2001, a band width of 1 kHz and a machine resolution of 0.07 nm. The temperature of the laboratory atmosphere was measured using a digital thermocouple. The Bragg gratings were mounted along the diameter of a circular metallic frame of 88 mm outer diameter and 60 mm inner diameter, with the 15 mm stripped length lying approximately at the centre of the frame. The fibre was clamped to the metallic frame using magnets. Care was taken to avoid bending of fibre during mounting. This frame was mounted vertically at a distance of 190 mm from the exit point of the beam using a suitable optical mount. The mount was positioned such that the alignment beam passes approximately through the centre of the 15 mm stripped length. This was done to expose the rectangular output beam along the length of the grating. The energy detector-head was mounted 25 mm from the metallic frame. The experimental setup is illustrated in Figure 5-14.

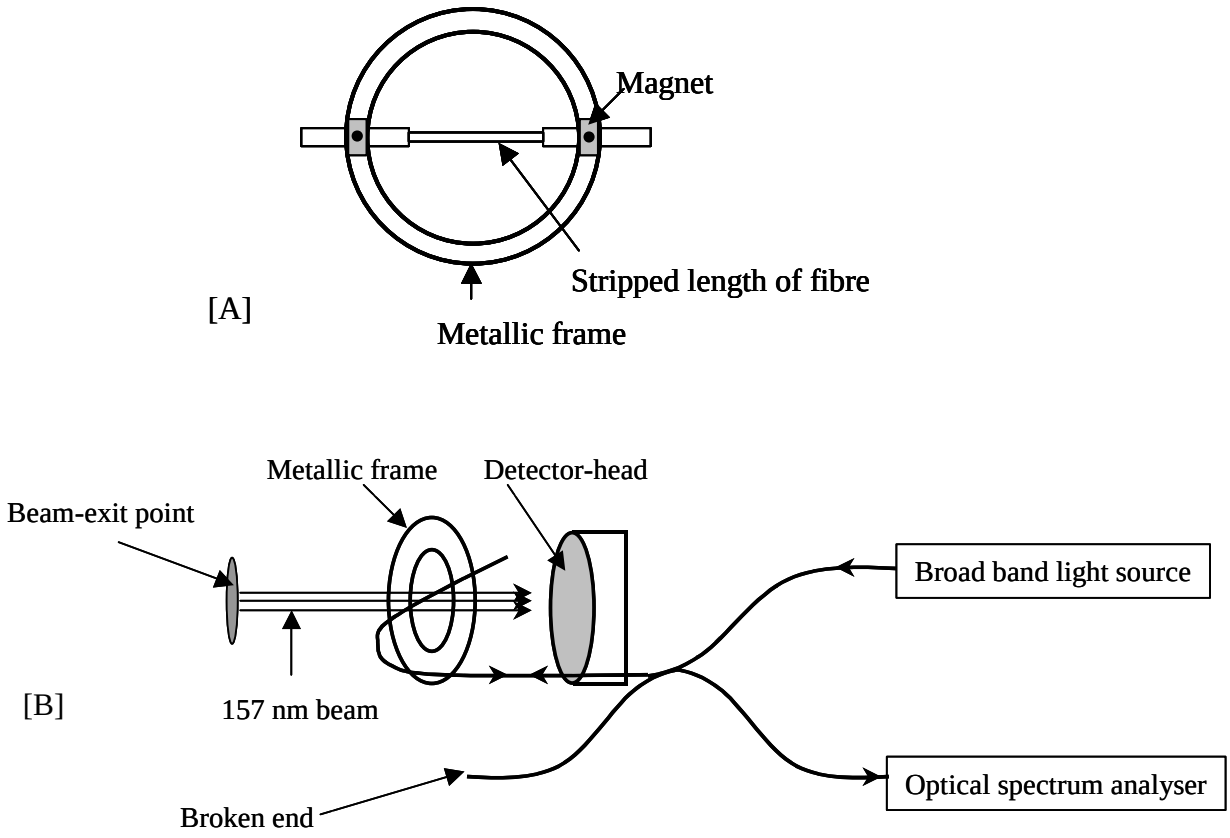

Figure 5-14: Schematic illustration of the exposure of fibre Bragg gratings to 157 nm beam; [A] Illustration of clamping Bragg grating to the metallic frame and [B] Experimental setup.

The fibre Bragg gratings were exposed to a 157 nm laser beam with an increment of 1000 pulses to a total of 10000 pulses. A duration of 15 minutes was maintained between any two consecutive 1000 pulses of irradiation. Two gratings were used in these experiments. One of the gratings was exposed to a total accumulated fluence of 2470 kJm^{-2} and the other to 1364 kJm^{-2}. The changes in the Bragg reflection peak during and after exposure were measured using the optical spectrum analyser.

5.8.3 Temperature Calibration of Bragg Gratings

After 157 nm exposure, the temperature calibration of the Bragg gratings was carried out using a temperature-controlled water bath. The Bragg gratings were freely suspended in water bath such that they were immersed in water. The Bragg reflection peaks at different temperatures were recorded. The Bragg spectra were recorded at a

centre wavelength of 1535 nm, span of 5 nm, bandwidth of 1 kHz, a total sampling points of 2001 and a machine resolution of 0.07 nm.

5.8.4 Ablation of Bragg Gratings

The Bragg gratings were aligned using the procedure described in Section 5.6.2. As mentioned in Section 5.8.1, the length of the gratings was known. The fibres were translated along the grating by 2 mm from one end of the grating and ablation was carried out through the diameter of the optical fibre. One of the Bragg gratings was ablated at an energy density of 19 x 10^4 Jm^{-2} and the other at 21 x 10^4 Jm^{-2}. After micro-machining cavity through the diameter, the fibre was fractured by inducing a bent radius. This was done to avoid unwanted reflection from the cavity wall surfaces. Then Bragg reflection peak was measured and compared with the Bragg reflection peak before ablation. The Bragg reflection spectra were recorded at a centre wavelength of 1535 nm, span of 5 nm, bandwidth of 1 kHz, a total sampling points of 2001 and a machine resolution of 0.07 nm.

5.9 Application of Micro-machined Optical Fibres

The chapter is aimed at demonstrating applications of F_2-laser ablated cavities in fused silica optical fibres and the feasibility of fabricating FP designs for various sensing applications. The applications and feasibilities that were aimed to be demonstrated were as follows:

1. To demonstrate a pH sensor using micro-machined MM 800 fibre;
2. To demonstrate a chemical sensor for detecting the amine in poly (oxypropylenediamine) using a micro-machined MM 800 fibre;
3. To demonstrate the feasibility of fabricating a FP pressure sensor and a temperature sensor.

5.9.1 pH Sensor

5.9.1.1 Sensor Fabrication

A MM 800 step index fibre was micro-machined at an energy density of 23 x 10^4 Jm^{-4} to produce 10 cavities along the diameter of the optical fibre along its length. The cavities were approximately separated by 300 μm. The alignment of the fibre for micro-machining was described in Section 5.6.2. The sensor was mounted along the centre of a glass slide and was bonded to the slide using UV-curing adhesive, Loctite 350 Adhesive, Henkel Loctite Adhesives Ltd., UK. An illustration of the mounted sensor on the glass slide is presented in Figure 5-15.

5.9.1.2 Preparation of Bromocresol Dye-based Solution and Experimental Setup

Bromocresol dye-based solution was prepared using 4.0026 x 10^{-3} kg of bromocresol dye (Hopkins & Williams Ltd., UK), 200 ml of isoproponal and 200 ml of distilled water. This combination was made upto one litre by adding distilled water. Bromocresol dye indicates the pH of the solution by changing the colour (yellow to blue) of the solution when the pH of the solution changes from 4 to 5.4 respectively. This solution was acidified by adding 70 % nitric acid (Aldrich, UK). A basic solution of NaOH (sodium hydroxide) was made using 20.0586 x 10^{-3} kg of NaOH (BDH laboratory supplies, UK) and 100 ml distilled water. The pH of the solution was changed by adding nitric acid and NaOH solution. The rationale of this experiment was that the changes in pH accompanied by a change in colour of dye-based solution could be detected from the transmission spectrum of the micro-machined fibre. An illustration of experimental setup is presented in Figure 5-16.

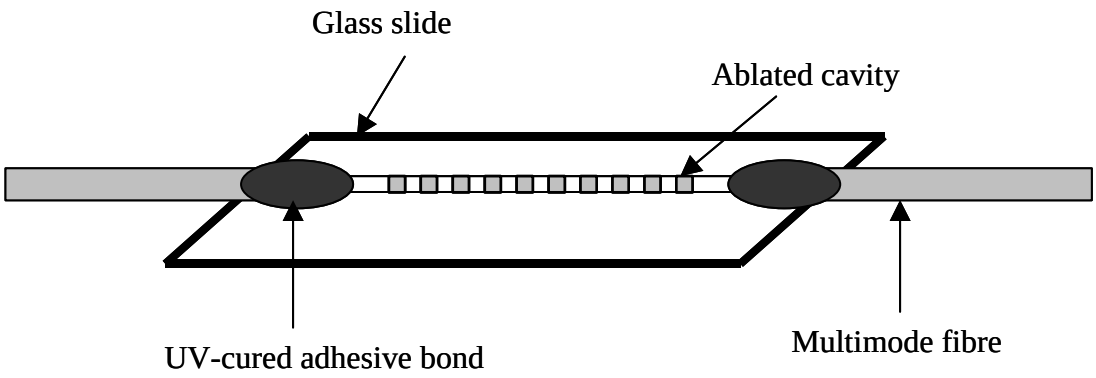

Figure 5-15: Schematic illustration of a multi-cavity fibre surface-mounted on a glass slide.

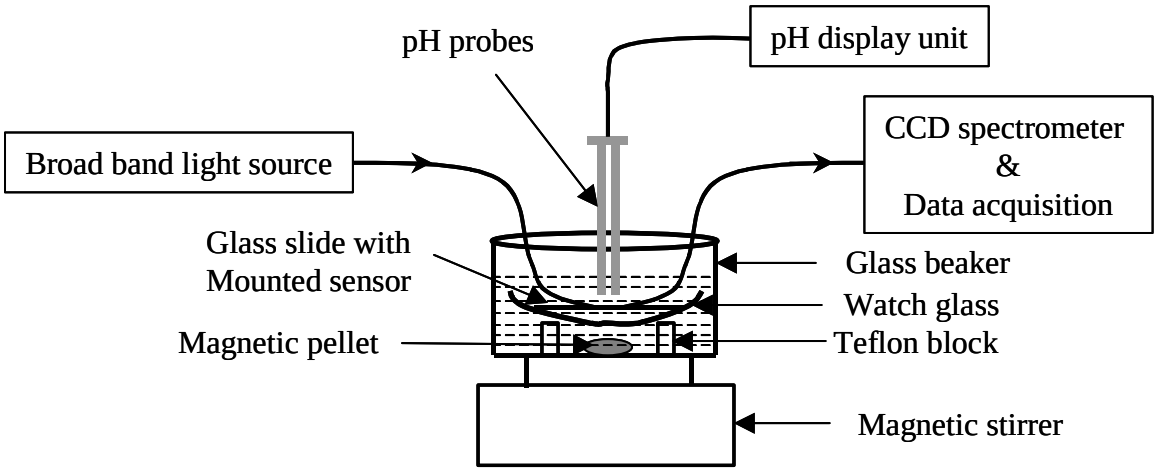

Figure 5-16: Schematic illustration of the experimental setup for pH sensing.

From Figure 5-15, it can be observed that the mounted-sensor was placed in a watch glass, which was resting on two Teflon blocks inside the glass beaker. The beaker was filled with dye-based solution such that the watch glass was completely immersed in the solution. The glass beaker was placed on a magnetic stirrer. The magnetic stirrer was used to reduce non-uniformities in the pH of the entire solution in the beaker. The sensor was interrogated using a tungsten halogen lamp (LS-1, Ocean Optics Inc., UK) and a CCD spectrometer (S2000, Ocean Optics Inc., UK) equipped with a data acquisition unit. The pH of the solution was measured using a pH meter (Kent EIL 7015). The pH-meter was calibrated prior to measurements using a standard buffer solution (Oakton, USA). The pH measurements of the solution were taken 15 minutes after the addition of acidic/basic solution to the dye-based solution in order to obtain a stabilised pH reading.

5.9.2 Chemical Sensor

The aim of this experiment was to investigate whether the micro-machined cavities could be used as miniature transmission cells for chemical detection. To investigate this, a micro-machined fibre as described in Section 5.9.1.1 was used. This fibre was mounted on a glass slide as shown in Figure 5-14. An optical spectrum analyser (MS9710B, Anritsu Ltd., UK) equipped with a broadband light source (LPB-1550-D) emitting in the wavelength range of 0.6 to 1.75 μm were used for sensor interrogation. The transmission spectrum of an un-ablated MM 800 fibre was taken as the background. A drop of polyoxypropylenedyamine was put over the length of the fibre with multiple cavities and the transmission spectrum was taken. An FTIR (Fourier transform infrared) spectrum of polyoxypropylenediamine was also measured using an FTIR spectrometer. The spectrum measured using the sensor and the spectrum measured using the FTIR spectrometer were compared.

5.9.3 Feasibility Experiment for the Fabrication of a Pressure Sensor

The aim of this experiment was to demonstrate a pressure-sensing technique bypassing the fabrication of a diaphragm. A cleaved SM 800 fibre was mounted on a glass slide in a manner similar to that shown in Figure 5-10, except that the cleaved end-face was not clamped using a magnet. A 50 μm x 50 μm feature was ablated approximately at a distance of 50 μm from the cleaved-end of the fibre with an energy density of 25×10^4 Jm^{-2}. Then the response was measured using the CCD interrogation scheme shown in Figure 5-2.

6 Chemical Etching of Optical Fibres

6.1 Introduction

The results from the experiments carried out using the methods explained in Section 5.3, which is concerned with the fabrication of intrinsic Fabry-Perot optical fibre sensors, are presented and discussed in this chapter. The results of etching SM 800 (unprotected) fibres for different etch times are presented. The dimensions of the etched optical fibres were studied using optical microscope and etch rates of fibre diameter and doped-core determined. Scanning electron microscope was used to inspect the morphology of etched cavities. The quality of etched fibres to serve as strain sensors was determined using the CCD interrogation scheme. Quantitative data on the roughness of etched cavities was determined using an interferometric surface profiler. Finally, the results of tensile tests of surface-mounted etched interferometers are presented.

6.1.1 Etch Rate of Fibres

Representative optical micrographs of SM 800 fibres etched for different times are presented in Figure 6-1. The acid dissolves both the fused silica cladding and germania-doped core of the optical fibre. However, a cavity was formed around the core of the optical fibre. In picture '[1]' of Figure 6-1, the cavity formed at the core of the optical fibre can be seen. It can be observed from pictures '[2]', '[3]', '[4]' and '[5]' of Figure 6-1 that the etch depth and diameter of the cavities increased with etch time. The diameter of the cleaved-ends of the fibres decreased with the etch time. The diameter of the cleaved-end of the fibre and the etch-depth were measured using Leica-Qwina image analysis software. The etch-depth is the distance from the cleaved-end to the crater of the cavity. According to the optical magnification, the measurement options were calibrated by the image analysis software.

The measurements of the diameters of the cleaved-end of the fibres and the corresponding etch-depths were measured on a batch of 8 fibres for each etch-time. The average etched-diameter of the cleaved-end and the etch-depth of cavities etched for different times are presented in Table 6-1. The definition of cone-angle of an etched cavity is presented in Figure 6-2. Two tangents are defined along the surface of the cavity walls. The tangents intersect on the core of the fibre at a finite distance from the crater surface of the cavity. The angle between the tangents is measured using the image analysis software. Half of the angle between the tangents is taken as the cone angle 'θ' of the cavity. The cone-angle of cavities at different etch times is also presented in Table 6-1.

The etch-depth of the cavities and etched fibre diameters were plotted against etch time and are presented in Figure 6-3 and Figure 6-4 respectively. The diameter of the optical fibres was found to decrease in a linear fashion under the experimental conditions used in these investigations. The rate of decrease of etched fibre diameter at the cleaved end was found to 3 μm minute^{-1}. The etch-depth of the cavities was found to increase in a linear fashion up to 22 minutes of etching. The rate of increase of etch depth up to 22 minutes of etching was found to be 1μm minute^{-1}. However, a decrease in the etch rate was observed after 22 minutes of etching. The cone-angle of the cavities was found to decrease with the etch-time up to 16 minutes after which the cone-angle was found to increase.

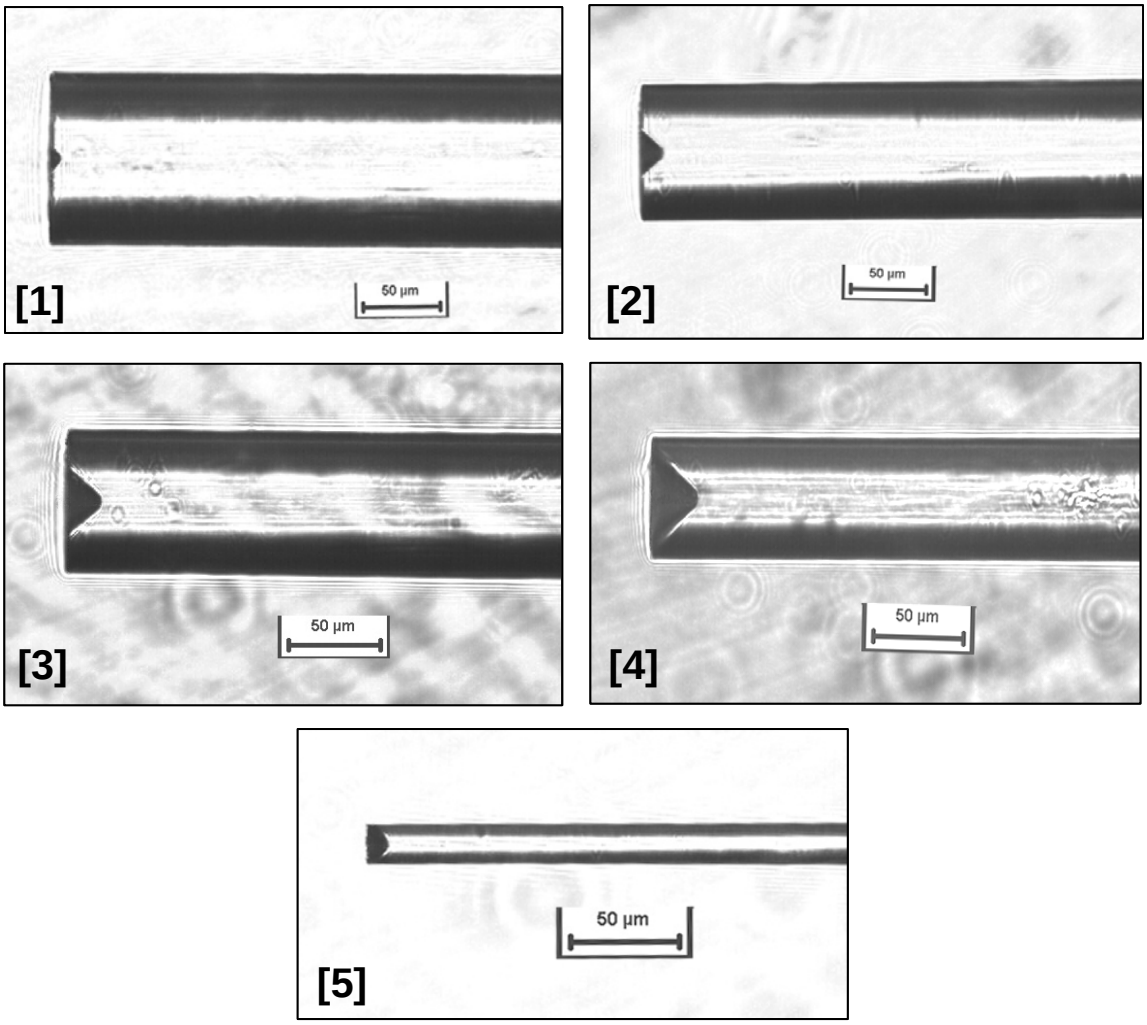

Figure 6-1: Optical micrographs of SM 800 fibres etched for different times at 20 ± 0.5 °C; (1) 5 minutes, (2) 12 minutes, (3) 16 minutes, (4) 22 minutes and (5) 35 minutes.

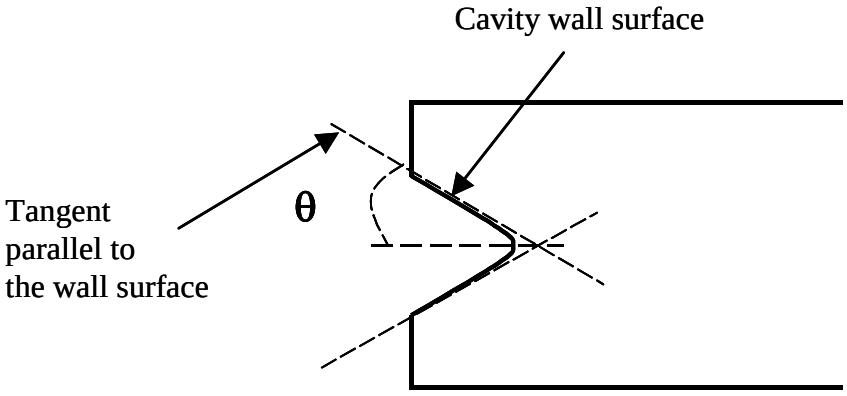

Figure 6-2: Schematic illustration of cavity cone-angle of etched cavity.

Table 6-1: Average etched-diameters, etch-depths and cavity angles for different etch times.

Etch time [minutes]	Etched fibre diameter [μm]	Standard-deviation of etched diameter [μm]	Etch-depth [μm]	Standard-deviation of etch-depth [μm]	Cavity cone-angle
5	108.8	± 0.6	7.4	±0.4	50.3°
12	89.6	±0.7	15.7	±0.6	43.3°
16	76.5	±0.4	18.9	±0.9	39.8°
22	59.7	±0.4	24.6	±0.5	45.3°
35	18.3	±0.5	9.3	±0.5	53.2°

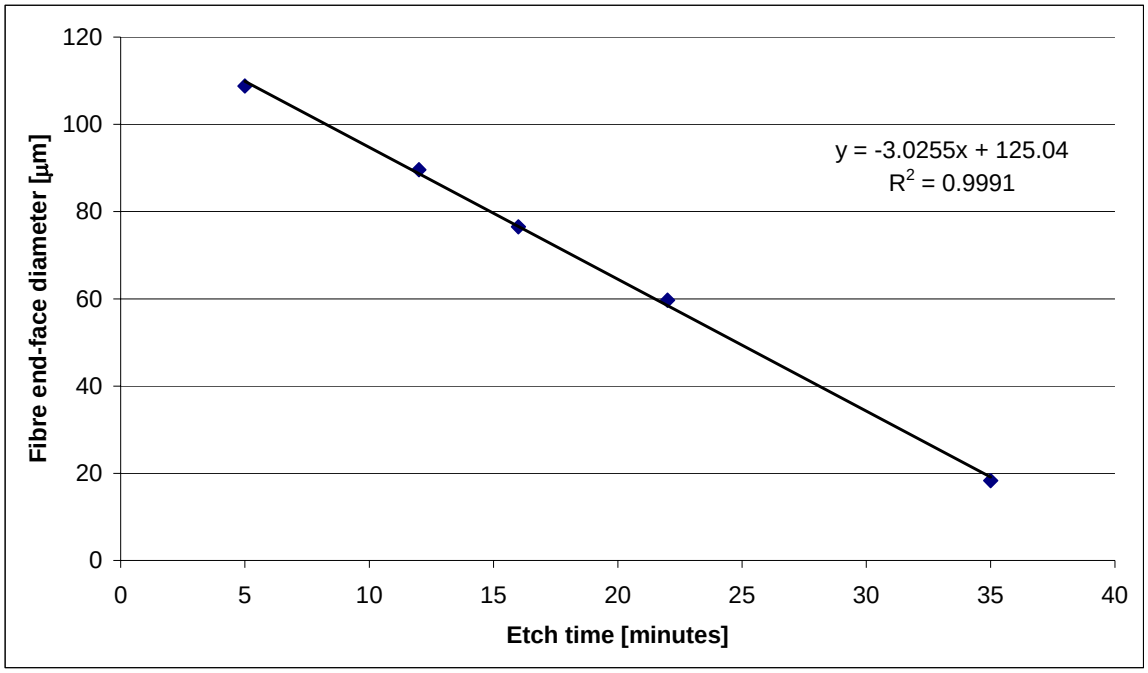

Figure 6-3: Average etched fibre diameter at the cleaved end as a function of etch-time at 20 ± 0.5 °C using 48% HF.

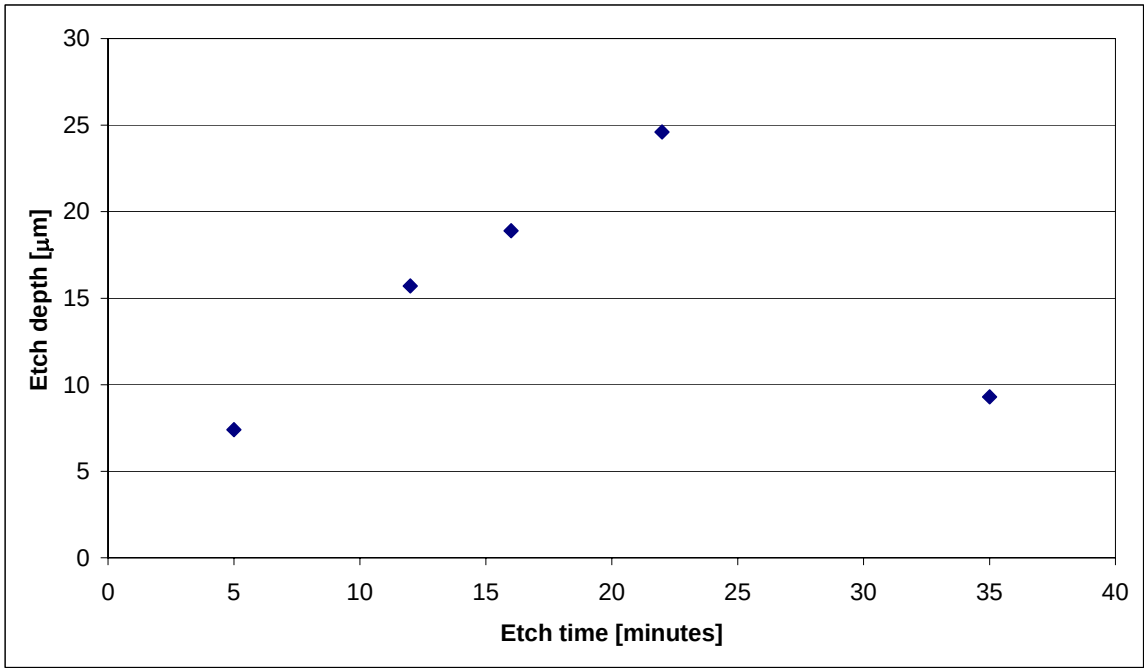

Figure 6-4: Average etch-depth of the cavities as a function of etch-time at 20 ± 0.5 °C using 48% HF.

6.1.2 Effect of Cavity Formation

The etching mechanisms of HF with SiO_2 and GeO_2 and the reasons for preferential etching of the doped-core were presented in Section 2.9.1. With the formation of a cavity at the core of the optical fibre, the acid attacks a larger area of cladding around the cavity. At the same time, the acid also etches the cylindrical surface of the fibre. This combined effect leads to decrease in the cleaved end-face diameter at a rate of 3 µm minute^{-1}.

The cone-angle of the cavities was found to decrease with the etch-time up to 16 minutes. The reason for the decrease in cavity wall angle could be explained as follows. The cavity formation starts at the pristine surface of the cleaved fibre with core and cladding of the fibre at the same surface level. The first 5 minutes of etching produces a depression across the core and a cavity wall surface with slanted walls. The area of core exposed to the acid always remains constant, whereas the area of cladding exposed to the acid increases around the cavity. However, the etch-rate of the germanium-doped-core proceeds at a faster rate than the fused silica cladding surface of the cavity, a decrease in cone-angle was observed up to 16 minutes of

etching. Another reason could be that the walls of the cavity may confine the HF-etching reaction by-products, which could reduce their rate of diffusion into the bulk of the acid, whereas the reaction by-products due to etching of the outer cylindrical surface are not confined. The acid was not agitated during these fibre-etching experiments. With a further increase in etch-time i.e. after 22 minutes of etching, the cavity diameter approaches closer to the outer diameter of the fibre, which leads to an increase of cavity cone-angle. This is obvious from [4] of Figure 6-1. After 35 minutes of etching, there is no evidence of cladding thickness and the cavity cone-angle further increased. After 1 hour of etching, the cleaved-end of the fibre was reduced to a tip. Tip formation via HF etching, for the fabrication of near-field scanning microscopy probes has been reported [124], [125], [126].

The etch rate of the unprotected fibre core was linear for the first 22 minutes of etching and then decreased. The etch depth of the cavity is defined with the cleaved end-face of the fibre as the reference. After 35 minutes of etching, the cladding thickness was fully dissolved in the acid. The front-face, which is the reference surface for measuring the etch-depth, of the optical fibre was fully etched. This lead to a relative shift of the reference surface towards the cavity crater and hence a decrease in etch depth was observed after 35 minutes of etching.

6.1.3 SEM Analysis

The optical quality of the etched surface of the cavities is a significant factor, which determines their optical reflectivity. This is an essential criterion for producing Fabry-Perot etalons. The morphology of the cavity surfaces etched for different times is presented in Figure 6-5, Figure 6-6, Figure 6-7, Figure 6-8, Figure 6-9 and Figure 6-10. These representative SEM pictures also provide qualitative evidence of the formation of cavity and the evolution of a cavity with etch-time.

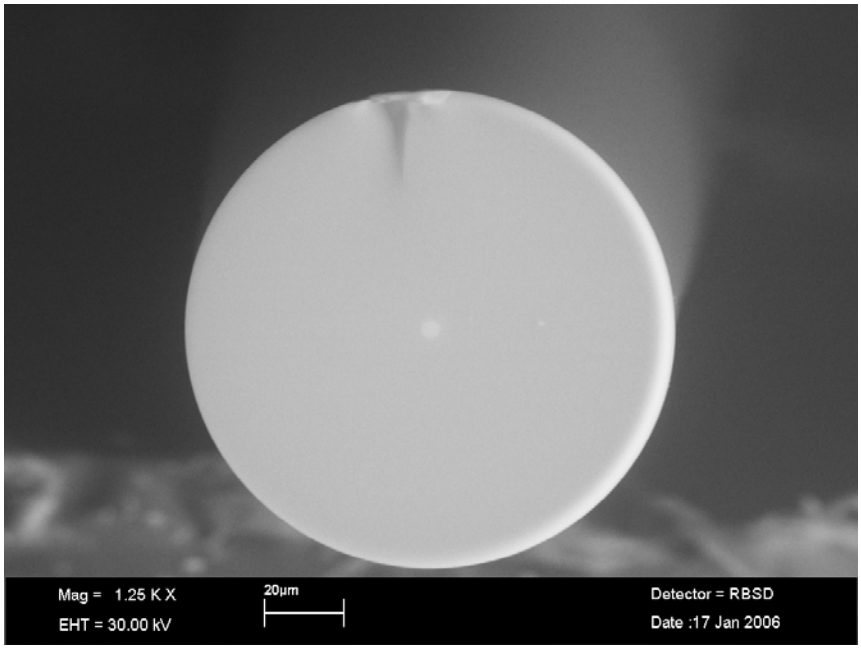

Figure 6-5: SEM micrograph of an as-cleaved end-face of an SM 800 fibre.

From Figure 6-5, the cladding and the central doped-core of the fibre are obvious. The surface of the core and the cladding are at the same surface level prior to HF etching. The notch near the circumference of the cladding in Figure 6-5 could be due to fibre fracture.

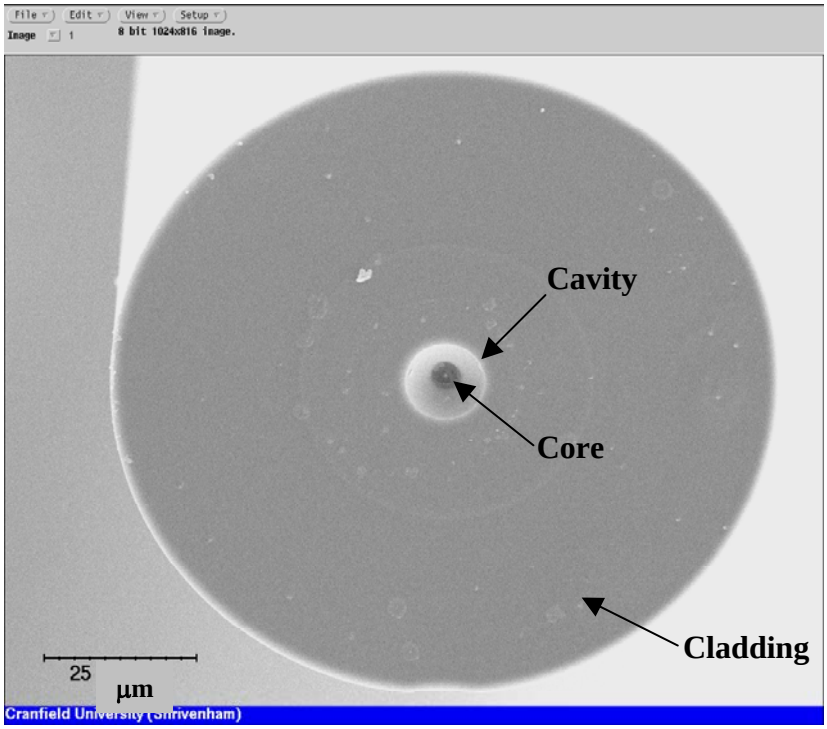

Figure 6-6: SEM picture of SM 800 fibre etched for 5 minutes.

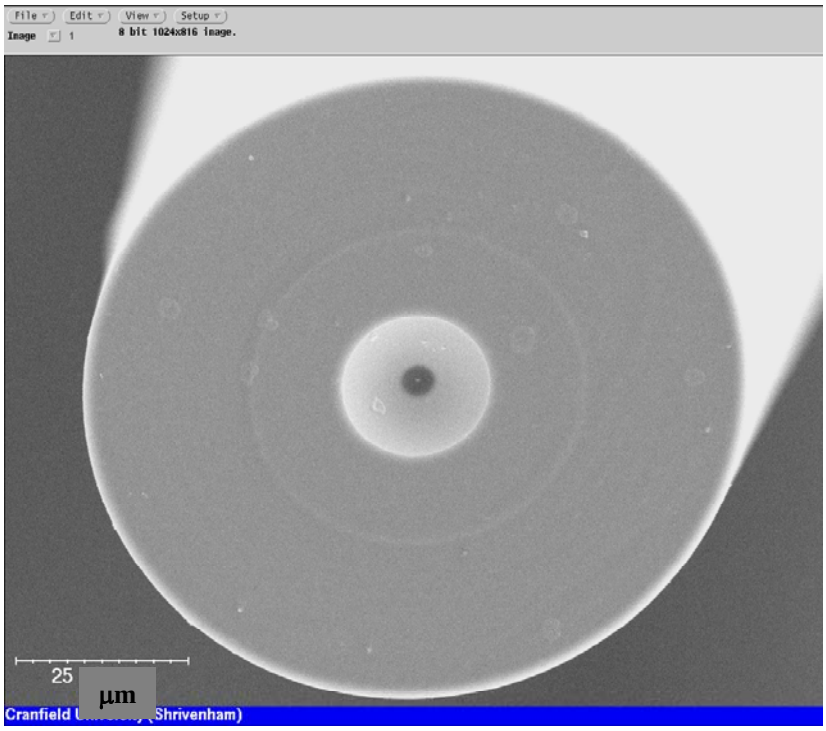

Figure 6-7: SEM picture of SM 800 fibre etched for 12 minutes.

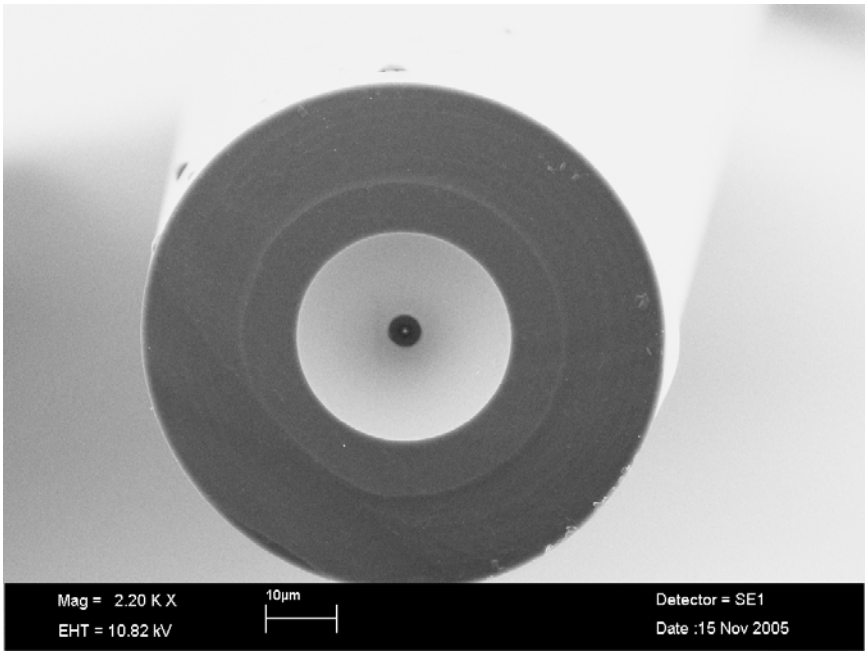

Figure 6-8: SEM picture of SM 800 fibre etched for 16 minutes.

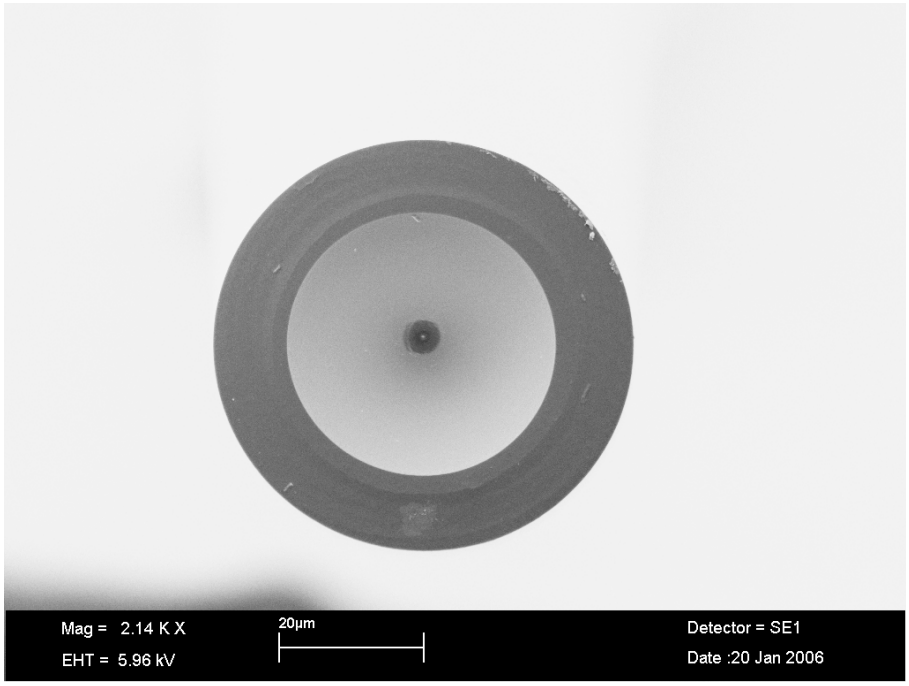

Figure 6-9: SEM picture of SM 800 fibre etched for 22 minutes.

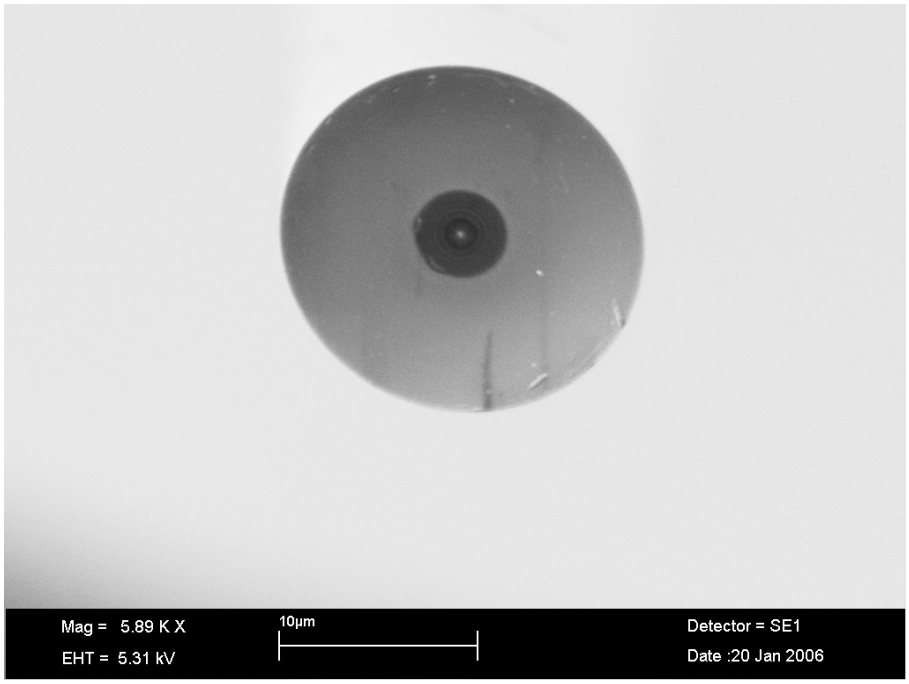

Figure 6-10: SEM picture of SM 800 fibre etched for 35 minutes.

From Figure 6-6, Figure 6-7, Figure 6-8, Figure 6-9 and Figure 6-10, it can be observed that the cavity wall surfaces and the core of the optical fibres had a smooth morphology. The cavity formation, cavity wall surfaces, central core and cladding thickness of the etched fibres are obvious. It can also be observed that the cavity

perimeter and the outer perimeter of the fibre were concentric. The diminishing cladding thickness and increasing cavity diameter with etch-time are also obvious from these pictures. The cladding thickness is a significant factor, which determines the contact area of the fusion weld of two etched fibres of the same etched-diameter, when they were deployed for fabricating intrinsic FP interferometers. As mentioned in Section 6.1.2, the cladding thickness of the fibre was not obvious after 35 minutes of etching. This absence of cladding thickness can be clearly observed by comparing Figure 6-10 with Figure 6-9, Figure 6-8, Figure 6-7 and Figure 6-6.

Another important factor is the cleanliness of the cavities. Any contamination such as dust particles and hydrocarbon particles on the etched fibre cross-sectional surfaces could be detrimental to the optical reflectivity and fusion weld of the etched fibres.

An SEM picture of an SM 800 fibre etched for 16 minutes, which shows the tapering of the fibre along the length of the fibre dipped in the acid, is presented in Figure 6-11. When the unprotected fibre is dipped in acid, the acid level rises above the horizontal around the cylindrical surface of the fibre due to surface tension. This region of the cylindrical surface of the fibre corresponds to the beginning of the tapering towards the cleaved end of the fibre. The tapered length of the fibre is shown in Figure 6-11. This tapering along the immersed length of the fibre is in agreement with the findings of other researchers on the influence of the meniscus height on the tapering [125], [127].

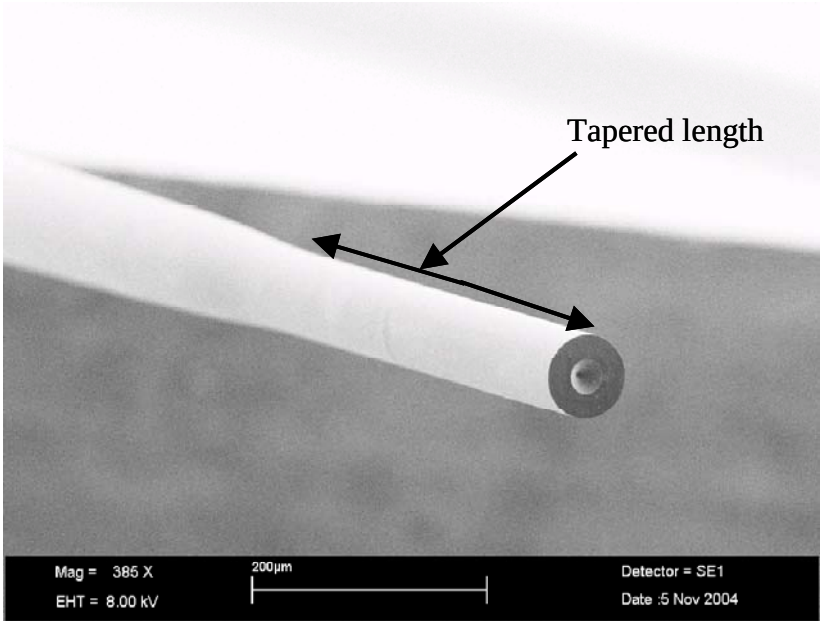

Figure 6-11: SEM picture showing tapering of fibre diameter due to unprotected etching.

The cleaved-ends of fibres etched for one-hour were reduced to a tip. The formation of a tip could be explained as follows. From picture '[5]' of Figure 6-1 and Figure 6-10, it can be observed that the cone-angle of the cavity increases after 35 minutes of etching and the thickness of the cladding was no longer evident. Therefore, further etching of the fibre could transform the concave shape of the cavity to convex due to the increasing cone angle associated with the decreasing diameter of the cleaved end-face. This could eventually lead to the formation of a tip at the cleaved-end of the fibre. From Figure 6-12, the tip formed at the cleaved end-face of the optical fibre after 1 hour of etching is obvious.

From Figure 6-12, the dimension of the tip shown in between the arrows is approximately 5 μm. A mark on the surface in between the two arrows can be clearly seen. This could be the interface of the core and cladding of the fibre. The dimension of the tip indicates that the tip of the fibre is the core of the fibre. The SM 800 fibre has a core diameter of 5.6 μm.

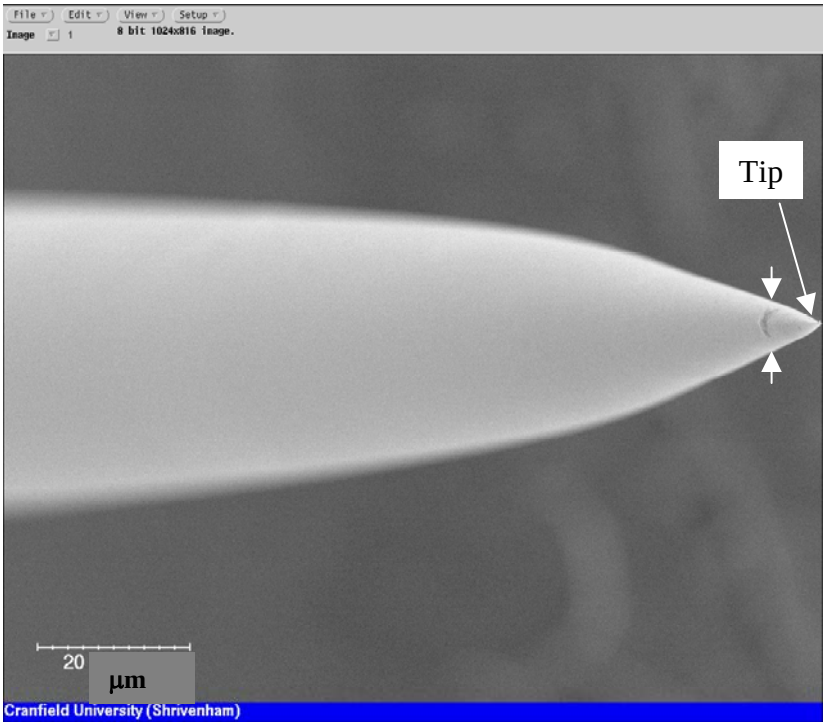

Figure 6-12: SEM picture of SM 800 fibre etched for one hour.

6.1.4 Interferometric Surface Profile Analysis

Quantitative data on the roughness of the cavities was obtained by carrying out a surface profile analysis. When the etched end-faces of the fibres were studied using the surface profiler, a common observation with respect to fibres etched for different times is that reflection from the cavity wall surface was not obtained. This is due to the slanted surfaces of the etched cavity walls. The angle at which the light undergoes reflection does not couple it back into the profiler. However, a good reflection of light was produced from the surface of the cladding thickness and core surfaces of the fibres etched for different times. The surfaces of the core and the cladding thickness are normal to the direction of the light from the interferometer. A representative surface profile picture of the etched end-face of a fibre etched for 22 minutes is presented in Figure 6-13.

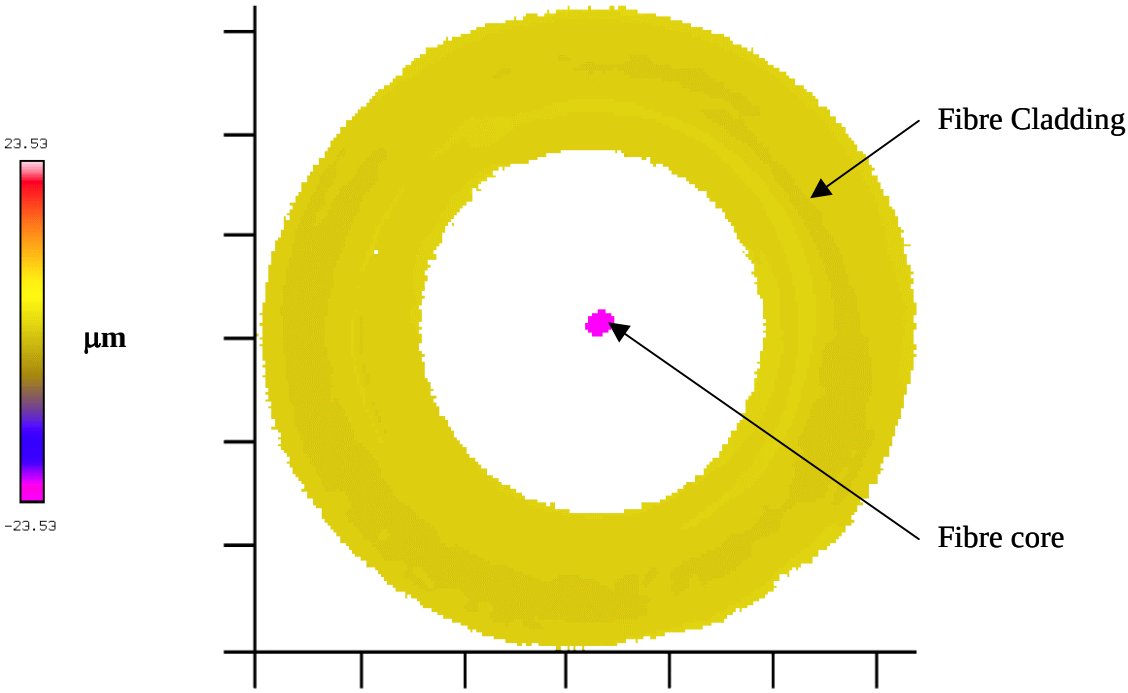

Figure 6-13: Surface map of etched end-face of a 22 minute etched fibre.

The colour scale bar indicates the relative surface levels of different regions of the profiled surface. The coloured regions of the picture indicate surfaces of good optical reflection. It can be observed from the scale bar of Figure 6-13, that the core of the surface is at a lower level than that of the cladding. The white region in between the core and core and cladding indicates no data has been obtained from the cavity wall surface due to the lack of reflection from these surfaces. The slanted wall surfaces of the cavities etched for different etch-times are obvious from the cone-angle data presented in Table 6-1 and from the optical micrographs of Figure 6-1.

Three-dimensional profiles of the surface maps of fibres etched for 16 and 22 minutes are presented in Figure 6-14 and Figure 6-15.

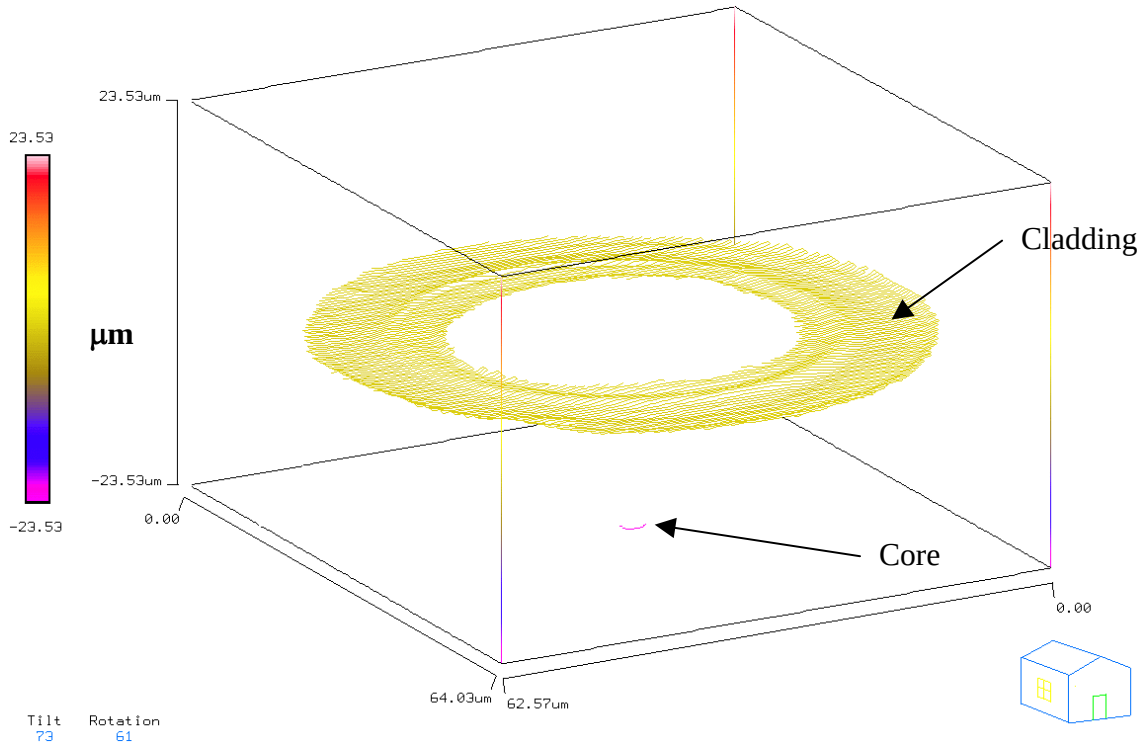

Figure 6-14: 3D-profile of a fibre etched for 22 minutes.

From Figure 6-14 and Figure 6-15, it can be observed that the etched core of the fibre has a curvature across its surface. The curvature indicates a concave core surface. The curved surface of the core became more obvious when the profile along the line-segment defined across the core was studied. The line-segment profile of the core surface is presented in Figure 6-16. This curvature was observed for all the etch-times.

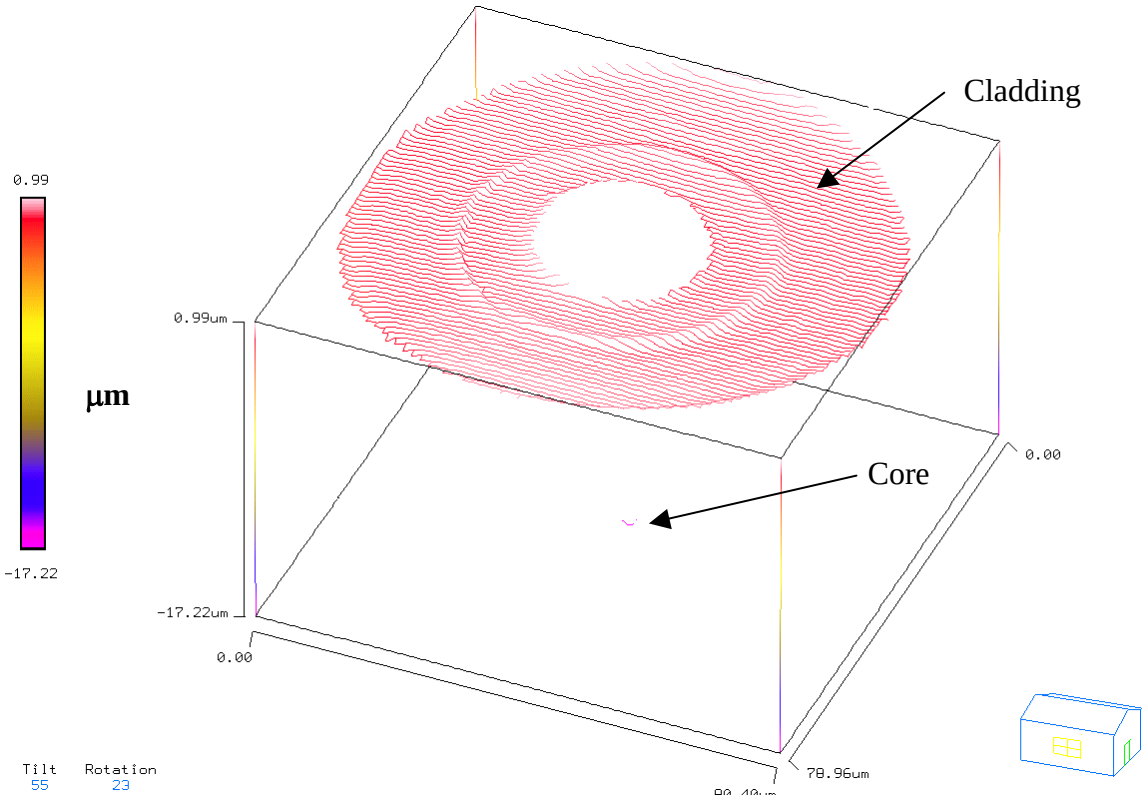

Figure 6-15: 3D-profile of a fibre etched for 16 minutes.

From Figure 6-16, it can be observed that the surface of the core is not flat. The difference in height of the core surface from the tag position to the cursor position is 350nm. The tag and cursor are separated by 2.46 µm. The positions of tag and cursor are chosen such that they are at either ends of the reflecting surface of the core. Therefore the line-segment profile data across the core is due to reflection from a fractional area of the surface of the core of the fibre. This area of the surface of the core that is producing reflection is more likely to be around the centre of the core as the central region of the core will be more normal to the light from the profiler. The concave nature of the core surface as observed from Figure 6-14, Figure 6-15 and Figure 6-16 indicates a higher etch rate at the centre of the core than that around its circumference. The circumference of the core (step-index profile) is the interface of the core and cladding of the fibre. This could be due to accumulation of etching-reaction by-products at the core/cladding interface. Another reason for this curvature could be the deviation of the refractive index profile of the SM 800 fibre from the ideal step-profile.

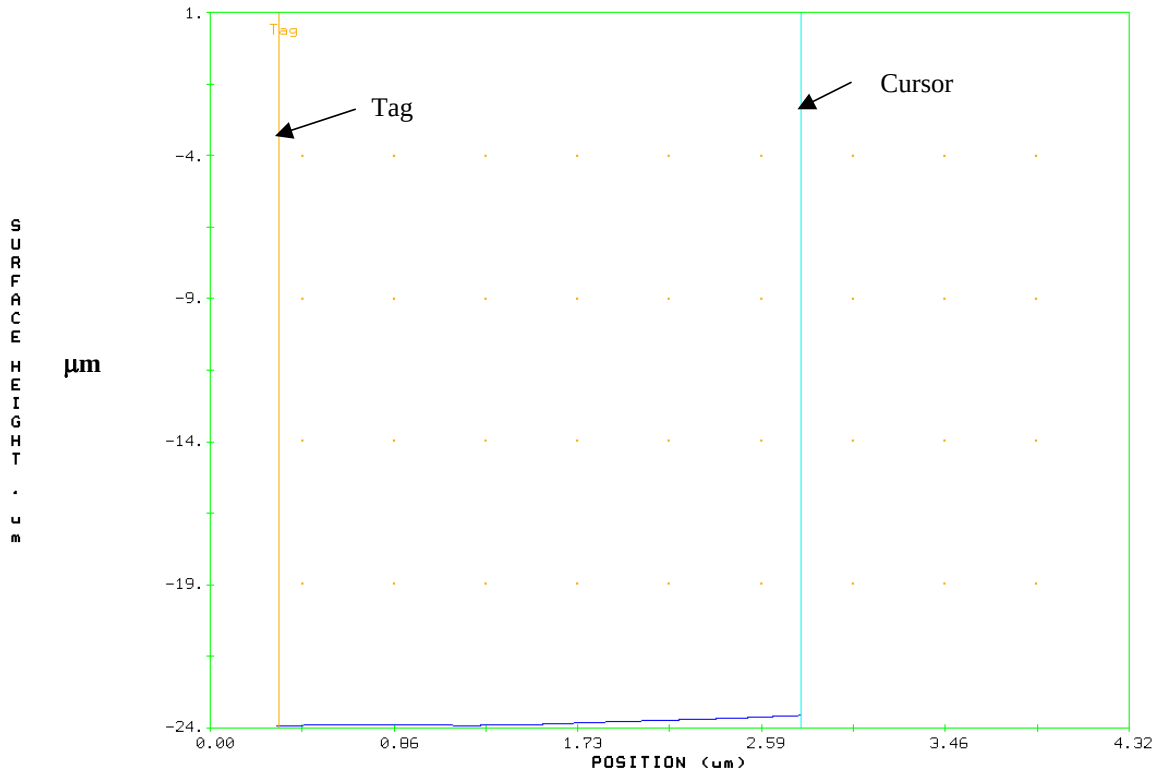

Figure 6-16: A representative profile across the surface of the core.

The roughness across the reflecting surface of the core and the cladding were measured from the surface maps of the fibre end-faces etched for different times. The roughness measurement method of cladding and core of an etched fibre is presented in Figure 6-17.

The blocks that were numbered from 1 to 9 in Figure 6-17 were defined at different locations on the cladding surface. Each block has an area of 8.33 µm x 8.36 µm. The average of RMS (root mean square) roughness measured across these nine blocks is taken as the RMS roughness of the cladding. A block of 2.01 µm x 2.01 µm was defined on the central region of the core and the RMS roughness of the core was measured across that area. All these blocks were defined on the regions of the surface map where the reflection data was obtained. The roughness data of cladding and core of the fibres etched for different times measured according to the method described in Figure 6-17 is presented in Table 6-2.

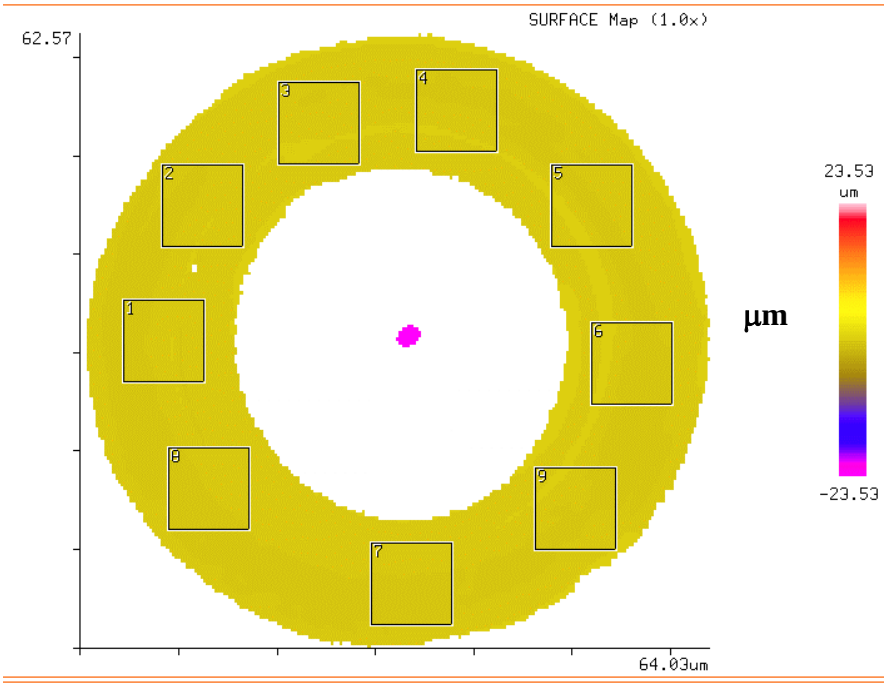

Figure 6-17: Surface map of the etched end-face of a 22 minute-etched fibre.

Table 6-2: Roughness of cladding and core of fibre end-faces etched for different times.

Etch-time [minutes]	Average rms roughness of cladding [nm]	Roughness of core [nm]
Cleaved fibre end-face	21	5
5	23	120
12	53	80
16	44	76
22	147	159

From Table 6-2, it can be observed that the roughness of the core and cladding increased after HF etching. It can be observed that the maximum RMS roughness values of the core and cladding as a result of etching are less than 0.25λ, where 'λ' is the operating wavelength of the SM 800 fibre. Although no reflection was obtained from the steep wall surface of the etched cavities, the roughness of the cavity surfaces could be similar to that of the cladding (as shown in Table 6-2) as the material of the cavity surface (un-doped fused silica) is the same as that of the cladding. The roughness produced via acid etching could reduce the reflectivity of the etalon surfaces of the cavity, which in turn could reduce the relative intensity and contrast of the FP interference fringes.

6.1.5 CCD Interrogation of Etched Cavities

In order to investigate the optical reflectivity of the etched cavities, two etched cavities of equal fibre diameter were interrogated using the CCD interrogation scheme described in Section 5.3.5. The etched faces of the fibres were aligned in the XZ-plane and YZ-plane using the manual controls of the fusion splicer. Fabry-Perot interference fringes were observed when the etched-faces of the fibres were butted together. This result demonstrates that the optical quality of the surfaces of the etched cavities is sufficient to produce FP etalons. However, the relative intensity and contrast of FP interference fringes produced from the acid-etched etalons was lower than that produced by using cleaved fibre-ends as partial reflectors. This could be due to the roughness produced via etching. This etching-induced roughness is obvious from Table 6-2.

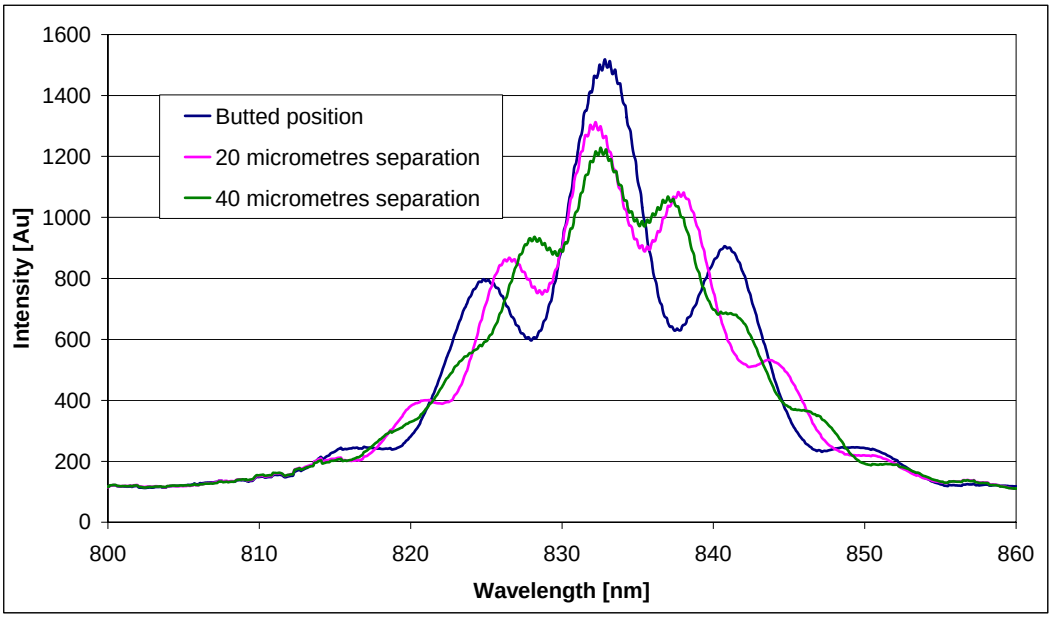

Figure 6-18: Evolution of FP interference from the butted position to 40 μm separation.

The separation between the etched-faces was increased using the manual controls of the fusion-splicer. The separation along the fibre-axis could be increased in increments of 1 μm. The changes in the FP spectral interference fringes with increasing separation distance between the etched-faces is presented in Figure 6-18

and Figure 6-19. In the FP interferometer, an increase in etalon separation results in a closer spacing of airy rings and the path length difference at a specific wavelength increases and hence the number of fringes increases. The sharpness of the fringes decreases with increasing separation. The increase in the number of fringes and decrease in the sharpness of the fringes with increasing separation can be clearly observed from Figure 6-18 and Figure 6-19. From 60 μm separation to 100 μm separation, the fringe sharpness decreased significantly and fringes were barely visible at a separation of 100 μm. A plot of cavity length calculated from the FP interference fringes using Equation 2-6 against the manually translated distance is presented in Figure 6-20. It can be observed from Figure 6-20 that the calculated cavity length changes in a linear fashion with the distance translated. The calculated cavity lengths and translated distances are presented in Table 6-3. The calculated cavity length for a translated distance of 100 μm is not presented because of poor visibility of FP interference fringes. These changes in FP interference with increasing etalon separation show that the etched fibres in principle can be used for fabricating FP sensors and can be used within the failure strength of the device.

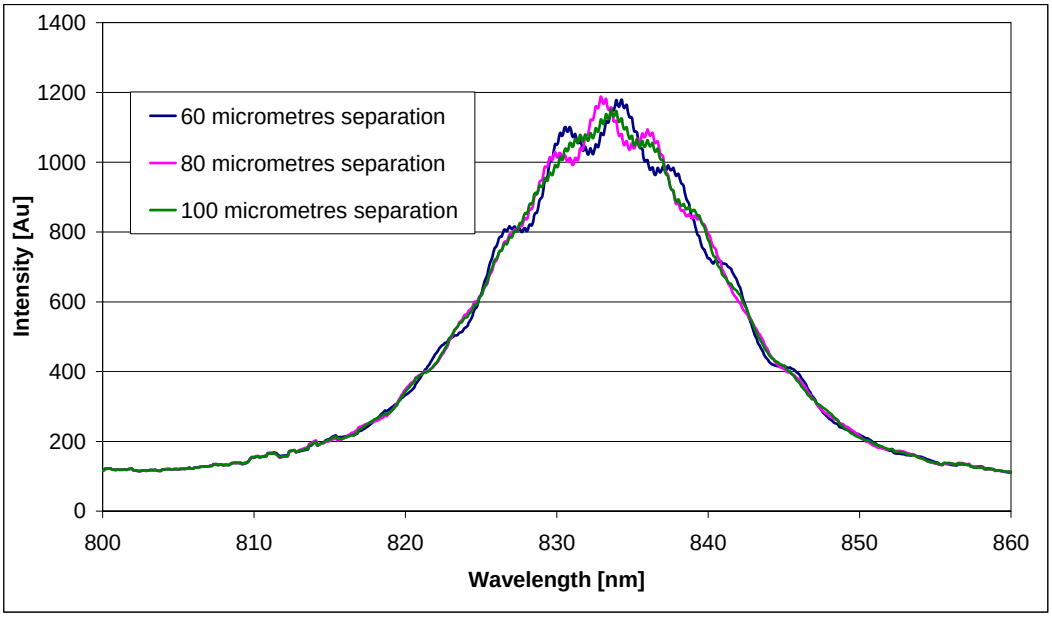

Figure 6-19: Evolution of FP interference from 60 mm separation to 100 μm.

Table 6-3: Table of calculated cavity lengths and translated distances.

Translated distance [μm]	Calculated cavity length [μm]
0	43.6 (Butted position)
20	61.8
40	78.4
60	105.9
80	123.6

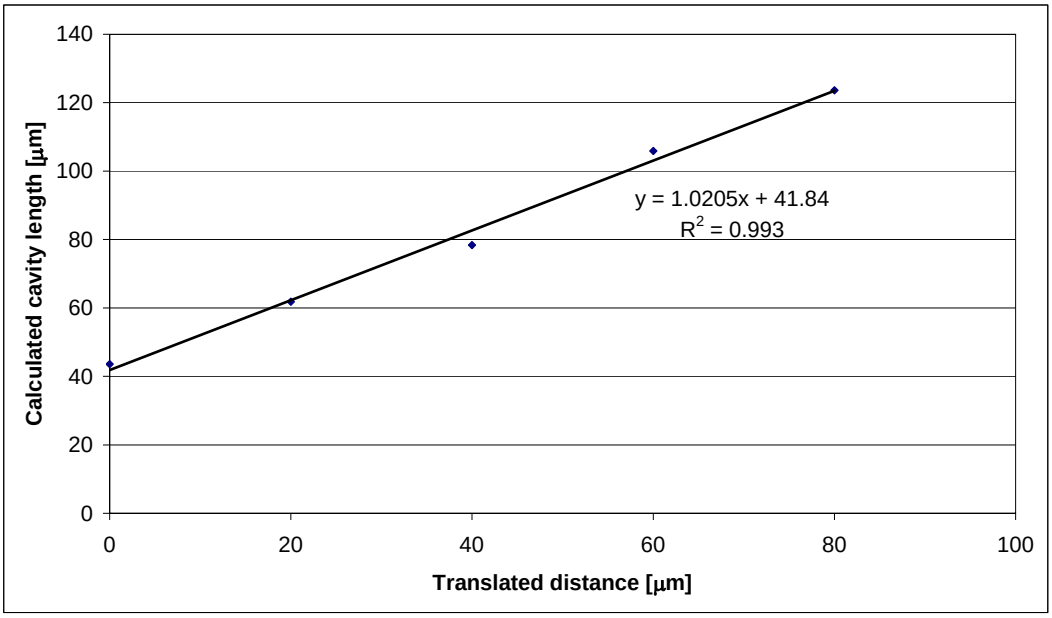

Figure 6-20: Influence of increasing separation between the acid-etched fibre etalons.

6.1.6 Fabrication of Intrinsic Fibre Fabry-Perot Interferometers

Etched optical fibres of equal etched end-face diameters were used for fusion splicing. The fusion splicing parameters were presented in Section 5.3.6. It is difficult to fuse etched fibres using the standard fusion-splicing programme for single mode fibres. This unsuitability of the standard fusion-splicing programme is due to the reduced cleaved end-face diameters. The reduction in the initial and final arc currents to the fusion spliced fibres etched for 22 minutes is to avoid the collapse of the cladding into the etched cavities. The fibres etched for less than 20 minutes sustained a final fusion current of 12 mA, whereas this was reduced to 10 mA to fuse fibres etched for 22 minutes. The splicing of etched fibres was carried out by simultaneously monitoring the FP interference via CCD interrogation. Fabry-Perot interference was observed from the fusion spliced etched fibres. It became obvious from these observations that

the intrinsic interferometers fabricated from fibres etched for a shorter duration will have a larger contact area around the intrinsic cavity due to a larger area of the cladding at the etched end-faces.

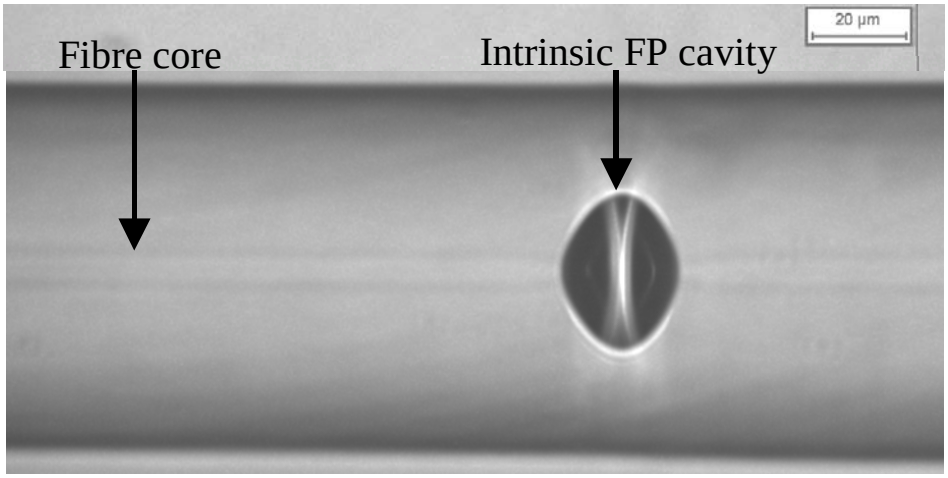

Figure 6-21: Optical micrograph of an intrinsic fibre Fabry-Perot cavity.

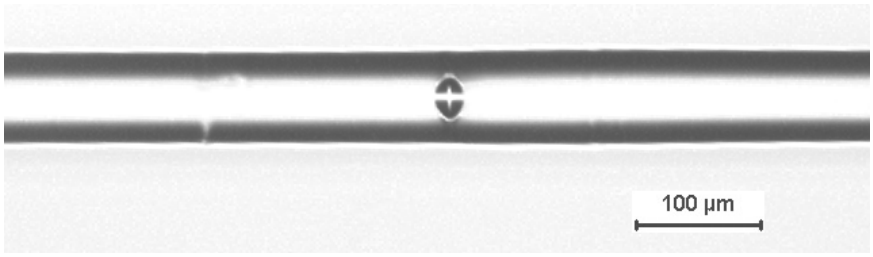

Figure 6-22: Representative micrograph of an IFFPI.

The intensity of the FP fringes increased after splicing the etched fibres. This could be due to surface cleaning or smoothness across the cavities produced due to the high temperature generated by the fusion arc. Representative optical micrographs of the intrinsic fibre Fabry-Perot (IFFPI) interferometers are presented in Figure 6-21 and Figure 6-22. From Figure 6-21, the cores of the fibres across the etched etalon surfaces are obvious. The representative FP interference fringes of two IFFPIs are presented in Figure 6-23 and Figure 6-24. The cavity lengths of the IFFPIs were calculated from the interference fringe pattern of Figure 6-23 and Figure 6-24 using Equation 2-6. Therefore the fabrication of IFFPIs was demonstrated.

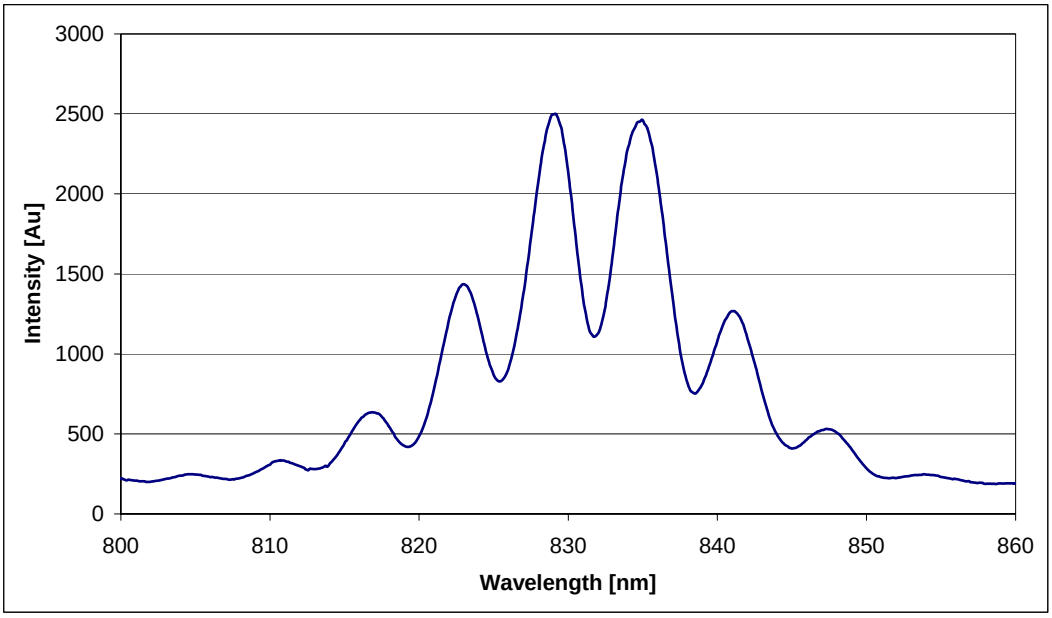

Figure 6-23: Interference fringes of an IFFPI of cavity length of 38 μm.

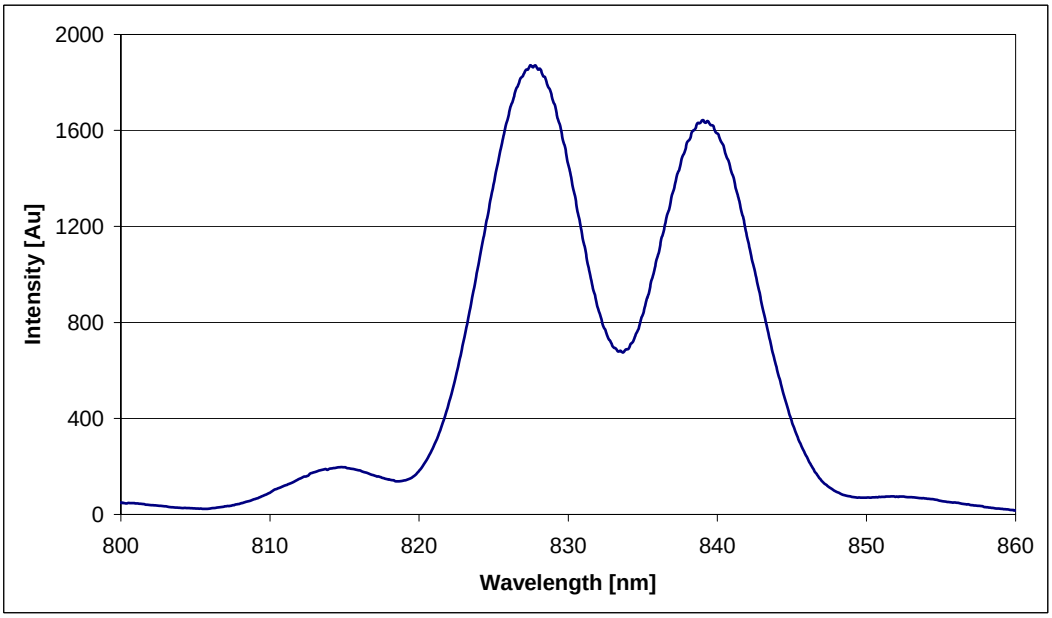

Figure 6-24: Interference fringes of an IFFPI of cavity length of 31 μm.

6.1.7 Tensile testing of etched FP interferometers

The distance between the bonded points of the surface mounted FP-interferometer described in the experimental Section 5.3.7 was found to be 17.8 mm. The sensor was actually bonded to the coupon at 10 mm markings on either end from the centre

of the coupon. However, the flow of resin due its viscosity has caused a slight reduction in this predetermined distance of 22 mm.

6.1.7.1 Geometry of the intrinsic FP sensor

The taper profile of the fibre diameter along its length between the two bonded points was measured under a microscope and is shown in Figure 6-25.

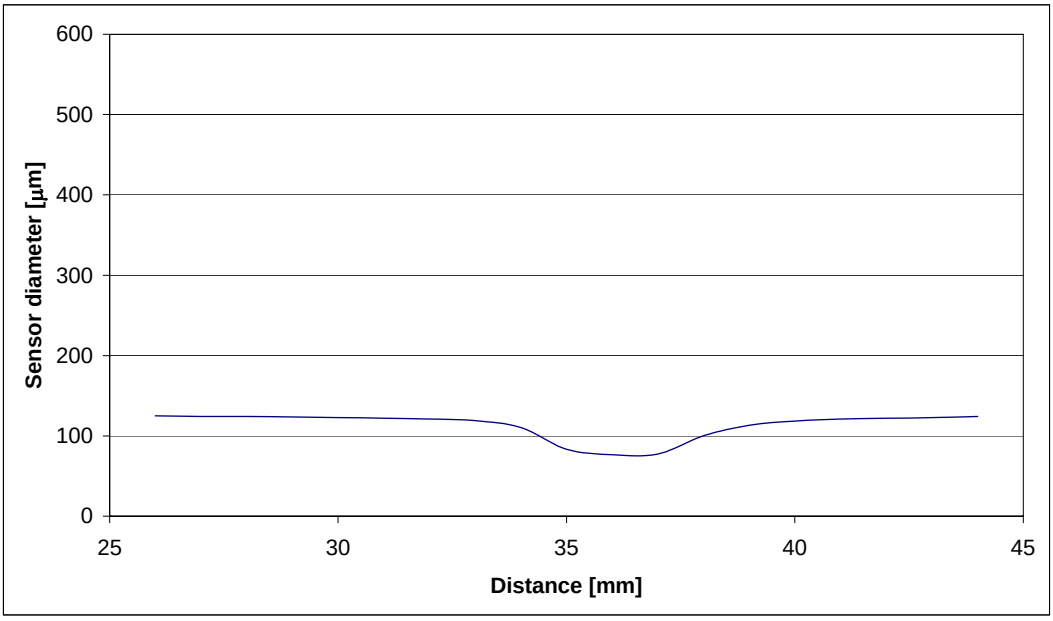

Figure 6-25: Tapering profile of fibre diameter between the two bond points on the coupon.

The minimum fibre diameter was 76.5 µm, which corresponds to the fusion-spliced region of the sensor. From the tapered profile it was determined that the fibre diameter was a minimum in the fusion-spliced region and therefore the strain on the fibre due to a longitudinal force will act at the fusion spliced region of the sensor. Irrespective of the cavity length the tapering profile will be similar to that shown in Figure 6-25, in particular, the diameter in the fusion-spliced region will be smaller for sensors with a larger cavity length as they are produced using fibres etched for longer duration.

6.1.7.2 Demonstration of cavity gap change with applied load

During the tensile testing of coupons with surface-mounted IFFP sensors, the cavity gap length will increase with the applied load and must regain its initial cavity length when the load is removed. The response of the intrinsic interferometer with a 44 μm cavity length as a function of applied load is shown in Figure 6-26.

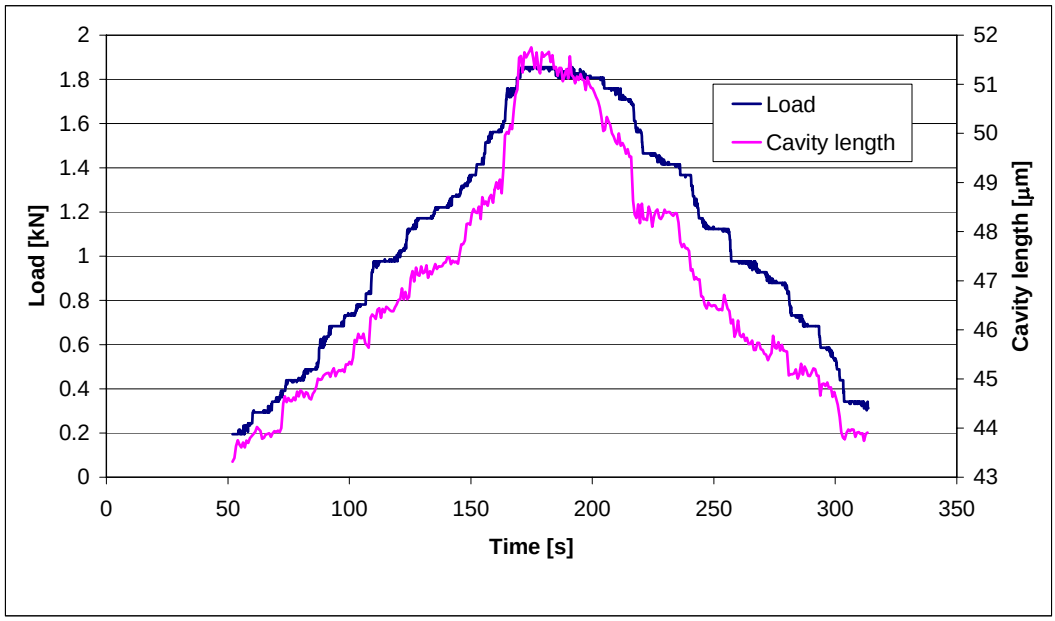

Figure 6-26: Response of a 44 mm gap length intrinsic FP sensor to an applied load varying from 0-2-0 kN.

This test was repeated again to establish its performance with external loading. This response is shown in Figure 6-27. From Figure 6-26, the cavity length increased by approximately 7 μm for a load of 1.8 kN. From Figure 6-27, the cavity length increased by approximately 6 μm for a load of 1.7 kN. In both tests, the changes in cavity length showed a good linearity with loading. This is obvious from the plots of cavity length versus load during increasing and decreasing load as shown in Figure 6-28 and Figure 6-29 respectively. The plots of Figure 6-28 and Figure 6-29 correspond to the response of the sensor shown in Figure 6-27. The sensor regained its original cavity length after being removed from the tensile machine. These tensile tests were carried out using a servo-hydraulic machine. The data presented in Figure 6-26 and Figure 6-27 illustrate the fact that at low applied loads, the vibrations and fluctuations caused by the hydraulic system are readily apparent.

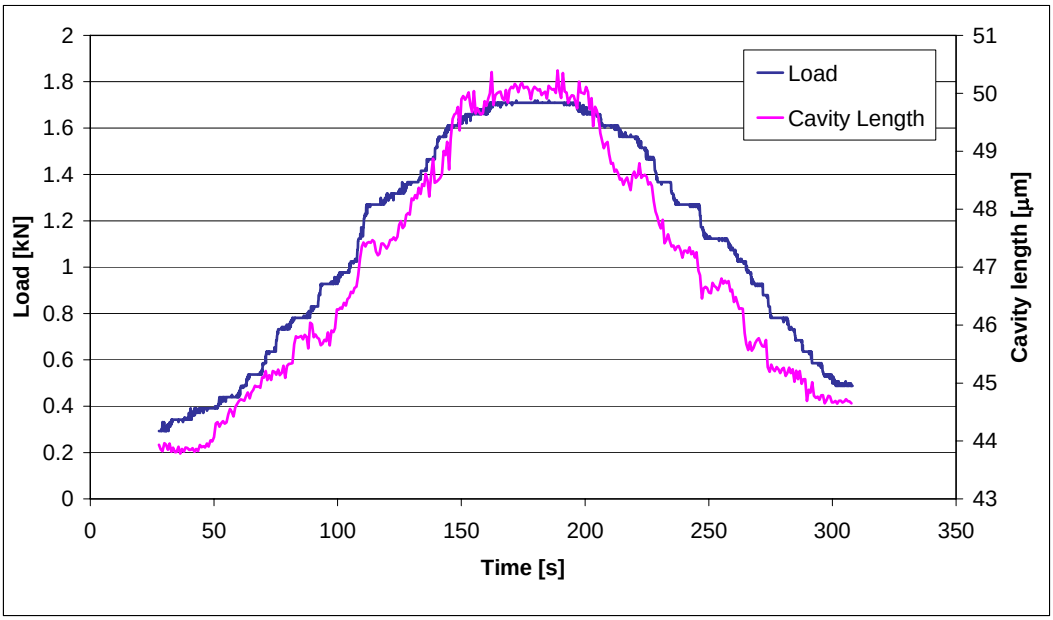

Figure 6-27: Response of a 44 mm gap length intrinsic FP sensor to an applied external load varying from 0-2-0 kN.

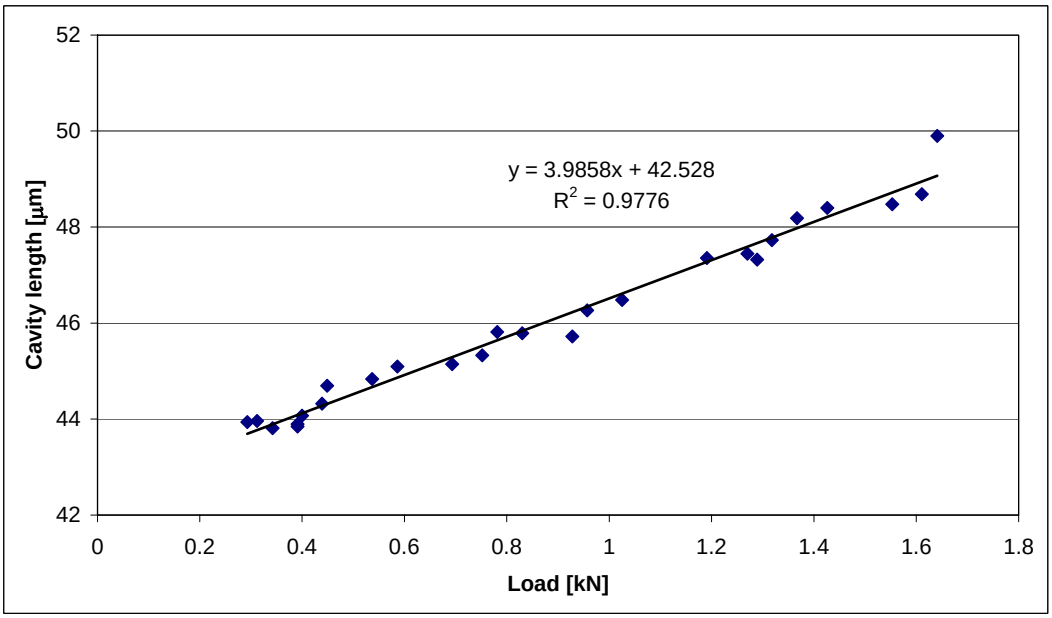

Figure 6-28: Variation of cavity length with increasing load.

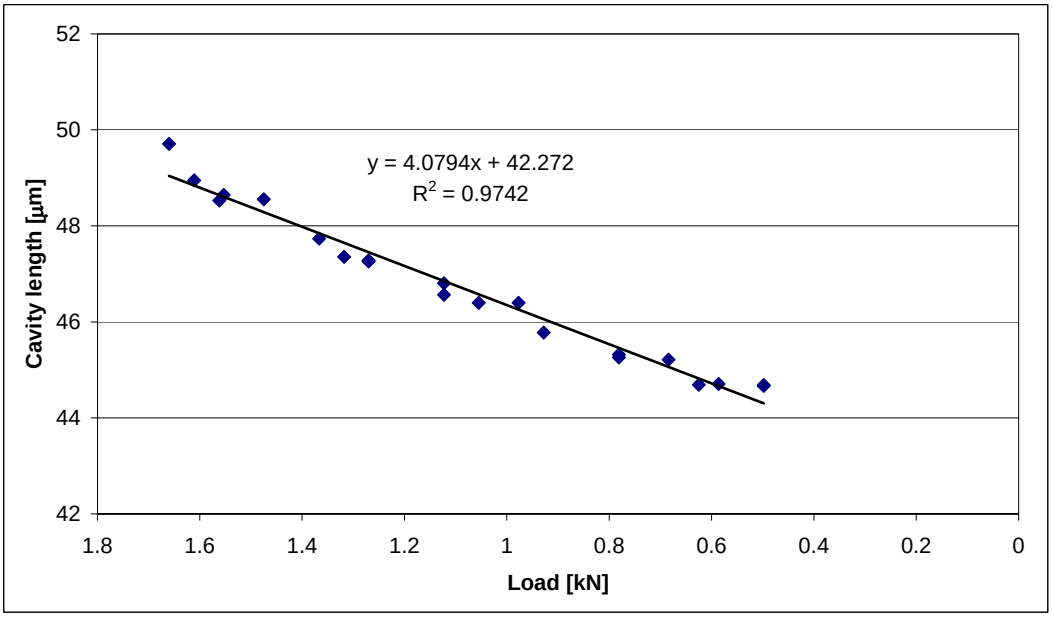

Figure 6-29: Variation of cavity length with decreasing load.

6.1.7.3 Tension-tension fatigue tests

During the triangular waveform loading, the cavity length of the sensor at zero strain was 35.3 μm. For a strain of 1000 με, the gap change increased by 1.8 μm. The change in the cavity length was linear with the applied strain when a triangular waveform loading was used. However, this linear variation of cavity length was only observed over 13 oscillations. The response of the sensor to a loading cycle of 1.5 – 3 – 1.5 – 0 – 1.5 kN at 0.05 Hz during the first 13 cycles is presented in Figure 6-30.

The difference between the maximum and minimum values of the cavity length was proportional to the difference between the maximum and minimum values of the strain during the period of the first 13 cycles. This is shown in Figure 6-31.

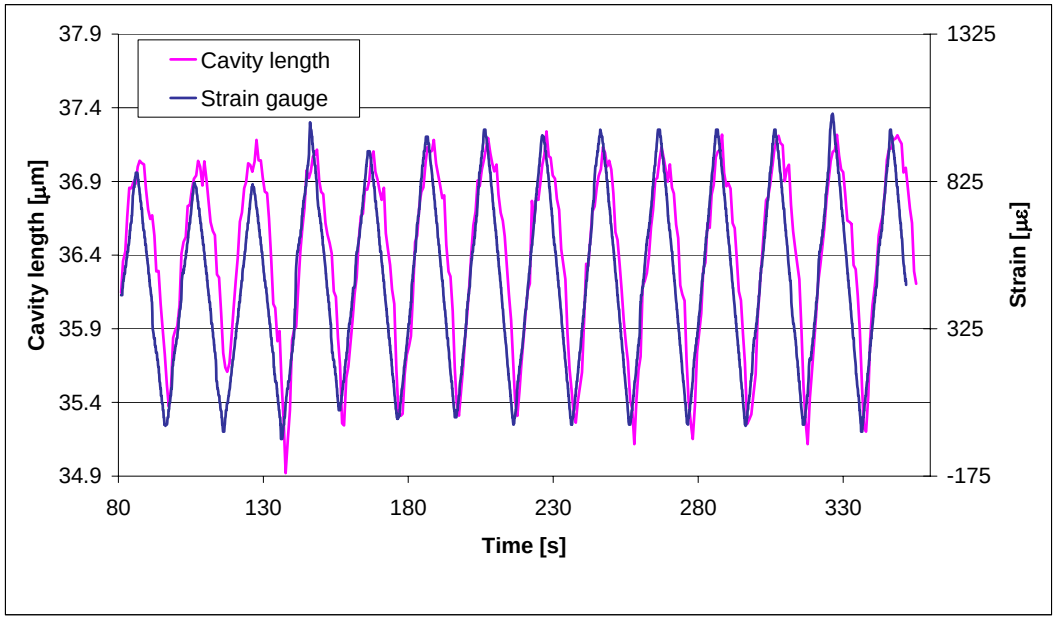

Figure 6-30: Response of an intrinsic FP sensor to a load cycle of 1.5-3-1.5-0-1.5 kN at a frequency of 0.05 Hz.

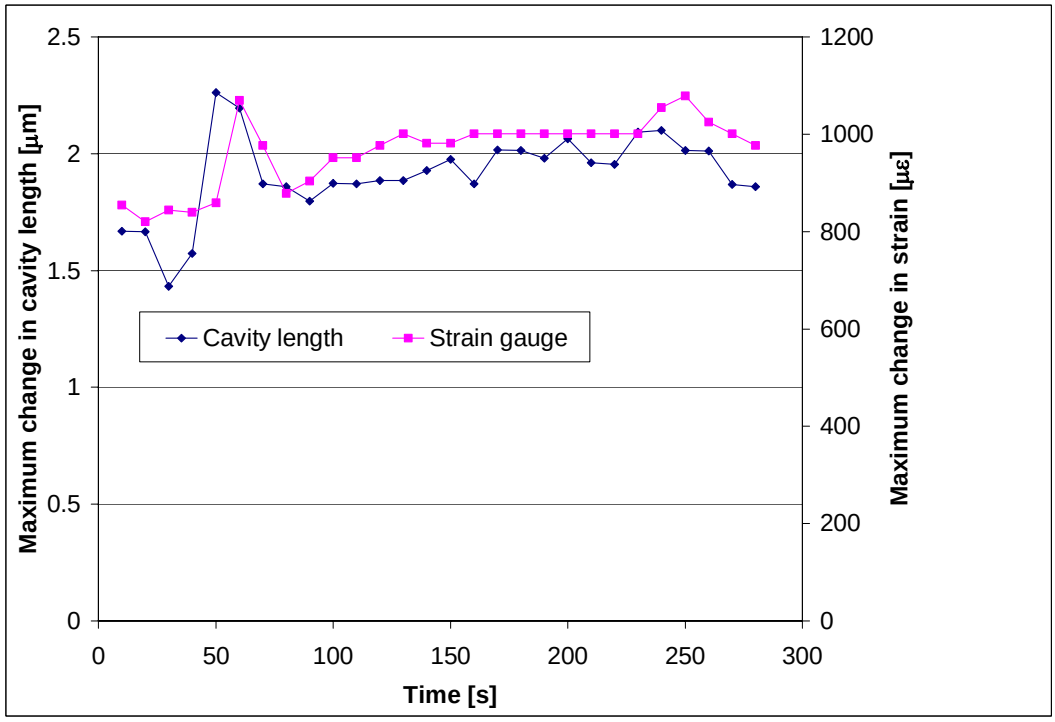

Figure 6-31: Linearity of maximum cavity length change with the maximum strain change during the first 13 cycles.

With an increase in the number of cycles, the difference between the maximum and minimum values of the cavity length (maximum change in cavity length) gradually

decreased. After the execution of 150 cycles of the waveform, the maximum change of cavity length was found to be 0.99 μm for a maximum change of strain of 1000 με. This is 0.8 μm smaller than the maximum cavity length change that was measured during the first 13 cycles. In principle, the maximum change in cavity length should be linearly proportional to the maximum change in strain. The change in strain is fairly constant during the entire fatigue test. The reduction of maximum cavity length change during different times of the fatigue test is plotted in Figure 6-32, Figure 6-33 and Figure 6-34.

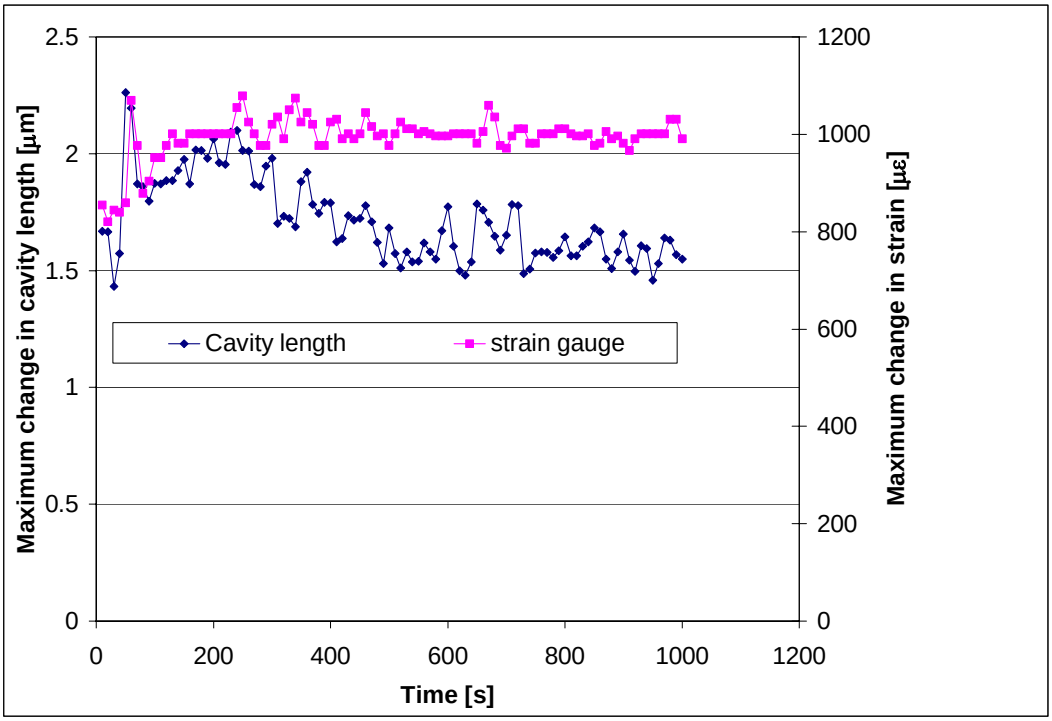

Figure 6-32: Decreasing maximum change of cavity length during first 1000 s of fatigue test.

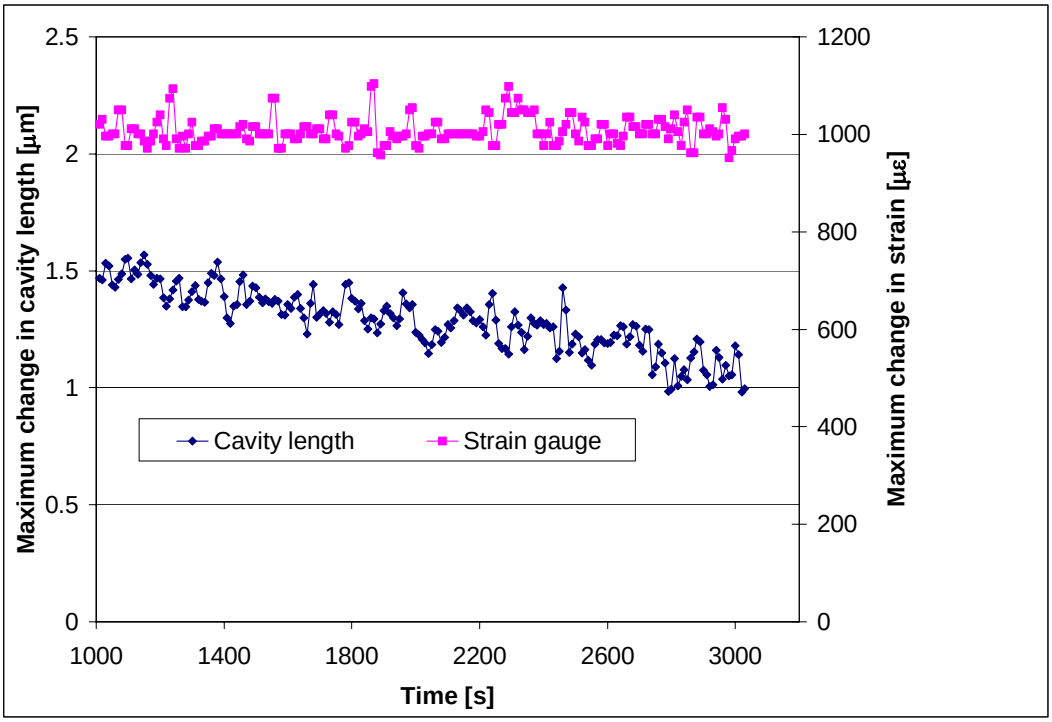

Figure 6-33: Decreasing maximum change of cavity length during 1000 to 3000 s.

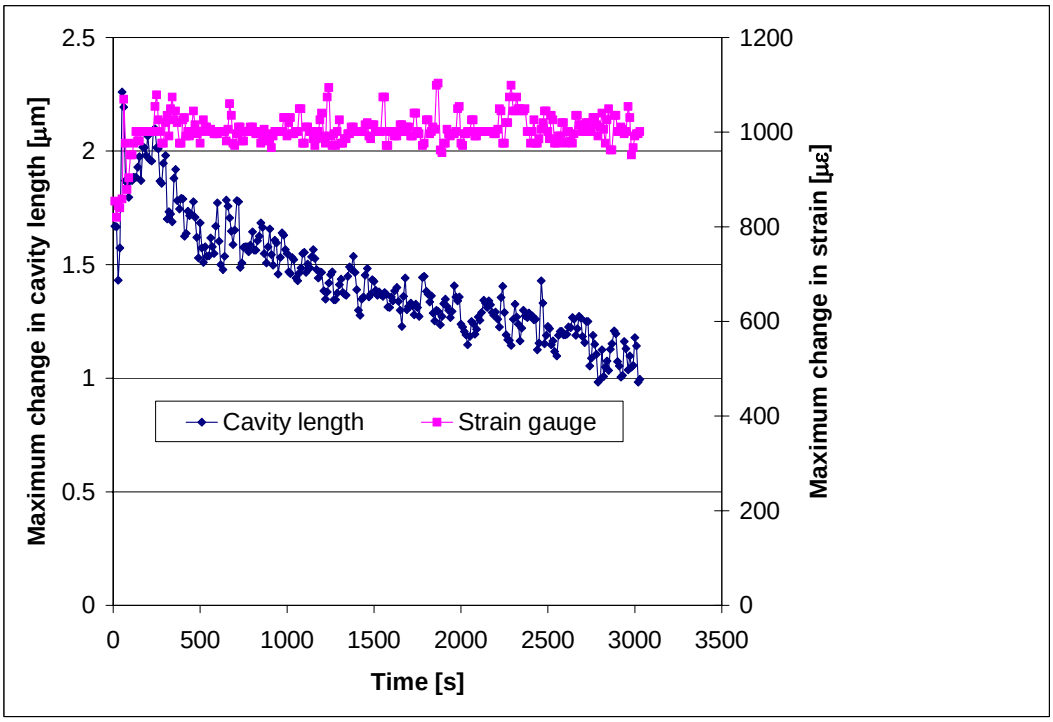

Figure 6-34: Variation of maximum change of cavity length over the entire duration of fatigue test.

However, the zero-load cavity length of the sensor was unchanged from its value prior to the fatigue test. The sensor was observed under an optical microscope after the fatigue test and no de-bonding of the fusion spliced ends was observed. However, a

crack was observed at one of the bonded regions of the sensor to the coupon. No crack formation was observed on the adhesive at the other bond point. The cracked bond towards the coupon surface was observed under a binocular microscope. The cracked bond is shown in Figure 6-35. The reason for the reduction in the change of the cavity length was due to gradual weakening of this bond between the sensor and the coupon surface, which in turn deteriorated the strain transfer from the coupon to the sensor.

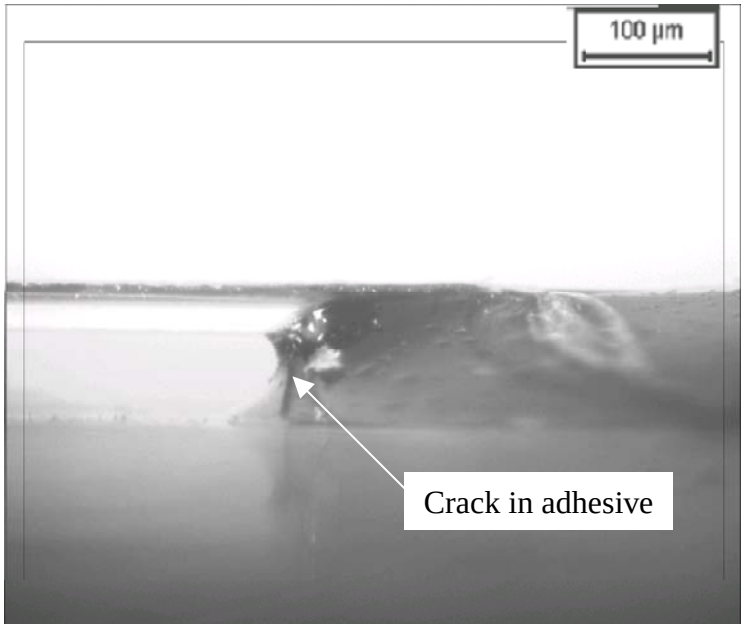

Figure 6-35: Optical micrograph showing a crack in the adhesive bonding after the fatigue test.

The gradual decrease in maximum change of the cavity length after 13 cycles could be due to initiation of crack in the adhesive. With an increasing number of cycles, the crack could have propagated further into the adhesive and thereby weakened the bonding to the coupon. This gradual weakening of bonding could have gradually reduced the strain transferred to the sensor and hence a smaller maximum cavity length change was observed. The sensor regained its initial cavity length after the coupon was removed from the fatigue machine.

The response of another sensor to a fatigue test with the same waveform as that used in the earlier fatigue test is shown in Figure 6-36. This test was carried at a frequency of 0.016 Hz. The cavity length changes were linear with the strain variations

measured by a foil strain gauge. This linearity of response of the sensor was observed for both the tension-tension fatigue tests. This indicates that these intrinsic FP-sensors could be used for fatigue monitoring of composite materials as long as the adhesive bonding between the sensor and the coupon is not weakened. The plots of cavity length versus strain during increasing strain (time: 345s-373s) and decreasing strain (373-403 s) are presented in Figure 6-36 and Figure 6-37 respectively. The linear response of the sensor to the applied strain is obvious from Figure 6-37 and Figure 6-38.

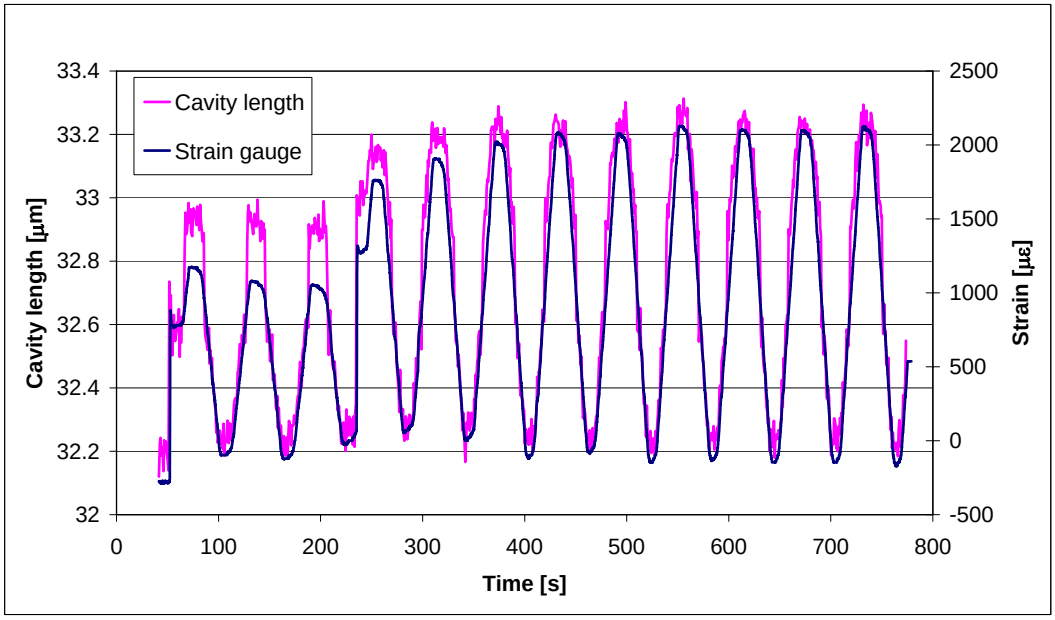

Figure 6-36: Response of intrinsic FP sensor to fatigue test [1.5-3-1.5-0-1.5 kN] at a frequency of 0.016 Hz.

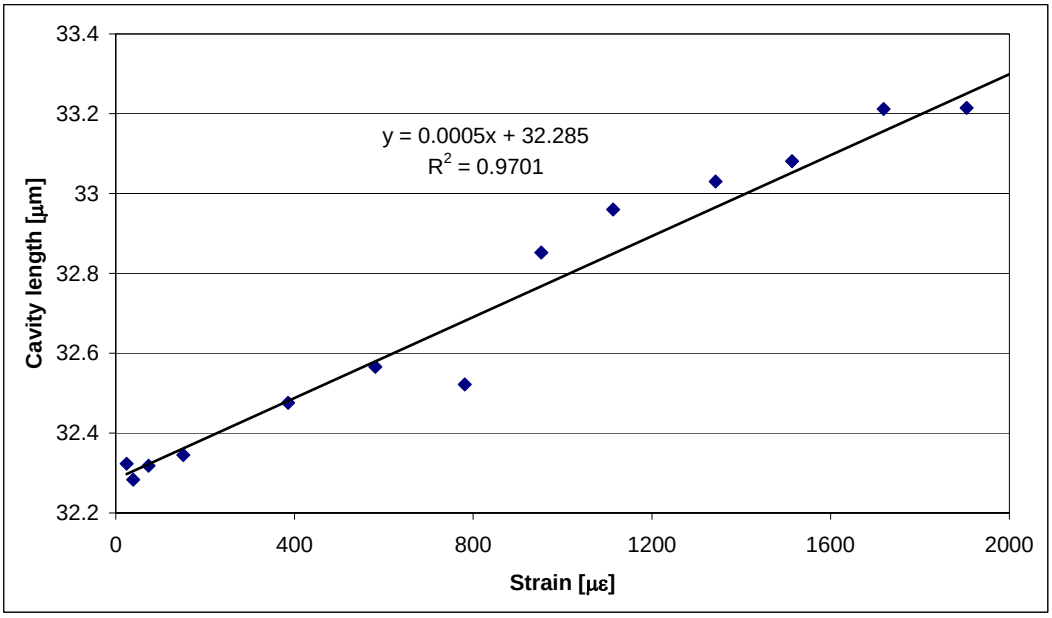

Figure 6-37: Variation of cavity length with increasing strain.

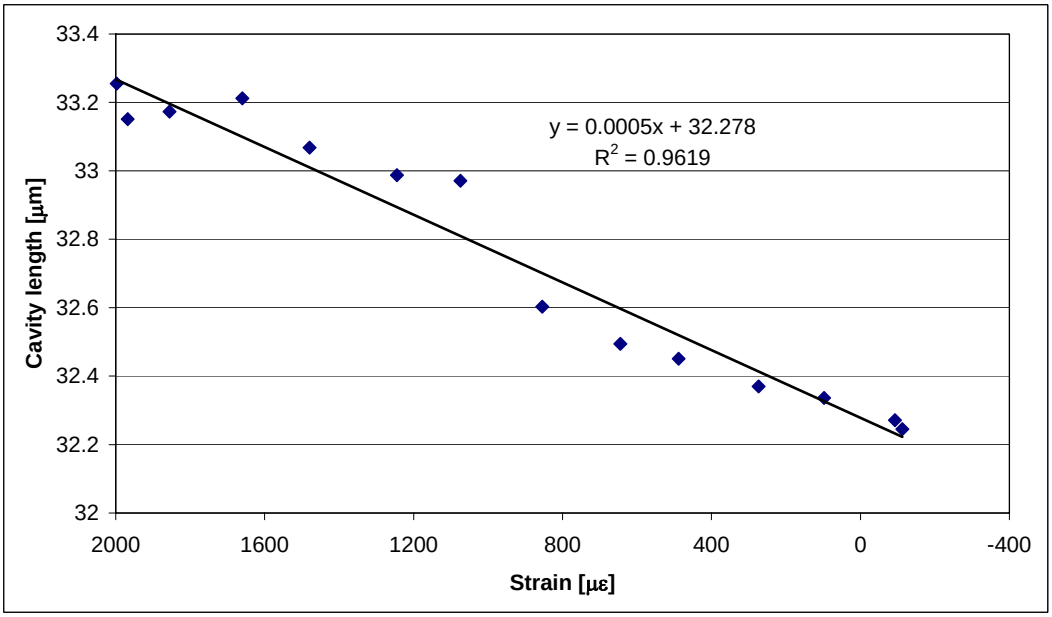

Figure 6-38: Variation of cavity length with decreasing strain.

A greater change in cavity length was observed in sensors with a larger cavity length for a given applied load. For example, the cavity length change in a sensor with a cavity length of 44 µm is 7 µm for a load of 1.8 kN as shown in Figure 6-26, whereas a cavity length change of 1.1 µm was observed for a load of 1.5 kN as shown in Figure 6-36, although the sensors were mounted on composite coupons of the same dimensions and the of same material. The sensors with a larger cavity length were

produced by using fibres etched for a longer period of time than those of the shorter cavity length. It was determined that with a longer etch time a smaller thickness of the cladding remained after etching. This is obvious from Figure 6-8 and Figure 6-9. From Figure 6-25, the sensor has a minimum diameter at the fusion-spliced region and therefore the strain on the fibre acts at that point. As the cladding thickness decreases with etching time, the sensors of larger cavity length will have a smaller contact surface area at the fusion-spliced region. Therefore, the strain on the sensor of larger cavity length will be higher than that of a smaller cavity length sensor for the same applied load. Therefore, the sensitivity of these sensors could be controlled by varying the etch-time.

6.1.8 Summary of Chemical Etching

A low cost fabrication technique for the production of intrinsic Fabry-Perot sensors based on hydrofluoric acid etching was developed. This technique basically involves etching of optical fibres, cleaning and fusion splicing. Cavities of repeatable gap length could be produced by controlling the etching time, temperature and concentration of acid. The optical quality of cavities produced is adequate to produce FP interference. Surface tension of the acid with the cylindrical glass surface of the fibre produces gradual tapering along the immersed length of the fibre. Controlled fusion splicing of etched fibres produces intrinsic FP cavities in optical fibres.

Unlike EFFPI sensors, the acid-etched IFFPIs have a well-defined fusion spliced point at the etched fibre-ends; the cavity lengths are repeatable; the sensors have a cavity length same as the gauge length and do not require independent calibration prior to use; the sensors do not have an abrupt change of geometric dimensions along their length and this could reduce the problem of void formation around the sensor in embedded applications; the size of the sensors is significantly reduced as the sensor design does not involve a glass capillary; the material costs involved in fabrication are low.

The cavity length changes of these sensors are repeatable and the tensile and fatigue tests showed an excellent linearity of cavity length changes with the strain measured

by the electrical resistance strain gauges. Therefore a low cost fabrication technique for strain sensors is demonstrated.

6.1.9 Novelty of this Chapter

The etched end-faces of SM 800 fibres were successfully fusion-spliced by controlling the fusion parameters to yield intrinsic Fabry-Perot interferometers. Tuck and Fernando [133] demonstrated this technique of fabricating intrinsic FP sensors for strain sensing. As advancement to the first studies of Tuck and Fernando [133], the author has fabricated intrinsic fibre FPs of repeatable gap length and investigated their response under harsh environments. The tension-tension fatigue tests have shown excellent linearity of cavity length changes with respect to the applied strain and load. The sensors have survived several tens of cycles of fatigue and their initial cavity lengths were retrieved after unloading the specimens. The author has experienced the problem of adhesive cracking, which has affected the response of the sensor. Therefore, further investigations are required to study the response of these sensors by using suitable adhesives, which can withstand fatigue of specimen. This fabrication technique overcomes the problem of gauge length measurement. The cavity gap length is same as the gauge length. However, it is difficult to fabricate sensors of cavity length above 45 μm using this technique. It is difficult to fusion splice fibres etched for more than 22 minutes without compromising the fusion joint. Therefore, masking techniques need to be developed to protect the cladding thickness from being etched by the acid. In comparison to conventional EFFPI design and manual fabrication, this technique offers low cost fabrication, repeatable cavity lengths, overcomes gauge length measurements and reduction in the size and discontinuity of sensor geometry.

7 Beam Transmission Experiments

7.1 Introduction

Following the experimental methods described in Section 5.4, the results are presented and discussed in this chapter. The influence of purging the beam delivery chamber using dry N_2 gas and the influence of flow rate of the purge gas on the beam transmission are presented and discussed. The results of the influence of the purge gas flow rate reduction on the beam transmission and beam transmission through a specified mask feature are presented and discussed. Finally, an estimation of energy densities at the image plane that can be produced for a specified flow rate and mask feature taking the losses due to optical elements and the beam path length into account was presented.

7.1.1 Results of Purge Gas Flow Rate Experiments

The positive pressure of the purge gas creates a pressure differential across the vent orifice and causes the flow of gas inside the tunnel. The concentration of the contaminants such as atmospheric oxygen, water vapour and hydrocarbon particles gradually decreases with the time of purging [117]. In the experiment, where a flow rate of 25 litre minute^{-1} was applied, the laser pulse energy was not detected until 6 minutes of purging. This indicates that the contaminant concentration inside the chamber at that time fully attenuated the pulse energy before it reached the detector head. After 9 minutes, 2.4 % of the energy was detected. Then the transmission increased rapidly until 21 minutes and reached a plateau region, where the increase in transmission was slow. The rate of energy transmission during different times of purging were obtained using a linear fit to the corresponding percentage transmission values and is presented in Table 7-1.

Table 7-1: Rate of percentage transmission during different times of purging at a flow rate of 25 litre minute^{-1}.

Time of purging	Rate of transmission [minute^{-1}]
12th to 21st minute	1.48 %
24th to 33rd minute	0.18 %
34th to 45th minute	0.13 % (plateau region)

A maximum of 42.92 % of the pulse energy of 25 mJ, which is 10.73 mJ, was transmitted after 45 minutes of purging. The plot of percentage transmission versus purging time at a flow rate of 25 litre minute^{-1} is shown in Figure 7-1.

In the experiment where a flow rate of 35 litre minute^{-1} was applied, no transmission was observed after 3 minutes of purging. The plot of percentage transmission versus purging time at a flow rate of 35 litre minute^{-1} is shown in Figure 7-2. After 6 minutes, a rapid increase of transmission to 24.92 % was observed.

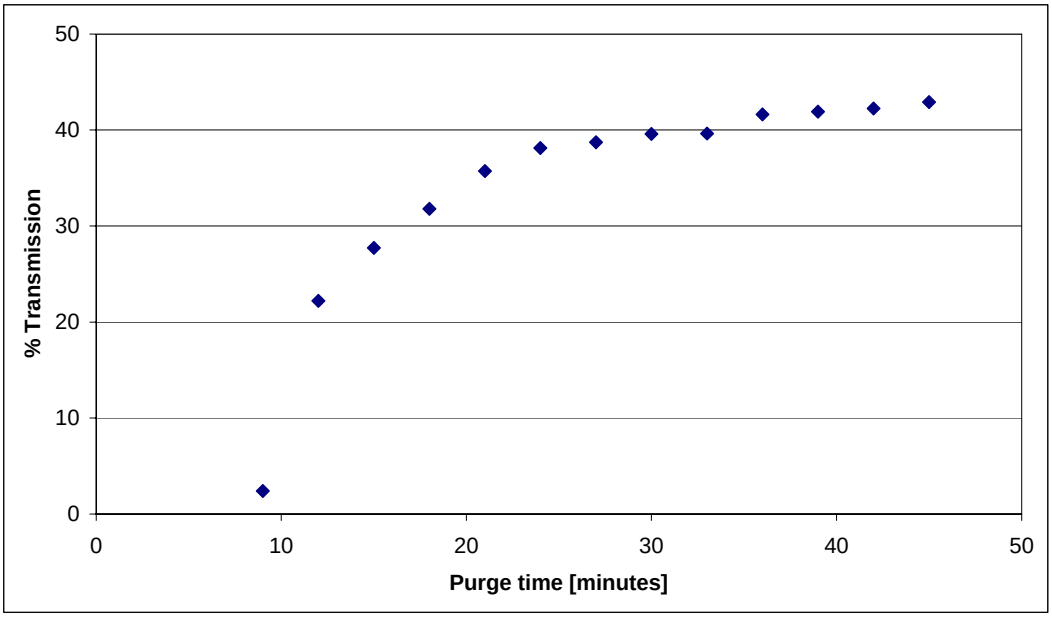

Figure 7-1: Plot of percentage transmission of pulse energy against purging time at a N_2 flow rate of 25 litre minute^{-1}.

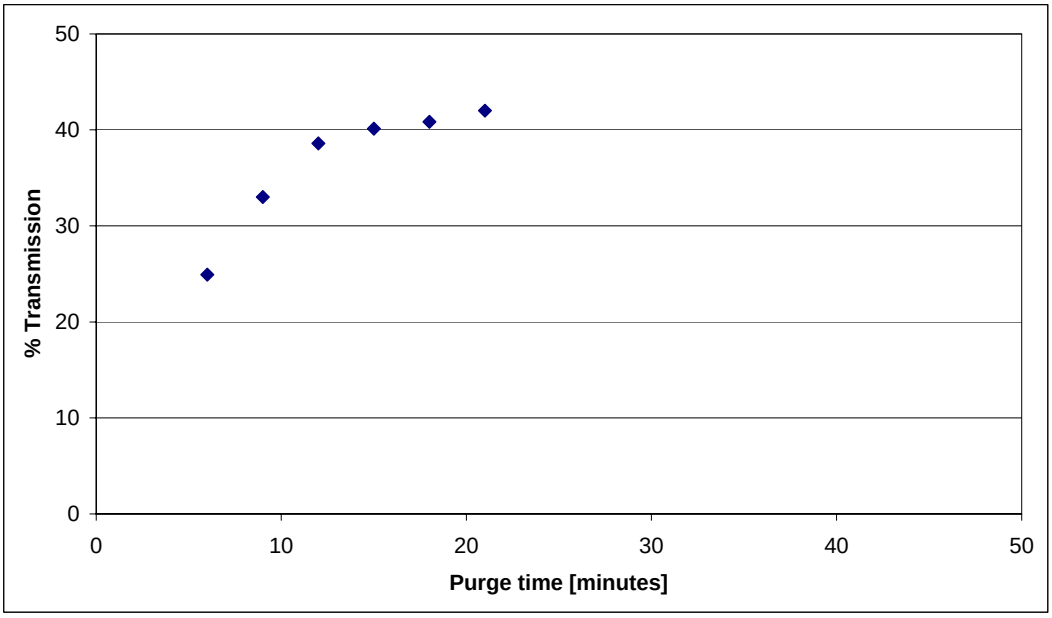

Figure 7-2: Plot of percentage transmission of pulse energy Vs purging time at a N_2 flow rate of 35 litre minute^{-1}.

The rate of energy transmission during different times of purging were obtained using a linear fit to the corresponding percentage transmission values and is presented in Table 7-2.

Table 7-2: Rate of percentage transmission during different times of purging at a flow rate of 35 litre minute^{-1}.

Time of purging	**Rate of transmission [minute^{-1}]**
6th to 12th minute	2.28 %
15th to 21st minute	0.31 % (plateau region)

The transmission reached a plateau region after 12 minutes of purging. A maximum transmission of 42% of pulse energy of 25 mJ, which is 10.5 mJ, was obtained after 21 minutes of purging. From Figure 7-1 and Figure 7-2, it can be observed that the energy was detected at a shorter time of purging at when a higher flow rate was used. The rate at which the transmission increased to reach the plateau was also higher at a higher flow rate. At a flow rate of 35 litre minute^{-1}, the transmission increased at a rate of 2.28% minute^{-1}, whereas it was 1.48% minute^{-1} at 25 litre minute^{-1}.

The transmission was also higher at a higher flow rate for the same time of purging. A transmission of 42% was obtained at 35 litre minute^{-1} after 21 minutes of purging, whereas it was 35.72% at 25 litre minute^{-1}.

The pressure differential across the vent orifice will be higher at a higher flow rate. This produces a higher flow velocity of contaminant air along with the purge gas across the vent orifice. Therefore, the contamination inside the chamber is sent out of the chamber at a faster rate, which results in a faster transmission rate at a higher flow rate.

As presented in Section 2.8.6.2, the oxygen concentration has to be less than 4 ppm to achieve a transmission greater than 70% [102]. The concentration of dry nitrogen purge gas used for these experiments has a purity of 99.998% (manufacturer's data), which corresponds to 20 ppm oxygen concentration. Therefore it was not possible to achieve a 70% transmission with the purge gas used for these experiments. However, the transmission could be improved further by using high purity inert gas argon. The plateau region of Figure 7-1 and Figure 7-2 could be explained in the following manner. When the concentration of oxygen inside the chamber approaches the value of concentration of oxygen in the dry nitrogen gas, the rate of transmission drops and reaches a plateau region. From Figure 7-1, it can also be observed that the rate of transmission was 0.18% minute^{-1} from the 24th to 33rd minute and it was 0.13% minute^{-1} during the last 9 minutes of transmission. This gradual stabilization in transmission could be due to the oxygen concentration approaching 20 ppm. However, the concentration levels of oxygen could not be quantified in these experiments due to the lack of access to high sensitive oxygen detectors. The plateau appeared faster at a higher flow rate due to a faster reduction in the concentration of contaminants.

In comparison to results presented by other researchers in Section 2.8.6.2, the volume of the purge gas used for these experiments was significantly higher. This could due to the fact that volume of the purge gas required to produce a transmission level over a certain path length of the beam depends on the volume enclosing the beam path. The higher the cross-sectional area of the tunnel, the larger the volume of the purge gas required to achieve a transmission level over a specified beam path length.

If the losses at the two high reflectivity mirrors, which is 4%, is neglected, a transmission of ~45% was produced over a beam path length of 3.3 m in both these experiments. This accounts for a loss of 16.6% per metre. The results of these experiments are summarised for a 40% beam transmission in Table 7-3.

In these experiments, when the flow rate of the gas was reduced to 10 litre minute^{-1} after 18 minutes of purging at 35 litre minute^{-1}, the energy transmission decreased gradually after 18 minutes and reached 29.9% after 27 minutes. From the 27th to 45th minute, i.e., over a period of 18 minutes a stabilised mean transmission of 29.23% with a standard deviation of ± 0.757% was obtained. Then the energy started to increase gradually after 45 minutes and reached 33.9% after 54 minutes. The plot of purging time versus percentage transmission is shown in Figure 7-3.

Table 7-3: Summary of influence of flow rate of dry N_2 on 157 nm beam transmission with a 2.6 mm vent orifice diameter.

Flow rate of gas [litre minute^{-1}]	Purging time [minutes]	Volume of gas [litres]	% Transmission over a path length of 3.3 m
25	33	825	~40%
35	15	525	~40%

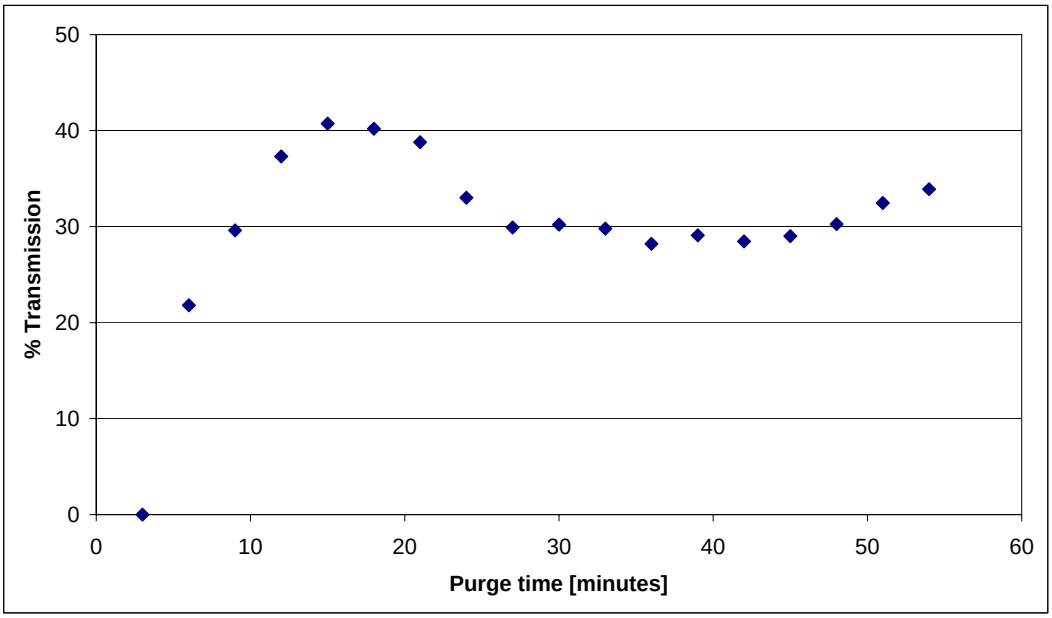

Figure 7-3: Plot showing the effect of reducing the flow rate from 35 to 10 litre minute^{-1}.

When the flow rate of the gas was reduced to 10 litre minute^{-1}, the pressure differential across the vent orifice decreases and in turn reduces the flow velocity of gas through the vent. The infiltration of contaminant particles through the vent orifice depends on the efflux velocity [119]. The reduction in transmission due to the reduced flow rate could be explained in the following manner. The reduced flow velocity through the vent due to the reduced flow rate of the gas may not be enough to exert an equal and opposite drag force on particles infiltrating through the vent. This could be the reason for gradual drop in transmission. The stabilised transmission from the 27th to 45th minute in Figure 7-3 corresponds to the region, where the concentration of contaminants infiltrating into the chamber through the vent is that same as that expelled through the vent. This could be a reason for stabilisation of the transmission. When the concentration of expelled contamination exceeds the infiltrating concentration, the transmission starts to increase again. This can be observed from the 48th to 54th minute of Figure 7-3.

7.1.2 Beam Transmission through the Mask Feature

In this experiment, where the transmission through the mask feature of dimensions of 1.5 x 1.5 mm was measured according to the arrangement shown in Figure 5-7, a transmitted energy of 0.34 mJ was measured after 60 minutes of purging. The increase in transmitted energy with time is shown in Figure 7-4.

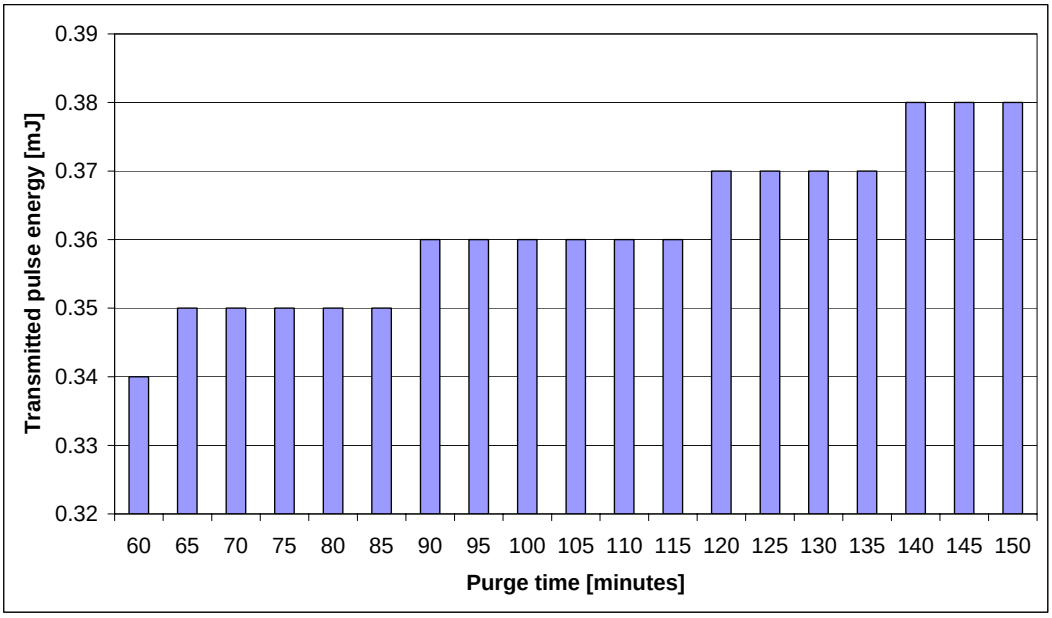

Figure 7-4: Column plot of purging time Vs transmitted pulse energy through the mask feature.

The transmitted energy remained constant at 0.35 mJ from the 65th to 85th minute. The transmitted energy increased in steps of 0.01 mJ and a maximum of 0.38 mJ was obtained after 150 minutes of purging. It can be inferred from the plot shown in Figure 7-4, that the transmitted energy remained constant over sufficiently long periods of time in which the micro-machining experiments can be carried out. Over a period of 90 minutes, a mean transmitted energy of 0.36 mJ with a standard deviation of ± 0.01 mJ was obtained.

7.1.3 Approximation of Energy densities at the Image Plane

The energy at the image plane cannot be measured exactly using the detector head, since the energy densities may cause damage to the pyroelectric detector head. Therefore, the energy density is approximated by considering the losses due to calcium fluoride lens elements of the objective and the working distance.

From the information provided in Section 5.2.3, if the transmission loss due to a 10 mm thick sample of the calcium fluoride is approximated to be 1%, then the loss due to a path length of 31 mm through the calcium fluoride is 3.1%. The total thickness of calcium fluoride elements in the objective is 31 mm (manufacturer's data), as

presented in Section 3.2. It was already determined that the transmission loss per metre is 16.6%. Therefore the loss due to 40 mm working distance will be 0.6%. Therefore the total loss due to calcium fluoride and working distance can be approximated to 4%.

Considering the estimated losses, the measured transmitted energies of 0.34, 0.35, 0.36, 0.37 and 0.38 mJ through the 1.5 x 1.5 mm mask feature as shown in Figure 5-9, when coupled through the imaging system will correspond to energy densities of 23.1 x 10^4, 23.8 x 10^4, 24.5 x 10^4, 25.2 x 10^4 and 25.9 x 10^4 Jm^{-2} respectively at the image plane of the 40X magnification objective. This mask feature will be reduced to the dimensions of 37.5 x 37.5 μm at the image plane. These energy densities are much higher than the ablation threshold of fused silica (1 x 10^4 Jm^{-2} at 157 nm) and sapphire (3.8 x 10^4 Jm^{-2} at 157 nm) [89]. This shows that the short beam tunnel coupled to the ablation chamber, which was used for micro-machining experiments, is capable of delivering adequate energy densities for ablating fused silica and sapphire substrates.

The energy transmitted through the mask feature used in these experiments was only a small fraction of the pulse-energy. For example, a maximum transmitted energy of 0.38 mJ through a 1.5 mm x 1.5 mm mask feature is 0.76% of the 50 mJ pulse-energy. A higher transmission of energy can be achieved by using a mask feature of larger dimensions. However, the effective energy density at the image plane will be correspondingly reduced. Therefore, the energy density at the image plane of a specified mask feature can be increased either by purging the beam line for a longer time or by using an imaging system of higher demagnification.

7.1.4 Summary of Beam Transmission Experiments

The experimental results prove that increasing the flow rate increases the rate of transmission. A loss of 16.6% of pulse energy per metre was observed with the 3.3 m long beam tunnel. Higher transmission rates could be achieved by using a purge gas of higher purity. Energy densities as high as 26 x 10^4 Jm^{-2} were achieved with the short beam tunnel. The designed short beam tunnel and the ablation chamber were

suitable for delivering adequate energy densities for micro-machining of fused silica and sapphire.

8 Ablation of Fused Silica and Sapphire Disks

8.1 Introduction

The results from the experiments carried out using the methods explained in Section 5.5, which is concerned with the ablation of fused silica and sapphire disks, are presented and discussed in this chapter. Firstly, the results and discussion of the ablation of fused silica disks are presented. In fused silica disk ablation, an evaluation of beam delivery optical system from the geometry of ablated structures, the influence of edge roughness and undulations of metal stencil mask on the ablated features, the SEM analysis of microstructures ablated at different energy densities and the interferometric surface profile analysis of ablated structures are presented. Secondly, the results and discussion of the ablation of sapphire disks are presented. The SEM and interferometric surface profile analysis of microstructures ablated at different energy densities are presented.

8.1.1 Ablation of Fused Silica Disks

The mask feature of dimensions of 1.5 x 1.5 mm was reduced to a 38 x 38 μm feature at the image plane. The shape of the mask feature was replicated to the required demagnification at the image plane. This demonstrated that the performance of the illumination design, target monitoring and alignment system was as desired. Optical micrographs of ablated structures on fused silica disk and the projected mask feature are shown in Figure 8-1 and Figure 8-2.

In Figure 8-1, some roughness of surface around ablated structures can be observed. A detailed analysis of roughness measurements will be presented in Section 8.1.1.2. This is caused by scattering of laser radiation around the rough edges of the projected mask feature. The scattered radiation, although it does not participate in the imaging, produces roughness on the surface around the ablated structure. The imaging objective images the mask features only to +1 and –1 orders of diffraction. The energy density of the scattered radiation is not sufficient to cause material ablation,

however, it produces surface roughness similar to the incubation phase as mentioned in Section 2.8.1. This roughness around the structure increases with the irradiation time and energy density of ablation. From Figure 8-1, it can be observed that the roughness around the structure ablated for 60 pulses is more pronounced than that of 20 pulses.

The roughness and undulations along the edge of the mask feature are shown in Figure 8-2 and Figure 8-3. A deviation from straightness along the edge of the mask feature shown in Figure 8-2 is a result of Nd-YAG laser cutting. The stainless steel metal substrate translates along the dimensions of the desired mask feature and reaches the point where it has started cutting the metal and this produces the deviation from straight edge. The effect of deviation from the straightness of the mask edge can be clearly observed along one of the edges of the ablated structures. To illustrate the contrast between the edge definition of the metal stencil mask and a chrome mask on the excimer grade fused silica substrate (used for 193 nm and 248 nm mask projection), an optical micrograph of the edge of the chrome (chromium) mask is presented in Figure 8-4. The sharpness of the edge definition of the chrome-mask can be observed from Figure 8-4.

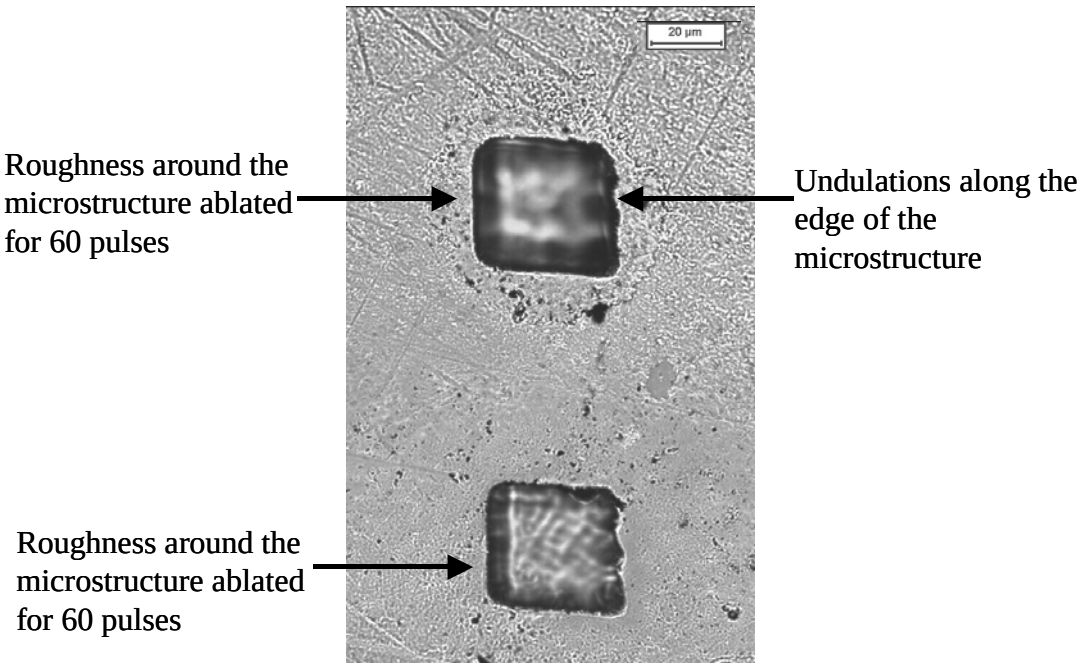

Figure 8-1: Optical micrograph of ablated structures on fused silica showing surface roughness.

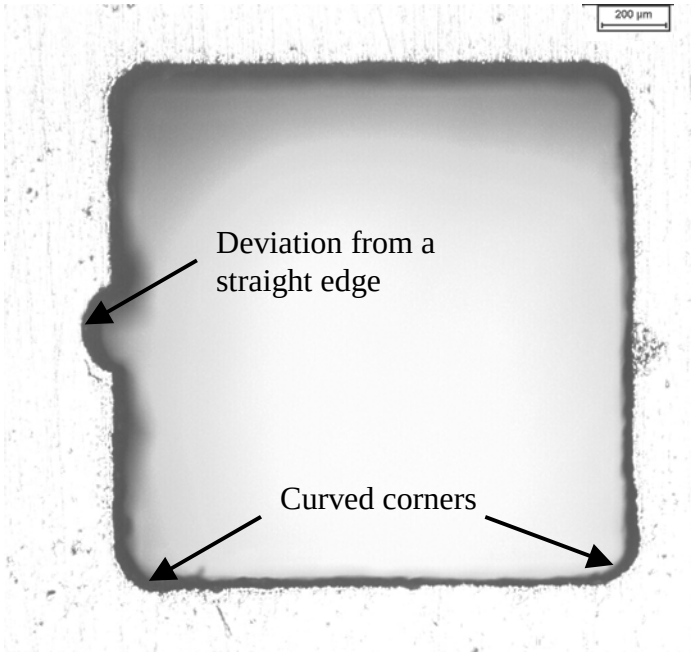

Figure 8-2: Optical micrograph of a 1.5 mm x 1.5 mm mask feature.

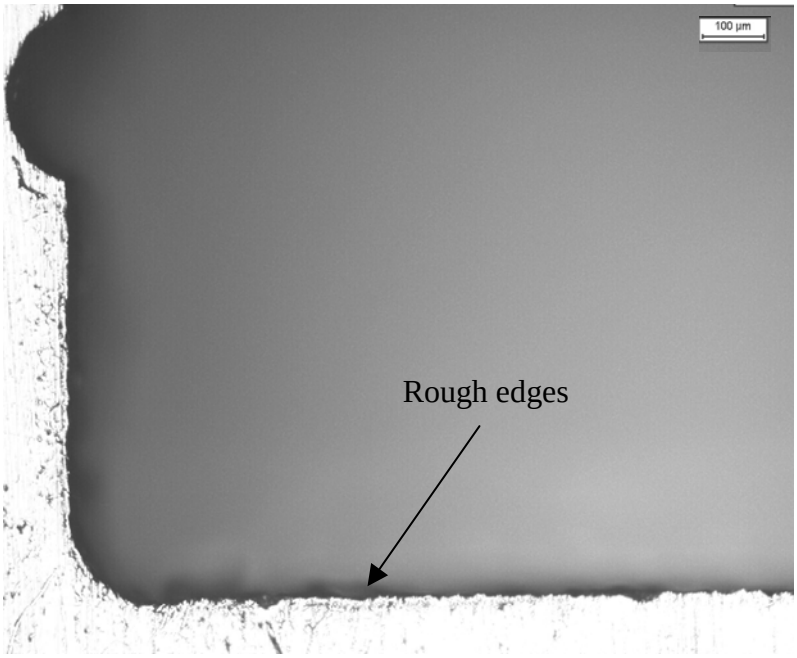

Figure 8-3: Optical micrograph showing undulations and roughness along the edge of a mask feature.

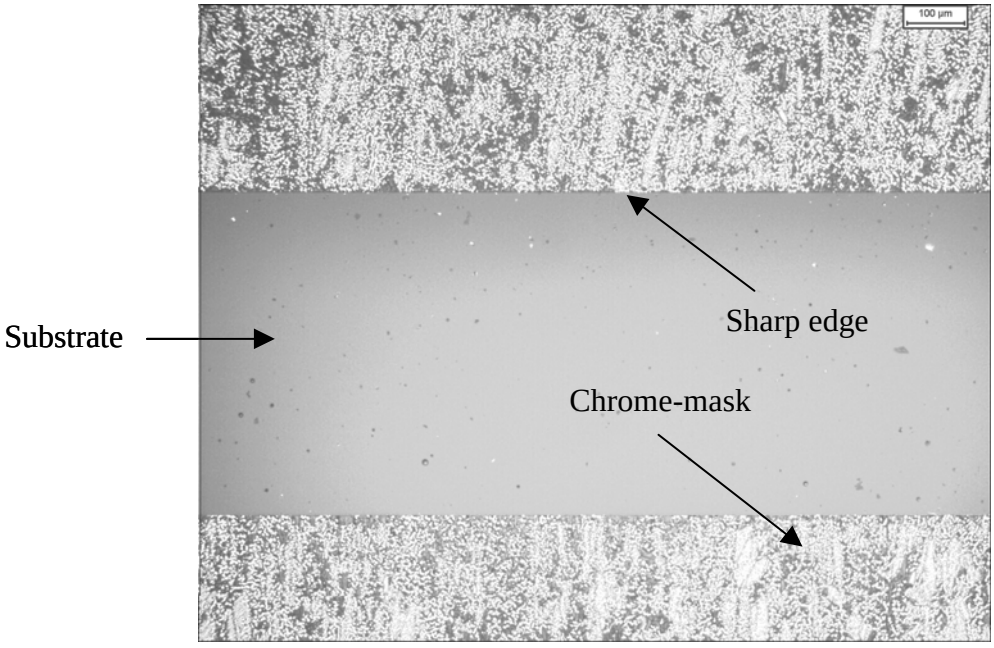

Figure 8-4: Optical micrograph of edges of a mask feature on chrome-mask.

From Figure 8-3 and Figure 8-4, it can be observed that the edges of the chrome-mask feature have a better straight edge definition than the edges of the metal stencil mask. The effect of undulations along the edge of the metal stencil on the cavity wall is presented at a later stage of discussion in Section 8.1.1.1. Unfortunately the author did not have access to a chrome-mask on a calcium fluoride substrate to use with the 157 nm mask projection. However, the optical micrograph of Figure 8-2 shows that only one edge of the structure has extensive deviations from the straight edge along its length and the other three are fairly straight. Therefore, the parallel edges of the metal stencil mask shown in Figure 8-2, which have no deviation from straight edges, could be used for producing etalons across the core of optical fibres. Therefore, the ablation experiments were carried out using the metal stencil mask.

8.1.1.1 SEM Study of Ablated Fused Silica Disks

Ablation at 7 x 10^{4} Jm^{-2} yielded microstructures with rough craters and wall surfaces. The debris deposition on the craters and wall surfaces was very obvious. There was no significant improvement in general morphology with increasing number of shots at this energy density. This can be seen from SEM micrographs presented in Figure 8-5 and Figure 8-6.

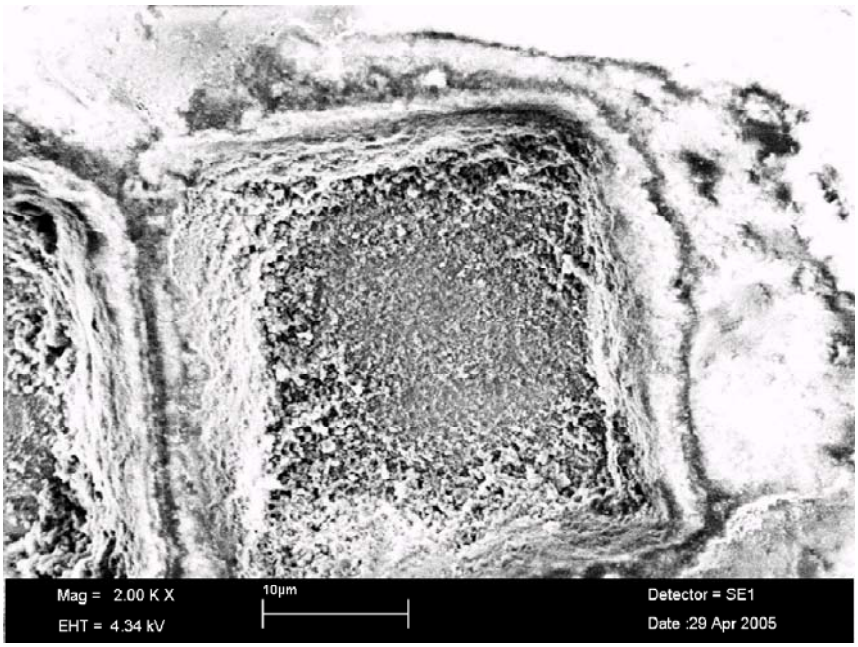

Figure 8-5: Fused silica disk ablated at 7 x 10^4 Jm^{-2} at 5 Hz for 60 pulses.

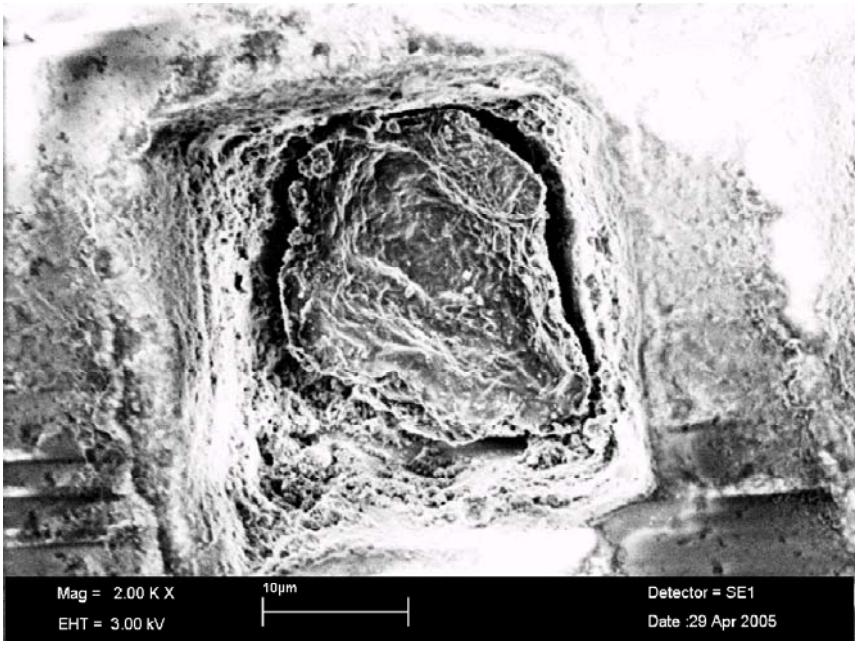

Figure 8-6: Fused silica disk ablated at 7 x 10^4 Jm^{-2} at 5 Hz for 160 pulses.

When the energy density was increased to 15.4 x 10^4 Jm^{-2}, the morphology of the ablated structure showed significant improvement in the formation of cavity walls and crater. This is obvious from the SEM micrograph of a microstructure ablated at 15.4 x 10^4 Jm^{-2} as shown in Figure 8-7. The sidewalls and crater surface were very obvious.

However, the ablation debris on the cavity walls and the crater surface was also obvious. A significant portion of the pulse duration of the laser beam is attenuated by the expanding plume, which attenuates the energy reaching the target surface [51]. This affects the ablation rate and also decreases the energy transferred to the ablated material and could result in re-deposition of ablated material [46]. The re-deposition of ablation debris could be higher with increasing ablation depth as the plume takes a longer time to expand out of the cavity, which results in attenuation of the longer duration of the temporal pulse energy. These experiments were carried out inside a chamber that was continuously flushed with dry-nitrogen. Therefore the effective pressure inside the chamber is higher than that outside the chamber. This higher gas pressure surrounding the ablation site could further hinder the expansion of the ablation plume. The hindrance in the expansion of the ablation plume was lower when the ablation was carried out in vacuum than that in a gas atmosphere [51].

In large band gap materials such as fused silica and sapphire, which are not as strongly absorbing as materials such as soda lime glass, at 157 nm, the debris deposition could be more pronounced. As mentioned in Section 2.8.6, the optical quality of ablated structures produced using 157 nm laser ablation was significantly higher than that at higher wavelengths such as 248 nm and 193 nm.

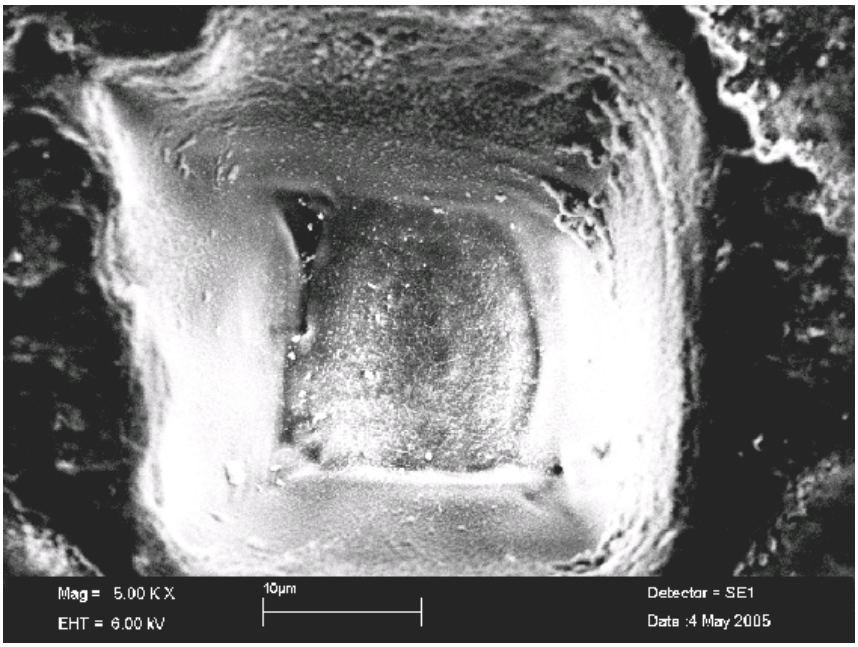

Figure 8-7: Fused silica disk ablated at 15.4 x 10^4 Jm^{-2} at 5 Hz for 160 pulses.

The most important criterion for the fabrication of Fabry-Perot microstructures is the optical quality of sidewalls and crater surfaces. The debris on the sidewalls and the crater surface deteriorates the smoothness of surfaces, which in turn reduces the surface reflectivity. The ablation debris scatters the incident light (visible light), depending on the size of the debris particles and the normal Fresnel reflection becomes diffused [46].

It can also be observed from Figure 8-7 that the crater area was smaller than the entrance of the cavity due to wall tapering. The quantitative data on crater areas is presented at a later stage of this discussion (Section 8.1.1.1). The tapering of cavities could be due to four main reasons.

i. Although the quality (or contrast) of an image is retained without unacceptable deterioration along the depth of focus of the imaging system, it loses its contrast as it moves away from the depth of focus as aberrations dominate the imagery. Therefore, the shape of the microstructure no longer represents the projected mask feature. This deviation from the required imagery produces cavity tapering.

ii. The intensity of the beam decreases as the target surface moves away from the depth of focus of the imaging system. This decrease in intensity lowers the ablation rate across the area of the beam. This effect combined with the aberrations of the optical system produces cavity tapering.

iii. The energy density reaching the target surface is attenuated continuously by the ablation plume as mentioned Section 2.8.2. The plume attenuation is very dominant in nanosecond pulsed laser ablation due to the long duration of pulse. The energy attenuation is also determined by plume expansion dynamics [51]. Therefore, the non-uniformity of attenuation of the pulse energy across the focussed spot produces non-uniform ablation resulting in cavity tapering.

iv. The non-uniform spatial intensity distribution across the image plane produces uneven ablation. This effect combined with the above three reasons could result in cavity tapering.

The tapering of cavity walls is an unwanted effect that reduces the contrast of Fabry-Perot (FP) fringes and may even lead to a loss of detectable interference by reducing the intensity of Fresnel reflections from the wall surfaces. If the etalon-forming walls of a cavity micro-machined through the diameter of the optical fibre depart from parallelism, the Fresnel reflection at the core/air interface increases. However, the resulting FP interference is determined by the direction of oblique Fresnel reflection at the air/core interface and the diameter of the core. A detailed analysis of the calculated Fresnel reflections for different taper angles of cavities through diameter of the optical fibres is presented in next chapter (Section 9.1.4).

The tapering of cavity walls can be reduced by increasing the energy density of ablation [92]. In order to study the affect of increasing pulse number and energy density on the general morphology and wall tapering of cavities, ablation was carried out at higher pulse numbers and energy densities. An SEM micrograph of a microstructure ablated at 15.4 x 10^4 Jm^{-2} for 300 pulses is shown in Figure 8-8.

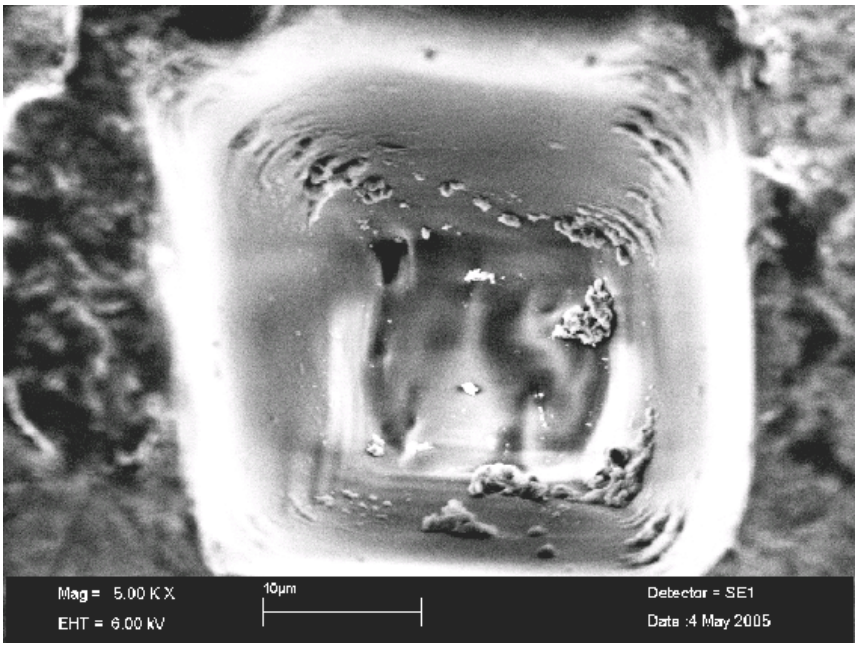

Figure 8-8: Fused silica disk ablated at 15.4 x 10^4 Jm^{-2} at 5 Hz for 300 pulses.

The smoothness of the cavity walls and the crater improved with an increase in the number of pulses. However, the ablation debris on the cavity walls was greater. As mentioned in Section 2.8.2.1, the lateral confinement of plasma is larger in higher aspect ratio cavities and it takes a longer time to expand out of the cavity. Therefore, the attenuation of the pulse energy will be greater, as the energy has to travel a longer distance through the plume to reach the target surface at a larger ablation depth. This obviously results in a lower ablation rate and re-deposition of ablated material.

It can also be observed that the debris deposition was larger along the corners of the cavity walls. This can be explained by edge-ringing as mentioned in Section 2.8.5.3. The higher intensity of the beam near the edges of the image plane causes a higher ablation rate that produces notches near the corners of the crater (see Figure 8-8). These notches are characteristic of edge-ringing, which in turn is a characteristic of highly coherent illumination. The higher ablation rate near the corners results in a higher deposition or condensation of ablation debris along the corners of the walls in higher aspect ratio cavities.

The improvement in smoothness of cavity walls and crater could be explained by two reasons. The layer of material remaining after the pulse could have enhanced absorption due to the colour centres and defects created on the surface. Enhanced absorption due to colour centre formation was reported by Dyer *et al.* [41] and Ihlemann *et al.* [39]. Therefore absorption and material ejection could be more efficient during the interaction with successive pulses. This reason can also be supported by the fact that 157 nm laser radiation produces strong photo-refractive index changes due to its high photon energy that encroaches on the energy band gap of fused silica via colour centres. The 157 nm laser-induced photosensitivity is presented in Section 2.8.6.1. The convexity of the crater surface decreases as the target surface is moved away from the image plane due to flattening of edge-ringing profile across the irradiated area [85]. This reduction in the amplitude of spurious ringing could reduce the uneven ablation across the irradiated area.

To study the effect of higher energy densities and number of pulses on debris deposition, microstructures were ablated at 23.1 x 10^4 Jm^{-2}. SEM micrographs

showing effect of higher energy density and number of pulses are shown in Figure 8-9 and Figure 8-10.

From Figure 8-9 and Figure 8-10, it can be observed that the increased energy density not only improved the smoothness of microstructures but also reduced the deposition of debris. However, the debris deposition again increased with the number of pulses and could not be avoided completely by increasing the energy density. This is obvious from Figure 8-10.

In order to study the effect of increasing energy density on structural morphology, fused silica was ablated at an energy density as high as 25 x 10^4 Jm^{-2}. A microstructure was also ablated at an energy density of 21.7 x 10^4 Jm^{-2} to compare with the microstructure ablated at an energy density of as high as 25 x 10^4 Jm^{-2}. An SEM micrograph of a structure ablated at 21.7 x 10^4 Jm^{-2} is presented in Figure 8-11. SEM micrographs of structures ablated at 24.5 x 10^4 Jm^{-2} are presented in Figure 8-12 and Figure 8-13. A significant improvement in general morphology was observed with increasing energy density. This can be observed by comparing Figure 8-11 and Figure 8-12.

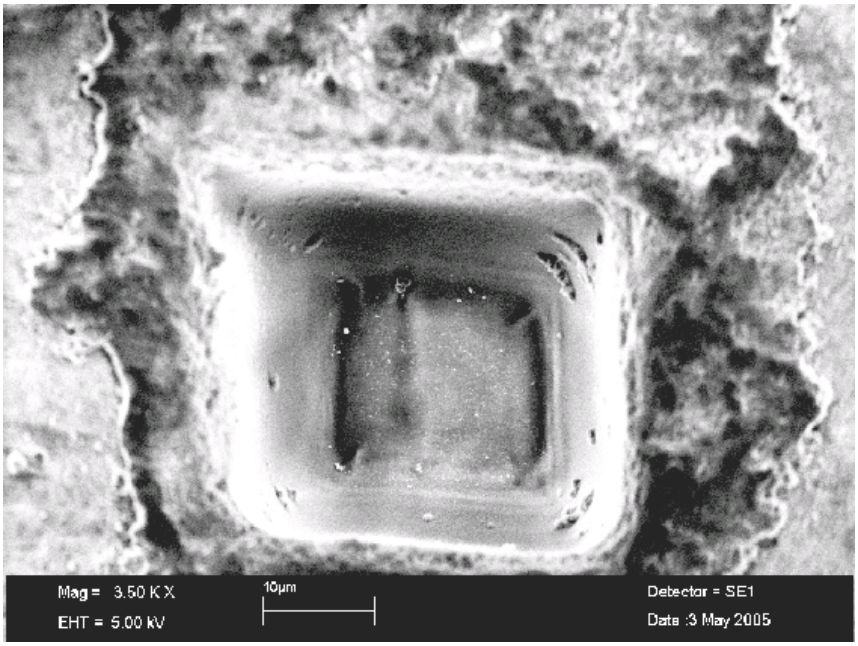

Figure 8-9: Fused silica disk ablated at 23.1 x 10^4 Jm^{-2} at 5 Hz for 260 pulses.

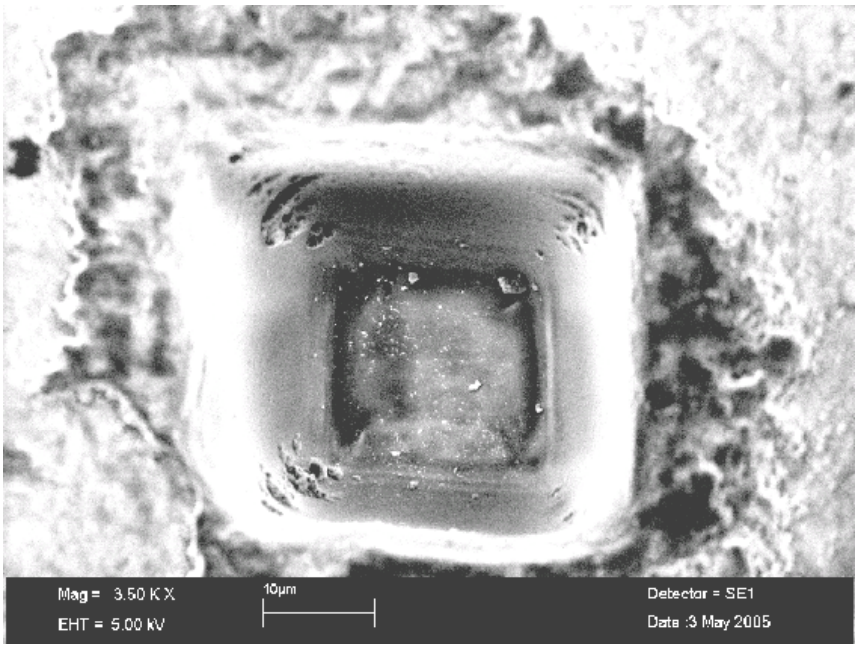

Figure 8-10: Fused silica disk ablated at 23.1 x 10^4 Jm^{-2} at 5 Hz for 300 pulses.

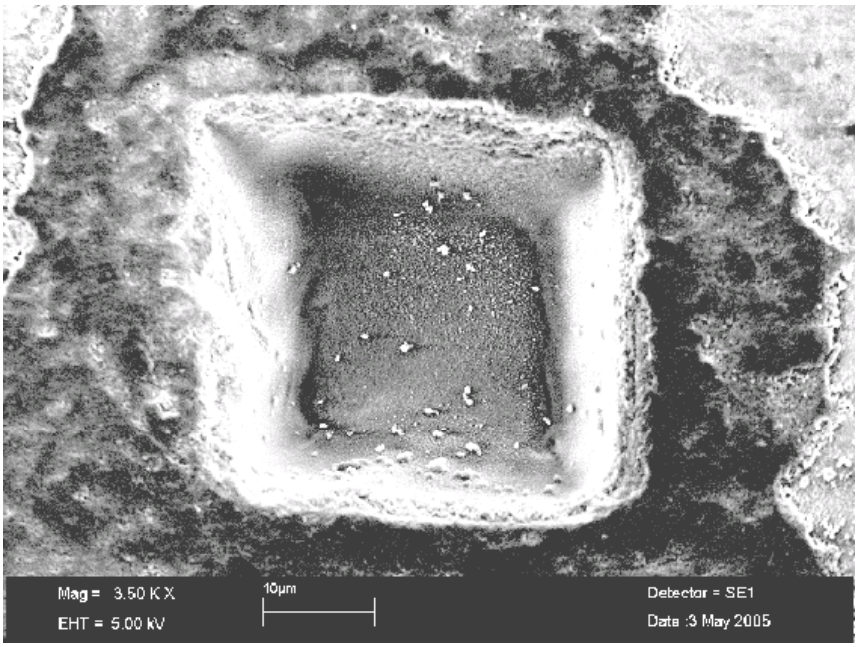

Figure 8-11: Fused silica disk ablated at 21.7 x 10^4 Jm^{-2} at 5 Hz for 100 pulses.

By comparing Figure 8-11 and Figure 8-12, it can be observed that the debris deposition, wall definition and crater smoothness and uniformity were improved by

increasing the energy density. To get quantitative data on the tapering of cavities at different energy densities, the crater areas at different energy densities for 100 pulses at a pulse repetition rate of 5 Hz were measured and are presented in Table 8-1.

Table 8-1: Table showing the improvement in crater area with increasing energy density.

Energy density [Jm^{-2}]	Entrance dimensions [μm]	Crater dimensions [μm]
24.5×10^4	38 x 38	23 x 23
18.2×10^4	38 x 38	19 x 19
14.7×10^4	38 x 38	16.5 x 16.5

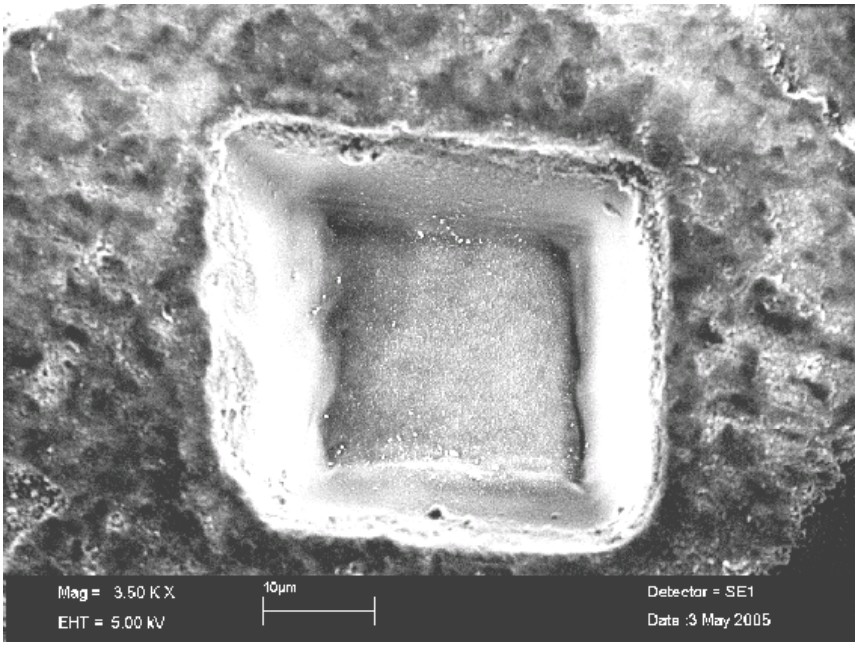

Figure 8-12: Fused silica disk ablated at 24.5×10^4 Jm^{-2} at 5 Hz for 100 pulses.

This demonstrates that the debris deposition and taper angle of the microstructures can be reduced by increasing the energy density of the ablation. These results are in good agreement with the findings in reference [92]. At 24.5×10^4 Jm^{-2} and 5 Hz repetition rate, a microstructure at a larger number of shots was ablated. This is shown in Figure 8-13. As explained earlier, improvement in smoothness of sidewalls and crater was observed with increasing number of shots. The significant improvement in morphology of the ablated structures at higher energy density is probably due to the reduction in the influence of various factors such as plume attenuation, enhanced

absorption due to colour centre generation [39] and evolution of aerial image in such a way that the taper angle is reduced [92].

The influence of pulse repetition rate was studied by ablating fused silica at 5 and 20 Hz. SEM micrographs of microstructures ablated at 24.5 x 10^4 Jm^{-2} at 5 Hz and 20 Hz can be observed in Figure 8-13 and Figure 8-14.

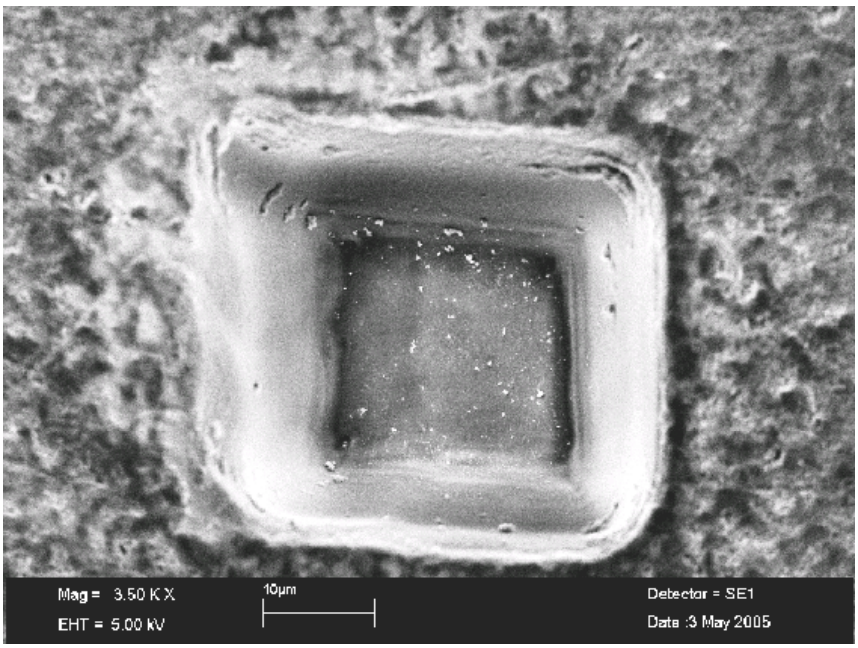

Figure 8-13: Fused silica disk ablated at 24.5 x 10^4 Jm^{-2} at 5 Hz for 180 pulses.

A slight reduction in ablation debris can be observed by comparing Figure 8-13 and Figure 8-14. Further investigation of the influence of pulse repetition rate on the morphology of microstructures is required to arrive at some conclusions on frequency effects. Another important observation is the undulations on the wall surface (left side wall; see Figure 8-13 and Figure 8-14). This is due to the deviation along the straight edge of the mask feature as shown in Figure 8-2. This is a deleterious effect that could effect fabrication of Fabry-Perot microstructures as these undulations affect the taper angle on the wall and also deteriorate the flatness of the wall surface. The difference between the left sidewall and the other cavity walls can be clearly observed from Figure 8-13 and Figure 8-14. The feasible solution for this problem is to use a chrome-mask on a calcium fluoride substrate with sharp feature edges. However, due to the unavailability of a calcium fluoride mask, during optical fibre ablation, the

optical fibres were aligned such that the undulated cavity wall does not form a Fabry-Perot etalon-forming dimension, which is perpendicular to the length of the fibre.

No obvious micro-cracks were observed on the walls or on the craters of ablated microstructures at all the energy densities used in these experiments. Another important observation is that the energy densities used in these experiments were significantly higher than those used by other researchers in their F_2-laser micro-machining studies of fused silica mentioned in Section 2.8.6

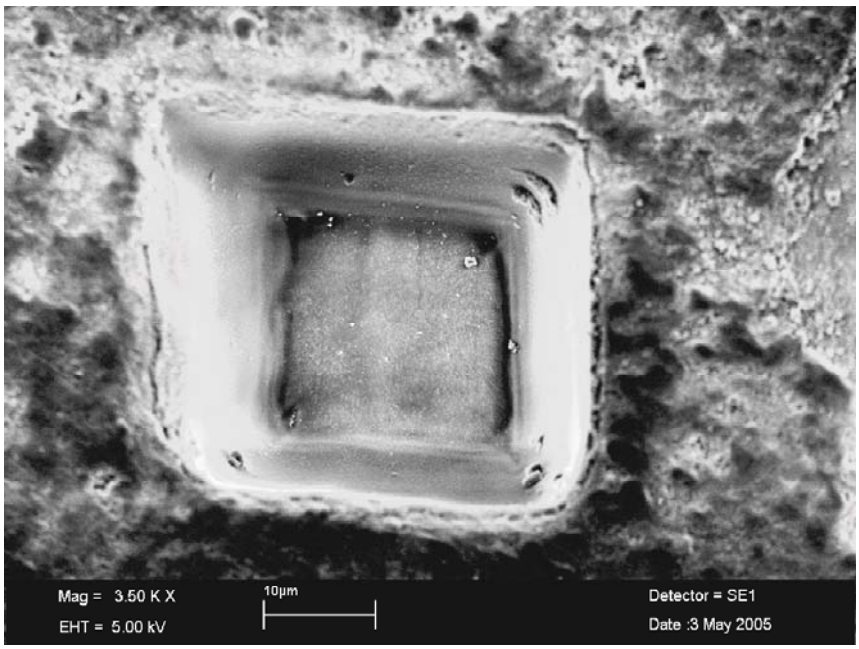

Figure 8-14: Fused silica disk ablated at 24.5 x 10^4 Jm^{-2} at 20 Hz for 180 pulses.

It must be emphasised here that the work carried out by other researchers was mainly aimed at surface micro-machining of fused silica, whereas the author's work is aimed at the fabrication of Fabry-Perot microstructures in optical fibres that imposes critical criteria such as high optical quality of cavity walls and crater surfaces; and a vertical wall angle of high aspect ratio cavities to be micro-machined typically to a depth of 125 μm. From reference [102], it can be observed, that energy densities as high as 9 x 10^4 Jm^{-2} were used to produce vertical walled cavities in microscope glass slides to a depth of 35 μm using beam homogeniser optics. Microscope glass slides are made of soda lime glass (Corning 2947), which has a much lower melting temperature and higher absorption than fused silica. If energy densities as high as 9 x 10^4 Jm^{-2} are

required for producing vertical walled cavities in soda lime glass, the use of energy densities as high as 25 x 10 ^{4} Jm^{-2} for controlling the geometric shape of high aspect ratio cavities in fused silica that has a much higher melting temperature and lower absorption at 157 nm than soda lime glass is reasonable. The use of homogeniser optics for F_2-laser micro-machining involves more optical elements and longer beam path than the system used by the author. Therefore, it will be more difficult to produce energy densities as high as 25 x 10^4 Jm^{-2} at the image plane due to the attenuation through the nitrogen ambient and lens elements. The experimental results show the advantage of designing a short beam path length 157 nm micro-machining station with a low numerical aperture imaging system for the fabrication of high-aspect ratio cavities in large band gap materials such as fused silica.

8.1.1.2 Profiler Analysis of Ablated Structures in Fused Silica Disks

Ablated structures in fused silica disks were observed under an interferometric surface profiler to gain quantitative information of cavity morphology. A surface map of a microstructure ablated at 24.5 x 10^4 Jm^{-2} for 20 pulses is shown in Figure 8-15.

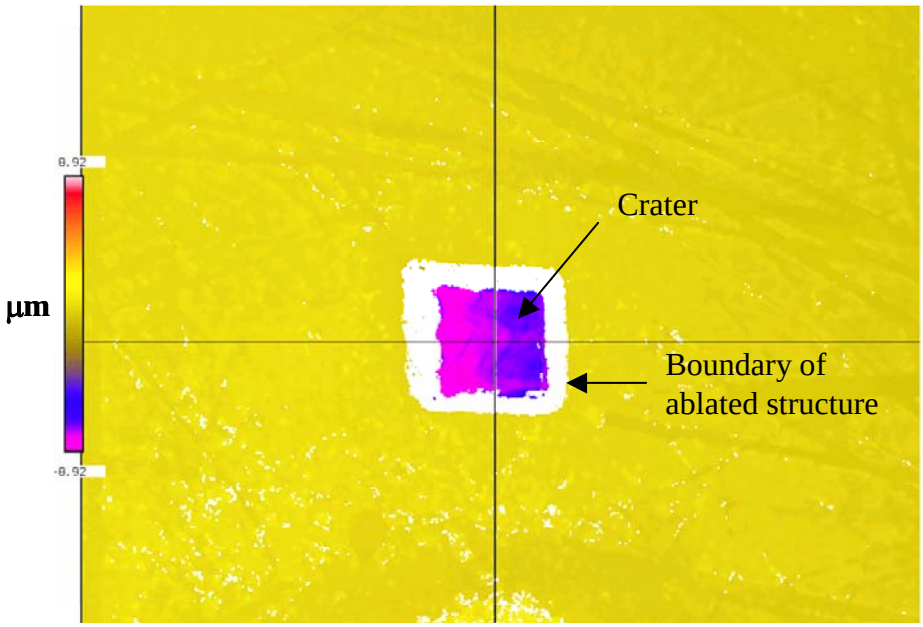

Figure 8-15: Surface map of microstructure ablated at 24.5 x 10^4 Jm^{-2} for 20 pulses.

The colour scale bar in Figure 8-15 indicates that different colours on the surface map correspond to different surface heights. The green-coloured region around the boundary of the ablated structure corresponds to the surface of the disk. The central square corresponds to the crater of the ablated structure. The white region around the crater has no light reflected into the interferometer and hence no data is obtained from that region. The reflection of incident light from steep wall surface of the cavity is not coupled back into the profiler. The coloured region on the crater indicates a high reflectivity of the crater surface. As the interferometric profiler operates in a similar manner to a Fabry-Perot interferometer, the reflectivity of the crater surface indicates that the surface has the required optical finish to produce Fabry-Perot interference. However, different coloured regions on the crater surface indicate unevenness across the crater surface area. The XY-profile along the crossed lines passing through the crater shows the unevenness along the length of lines across the crater surface. The ablation depth of the structure is the difference between the heights of the un-ablated surface and the cursor position on the crater as shown in Figure 8-16. The ablation depth of this structure is 8 μm. The unevenness on the crater surface is obvious from the profile of the blue line shown in Figure 8-16.

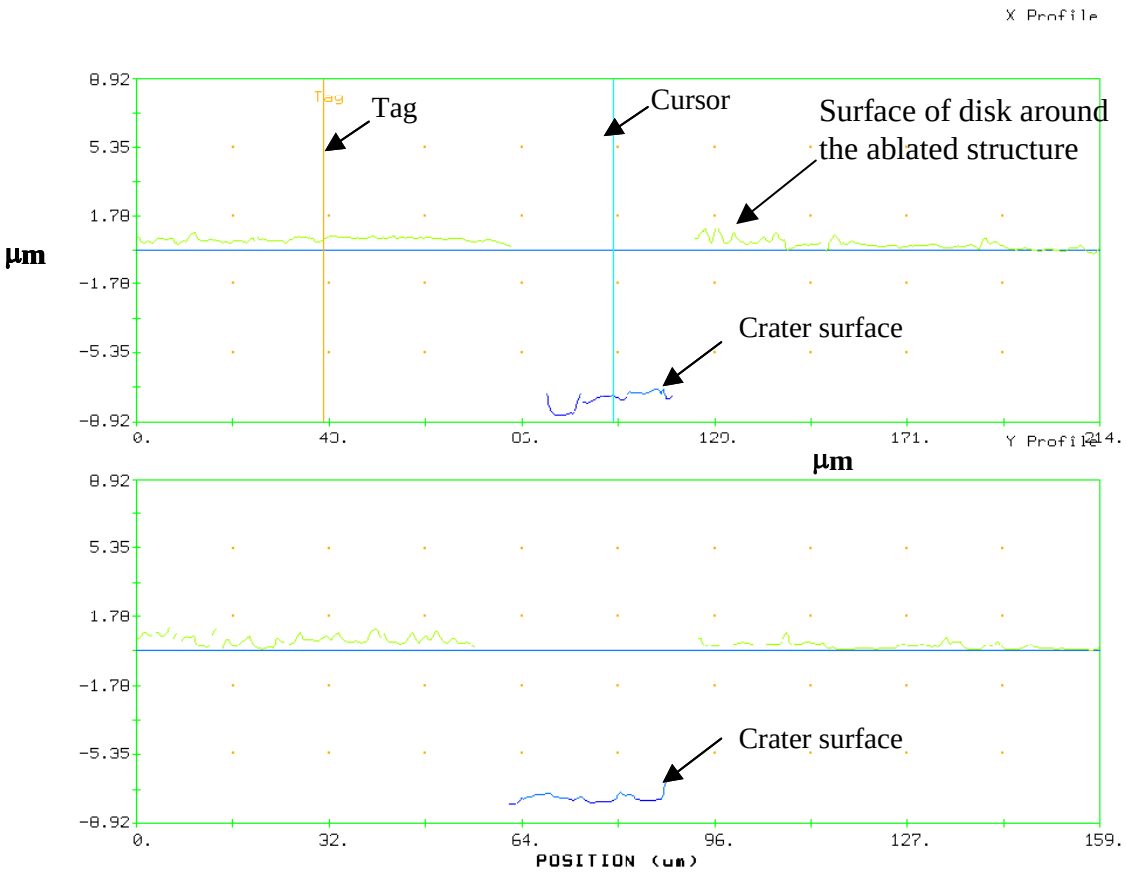

Figure 8-16: XY-profile of crater surface of structure ablated at 24.5 x 10^4 Jm^{-2} for 20 pulses.

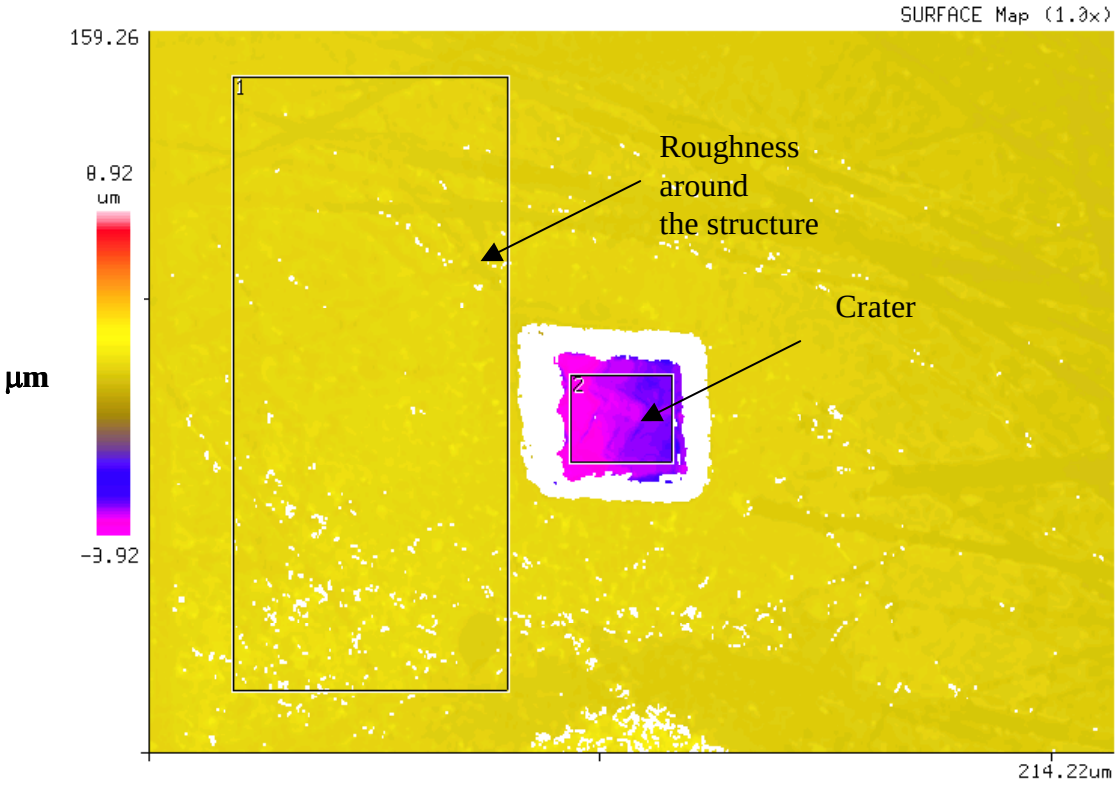

Figure 8-17: Area difference plot of structure ablated at 24.5 x 10^4 Jm^{-2} for 20 pulses.

The area defined by block 2 in Figure 8-17 shows that an RMS (root mean square) roughness of 440 nm over an area of 22.97 µm x 19.41 µm. The RMS over an area of 61.16 µm x 135.51 µm denoted by block 1 is 190 nm. This corresponds to a surface roughness induced by scattered light around the ablated structure.

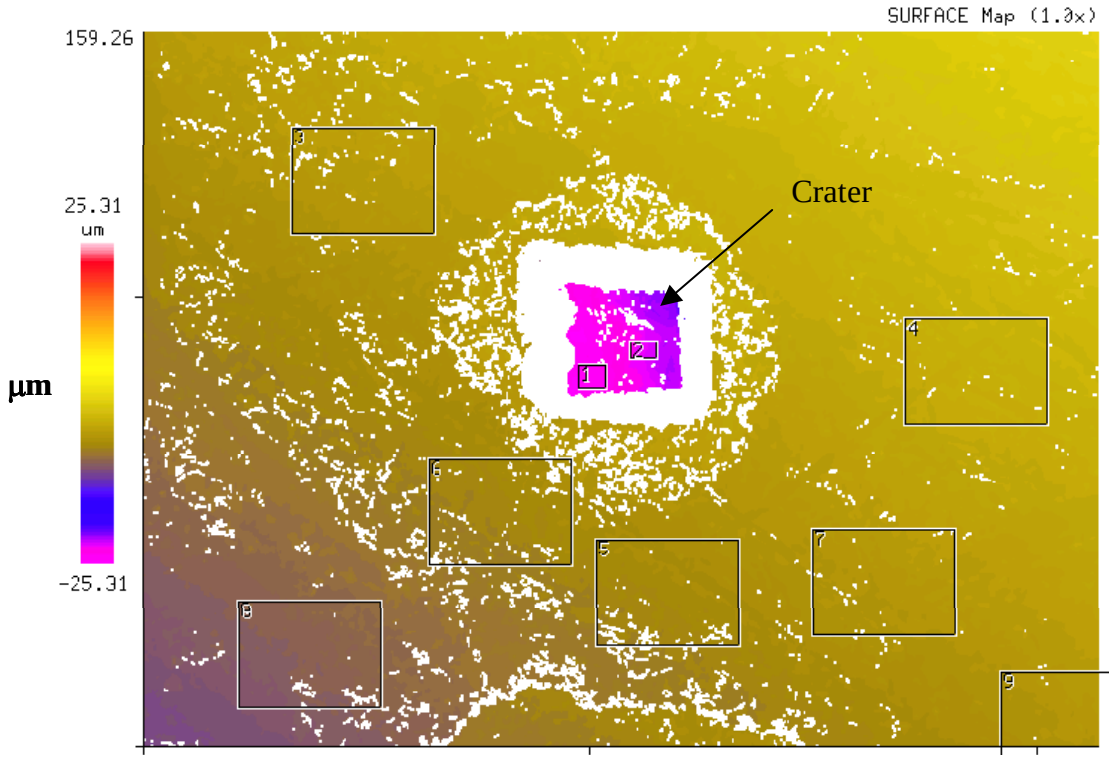

Figure 8-18: Area difference plot of structure ablated at 24.5 x 10^4 Jm^{-2} for 60 pulses.

The white regions on the crater surface shown in Figure 8-18 indicate missing data due to poor reflection from the corresponding regions. This could be due to ablation debris on the crater surface as observed in the SEM studies. Two blocks 1 and 2, which enclose areas of high reflectivity from the crater surface were chosen to get a quantitative value of roughness from the crater surface. The RMS roughness of blocks 1 and 2 corresponding to areas of 6.32 µm x 5.35 µm and 6.32 µm x 4.02 µm is 310 nm and 290 nm respectively. The XY-profile of this cavity is presented in Figure 8-19. It can be observed from Figure 8-19, that the flatness of the cavity improved with increasing number of shots. The improved flatness of the crater surface can be observed from the profile of the blue line of the crater surface shown in Figure 8-19. This is in agreement with the SEM studies. The ablation depth of this cavity is 20 µm.

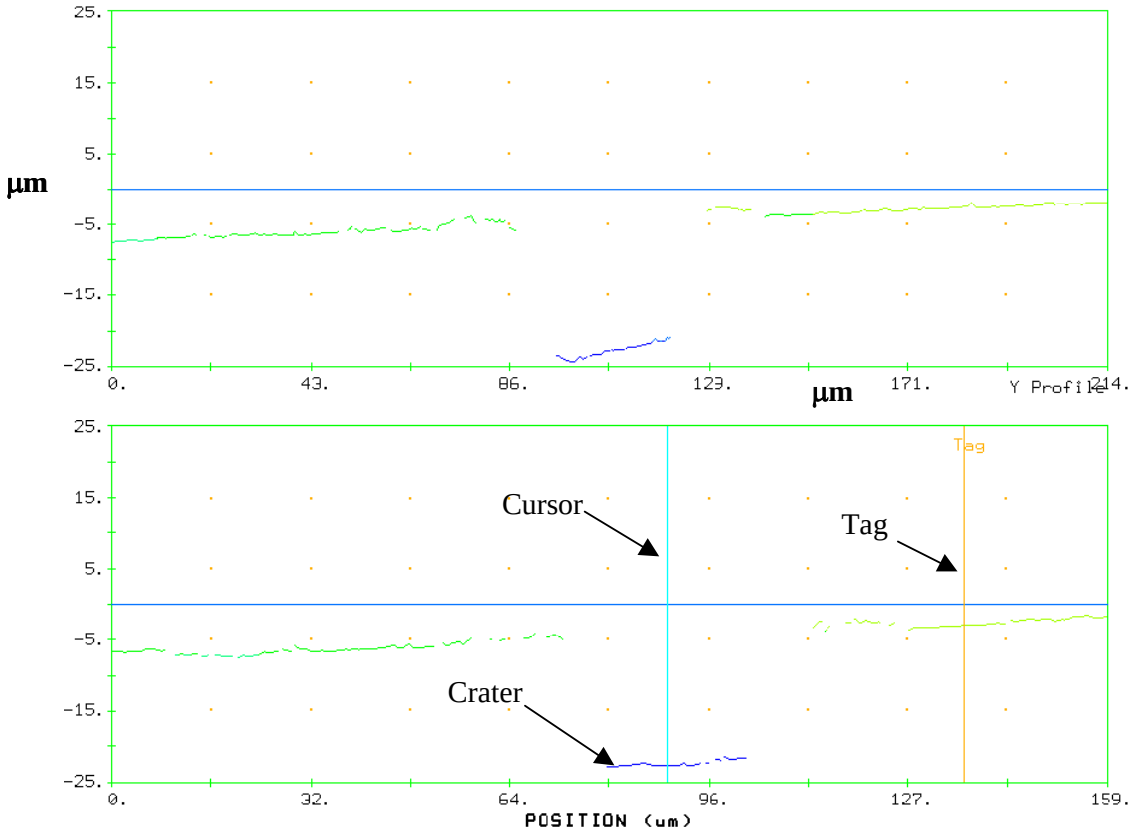

Figure 8-19: XY-profile of structure ablated at 24.5 x 10^4 Jm^{-2} for 60 pulses.

In this manner crater roughness of different microstructures ablated at an energy density of 24.5 x 10^4 Jm^{-2} for varying number of pulses was measured and is presented in Table 8-2. The ablation depths measured for different number of pulses at different energy densities is presented in Table 8-3.

Table 8-2: RMS roughness of craters of structures ablated at 24.5 x 10^4 Jm^{-2}.

Number of pulses	Defined area [μm^2]	RMS roughness [nm]
20	22.97 x 19.41	440
60	6.32 x 4.02	290
100	4.02 x 3.35	120
180	4.59 x 5.35	240
300	2.58 x 2.34	100

Table 8-3: Ablation depth of cavities and ablation rates at different energy densities.

Number of Pulses	Energy density x 10^4 [Jm^{-2}]		
	8	**16**	**24**
	Ablation depth [μm]		
10	1.36	2.63	3.17
40	6.07	8.65	11.23
60	8.55	13.01	17.21
100	13.95	21.75	28.67
120	18.11	26.07	34.08
160	22.13	34.17	42.86
180	27.29	37.23	46.67
220	33.46	47.06	55.57
280	39.47	58.54	67.11
300	42.58	62.38	74.33
Ablation rates from a linear curve fit [nm $pulse^{-1}$]	143	206	238

8.1.1.3 Summary of Ablation of Fused Silica Disks

Fused silica disks were ablated at different energy densities and pulses. The general morphology of cavities at 7 x 10^4 Jm^{-2} was very rough and no reflectivity was obtained from these surfaces during surface profile measurements. When the energy density was increased to 15.4 x 10^4 Jm^{-2}, a significant improvement in the geometric shape and smoothness of the cavities was observed. The smoothness of craters and cavity walls improved with an increase in the number of pulses. However, the deposition of ablation debris increased with ablation depth. The tapering of cavity walls decreased with increasing energy density. When the energy density was increased to 24.5 x 10^4 Jm^{-2}, smooth sidewalls and well-defined crater surfaces were obtained. There was no obvious micro-crack formation at all the energy densities used in these experiments. The deposition of ablation debris was also significantly reduced at an energy density of 24.5 x 10^4 Jm^{-2}. The undulations along the mask edge were clearly replicated along the corresponding wall surface of the ablated microstructure. The edge-ringing of intensity produced a higher ablation around the margins of the

crater and the highest ablation was observed at the corners of the crater. This resulted in higher debris deposition along the cavity wall edges.

Surface profile analysis showed that the optical quality of microstructural craters ablated at an energy density of 24.5 x 10^4 Jm^{-2} was adequate to produce Fabry-Perot interference. The RMS roughness measured on crater surfaces varied over a range of 100 to 500 nm. The flatness of the crater surfaces improved with an increase in the number of pulses. The depth of the cavities could be controlled from the ablation rate data obtained at different energy densities. No quantitative data about the roughness of cavity wall was obtained due to a lack of reflection from the steep walls. One major problem identified in these studies was deposition of ablation debris. The ablation parameters determined in these studies for producing Fabry-Perot microstructures could be implemented on cleaved end face of fibres to produce craters of high optical finish across the core of the optical fibres as mentioned in Figure 2-11 [B].

8.1.2 Ablation of Sapphire Disks

8.1.2.1 SEM Study of Ablated Structures in Sapphire

Sapphire discs were ablated by projecting a transparent 1.5 mm x 1.5 mm mask feature at energy densities ranging from 12 x 10^4 to 25 x 10^4 Jm^{-2} with different number of pulses. The intention of this study was to identify ablation parameters for micro-machining Fabry-Perot microstructures. An SEM micrograph of a microstructure ablated at an energy density of 12.6 x 10^4 Jm^{-2} is shown in Figure 8-20. The laser-induced surface modification produced regular and pattern-like structures in the ablated region and around the irradiated area. With an increasing number of pulses, these structures were suppressed and smoother craters and wall surfaces were produced. This can be observed from Figure 8-21, Figure 8-22 and Figure 8-23.

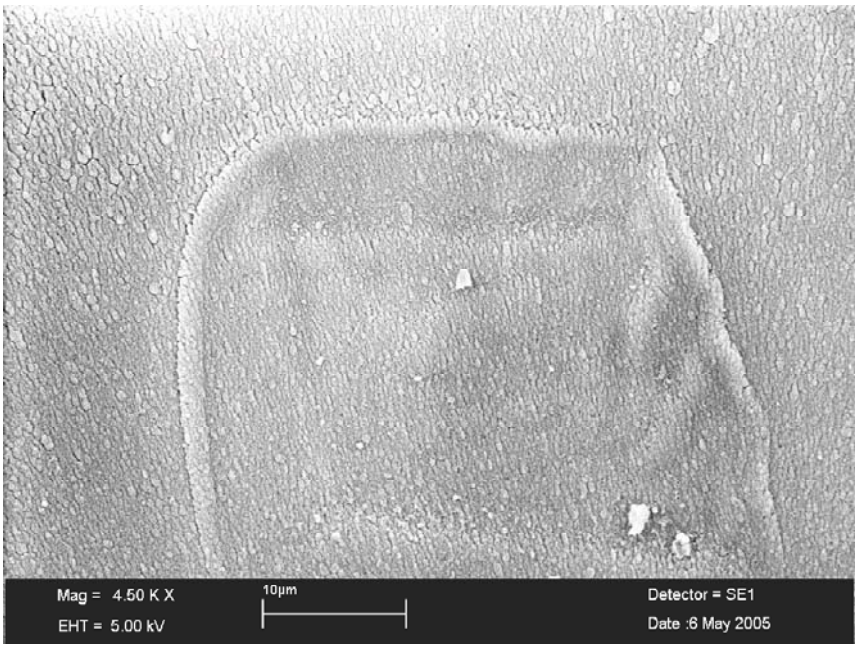

Figure 8-20: Sapphire ablated at 12.6 x 10^4 Jm^{-2} at 5 Hz for 10 pulses.

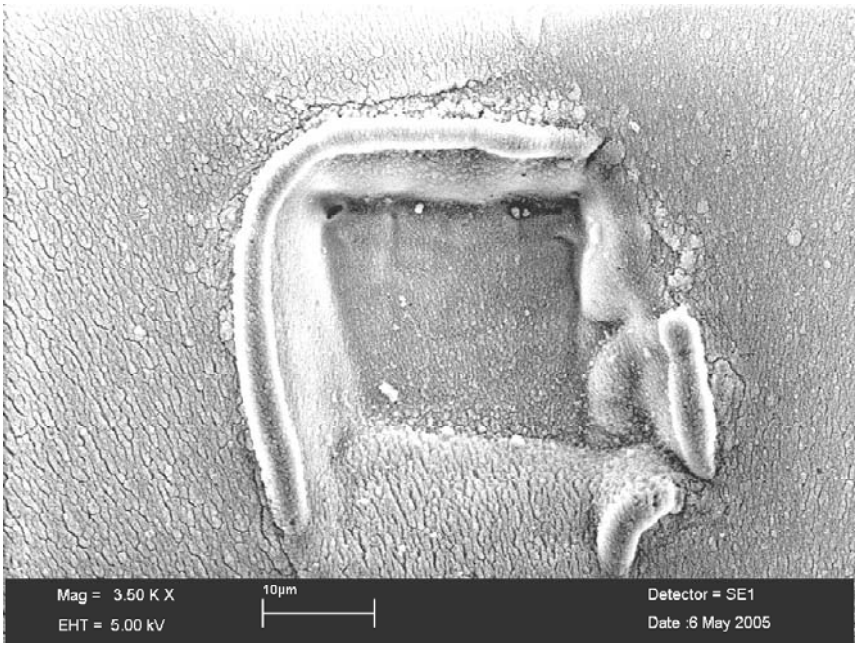

Figure 8-21: Sapphire ablated at 12.6 x 10^4 Jm^{-2} at 5 Hz for 60 pulses.

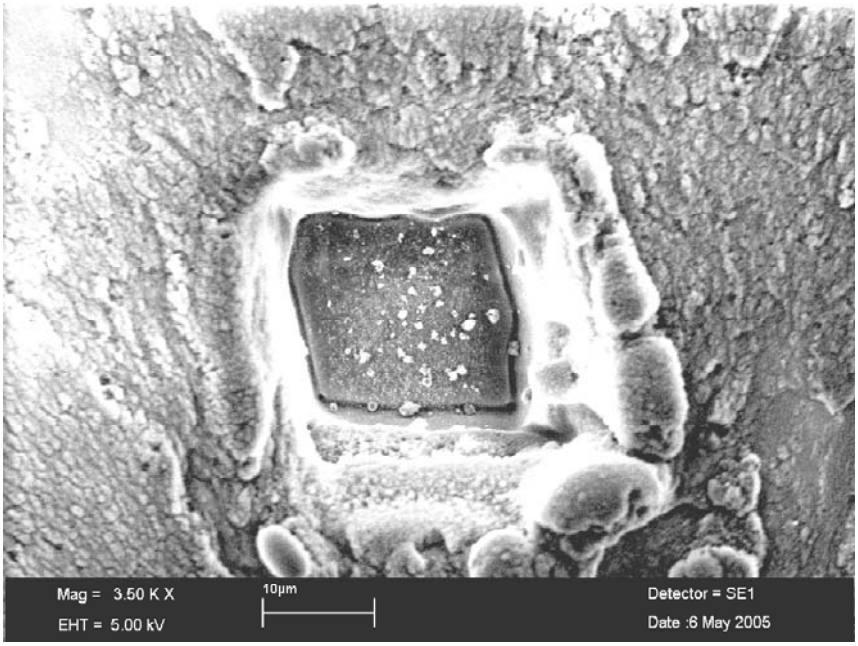

Figure 8-22: Sapphire ablated at 12.6 x 10^4 Jm^{-2} at 5 Hz for 300 pulses.

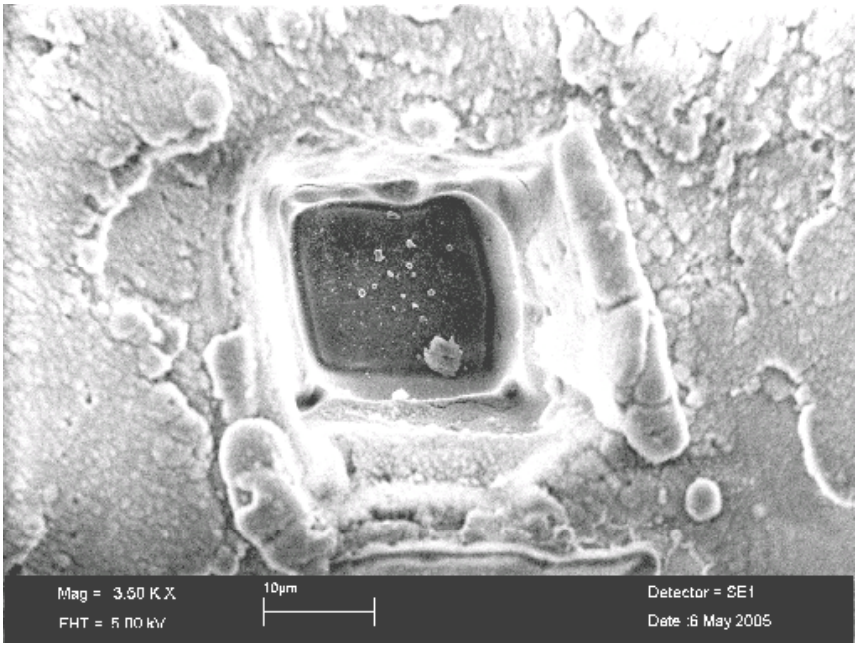

Figure 8-23: Sapphire ablated at 12.6 x 10^4 Jm^{-2} at 5 Hz for 400 pulses.

The surface roughness around the ablated structures is obvious from Figure 8-22 and Figure 8-23. The entrance of the structure and surrounding area is dominated by a recast of the material. This effect was greater for structures ablated for a larger number of pulses, which produced uneven wall surfaces near the entrance of the structure. These features were not observed during the ablation of fused silica. Ablation debris was obvious on the crater surfaces.

Sapphire has an energy band gap of 9.9 eV [42], which is larger than that for fused silica. Therefore, the ablation of this material occurs by multi-photon ionisation. The recast of the material around the ablated structure is due to large heat affected zones. As mentioned in Section 2.8.1, the thermal effects of ablation will be higher in weak absorbers. The absence of these effects in fused silica is due to stronger absorption. In addition to weaker absorption of sapphire at 157 nm than fused silica [96], the melting point of sapphire is much higher than fused silica (see Table 5-2). During nanosecond pulse durations, material ablation occurs when the deposited laser energy coverts the material to vaporization state via molten state. Due to the higher melting point of sapphire, the duration of pulse energy expended in producing the melting temperature in the absorbed volume could be higher. Meanwhile, the heat dissipates into the surrounding volume of the irradiated area. Only the volume of the molten material that has reached its vaporization temperature undergoes ablation. After the onset of ablation, the energy reaching the target surface will be lowered due to plume attenuation effects. The remaining duration of the pulse heats up the material to its melting temperature, however not to its vaporization temperature. The molten material deposits around the ablated structure and solidifies by radiation and conduction. This produces recast of molten material or residual material around the ablated structures. These effects are a consequence of weak absorption of sapphire combined with its high melting temperature.

The improvement in crater smoothness and wall definition of the cavity with increasing number of pulses could be due to the enhanced absorption of the remaining material as a result of colour centre formation. The enhanced absorption in sapphire during 248 and 193 nm laser ablation has been reported [42], [43].

When the energy density of ablation was increased to 21.7 x 10^4 Jm^{-2} and then to 23.1 x 10^4 Jm^{-2}, an overall improvement in general morphology of the structures was observed. This can be observed from Figure 8-24 and Figure 8-25. Higher energy densities produce higher temperatures in the absorbed volume of the material and hence more effective removal of material. Reduction in recast material near the entrance of the cavity, improvement in cavity wall definition and crater smoothness was observed. Flaky structures along the wall surfaces were also observed. This is obvious from Figure 8-24. The smooth morphology of the sidewalls and crater are

obvious from Figure 8-25. However, particulate ablation debris is also obvious on the craters.

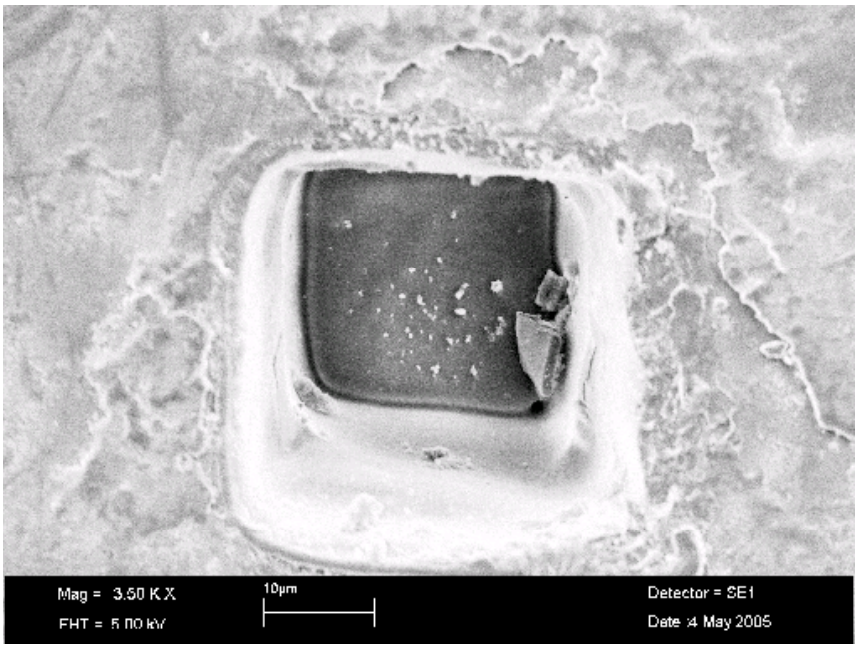

Figure 8-24: Sapphire ablated at 21.7 x 10^4 Jm^{-2} at 5 Hz for 300 pulses.

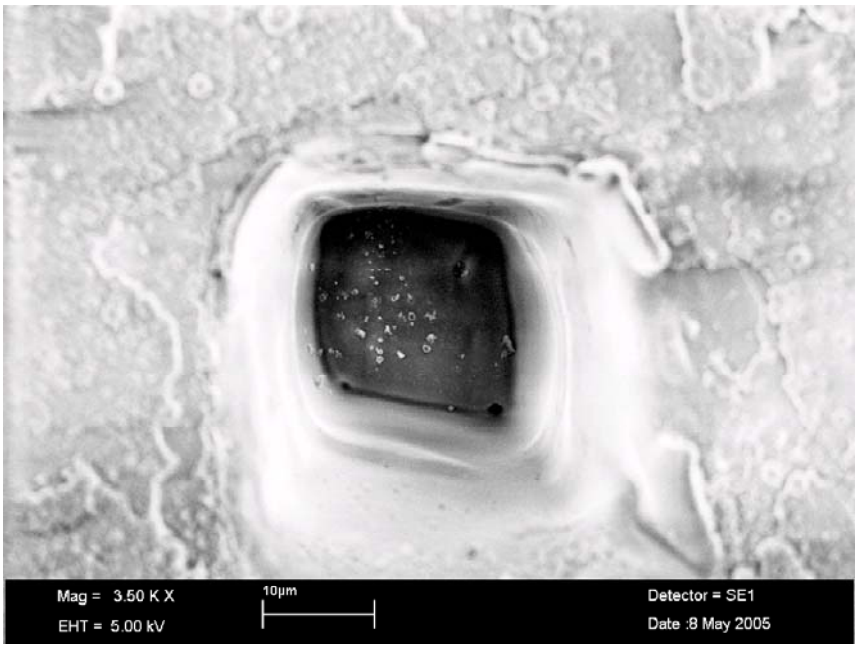

Figure 8-25: Sapphire ablated at 23.1 x 10^4 Jm^{-2} at 5 Hz for 500 pulses.

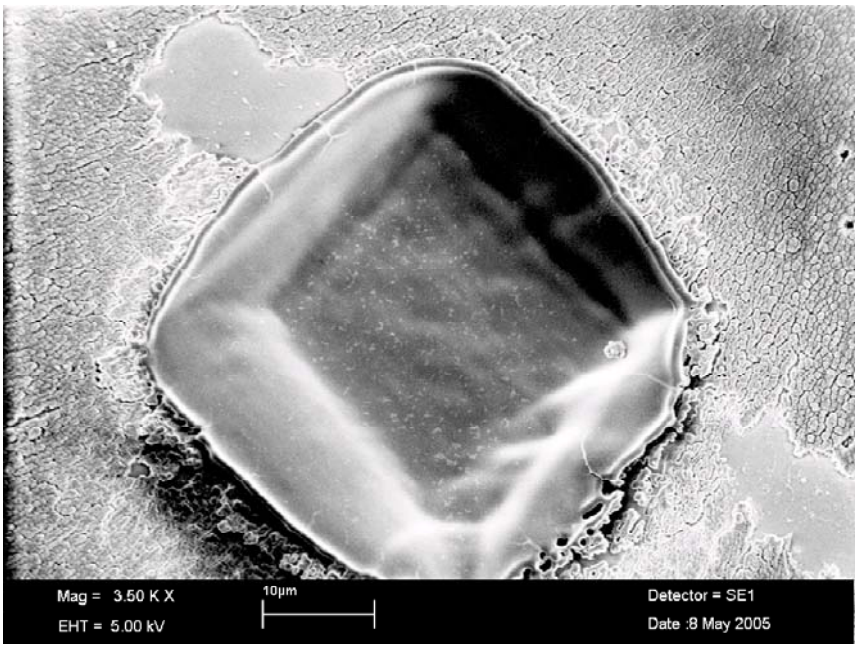

Figure 8-26: Melt-zone around the structure ablated at 24.5 x 10^4 Jm^{-2} for 20 pulses.

The effect of high energy density can be clearly observed from Figure 8-26 ablated at a pulse repetition rate of 20 Hz. The smooth surface of the ablated structure is probably due to spread of the molten layer. The molten layer remaining beneath the ablated volume spreads across the area of ablation due to recoil exerted by the vaporised volume of the material [55]. These large melt zones could occur as a result of long pulse duration and high temperatures produced at higher energy densities.

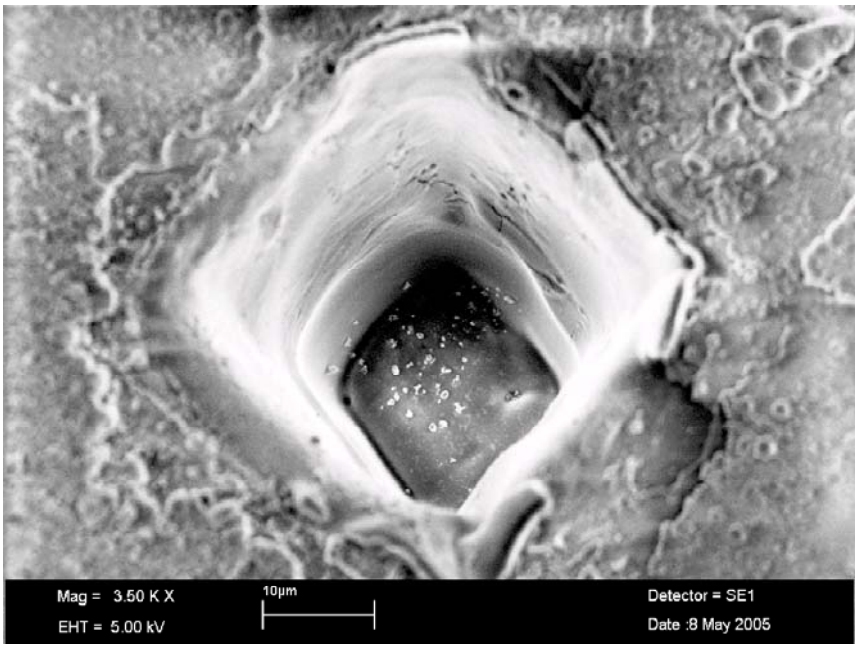

Figure 8-27: Sapphire ablated 24.5 x 10^4 Jm^{-2} at 5 Hz for 500 pulses.

Figure 8-27 and Figure 8-28 show the morphology of cavity walls and crater ablated at 24.5 x 10^4 Jm^{-2} for 500 pulses. At this energy density, micro-cracks on wall surface were observed. These can be seen clearly in Figure 8-27. Crack formation during femtosecond ablation of sapphire substrates has been reported [58]. The ablation-induced stresses could be one explanation for micro-crack formation [105]. Reasons such as sudden cooling of cavity wall surfaces after expansion of the laser-induced plasma out of the cavity and thermal shock due to heat transfer from the plasma to cavity walls at high energy densities could also be possible reasons [50]. Crack formation was not observed at energy densities lower than 24.5 x 10^4 Jm^{-2}. However, more research is required to establish exact reasons for the crack formation in sapphire cavities.

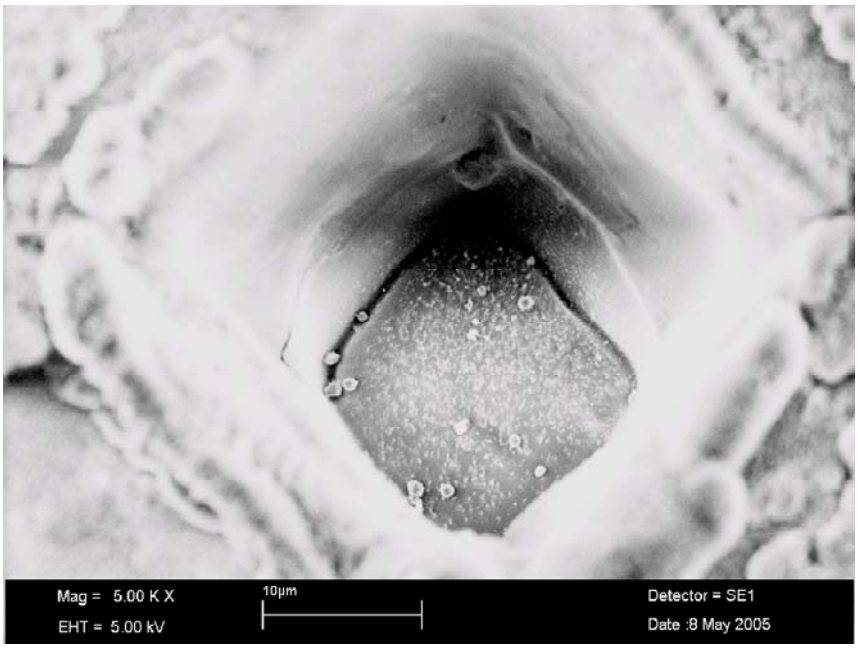

Figure 8-28: Sapphire ablated 24.5 x 10^4 Jm^{-2} at 5 Hz for 500 pulses.

The notches near the corners due to edge-ringing are obvious in Figure 8-27. In Figure 8-28, smooth wall surfaces can be observed. However, the cavity walls were not as flat as those produced in fused silica microstructures. The crater surface, although smooth, is dominated by powder-like ablation debris. Quantitative data on the surface roughness of craters is presented in the next section.

Besides ablation debris, two important problematic issues arose with reference to fabrication of Fabry-Perot structures in sapphire. One is micro-crack formation and the other is tapering of cavity walls associated with undulations. It was verified from fused silica ablation that increasing the energy density of ablation could reduce the tapering of cavity walls and improve the optical quality of the ablated surfaces. It is important that the walls of the micro-machined structure are parallel to each other and have an adequate optical finish to produce Fabry-Perot interference. However, increasing the energy densities resulted in flaking and micro-cracking of cavity wall surfaces during sapphire disk ablation that would be detrimental to optical reflectivity.

8.1.2.2 Surface Profile Analysis of Ablated Structures on Sapphire

Ablated structures on sapphire were examined using a surface profiler to gain quantitative data on roughness of cavities. Figure 8-29 shows an area difference plot of a microstructure ablated for 20 pulses at an energy density of 24 x 10^4 Jm^{-2}.

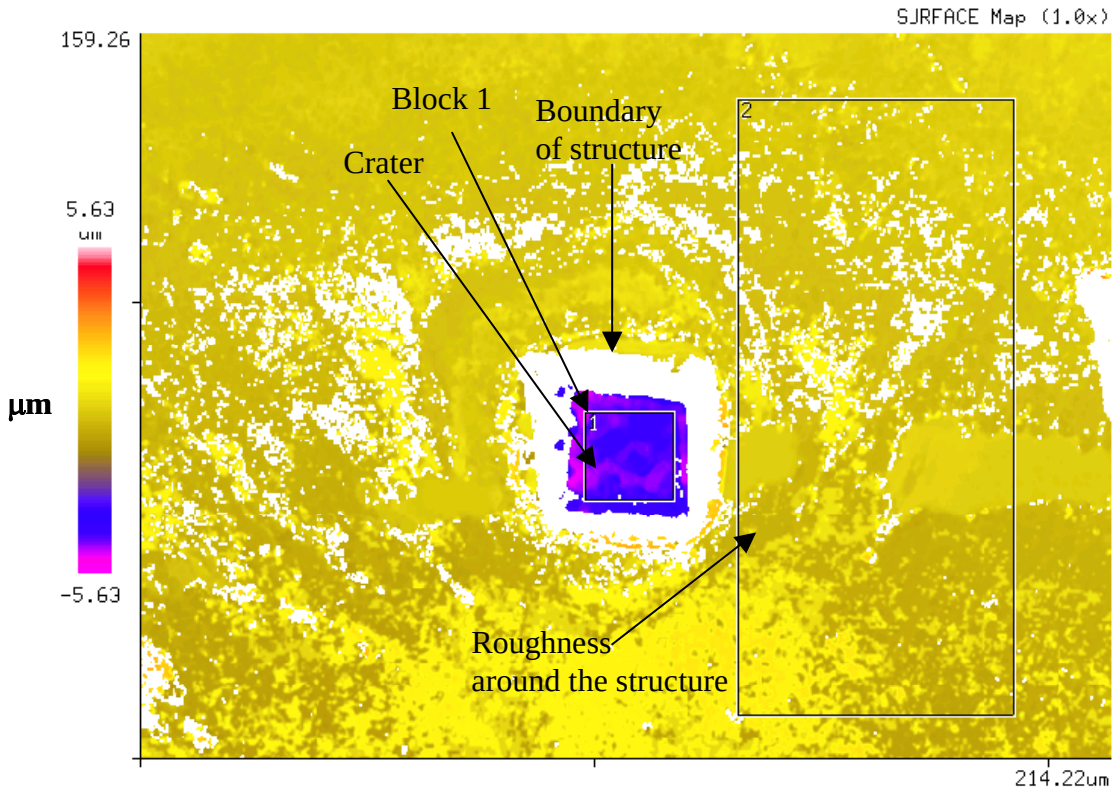

Figure 8-29: Surface map of a microstructure ablated on sapphire at 24 x 10^4 Jm^{-2}.

The high reflectivity of the crater is indicated by the central blue region, which shows that the optical finish of the crater surface was adequate Fabry-Perot interference. Different colours on the colour scale bar correspond to different heights on the surface. The roughness produced due to residual material around the entrance of the structure can be seen as the scattered green colour around the boundary of the white region that corresponds to no reflection from the steep walls of the structure. The root mean square roughness (RMS) of block 1, which corresponds to an area of 19.53 µm x 19.41 µm on the crater surface is 220 nm. The roughness around the ablated structure on block 2, which corresponds to an area of 61.16 µm x 135.51 µm on the un-ablated surface around the structure is 550 nm.

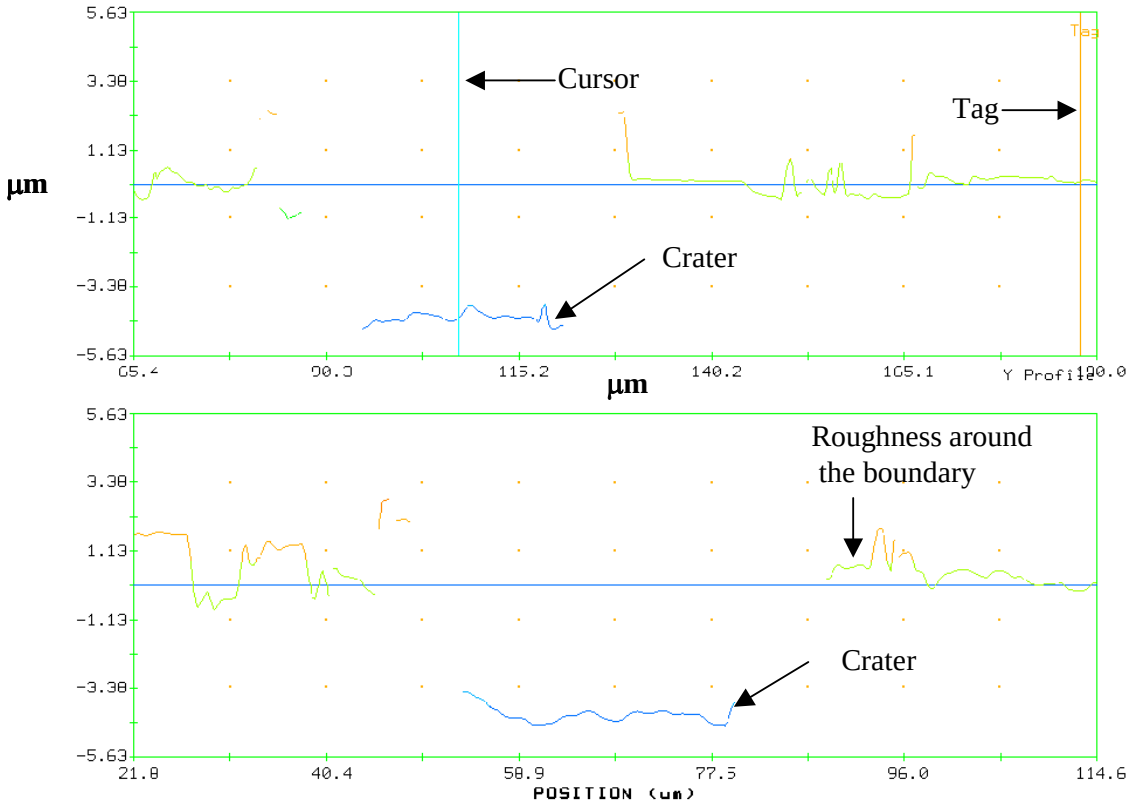

Figure 8-30: XY-profile of crater surface of structure ablated at 24 x 10^4 Jm^{-2} for 20 pulses.

The XY-profile of the crater surface shown in Figure 8-29 is presented in Figure 8-30 to study the flatness of the crater surface. This structure has an ablation depth of 4.5 µm. The blue curves show the profile of the crater surface along X and Y directions. The rugged surface near the entrance of the structure is obvious from the profiles on either side of the crater. To measure the roughness of craters of deeper cavities, microstructures ablated at energy density of 24 x 10^4 Jm^{-2} for 100 and 60 shots were profiled and their area difference plot is presented in Figure 8-31.

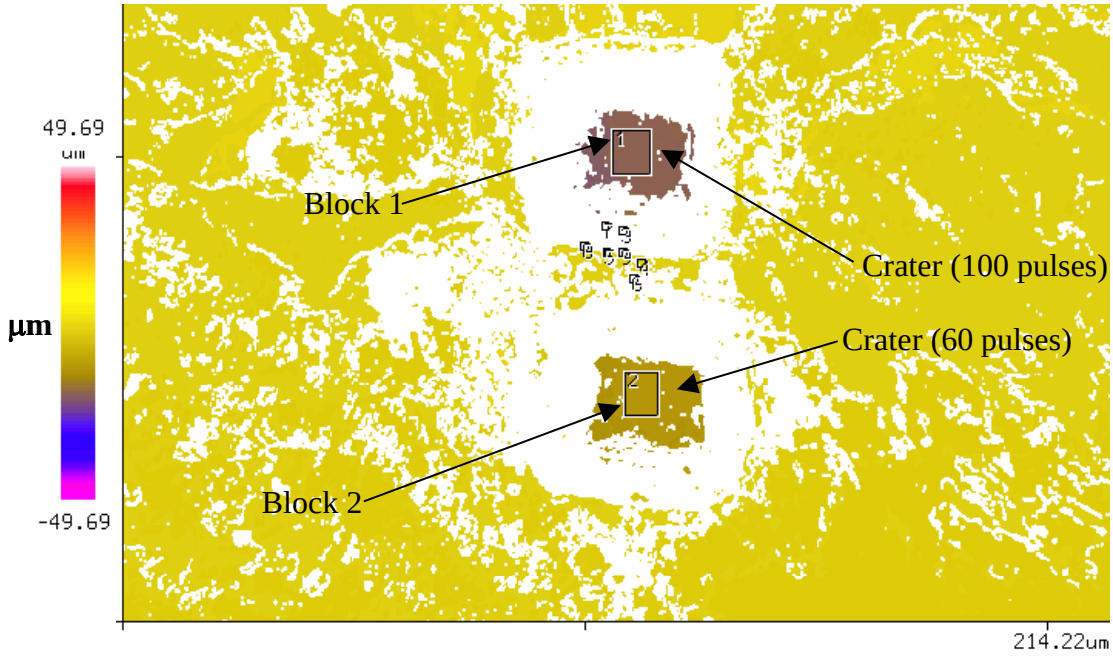

Figure 8-31: Area difference plot of structures ablated at 24 x 10^4 Jm^{-2} for 60 and 100 pulses.

In Figure 8-31, block 2 corresponds to an area of 8.33 µm x 9.70 µm on the crater of the structure ablated for 60 pulses and block 1 corresponds to an area of 7.18 µm x 9.70 µm on the crater of the surface of the structure ablated for 100 pulses. The RMS roughness of block 1 is 190 nm and that of block 2 is 140 nm. The line segment profile of these cavities was taken to study the flatness of craters. The line segment profiles of the craters of the structures shown in Figure 8-31 are presented in Figure 8-32.

The line segments are defined through the centre of the cavities. It can be observed that the crater profiles were flatter than the profile of the crater ablated for 20 pulses. This can be observed by comparing Figure 8-30 with Figure 8-32. The tag position corresponds to surface of the un-ablated region on the disk. The improvement in crater morphology was clearly observed in SEM analysis. The ablation depth of the 60 and 100 µm craters is 11 and 19 µm respectively. The crater roughness measurements of structures for different number of pulses at 24 x 10^4 Jm^{-2} is presented in Table 8-4.

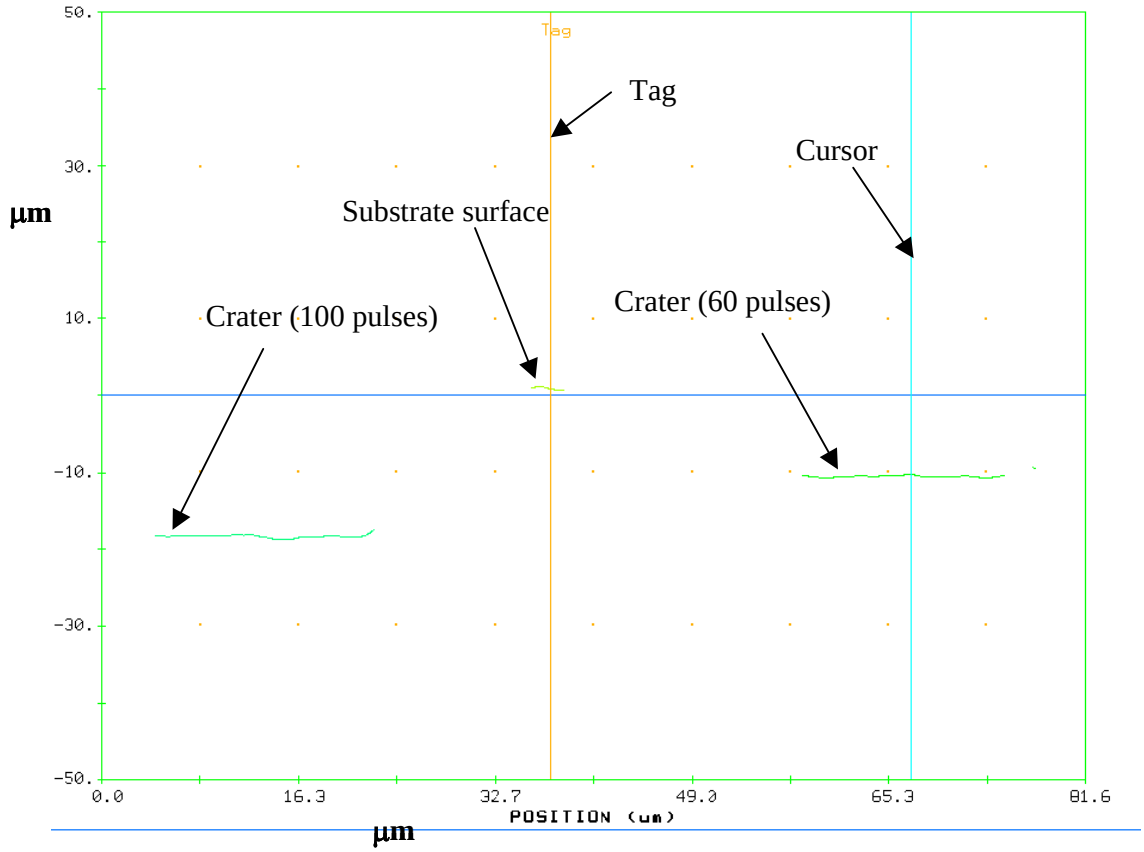

Figure 8-32: Line segment profile of craters of structures ablated for 60 and 100 pulses at 24 x 10^4 Jm^{-2}.

Table 8-4: Crater roughness of structures ablated on sapphire disks at 24 x 10^4 Jm^{-2}.

Number of pulses	Defined area [μm^2]	RMS roughness [nm]
20	19.53 x 19.41	220
60	8.33 x 9.70	140
100	7.18 x 9.70	190
300	2.01 x 2.01	110

The ablation depth of cavities micro-machined at different energy densities and number of pulses was measured using a surface profiler and is presented in Table 8-5. By comparing Table 8-3 with Table 8-5, it can be observed that the ablation rates in general are higher in fused silica than sapphire. This is due to weaker absorption of sapphire at 157 nm.

Table 8-5: Ablation depths at different energy densities and pulses on sapphire.

Number of Pulses	Energy density x 10^4 [Jm^{-2}]		
	12.6	16.8	23
	Ablation depths [μm]		
10	1.59	1.73	1.87
40	5.57	6.51	8.44
60	8.04	9.91	11.56
100	12.94	15.36	19
120	14.97	18.17	22.22
160	19.36	23.64	28.52
180	21.65	27.4	32.73
220	27.47	32.47	39.11
280	35.47	43.54	48.95
300	39.68	45.93	52.85
Ablation rates from a linear curve fit [nm $pulse^{-1}$]	127	151	172

8.1.2.3 Summary of Ablation of Sapphire Substrates

The SEM study of microstructures ablated at different energy densities revealed that the thermal effects of ablation deteriorate the quality of machined surfaces. The entrance of the cavities is dominated by residual un-ablated material. However, the wall formation and craters became evident with increasing number of pulses. This indicates enhanced absorption of the ablated surface due to colour centre formation. This was confirmed by sapphire ablation studies of other researchers. Smooth walls and crater surfaces were produced at energy densities of 23.1 x 10^4 and 24.5x 10^4 Jm^{-2}. Flaking of wall surfaces and micro-cracking were observed at 24 x 10^4 Jm^{-2}. The walls of the cavities are not as flat as those obtained during fused silica ablation. Undulations on the wall surfaces deteriorated the cavity wall definition. Although the crater surfaces are smooth, the deposition of ablation debris could deteriorate the optical quality of structures. The thermal effects are due to poor absorption and the high melting point of sapphire. These effects are detrimental for the fabrication of Fabry-Perot microstructures.

Surface profile analysis of the cavities ablated at 24 x 10^4 Jm^{-2} revealed that the optical finish of cavity craters is adequate to produce FP interference. The data on the optical quality of cavity wall surfaces could not be gathered due to the steepness of

walls. The flatness of craters was found to be higher for structures ablated for larger numbers of pulses. The conclusion of these studies is that high aspect ratio microstructures of optical quality sufficient to produce Fabry-Perot interference can be micro-machined in sapphire substrates.

8.1.3 Novelty of this chapter

Tuck's [8] research on the fabrication of Fabry-Perot cavities proved that 248 and 193 nm laser micro-machining of fused silica substrates was not suitable for the fabrication of high aspect ratio FP cavities. The experimental results of F_2-laser micro-machining of fused silica, published by Herman *et al.* [91] and Obata *et al.* [103] clearly demonstrated that high quality optical surfaces can be micro-machined in fused silica to a depth of few micrometers. However, their research does not give information about the optical quality of crater surface, wall surfaces and geometry of the microstructures with increasing ablation depth. These factors are very significant to the author's research. With respect to fused silica disk ablation, the author's research has clearly demonstrated that ablation debris across the crater and wall surfaces increases with the ablation depth of the cavities. This is detrimental to the optical quality of the microstructure as it lowers the Fresnel reflectivity of the ablated surface. The wall-definition, geometry of the cavity and general morphology of the cavity surface has been found to be improving with increasing energy density, even though it was found that the ablation debris could not be fully avoided under the experimental conditions used by the author.

Under the experimental conditions used by the author, increasing the energy density has been found to be the only way to achieving Fabry-Perot cavities. In this chapter, various factors, which influence the optical quality of high aspect ratio microstructures, have been investigated and optimised to produce the FP cavities of several tens of micrometres depth repeatably under the experimental conditions used by the author. The author's design of illumination using low numerical aperture and high demagnification imaging system and short beam path length enabled energy densities as high as 26×10^4 Jm^{-2}, which were found to be essential for the fabrication

high aspect ratio Fabry-Perot cavities in fused silica and sapphire substrates. These investigations to the best of the knowledge of the author have not been reported.

9 Ablation of Optical Fibres

9.1 Introduction

The results and the discussion of the results of the experimental methods described in Section 5.6 are presented in this chapter. This chapter presents the results and discussion of the ablation of SMF 28 and SM 800 fibres. The following results and discussion of fibre ablation are presented: (i) An evaluation of the alignment techniques used for the ablation of optical fibres for micro-machining cavities through their diameter are presented; (ii) The tapering of sidewalls of cavities ablated at different energy densities and some theoretical calculations of image defocusing due to the influence of fibre curvature are given; (iii) A CCD interrogation of micro-machined cavities is presented; (iv) A mathematical derivation of cavity tapering effects which includes a calculation of the threshold of cavity wall-angle to produce Fabry-Perot interference, a calculation of Fresnel reflection coefficients for different taper angles of cavity walls and a calculation of the position of incidence of the second Fresnel reflection; (v) An SEM analysis of cavities and cavity wall surfaces of fractured ablated fibres; (vi) Surface profile analysis of the wall surface of cavities; (vii) The ablation of cleaved end-face of optical fibres and their SEM analysis; (viii) The ablation of sapphire fibres and their SEM and surface profiler analysis of cavity wall surface.

9.1.1 Fibres Aligned During Ablation Through the Diameter

As described in Section 5.6.2, the fibres were aligned into the image plane of the objective and micro-machined through their diameter at different energy densities. The alignment techniques used were found to be suitable. An optical micrograph of a 38μm structure on the surface of the optical fibre is shown in Figure 9-1.

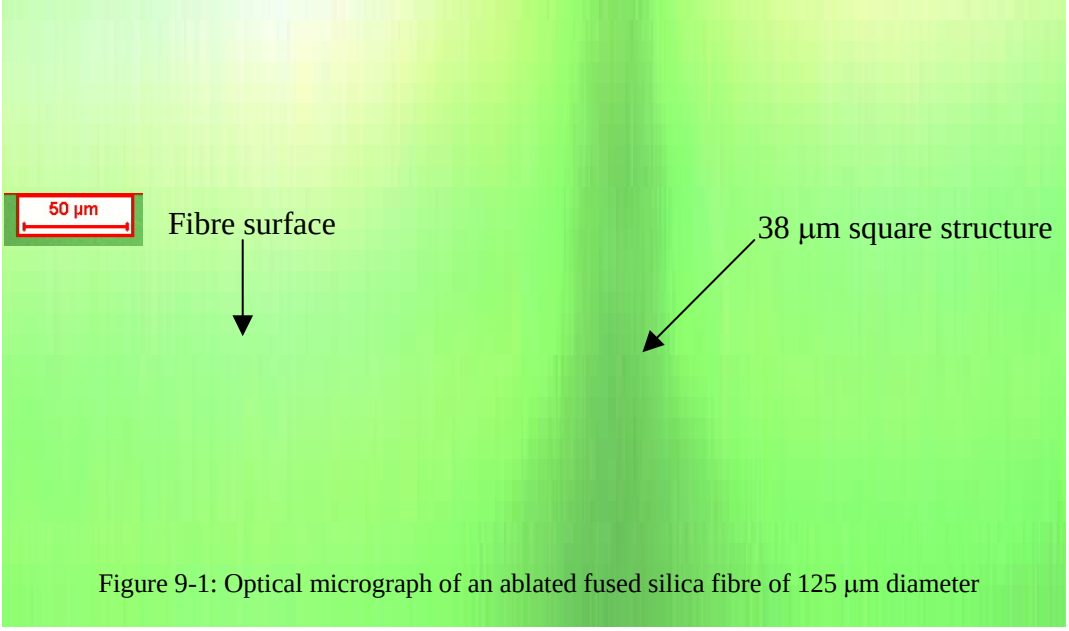

Figure 9-1: Optical micrograph of an ablated fused silica fibre of 125 µm diameter

The dark region around the ablated spot is a result of scattered and diffracted light around the rough edges of the mask features. During the translation of the centre of the fibre into the image plane of the objective, the surface of the fibre, besides the actual ablation area, undergoes slight ablation, which therefore produces roughness around the ablated structure. The laser was operated at low energy densities and pulse repetition rate to reduce the unwanted ablation on the fibre surface. The brightness of the laser-induced fluorescence gradually decreases with the number of pulses and falls abruptly when the fibre was ablated through its diameter. The abrupt decrease in brightness is due to the expansion of the beam towards the surface of the glass slide through the separation between the fibre and the glass slide. This can be observed in Figure 5-10 [A]. In order to confirm this observation, the laser was operated at a pulse repetition rate of 5 Hz and stopped immediately after observing the abrupt drop in fluorescence brightness via the CCD camera. Then the fibres were observed using optical microscope. These observations revealed the cavity formation through the diameter of the optical fibre. The optical fibres were micro-machined through their diameter at different energy densities using this technique.

9.1.2 Cavity-Tapering

The cavity wall angle of the fibres ablated at different energy densities was studied using an optical microscope. Optical micrographs of cavity wall profiles are presented in [A], [B], [C] and [D] of Figure 9-2.

Table 9-1: Taper angles of cavities machined in SMF 28 fibres at different energy densities.

Energy density [Jm^{-2}]	**Taper angle**
11.2 x 10^4	12°
18.2 x 10^4	9.3°
22 x 10^4	5.2°
25.5 x 10^4	<1°

The average taper angles measured at specified energy densities for a 38 μm x 38 μm microstructure machined along the diameter of the SMF 28 fibres is presented in Table 9-1. The taper angle is the angle made by the wall surface with the perpendicular to the axis of the fibre. It can be observed from the Table 9-1, that the tapering of cavity walls decreased with increasing energy density of ablation. This is in agreement with the findings of Paterson *et al.* [92].

Near-vertical cavity walls were achieved at an energy density of 25 x 10^4 Jm^{-2}. This is a very significant result with reference to the fabrication of Fabry-Perot cavities in optical fibres. Besides the optical quality of cavity wall surface, vertical walls of the cavity are an important criterion for producing Fabry-Perot interference. The aspect ratio (ratio of ablation depth to entrance diameter) of these cavities is 3.28. There has not been a previous report on F_2-laser micro-machined structures of aspect ratio of 3.28 with near-vertical wall angles in fused silica to the best of the knowledge of the author.

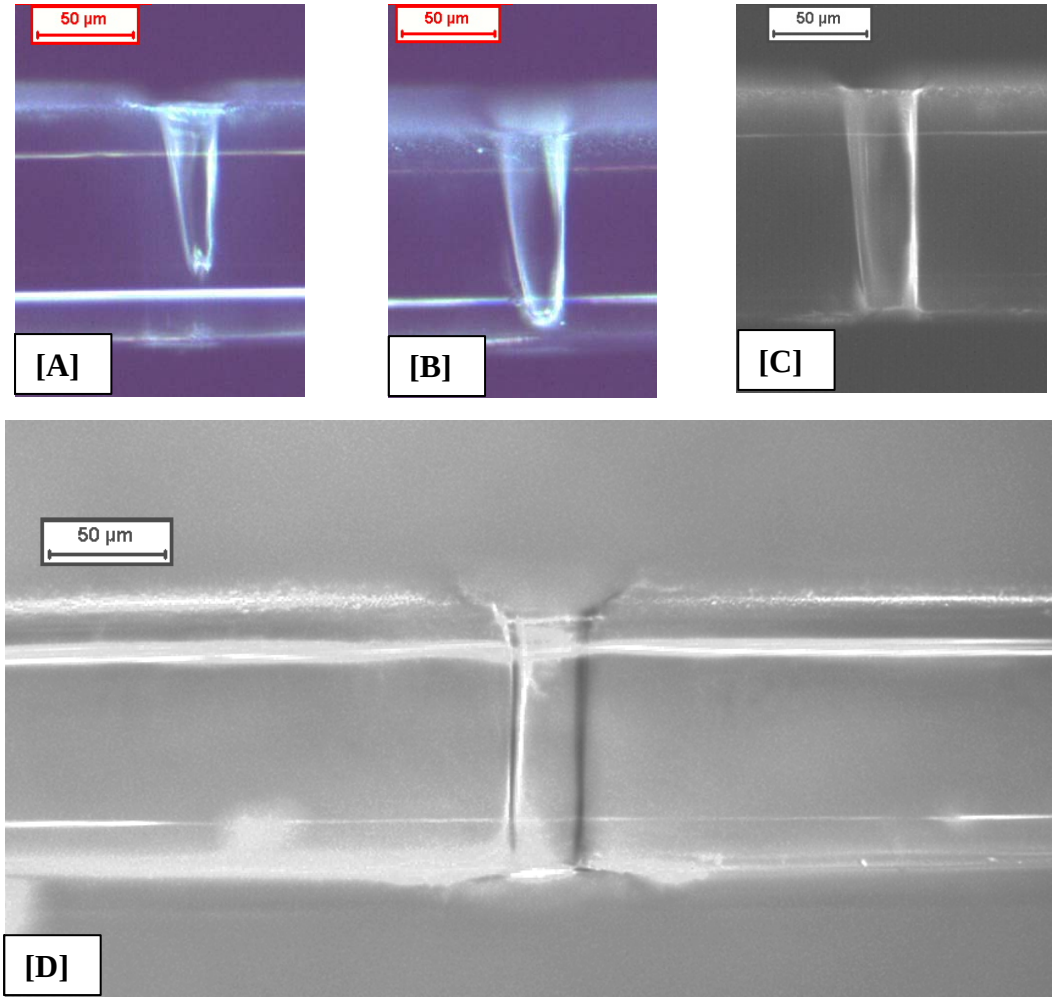

Figure 9-2: Optical micrographs of cavities drilled in SMF 28 fibres at different energy densities; [A] 11.2 x 10^4 Jm^{-2}; [B] 18.2 x 10^4 Jm^{-2}; [C] 22 x 10^4 Jm^{-2}, [D] 25 x 10^4 Jm^{-2}.

The primary reason for the tapering of cavity walls is de-focussing of image. The image remains in focus at the start of the ablation, however, as the material is removed by a series of pulses, the ablation depth increases and the image progressively becomes defocused. There are other factors such as plume attenuation and the non-uniform intensity profile of beam that are also responsible for the tapering. These are discussed in Section 8.1.1.1. According to reference [92], the evolution of the intensity distribution across the aerial image from the focal plane is determined by the energy density. This was found to be valid for photo-resist ablation at 193 nm using homogeniser optics. The energy densities used during their ablation studies of photo-resist to produce near-vertical wall angles were significantly lower compared to the energy densities used in fibre ablation experiments. The reason for this could be that the fused silica is much more weakly absorbing and has a higher

melting temperature than the photo-resist material. This reason can be supported by the Li *et al.* [102], in which energy densities as high as 9 x 10^4 Jm^{-2} at 157 nm were used to produce vertical walled cavities in microscope glass slides to a depth of 35 μm using beam homogeniser optics. Watanabe [83] proved that the depth of focus was higher for partially coherent illumination in lithographic applications. The ablation experiments of Paterson *et al.* [92] and Herman *et al.* [98] were carried out using an homogeniser-based partially coherent illumination optical beam delivery system, where as the illumination used by the author in fibre ablation experiments was fully coherent. However, the role partial coherence on wall angle of high aspect microstructures is unknown and requires in depth research.

Another important factor, which could effect the tapering of cavities, is the curvature of the work piece. During the ablation of a flat substrate, the image of the projected mask feature remains in focus on every area element on the surface and the entire irradiated area is exposed to a unique intensity profile for each pulse. If the substrate has a curvature, then different elemental areas of the irradiated region are exposed to different intensity profiles. For example, the 125 μm diameter optical fibre has a cylindrical symmetry with a curvature of 0.016 x 10^6 m^{-1}. When a 38 μm feature is focussed on the cylindrical surface of the fibre at its centre, then an elemental area on the centre of the fibre will be in better focus than the elemental area at the boundary of the irradiated area. This is schematically shown in Figure 9-3.

[A] and [B] of Figure 9-3, shows that the image de-focussing is higher for a microstructure of larger dimensions, when the image plane is symmetric about the plane passing perpendicularly through its centre and the axis of the fibre. [C] of Figure 9-3 shows that the defocusing is higher than [A] and [B], when the fibre is misaligned. To get a quantitative estimate of image distribution on the surface of the 125 μm optical fibre, the maximum difference in the height of a symmetrically distributed image plane on the surface of the fibre is calculated from Figure 9-4.

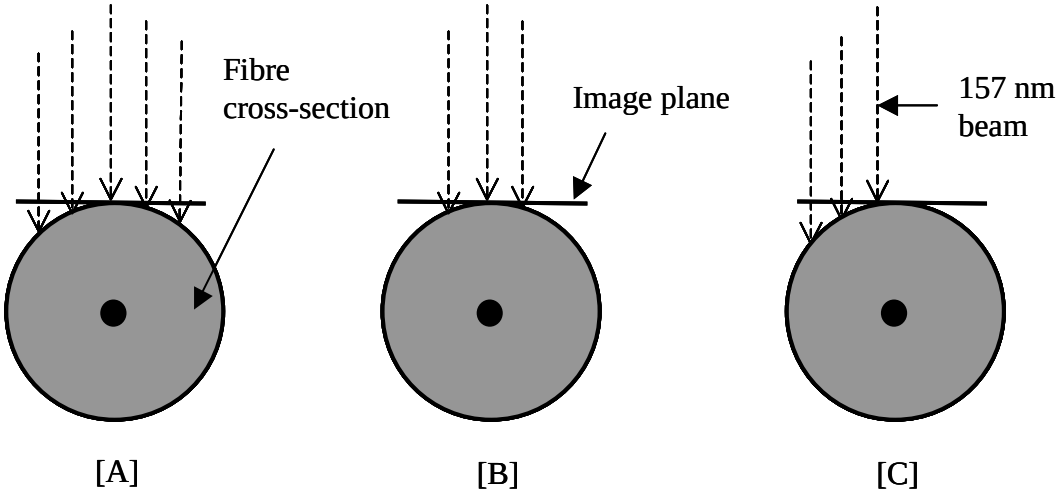

Figure 9-3: Schematic illustration of influence of substrate curvature on image de-focussing; [A] De-focussing of image of larger dimensions, [B] De-focussing of image of smaller dimensions, [C] De-focussing of image due to misalignment.

In Figure 9-4, ABC (= 38 μm) is the dimension of the image on the surface of the fibre; OA, OB, OC are radii of the fibre and BD is the maximum difference in height across the distributed image. From the calculation according to Figure 9-4, the maximum difference in height, which is the difference between the positions of image centre and image boundary, is 3.12 μm. This difference is a minimum when the fibre is symmetrically aligned. This is smaller than the depth of focus (=15.7 μm) of the imaging system according to Equation 3-1. The area of the image, which is at its boundary, experiences maximum de-focussing. In a similar calculation to that shown in Figure 9-4, if a 50 μm structure is symmetrically aligned on the surface of the optical fibre, then the corresponding maximum difference in distributed image height is difference 5 μm. If a 50 μm feature is aligned such that its boundary coincides with the central region of the fibre as shown in [C] of Figure 9-3, then the calculated maximum difference in height of the distributed image plane is 18.75 μm, which is larger than the depth of focus of imaging.

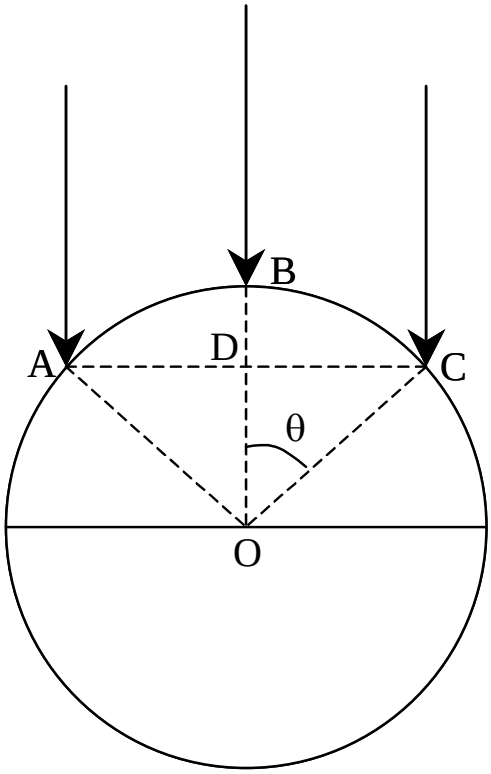

Figure 9-4: Schematic to illustrate the calculation of image plane distribution on fibre surface.

$$ABC = 38\mu m \qquad \text{Equation 9-1}$$

$$BC = OC \times \theta \qquad \text{Equation 9-2}$$

$$\Rightarrow \theta = \frac{19}{62.5} = 0.304rad$$

$$OD = OC \times \cos\theta \qquad \text{Equation 9-3}$$

$$\Rightarrow OD = 62.5 \times \cos 0.304rad = 59.38\mu m$$

$$BD = OB - OD = 62.5 - 59.38 = 3.12\mu m \qquad \text{Equation 9-4}$$

Therefore, purely from an optics point-of-view, it can be concluded that the micro-machined cavity tapering in a material, which is a result of image de-focussing, will be greater in curved substrates than flat substrates, for the same applied energy density. The de-focussing effect will be larger at greater surface curvatures of the substrate for specified dimensions of ablated structure due to higher difference in height. The image de-focusing will be greater for larger microstructures on a curved substrate. Misalignment of fibres in the image plane increases image de-focussing. The defocusing of the distributed image plane on the surface of the optical fibre will be a minimum when the fibre is symmetrically aligned. Therefore, the alignment of

optical fibres in the image plane determines the tapering of ablated micro-cavities. The problem posed by the curvature of the optical fibres could be overcome by polishing the cylindrical surface of the fibres.

9.1.3 Interrogation of Ablated Cavities

The etalons micro-machined at different energy densities across the core of the SMF 28 and SM 800 optical fibre were interrogated using an optical spectrum analyser and CCD spectrometer respectively. The interrogation scheme is presented in Section 5.3.5. Microstructures of dimensions of 38 μm x 38 μm and 50 μm x 50 μm were machined a different energy densities through the diameter of the optical fibres. Fabry-Perot interference was observed in cavities micro-machined at an energy density of 25 x 10^4 Jm^{-2}. This energy density is in good agreement with the energy density of 24.5 x 10^4 Jm^{-2} used for producing clean and smooth structures in fused silica disks. This proves that the micro-machined etalon surfaces have adequate optical finish and wall angle to produce FP interference. The representative FP interference fringes obtained from three different micro-machined cavities are presented in Figure 9-5 and Figure 9-6. These results are very significant as they demonstrate a novel technique for the production of intrinsic Fabry-Perot optical fibre devices. To the best of the knowledge of the author, there has been no previous report of intrinsic Fabry-Perot cavities produced via laser micro-machining in optical fibres.

In Figure 9-5, [A] represents a cavity length of 47.5 μm and [B] represents a cavity gap length of 42.2 μm. These cavity lengths were calculated using Equation 2-6. The cavity corresponding to [A] was produced by machining a 50 μm x 50 μm structure and the cavity corresponding to [B] of Figure 9-5 were produced by machining a 38 μm x 38 μm. The cavity lengths produced were not exactly the same as the feature dimensions. This gives an impression that the cavity walls are not vertical, however, they produce FP interference fringes. According to Paterson *et al.* [92], the wall angle of the cavities obeys an evolution of the aerial image. Their modelling also takes the ablation rate of the photo-resist material into account, which in turn is determined by absorption of radiation by the material. In the case of micro-machining FP cavities in optical fibres, the wall angle across the core diameter of 9 μm could be

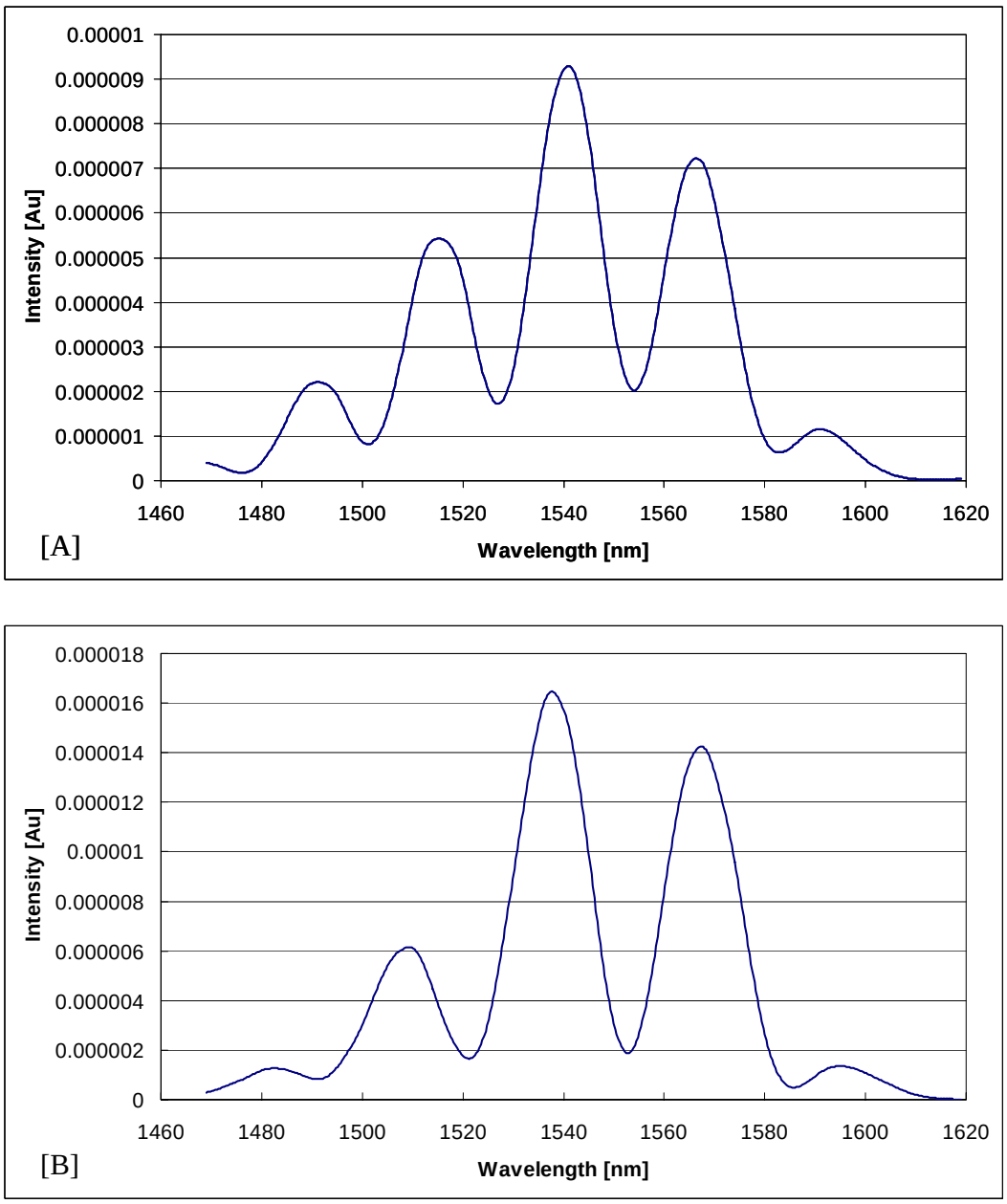

Figure 9-5: Interference fringes of a FP etalon micro-machined at 25 x 10^4 Jm^{-2} in SMF 28 fibre; [A] 47.5 μm cavity gap length and [B] 42.2 μm cavity gap length.

different from the wall angle of cladding. The aerial image from the cladding-core interface to core-cladding interface determines the wall angle across the core. The reason for this is that the germania-doped core of the fibre has a much stronger absorption of the 157 nm beam than the fused silica cladding and therefore the evolution of the aerial image across the diameter of the core could produce a vertical wall angle and hence producing FP interference.

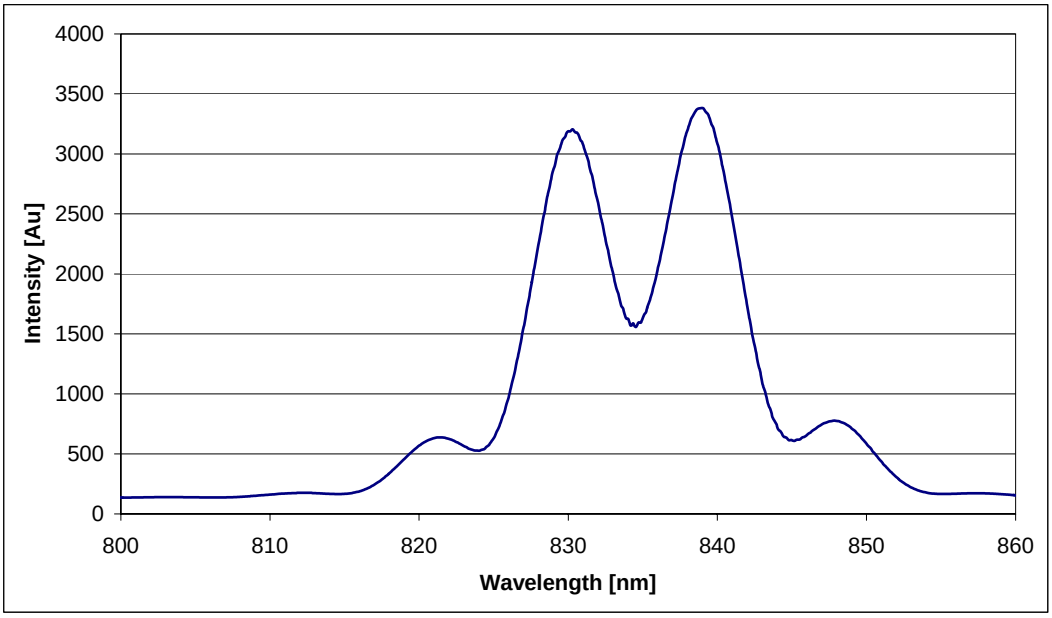

Figure 9-6: FP interference fringes produced from a cavity micro-machined at 25 x 10^4 Jm^{-2} in SM 800 fibre.

From Figure 9-6, the cavity gap length calculated using Equation 2-8 is 39.6 μm. The etalon surface across the core of the optical fibre has to have a higher optical finish for an SM 800 fibre than for an SMF 28 fibre due to its shorter operating wavelength. Therefore, in principle, it is relatively easy to fabricate Fabry-Perot devices in SMF 28 fibres. This is the reason why the ablation of SMF 28 was more extensively carried out. However, FP interference was also produced at 25 x 10^4 Jm^{-2} in SM 800 fibres. Therefore this energy density is suitable for producing FP structures in both SMF 28 and SM 800 fibres. The difference between the ablation of SMF 28 and SM 800 fibres is that their core-doping concentrations and core diameters are different as shown in Table 5-1. As mentioned earlier with respect to the calculated cavity gap length of cavities in SMF 28 fibres, the difference in 157 nm absorption due to the difference in doping concentrations could also influence the wall angle across the core surface.

From Figure 9-5 and Figure 9-6, the FP fringes produced by Fresnel reflections at the micro-machined etalon surfaces have adequate contrast to calculate cavity lengths. Therefore, F_2-laser based fabrication of intrinsic Fabry-Perot devices in optical fibres is a feasible technique. However, difficulty was experienced during precise alignment of the optical fibres in the image plane. This is due to a lack of uniformity of illumination brightness of the cylindrical surface of the fibre and insufficient

magnification for CCD camera monitoring. These problems can be overcome by designing a uniform illumination around the target surface and by using a higher magnification lens for the CCD camera.

9.1.4 Calculation of Cavity Tapering Effects

As mentioned in the preceding section, the evolving aerial image at the cladding/core interface could be a significant factor, which determines the cavity length and resulting FP interference. On a different perspective, there could be a threshold of the taper angle of the cavity walls above which FP interference cannot be produced or observed. The commercial fibre cleavers can produce a typical cleave angle of 0.5° or less (Furukawa Inc., Japan) and these cleavers are used for cleaving single mode fibres to produce extrinsic Fabry-Perot sensors. This implies that the departure of etalon surfaces from parallelism by 0.5° can still produce FP interference. Therefore an attempt was made to calculate theoretically the threshold of the cavity wall angle above which FP interference cannot be produced. The calculations were based on the following assumptions:

1. The optical finish of the ablated cavity wall surface is the same as that of a cleaved fibre.
2. The refractive index of air between the cavity walls is assumed to be equal to unity.
3. There are no absorption losses at the wall surface or in the medium between the cavity walls.

These calculations were classified into two parts. The first part determines the threshold of the cavity wall angle and the second part determines whether the second Fresnel reflection incidents across the core of the first wall surface for a specified cavity length and taper angle.

9.1.4.1 Calculation of Threshold of Cavity Taper Angle

These calculations were performed by using the well know Snell's laws of reflection and refraction. It is essential that the second Fresnel reflection from the air/core interface of the second wall of the cavity be coupled into the core across the first wall surface of the cavity for a specified cavity wall angle to interfere with the first Fresnel reflection. The second Fresnel reflection will couple into the core across the first wall of the cavity only when it is incident on the core and the angle of incidence complies with the numerical aperture (NA) of the fibre. Therefore, the angles of incidence of the second Fresnel reflection on the first wall surface for different taper angles of the cavity were calculated. An illustration of ray path between the two cavity walls is presented in Figure 9-7.

From Figure 9-7, the light is incident on the first wall surface along the axis of the fibre. 'θ_t' is the taper angle of the cavity and as the light ray is incident along the axis of the fibre on the first wall, the angle of incidence is the same as the taper angle of the cavity. Air (refractive index =1) is the medium in between the cavity walls. An SM 800 fibre has a numerical aperture of 0.13 and a cladding index of 1.457. The refractive index of the core is calculated by using the equation that defines the numerical aperture of the fibre. This equation is as follows:

$$Numericalaperture = \sin\theta = \sqrt{n^2_{core} - n^2_{cladding}} \qquad \text{Equation 9-5}$$

where 'n_{core}' is the refractive index of the core and '$n_{cladding}$' is the refractive index of the cladding and 'θ' is the maximum angle that a light ray can make with the fibre axis to be coupled into the core of the fibre. From this formula, the refractive index of the core was found to be 1.4627.

From Figure 9-7, the details of various angles are presented as follows:

(i) 'θ_{1i} (= θ_t)' is the angle of incidence of light along the axis at the first wall.

(ii) 'θ_{1r}' is the angle of refraction ($\sin^{-1}(n_{core}\sin\theta_t)$).

(iii) 'θ_{2i} ' is the angle of incidence of refracted ray at the second wall surface.

(iv) 'θ_{21i}' is the angle of incidence of second Fresnel reflection across the core of the first wall.

(v) 'θ_{21r}' is the angle of refraction of second Fresnel reflection into the core of the first wall.

(vi) '$(90 - \theta_t)$' is the angle between the extended incident ray (along the axis) on the first wall and the second wall.

(vii) '$(90 + 2\theta_t - \theta_{1r})$' is angle between the transmitted ray from the first wall and the second wall.

(viii) '$(\theta_{2i} = 2\theta_t - \theta_{1r})$' is the angle of incidence of transmitted ray from the first wall at the point of incidence on the second wall.

(ix) '$(90 - 2\theta_t + \theta_{1r})$' is the angle between the second Fresnel reflection and the second wall.

(x) '$(3\theta_t - \theta_{1r})$' is the angle between the second Fresnel reflection and the extended incident ray (along the axis) on the first wall.

(xi) '$(90 + \theta_t)$' is the angle between the extended incident ray (along the axis) on the first wall and the first wall.

(xii) '$(90 - 4\theta_t + \theta_{1r})$' is the angle between the second Fresnel reflection and the first wall.

(xiii) '$\theta_{21i} = (4\theta_t - \theta_{1r})$' is the angle of incidence of the second Fresnel reflection at the point of incidence on the first wall.

Assuming that the second Fresnel reflection is incident on the core of the first wall, the second Fresnel reflection will be coupled into the core when $(4\theta_t - \theta_{1r}) \leq \sin^{-1}$ (NA). For SM 800 fibres, $\sin^{-1}$ (0.13) = 7.4695°. The calculated values of 'θ_{1r}' and '$(4\theta_t - \theta_{1r})$' for different taper angles of the cavity, θ_t (= θ_{1i}) are presented in Table 9-2. From Table 9-2 it can be observed that the angle of incidence of the second Fresnel reflection on the core of the first wall surface complied with the numerical aperture of the fibre until the cavity taper angle is 2.9°.

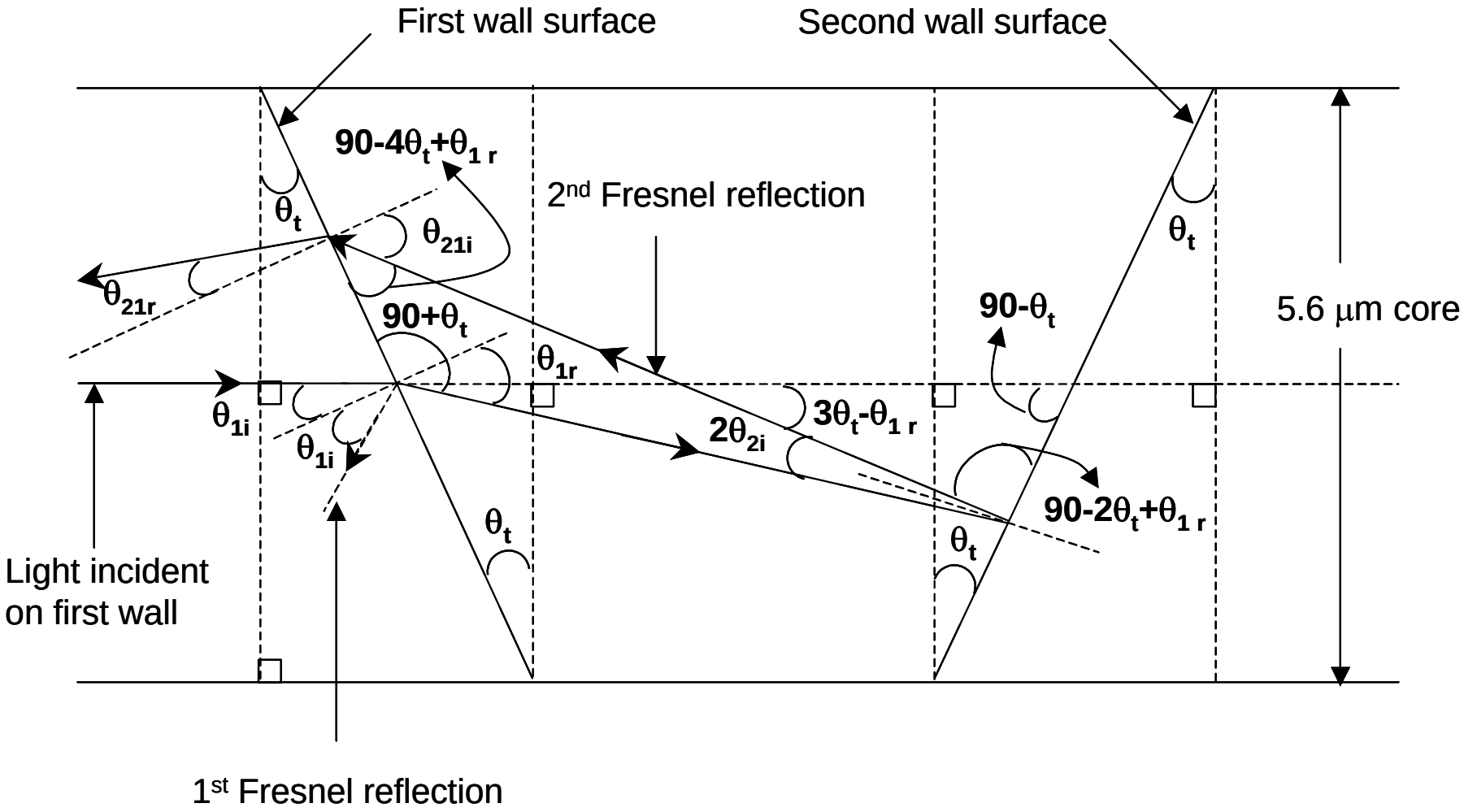

Figure 9-7: Schematic illustration of ray path across a tapered cavity.

Table 9-2: Table of calculated values of 'θ_{1r}' and '$(4\theta_t - \theta_{1r})$' for different taper angles of cavity.

Taper angle of cavity $[\theta_t (= \theta_{1i})]$	**Angle of refraction at core/air interface $[\theta_{1r}]$**	**Angle of incidence of 2nd Fresnel reflection on the core of the first wall $[\theta_{21i} = 4\theta_t - \theta_{1r}]$**
0.5°	0.7276°	$1.2724° < \sin^{-1}(0.13) = 7.4695°$
1°	1.4554°	$2.5446° < 7.4695°$
1.5°	2.1834°	$3.8166° < 7.4695°$
2.5°	2.9176°	$5.0824° < 7.4695°$
2.25°	3.2848°	$5.7152° < 7.4695°$
2.5°	3.6522°	$6.3478° < 7.4695°$
2.75°	4.0139°	$6.9861° < 7.4695°$
2.9°	**4.2322°**	**$7.3678° < 7.4695°$**
2.95°	4.3069°	$7.4931° > 7.4695°$
3°	4.3816°	7.6184°
3.5°	5.1175°	8.8825°
4°	5.8485°	10.1515°
4.5°	6.5805°	11.4195°
5°	7.3193°	12.6807°
5.5°	8.0536°	13.9464°
6°	8.7892°	15.2108°

Therefore, there is a possibility for the interference of two Fresnel reflections for a cavity taper angle in the range $0° \leq \theta_t \leq 2.9°$. The contrast of the resulting FP fringes will depend on the relative intensities of the Fresnel reflections coupled into the fibre. For $\theta_t \geq 2.95°$, there is no possibility for the second Fresnel reflection to couple into the core of the first wall surface, as the angle of incidence does not comply with the numerical aperture of the SM 800 fibre. This conclusion is true only for the assumptions on which these calculations are based on. The ray paths, which make non-zero angles with the axis of the fibre, are not considered in these calculations. The diffracted light emanating from the core is also not considered. However, these

calculations prove that departure of micro-machined etalon surfaces from parallelism to a specified degree ($0° \leq \theta_t \leq 2.9°$ according to the calculations) in the case of SM 800 fibres could still produce FP interference. In a similar fashion, there could be range of tolerance of cavity taper angle beyond which FP interference could not occur in the case of SMF 28 fibres as well.

In order to compare the Fresnel reflections of tapered cavities with that of an un-tapered cavity, the absolute reflectance (assuming the incident intensity to be 1) of the first and second Fresnel reflections as mentioned in Figure 9-7, are presented in Figure 9-8 and Figure 9-9 respectively. From Figure 9-8 and Figure 9-9, it can be observed that the reflectance of the first Fresnel reflection increases with the taper angle and the transmittance of the second Fresnel reflection into the first wall decreases. Therefore, the contrast of the resulting FP fringes for a tapered cavity will be smaller than that for an un-tapered cavity.

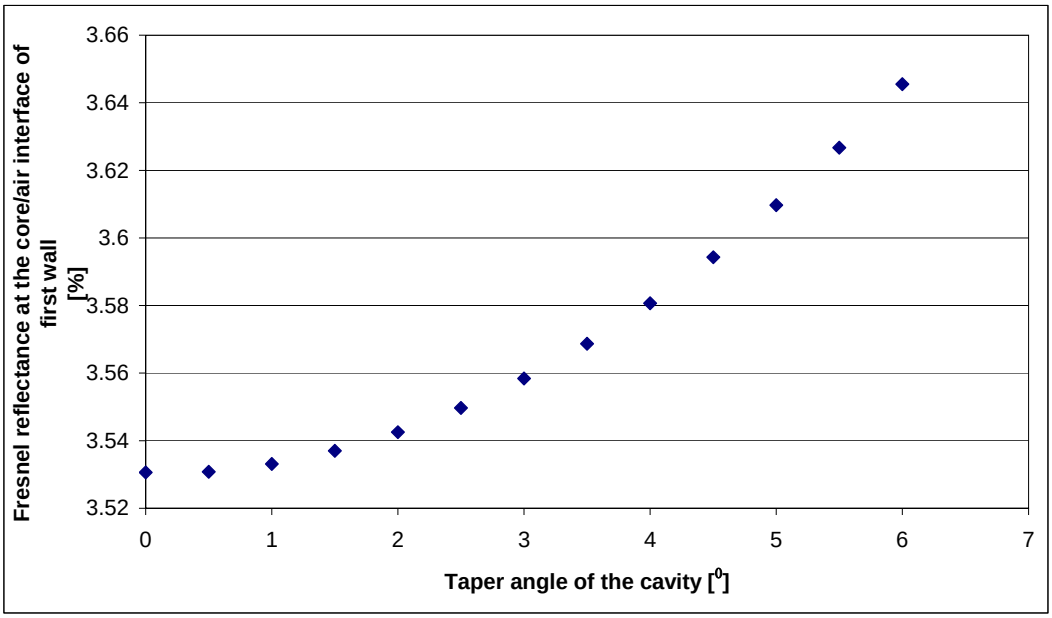

Figure 9-8: Influence of cavity tapering on first Fresnel reflection.

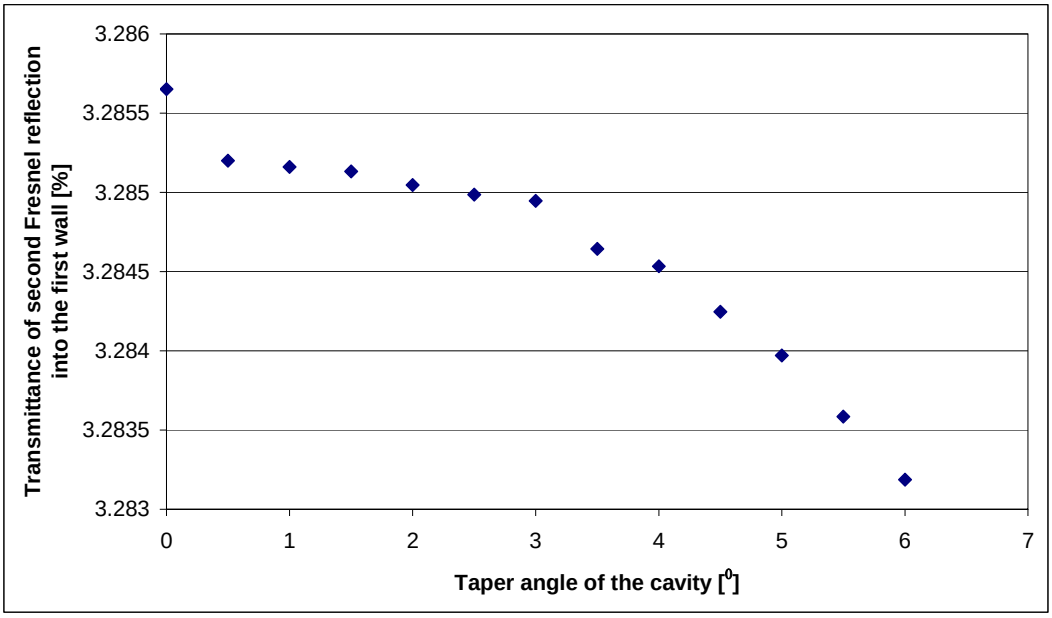

Figure 9-9: Influence of cavity tapering on the second Fresnel reflection.

9.1.4.2 Calculation of Position of Incidence of Second Fresnel Reflection

In the preceding section, the threshold of cavity taper angle that permits the second Fresnel reflection into the first wall was determined. However, the second Fresnel reflection must be incident on the core across the first wall to be coupled into the fibre. The following calculations determine whether the second Fresnel reflection is incident on the core across the first wall. The ray path between the tapered walls is presented in Figure 9-10. The calculations were based on the assumptions that the optical finish of the tapered wall surface is the same as that of a cleaved end-face of an optical fibre, the cavity entrance dimensions are 40 μm x 40 μm and the taper angle of the cavity, 'θ_t' is 2.75°. The calculation is presented in Appendix A with reference to the Figure 9-10. The calculation shows that the second Fresnel reflection will incident on the core of the first wall surface.

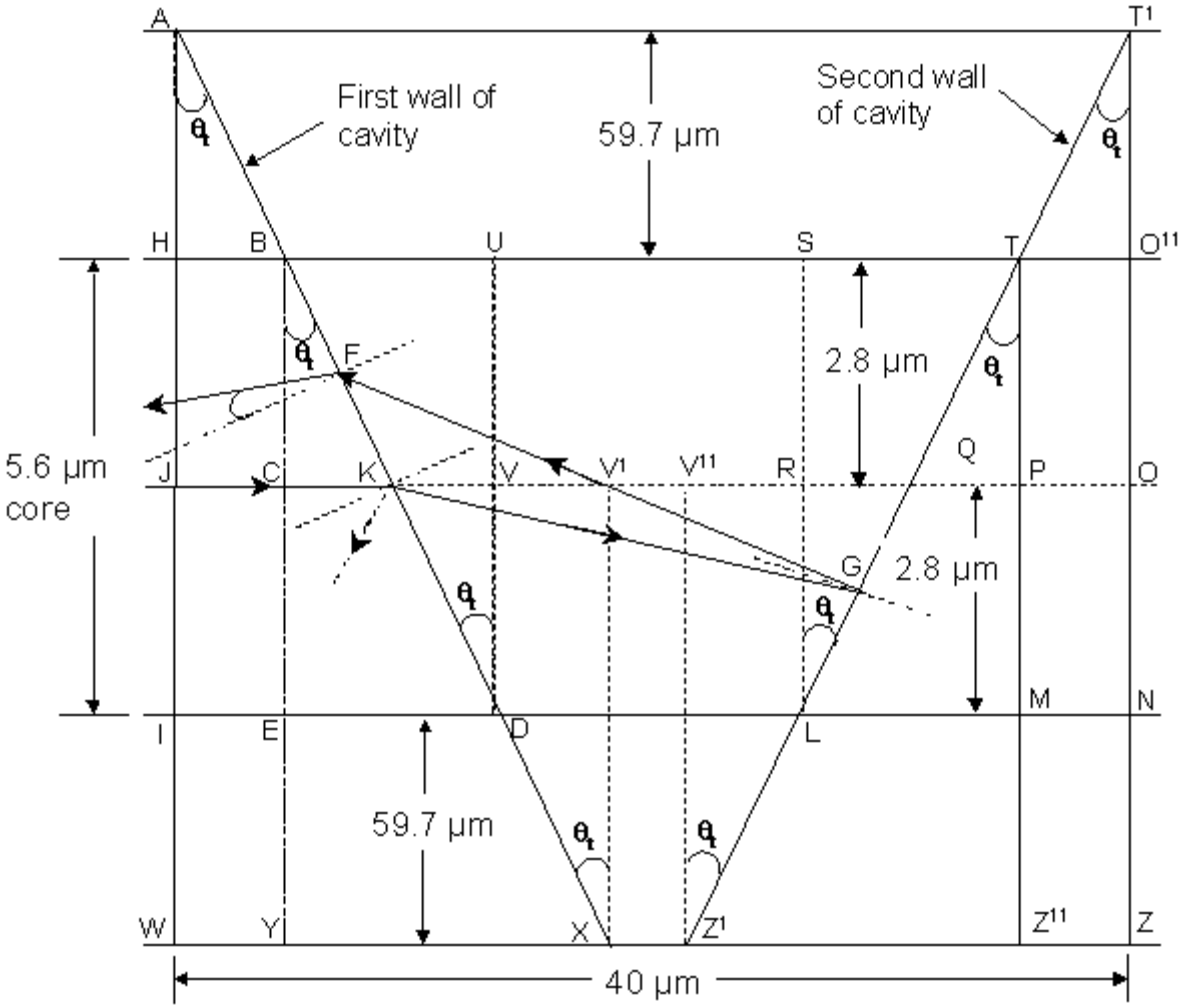

Figure 9-10: Schematic illustration of ray path in a cavity.

Therefore according to these calculations as presented in Appendix A, for $\theta_t = 2.75°$ and an entrance dimension of 40 μm, the second Fresnel reflection will be incident on the core across the first wall and according to the preceding calculations, will be coupled into the core. Although these calculations show that departure from parallelism to a certain degree can still produce FP interference, there are other factors such as the ablation-induced roughness of the cavities, ablation debris across the cavity walls and misalignment of fibres in the image plane that could affect the FP interference.

9.1.5 SEM Study of Micro-machined Fibres

The micro-machined optical fibres were observed using an SEM to study the morphology of cavities and wall surfaces. SEM micrographs of ablated cavities along the optical fibre diameter are presented in Figure 9-11 and Figure 9-12. Figure 9-11 shows the cavity drilled on the cylindrical surface of a fused silica fibre. Figure 9-12 shows the cavity formed through the diameter of the fibre. The entrance and exit of the cavity can be clearly seen. The wall surfaces of the cavities are smooth and clean.

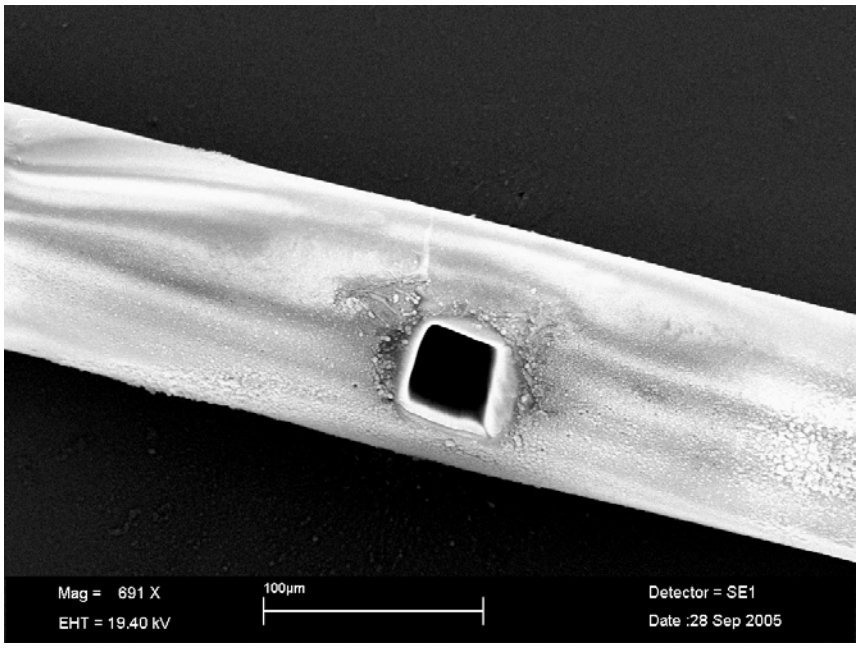

Figure 9-11: A 40 μm x 40 μm structure ablated at 25 x 10^4 Jm^{-2}.

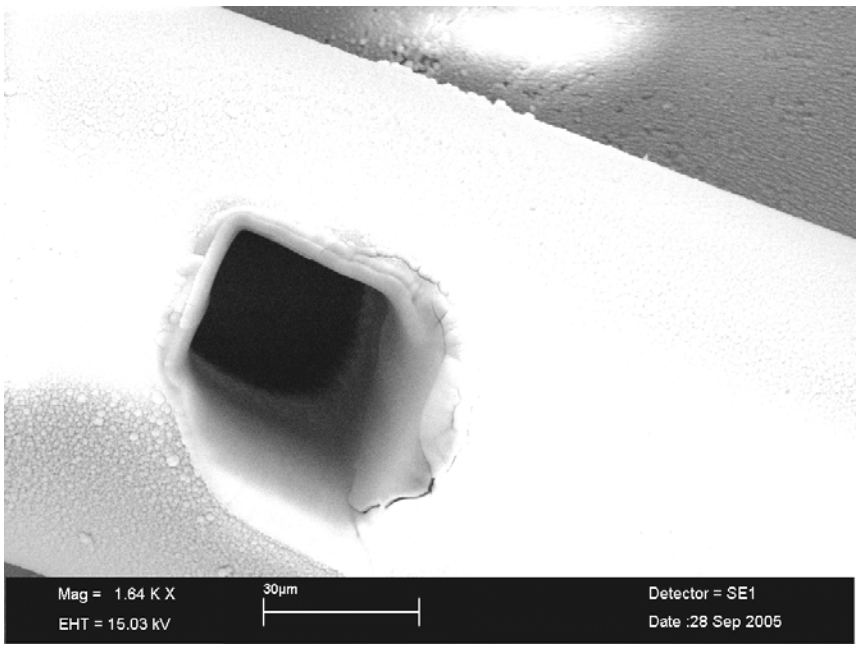

Figure 9-12: Entrance and exit of a cavity micro-machined through the diameter of a fibre.

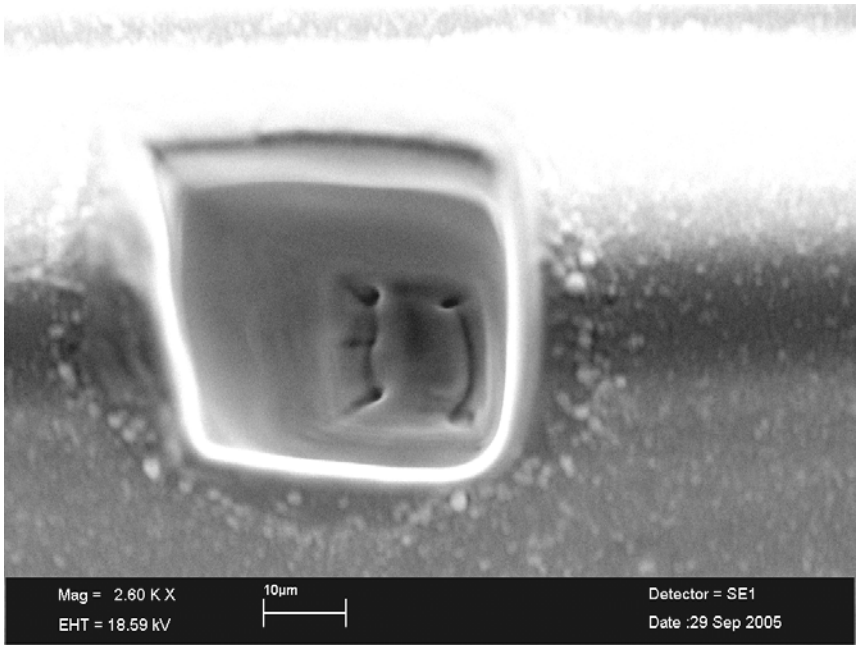

Figure 9-13: Cavity ablated at 21 x 10^4 Jm^{-2} in a fused silica fibre.

From Figure 9-13, it can be observed that the general morphology of sidewalls and the crater of the cavity are very smooth. The edge-ringing [77] effects on the crater surface are obvious. The general morphology of a cavity is much cleaner and smoother in silica fibres than in silica disks. This is probably due to the stronger absorption of the cladding fused silica via manufacturing process-induced defects as mentioned in Table 2-2. As mentioned in Table 5-1 and Table 5-2, the softening temperature of fused silica fibres is 1600 °C, whereas it is 1710 °C for fused silica disks. This could also be a reason for more efficient material ablation in fibres producing smoother and cleaner microstructures than in the disks.

The ablated SMF 28 fibres were fractured by bending the fibre and the cavity wall morphology was studied using SEM.

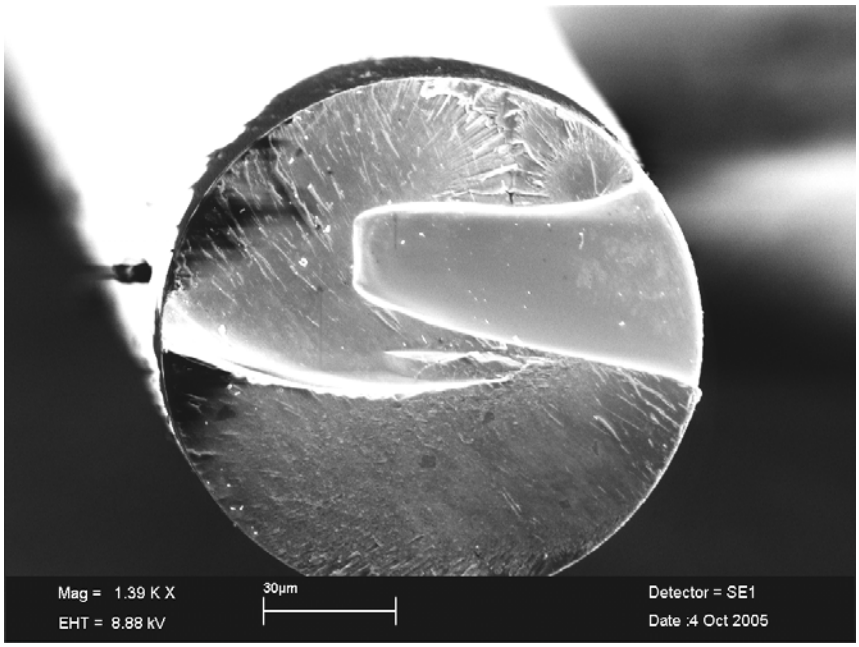

Figure 9-14: Cross-section of a cavity wall ablated at 22 x 10^4 Jm^{-2}.

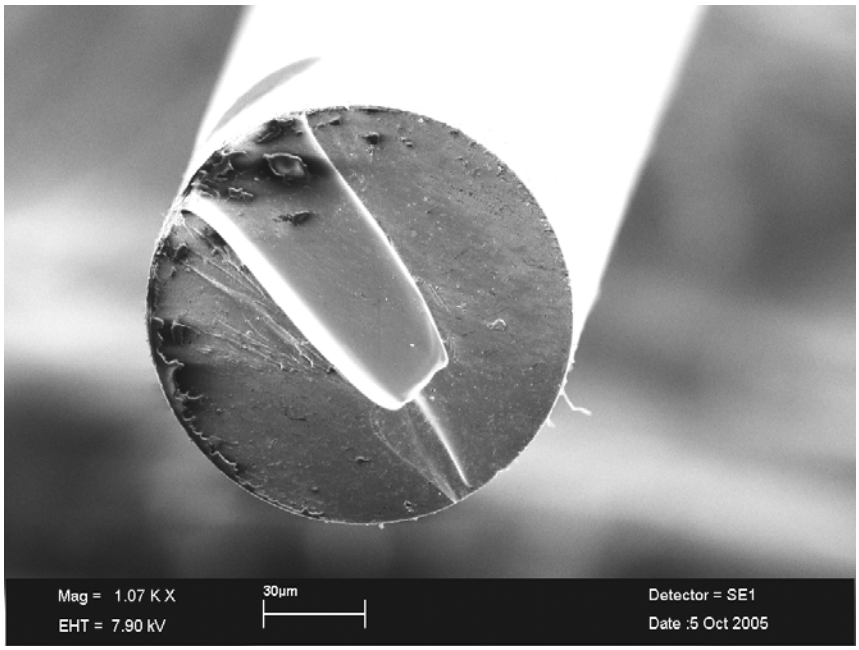

Figure 9-15: Cross-section of a cavity wall ablated at 23.8 x 10^4 Jm^{-2}.

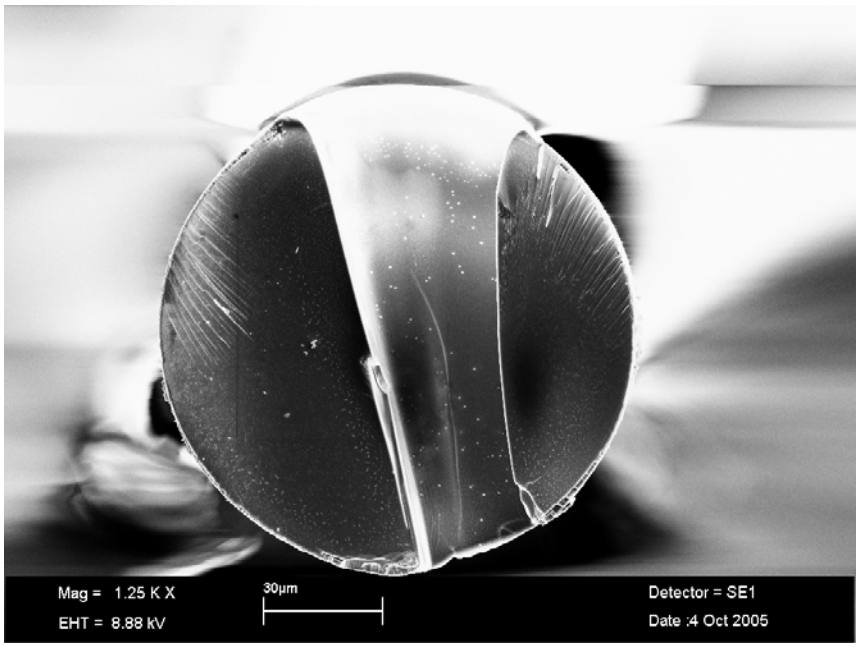

Figure 9-16: Cross-section of a cavity wall ablated at 23 x 10^4 Jm^{-2}.

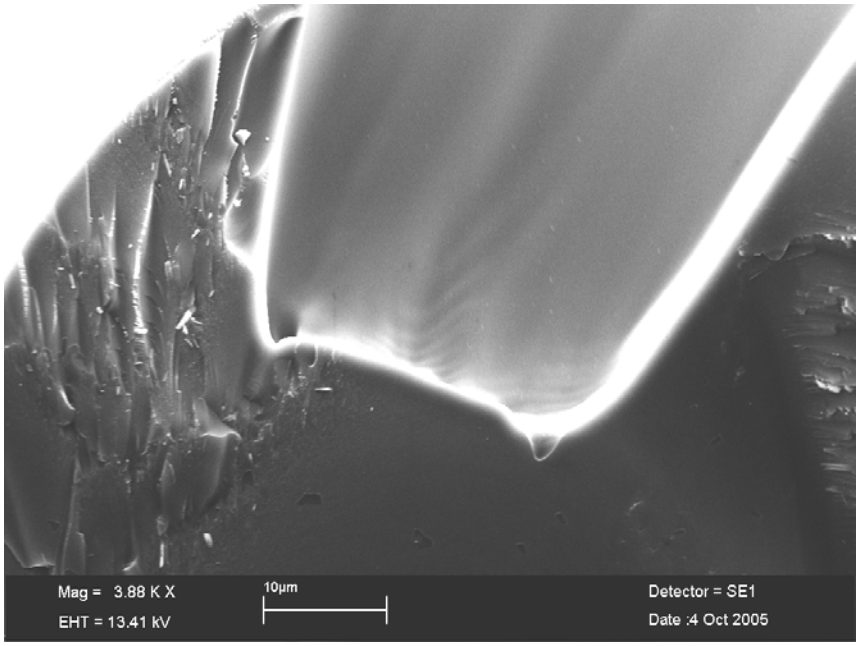

Figure 9-17: Cavity wall morphology and edge-ringing effects near a crater.

From Figure 9-14, Figure 9-15, Figure 9-16 and Figure 9-17 it can be observed that the cavity walls are relatively much smoother than in the fused silica disks used in these experiments. However, a small amount of ablation debris is also present. The cavities shown in Figure 9-15 and Figure 9-16, although produced at slightly different energy densities of ablation, the cavity wall tapering is significantly different from each other. The cavity of Figure 9-15 is nearer the centre of the fibre than that of Figure 9-16. According to Figure 9-4, the defocusing of the image plane will be higher for the cavity shown in Figure 9-16 than the cavity shown in Figure 9-15 and hence produce a different cavity tapering. This shows that the alignment of the fibre in the image plane is a significant factor, which determines the tapering of cavity walls. Therefore the cavity wall tapering must be minimum when the fibre is symmetrically aligned in the image. This can be observed from Figure 9-18. The cavity wall tapering is significantly lower in Figure 9-18 due to less defocusing of the image plane compared to Figure 9-14 and Figure 9-16. In Figure 9-16, there is an evidence of crack formation on the cavity wall surface. Figure 9-19 shows this crack at a higher magnification. It has width of 142 nm. This crack formation was not repeatedly observed.

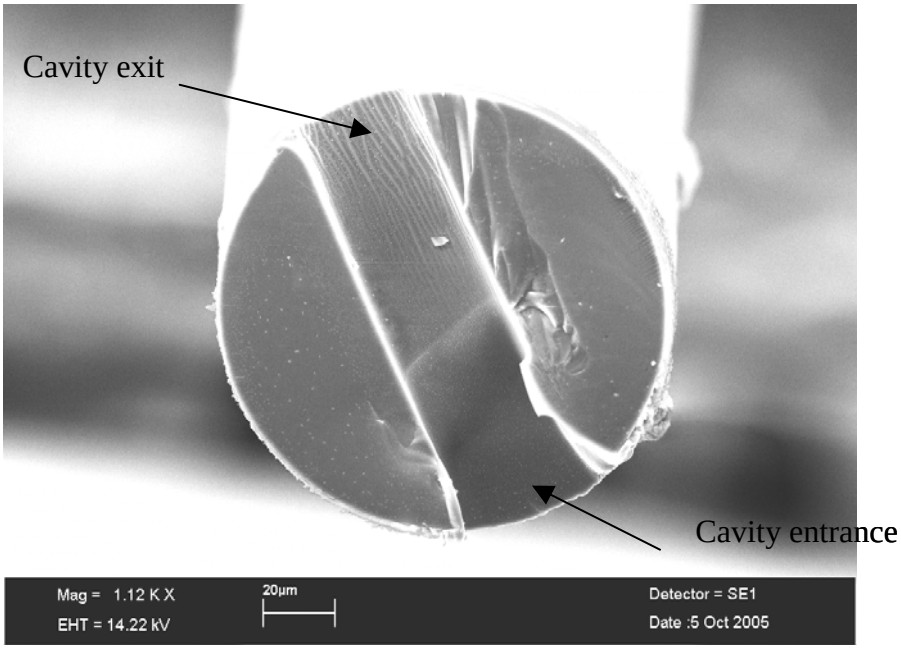

Figure 9-18: Cavity through the fibre diameter at 25 x 10^4 Jm^{-2}.

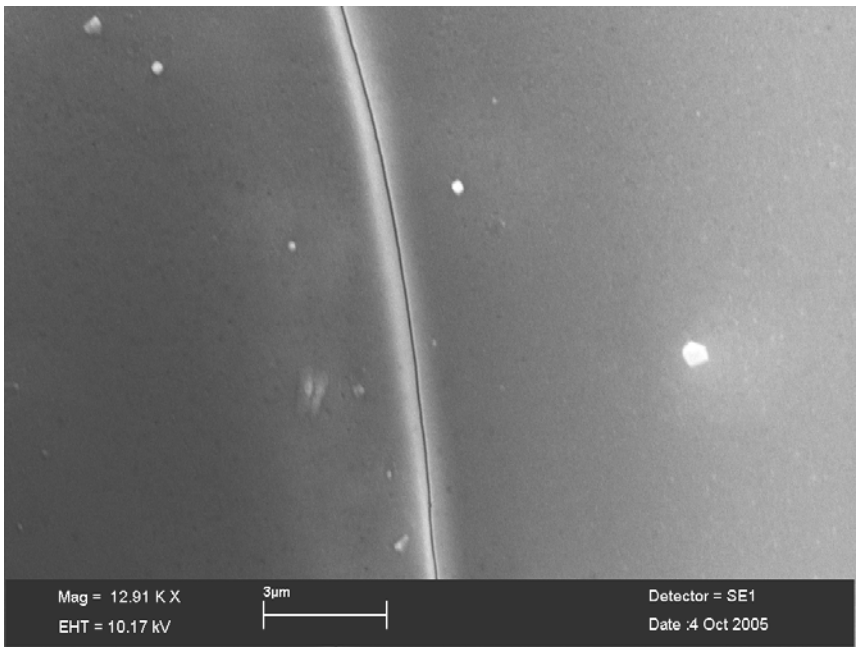

Figure 9-19: Crack on cavity wall surface.

Crack formation on ablated cavity wall surfaces could be explained by three reasons. Material compaction and tensile stresses produce cracks in fused silica at energy densities ranging from 1.9 - 4.7 x 10^4 Jm^{-2} during 157 nm laser ablation [105]. The energy densities used in fibre ablation experiments were significantly higher than the energy densities reported Konovalov and Herman [105]. In addition to that, as mentioned in Section 2.8.2.1, the laser-induced plasmas relax by transferring their heat to the cavity walls by conduction. The cavities drilled in optical fibres have aspect ratios higher than 3. The sudden cooling of cavity walls after the expansion of the plasma could lead to cracking of the wall surface. Another reason for cracking of ablated wall surfaces is stress corrosion of fused silica [75]. Atmospheric moisture can diffuse into the exposed fused silica surfaces resulting in structural relaxation of the surface layer. The diffused moisture forms hydroxyl groups in the silica matrix. The diffusion of water into silica surface is accelerated by the presence of tensile stresses in the surface layers. According to Konovalov and Herman [105], the ablated wall surface of the cavities in fibres could have ablation-induced tensile stresses. Therefore, the diffusion of atmospheric moisture into the ablated wall surface could be accelerated due to the presence of ablation-induced tensile stresses, which cause stress relaxation in the surface layer. This process could lead to crack formation on the cavity walls. The fibre fracturing process could also be a reason for crack formation on the wall surface.

Therefore, one or more of the above factors could be responsible for crack formation on the ablated cavity wall surfaces. However, the exact reason for crack formation could not be explained, as it requires further investigations focussed on material compaction and ablation-induced stresses during 157 nm ablation of high-aspect ratio cavities. The cracking of cavity wall surfaces is detrimental to the fabrication of Fabry-Perot devices in optical fibres as they deteriorate the optical reflectivity of the wall surface.

9.1.6 Surface Profile Analysis of Cavity Walls

The ablated cavity walls were studied using an interferometric surface profiler to gain quantitative information on their optical quality and for three-dimensional profiling of

wall geometry. The area difference plot of the wall surface of representative cavities ablated at 23 x 10^4 Jm^{-2} and 22 x 10^4 Jm^{-2} is presented in Figure 9-20 and Figure 9-21. The flatness of the wall surface of a cavity ablated at 24 x 10^4 Jm^{-2} is presented in Figure 9-22 and Figure 9-23. Contours of an ablated cavity wall are presented in Figure 9-24.

In Figure 9-20, each block area is defined on a highly reflecting region of the cavity wall surface. The significance of the coloured regions of the surface map has already been described in Section 8.1.1.2. All the blocks have an equal area of 10.05 µm x 9.70 µm and the average RMS roughness over an area of 10.05 µm x 9.70 µm on the wall surface is 445 nm. This RMS roughness is less than half the operating wavelength of the SMF 28 fibre. The cavity wall surface had an adequate optical finish to produce Fabry-Perot interference.

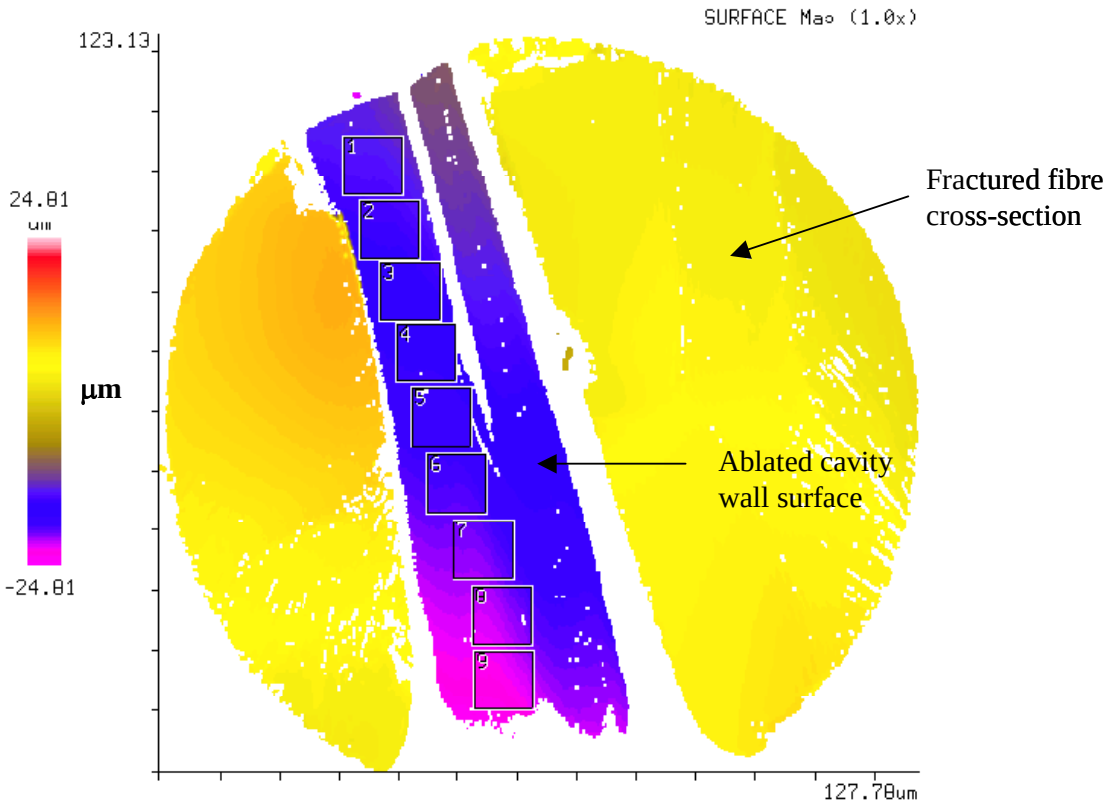

Figure 9-20: Area difference plot of the wall of a cavity ablated at 23 x 10^4 Jm^{-2}.

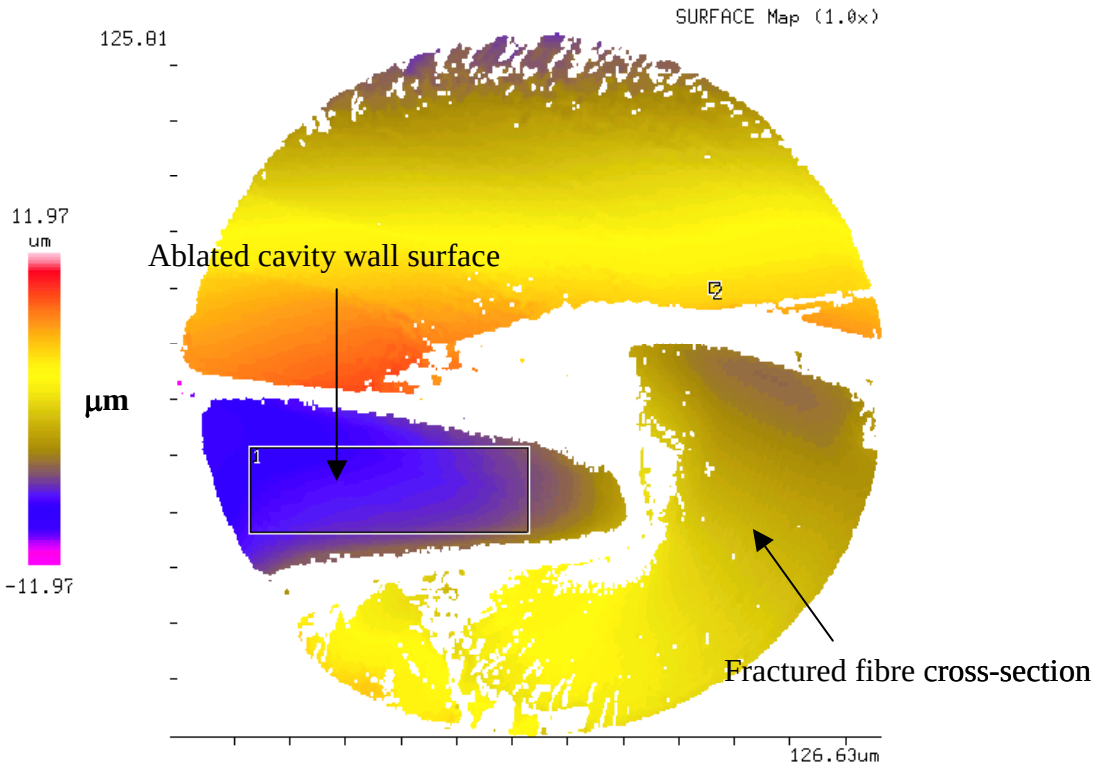

Figure 9-21: Long range roughness of the wall surface produced at 22 x 10^4 Jm^{-2}.

In Figure 9-21, the RMS roughness of the wall of the cavity ablated at 22 x 10^4 Jm^{-2} over an area of 50.25 µm x 15.73 µm is 720 nm. This RMS roughness is less than half the operating wavelength of the SMF 28 fibre. The long-range roughness is usually higher than the short-range roughness due to non-uniformities in the spatial intensity distribution across the image plane and a loss of intensity of the beam with increasing ablation depth.

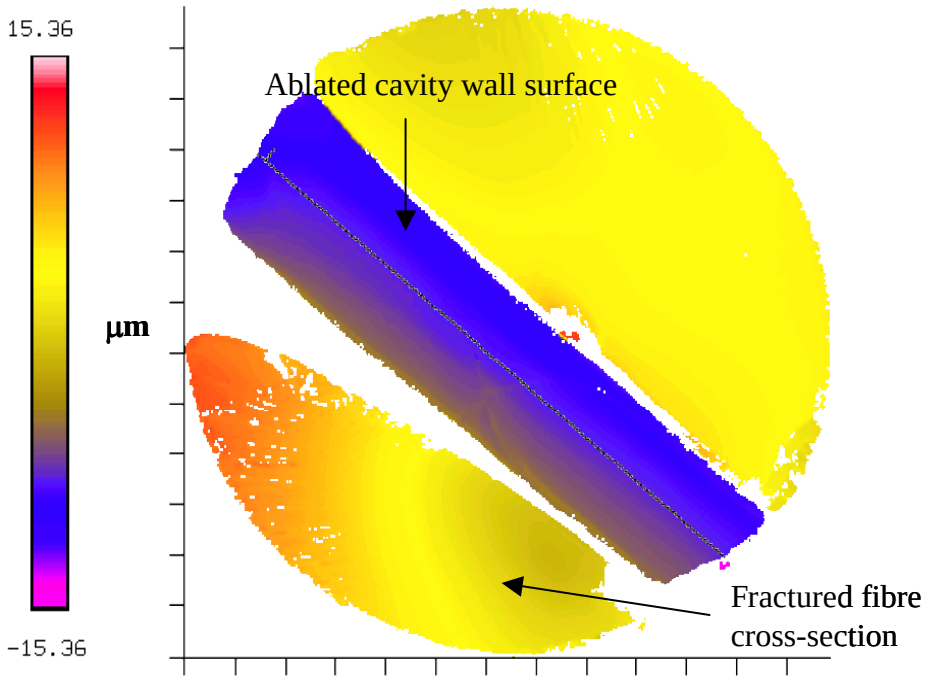

Figure 9-22: Surface map of the wall of a cavity ablated at 24 x 10^4 Jm^{-2}.

Figure 9-22 shows a surface map of the wall surface of a cavity ablated at 24 x 10^4 Jm^{-2}. A line segment is defined at the centre of the cavity along its length. The surface profile along the defined line segment is presented in Figure 9-23. The green curve in Figure 9-23 represents the wall surface profile along the line segment defined in Figure 9-22. It can be observed that the difference of height in the tag position to the cursor position is 265 nm over a length of 110.45 µm. This difference in height is a quantitative measurement of flatness of the cavity wall surface. Besides the RMS roughness of the wall surface, the flatness of the cavity walls determines the normal Fresnel reflection of light across the core of the etalon surface, which in turn determines the Fabry-Perot interference of Fresnel reflections. Three-dimensional contour plots of a symmetric cavity ablated at 25 x 10^4 Jm^{-2} are presented in Figure 9-24. The wall surface of the cavity, the formation of the cavity along the fibre diameter and the fractured region of the cladding surface can be clearly seen.

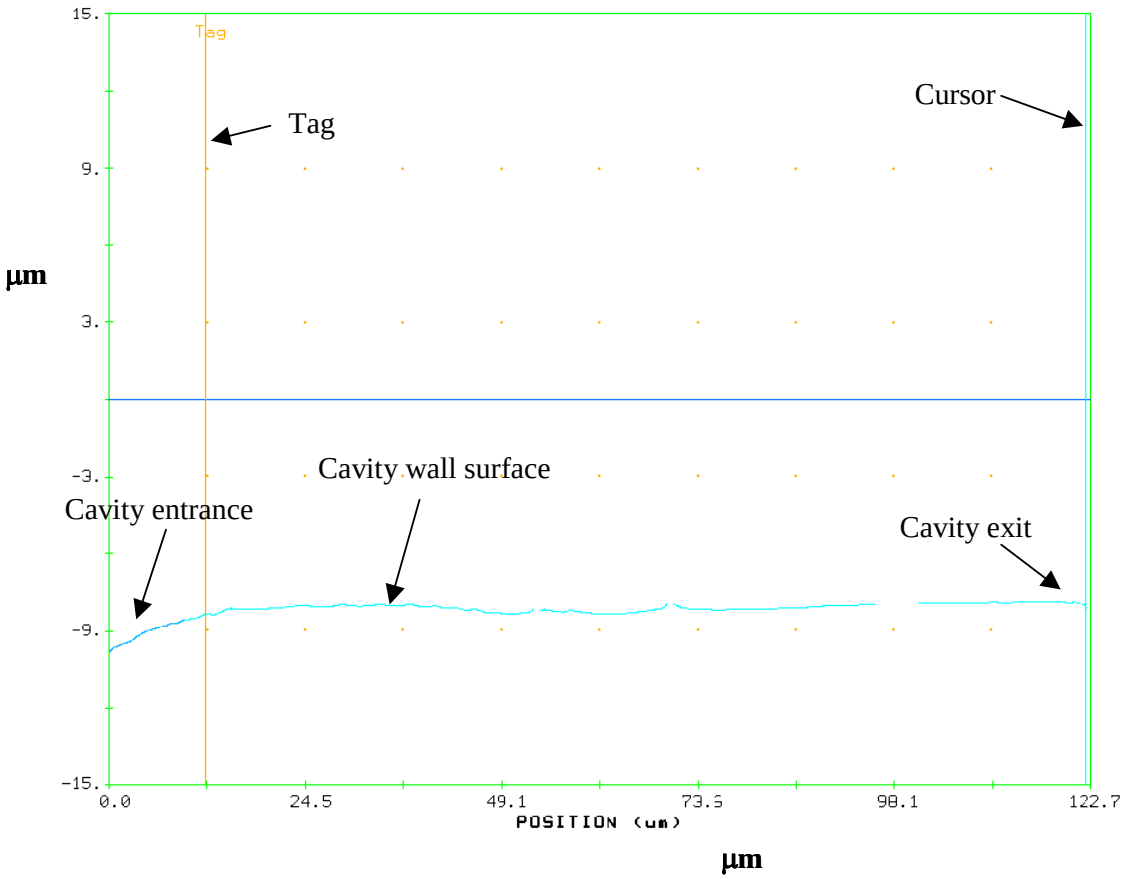

Figure 9-23: Line segment plot of the wall of a cavity ablated at 24 x 10^4 Jm^{-2}.

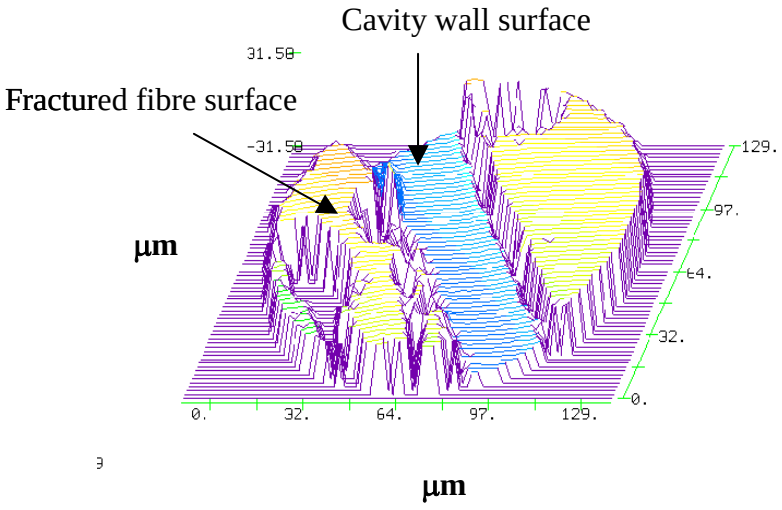

Figure 9-24: Contour map of a cavity micro-machined along the diameter of the optical fibre.

9.1.7 End-Face Ablation of Optical Fibres

As mentioned in Section 5.6.3, the SM 800 fibres of the ribbon cable were aligned into the image plane of the imaging objective and ablation was carried out. A 75 μm x 75 μm structure was ablated on the cleaved end-faces. Ablated ribbon fibres and the morphology of an ablated cavity are presented in Figure 9-25 and Figure 9-26 respectively. From Figure 9-25, it can be observed that the centre of the fibre was not aligned to the centre of the ablated structure. This misalignment is due to lack of brightness of the illumination at the cleaved end-faces of the fibres. Despite repeated trials, the alignment was not correctly achieved. However, it was found that the morphology of an ablated cavity crater was smooth and flat with little evidence of ablation debris. This is obvious from Figure 9-26. It can be observed from Figure 9-26, that the misalignment of a fibre leads to ablation of the core near the edge of the structure

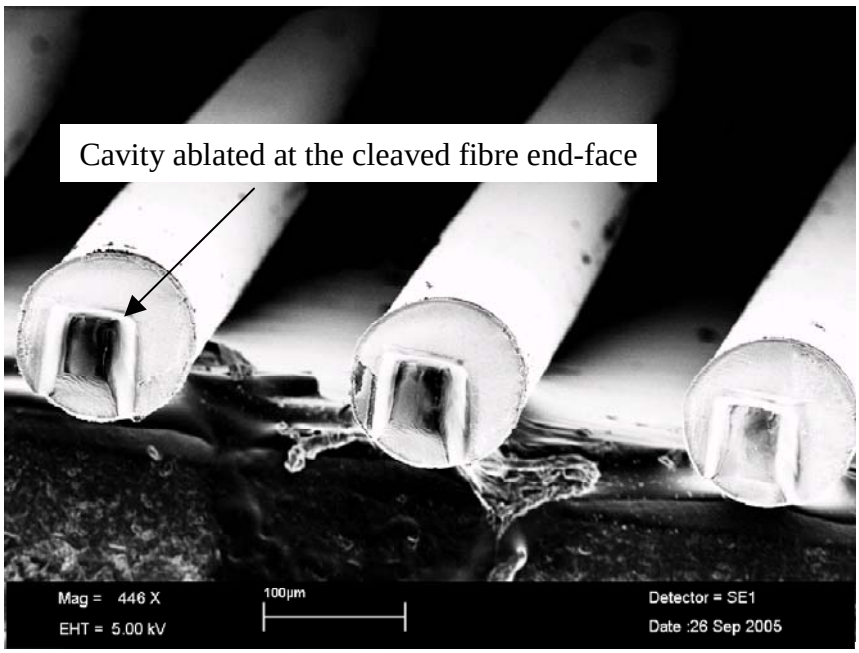

Figure 9-25: Ablated cleaved ends of the SM 800 fibre ribbon cable.

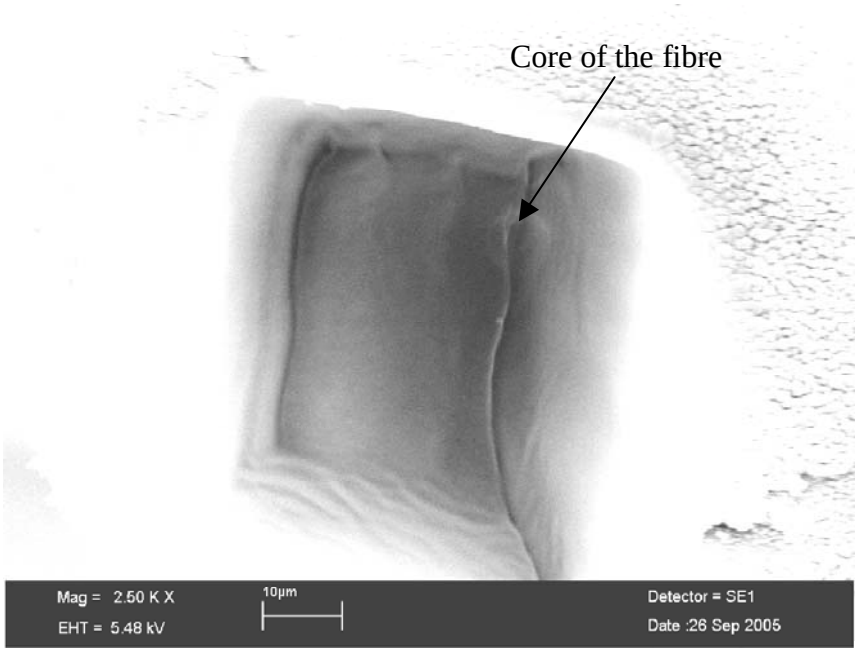

Figure 9-26: Cavity ablated at 13.4 x 10^4 Jm^{-2} for 500 pulses.

Ideally the centre of the crater has to coincide with the core of the optical fibre. Then a flat surface of the core surface could be produced. Unlike ablation through the fibre diameter, the cavity walls need not be vertical in this case. Therefore cavity ablation does not require energy densities as high as 25 x 10^4 Jm^{-2}. In addition to that, smooth and high optical quality surfaces could be produced across the core, due to stronger 157 nm absorption of the doped core. The possibility of high optical quality surfaces on germania-doped silica has been reported by Herman *et al.* [91].

The rationale of end face ablation is fabrication of intrinsic FP sensors by fusion splicing the ablated end face to the cleaved end of an optical fibre. Therefore, ablation of cleaved ends requires higher precision alignment and illumination techniques to be developed. Realization of this intrinsic Fabry-Perot design could offer many advantages over acid etched sensors. For example, the fibre tapering, which is inevitable during acid etching of bare fibres, could be avoided by this technique. Changing the number of pulses of irradiation can produce cavities of desired and repeatable ablation depths. The strain sensitivity of the intrinsic FP sensors could be tailored by ablating varying feature dimensions on the cleaved end face. For example, a 50 μm diameter circular structure,

ablated concentric with the core of the fibre will have a smaller contact area with the fusion spliced cleaved fibre end face than that of a 75 μm structure. Hence a higher cavity gap length could be produced in a sensor with a smaller contact area for the same applied tensile load due to higher stress.

9.1.8 Ablation of Sapphire Fibres

The morphology of ablated sapphire fibres and cavity walls were studied using SEM. Figure 9-27, Figure 9-28, Figure 9-29 and Figure 9-30 show the morphology of cavities ablated in 150 μm diameter sapphire optical fibres. The morphology of cavity wall surfaces of a fractured fibre and its surface profile analysis are presented in Figure 9-30 and Figure 9-31. A 38 μm x 38 μm feature was ablated at an energy density of 26 x 10^4 Jm^{-2}.

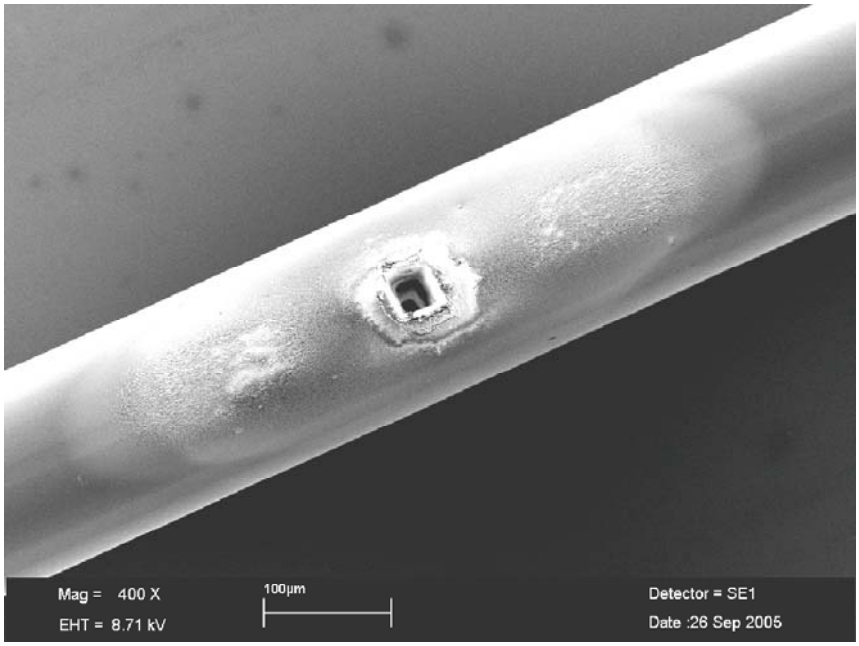

Figure 9-27: Ablated structure on the surface of a sapphire optical fibre.

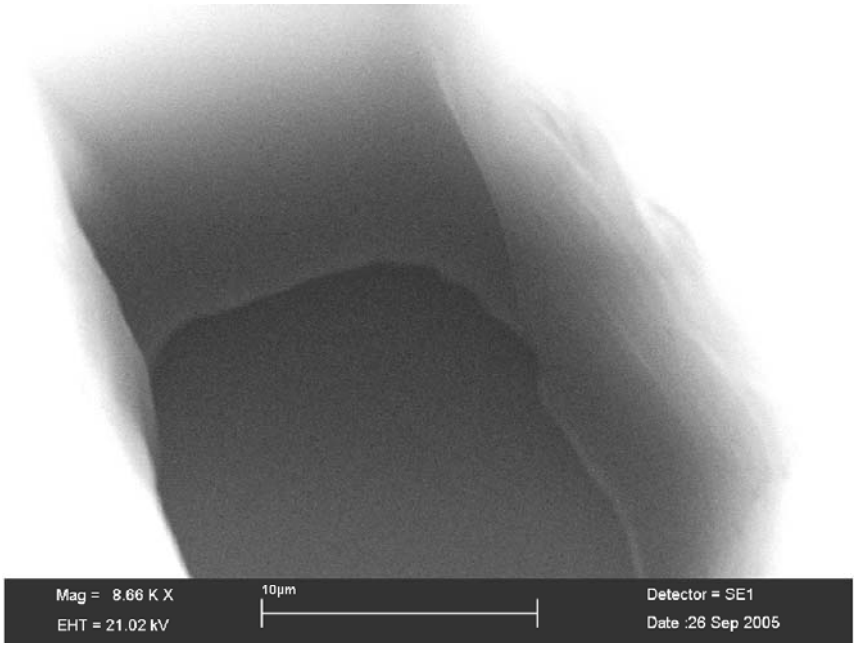

Figure 9-28: Cavity wall morphology in a sapphire fibre.

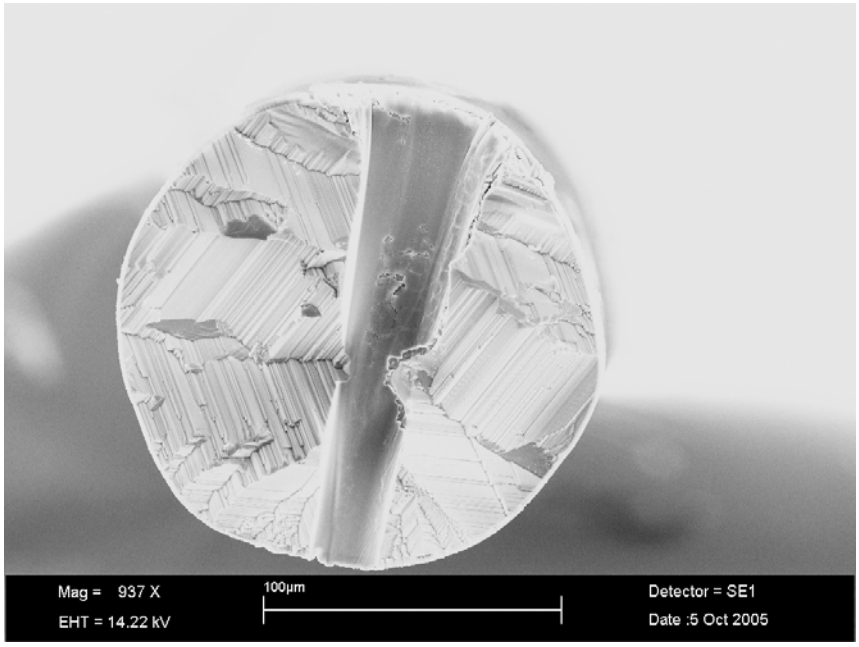

Figure 9-29: Morphology of the cavity wall surfaces of a fractured sapphire fibre.

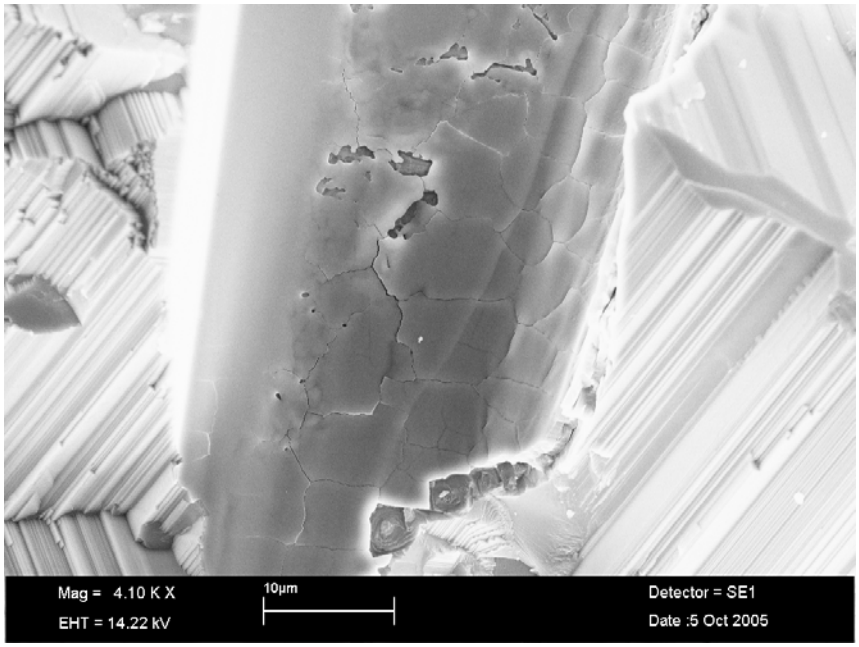

Figure 9-30: Micro-cracks and flaky structures on a wall surface.

From Figure 9-27, the deposited residual material around the entrance of the ablated structure ablated structure is obvious. This is in agreement with the observations made in sapphire disk ablation studies. A smooth morphology of cavity walls and entrance and exit of the cavity can be observed from Figure 9-28. The wall tapering of the cavity is obvious from Figure 9-29. Closer examination of the wall surface revealed micro-cracks and flaky structures. Besides cavity tapering micro-cracks and flaky structures are detrimental to the fabrication of FP cavities in sapphire fibres. The cracks and flaky nature of the surface is obvious from Figure 9-30. The probable reasons for micro-crack formation were already discussed in Section 8.1.2.1. The wall surface of the ablated cavity was surface profiled to gain surface roughness data. The area difference plot of the wall surface is presented in Figure 9-31. From Figure 9-31, it can be observed that a significant area of the wall surface has sufficient optical quality to produce FP interference. For example, the RMS roughness of block 1 defined over an area of 8.33 μm x 7.70 μm on the wall surface is 200 nm. The extent of greenish yellow and yellow coloured regions on the wall surface is due to the high optical reflectivity of the wall

surface. The white regions on the wall surface correspond to no data or otherwise insufficient optical quality to produce FP interference.

The ablated cavity of a sapphire fibre was interrogated using the CCD spectrometer and tungsten-halogen light source. The CCD interrogation scheme is the same as that described in Figure 5-2, except that the fibre coupler used is made from 50/125 μm fibre. Firstly the light was coupled into one end of an un-ablated sapphire fibre and the transmission spectrum was measured at the other end using the CCD spectrometer. Then the cleaved end of the sapphire fibre was butted to the cleaved end of multimode fibre by aligning them under a BFS 60 fusion splicer and the cavity was interrogated in reflection mode. The transmission spectrum and response of the ablated cavity is presented in Figure 9-32.

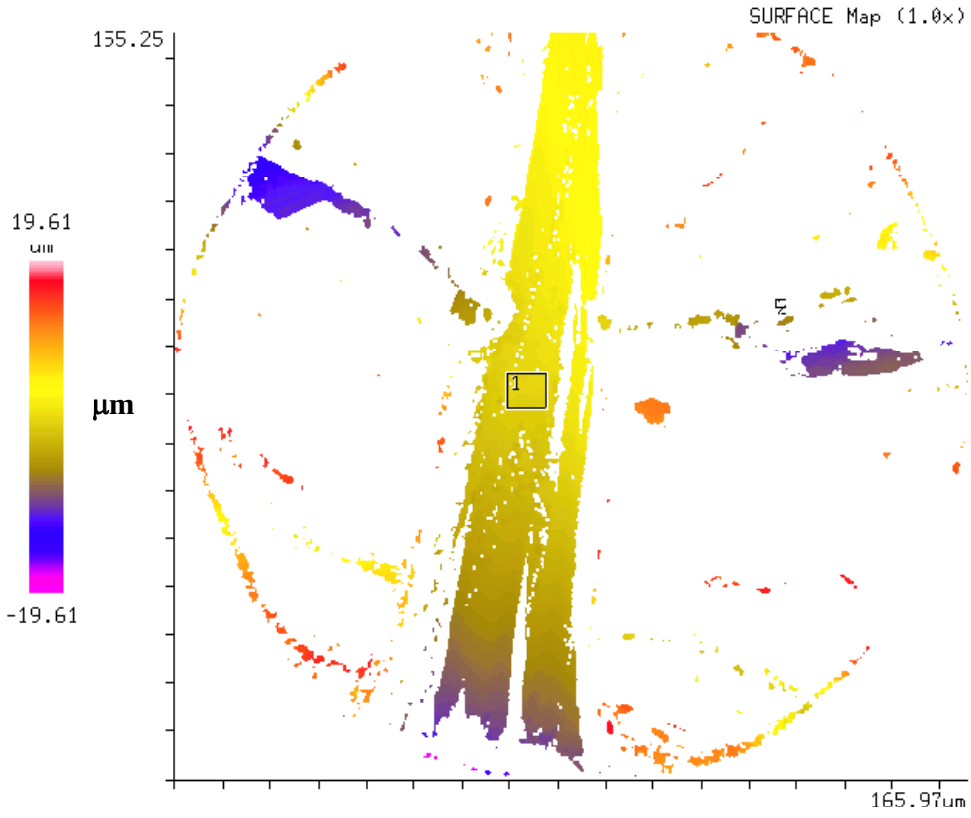

Figure 9-31: Area difference plot of cavity wall surface of sapphire fibre.

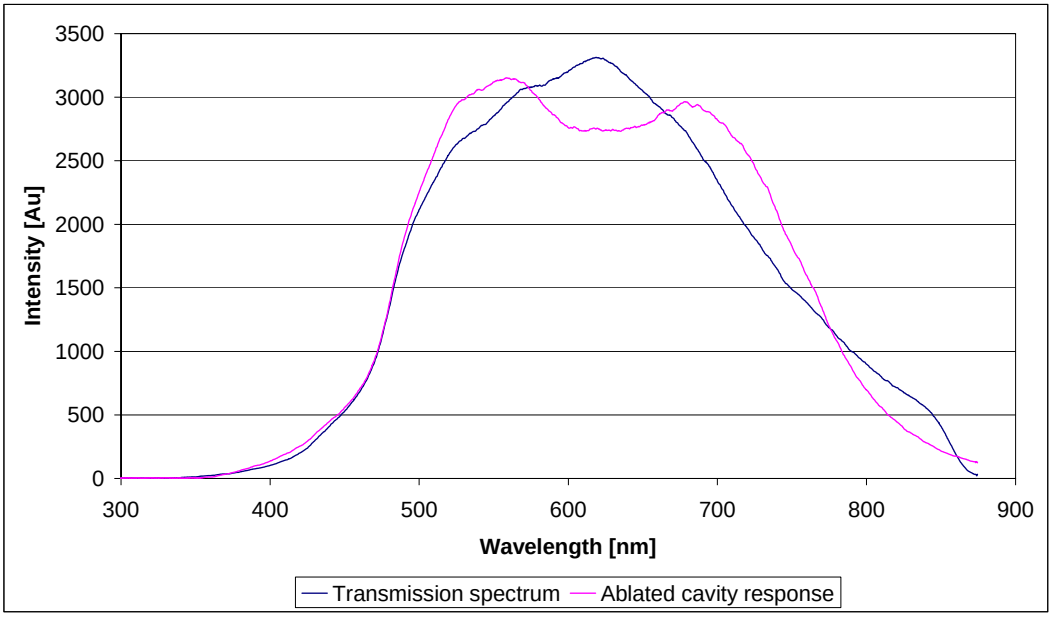

Figure 9-32: Response of a cavity ablated in a sapphire fibre at an energy density of 26 x 10^4 Jm^{-2}.

From Figure 9-32, the response of the cavity shows low contrast Fabry-Perot fringes. Although it was confirmed from the surface profiler analysis, that the optical quality is sufficient to produce FP interference, the cavity wall angle was not vertical. However, as the 150 μm sapphire fibre acts like a multimode fibre (with no core), the interference of multiple Fresnel reflections could produce FP interference. The poor contrast of the fringes is obviously due to cavity tapering. Therefore it can be confirmed from these results that the fabrication of FP etalons in sapphire fibres is feasible. However, factors such as cavity wall cracking and wall tapering must be controlled to produce high contrast Fabry-Perot interference. Realization of intrinsic FP cavities that produce high contrast interference fringes could lead to the development of interferometric temperature sensors for measuring temperatures above 1500 °C. For example, an intrinsic sapphire FP sensor can be surface mounted on a suitable substrate using high temperature resistant ceramic adhesives and cavity gap changes due to thermal expansion of the substrate can be measured to calibrate the temperature against intrinsic FP cavity length. The cavity may be filled with suitable materials and used for temperature sensing.

9.1.9 Summary of Ablation of Optical Fibres

Ablation of SMF 28, SM 800 and sapphire fibres was carried out at energy densities as high as 26 x 10^4 Jm^{-2}. The findings are summarised as follows:

- The curvature of the optical fibre, dimensions of the ablated structure and alignment of the image plane on the fibre surface significantly affect the taper profile of cavity walls. Minimum wall tapering at any energy density occurs when the fibre is symmetrically aligned in the image plane.
- Increasing the energy density of ablation reduced the taper angle of cavity walls in fibres.
- When the fibres are symmetrically aligned in the image plane and ablated at an energy density of approximately 25 x 10^4 Jm^{-2}, the etalons of the cavity produced Fabry-Perot interference. The FP interference fringes show that the optical quality and wall-angle across the core surface of the micro-machined etalons are adequate to produce intrinsic FP devices in both SMF 28 and SM 800 fibres.
- A relatively smooth and clean morphology of cavities ablated in silica optical fibres indicate stronger absorption of 157 nm than in fused silica disks. This could be due to a higher concentration of manufacturing process-induced defects and colour centres in optical fibre silica.
- The discrepancy in the dimensions of ablated structures and calculated cavity gap length indicate that the wall angle across the core could be different from the rest of the cladding. This reason could be supported by the fact that the influence of the evolving aerial image at the cladding/core interface of the fibre determines the wall angle across the core surfaces. This is due to stronger absorption of 157 nm radiation by the doped-core of the fibres. Theoretical calculations showed that there is a possibility for FP interference even for non-zero cavity wall-angles.
- Surface profile analysis of cavity wall surfaces showed that the average RMS roughness is less than half the operating wavelengths of SMF 28 and SM 800 fibres can be produced via 157 nm laser micro-machining.

- Cracks were observed on some cavity walls of fused silica fibres, however, they were not repeatedly observed. Although reasons such as, ablation-induced stresses, heat conduction from laser-induced plasmas and stress corrosion are mentioned, the exact reason for the wall surface cracking is not known. Wall-cracking is detrimental to the fabrication of intrinsic FP cavities.
- Cleaved end face ablation of the SM 800 fibres showed that ablated structures of clean and smooth morphology could be produced at energy densities as high as 13.4×10^4 Jm^{-2}. This FP configuration does not require vertical wall angles. However, severe difficulties were experienced during the alignment of fibre ends in the image plane of the objective lens due to poor illumination of the target surface.
- Sapphire fibre ablation showed that the optical finish of the wall surfaces of ablated cavities is sufficient to produce Fabry-Perot interference. CCD interrogation of cavities ablated in sapphire at an energy density of 26×10^4 Jm^{-2} revealed poor contrast FP fringes. SEM analysis of wall surface showed micro-cracking and flaking, which are deleterious to producing FP interference.

9.1.10 Novelty of this chapter

The industrial trials of 157 nm ablation of fused silica fibres and sapphire substrates carried out by Tuck [8] showed that well-defined shapes of microstructures can be created. However, no experimental work was carried out with respect to the fabrication of high aspect ratio FP microstructures in fused silica fibres using F_2-lasers. The cavities ablated to a depth of few tens of micrometers in sapphire fibre using 248 nm laser produced ablated surface of sufficient optical quality to act as Fabry-Perot reflector. However, the cavities were not machined through the diameter of the sapphire fibres and hence the cavities were not interrogated by coupling light into the fibre. Although his work provided useful insight into this technique, the work was inconclusive with reference to ablation of Fabry-Peort cavities in optical fibres.

Based on the findings of Tuck [8], Li *et al.* [102] and Herman *et al.* [91], the author has designed and constructed an F_2-laser micro-machining station with an aim to micro-machine FP cavities in fused silica and sapphire fibres to get near-parallel walled micro-cavities through the diameter of fused silica fibres. Low-coherence light interrogation of these cavities produced Fabry-Perot interference fringes of high visibility. This is the first demonstration of a laser ablated high aspect ratio cavity, with its walls functioning as Fabry-Perot etalons. This is a one-step fabrication process for the production fibre Fabry-Perot interferometers, which overcomes the problems involved in manual fabrication of EFFPIs and their gauge length. The short beam path length, which reduces the overall beam (157 nm) energy attenuation, and the low numerical aperture imaging system of high demagnification, which produced adequate energy densities and depth of focus, were found to be well suited for the fabrication of Fabry-Perot cavities in fused silica optical fibres. These results of fused silica and sapphire fibre ablation, to the best of the knowledge have not been previously reported.

10 In-situ Monitoring of Laser-induced Fluorescence

10.1 Introduction

With reference to the experimental methods explained in Section 5.7 the results and discussion of the F_2-laser-induced fluorescence (LIF) during the ablation of SMF-28 optical fibres are presented in this chapter. The evolution of the fluorescence spectra with the number of pulses of ablation is presented and the reasons for the corresponding evolution of fluorescence intensity are discussed. From the fluorescence spectra, a technique to determine whether the micro-machining has produced a cavity across the core of the optical fibre has been developed. Finally, the ablation depth is expressed as a function of peak intensity of laser-induced fluorescence at an energy density of 23×10^4 Jm^{-2}. The validity of this function is verified by calculating the ablation depth of two cavities from their respective LIF spectra recorded during ablation and compared with the ablation depth measured using an optical microscope.

10.1.1 Detection of Laser-induced Fluorescence

Fluorescence is the emission of photons of lower frequencies than the exciting radiation due to electronic transitions from the vibrational levels of an excited electronic state to the ground electronic state. A typical value of the fluorescence lifetime is 10^{-8} s. The CCD spectrometer used in these experiments can detect radiation in the range of 200-1100 nm. The fluorescence generated at the ablation site was coupled into the fibre and detected at the cleaved end of the fibre. Representative fluorescence spectra at energy densities of 23×10^4, 18.2×10^4, 11.2×10^4 Jm^{-2} during the cladding ablation of SMF 28 fibres are presented in Figure 10-1. From Figure 10-1, during cladding ablation, the LIF is a band of wavelengths ranging from 360 nm to 650 nm. The peak intensity of fluorescence is centred at 400 nm, which is the blue region of the visible spectrum. The visually observed fluorescence was blue in colour. A near infrared band ranging from 750 to 850 nm was also observed. At all the three specified energy densities the LIF spectral

shape remained the same, however, the full width at half maximum and peak intensities of the spectra increased with increasing energy densities.

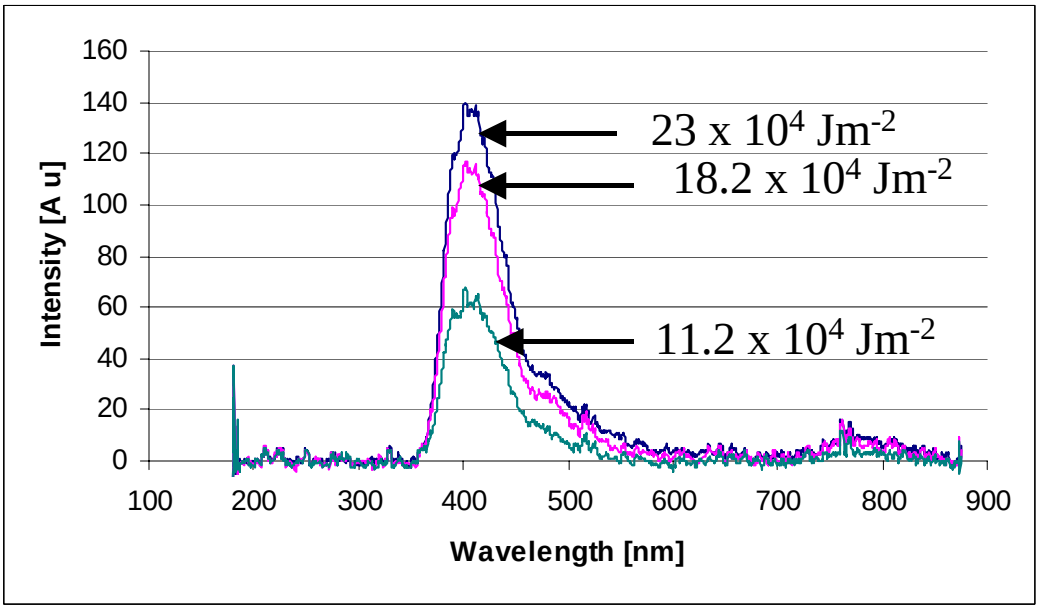

Figure 10-1: LIF spectra of fused silica of SMF 28 fibres at three different energy densities.

10.1.2 Evolution of Fluorescence Spectra

The evolution of fluorescence spectra during the ablation through the diameter of an optical fibre, at an energy density of 23 x 10^4 Jm^{-2}, is presented in Figure 10-2. The evolution of the LIF spectra is indicated by an arrow mark shown in Figure 10-2. The axis other than the wavelength and intensity axes represents the number of fluorescence spectra collected during ablation through the fibre diameter. When the fibre was ablated through its diameter, the intensity of the fluorescence spectra gradually increased with increasing time of irradiation up to the core of the fibre and then started increasing rapidly. The reasons for this rapid increase of fluorescence are discussed in the next section. After reaching a maximum, the fluorescence spectra gradually decreased over a period of irradiation and rapidly decreased to zero intensity. This trend of fluorescence intensity evolution was observed at all the three specified energy densities of ablation as shown in Figure 10-1, when the image plane was aligned along the diameter of the fibre.

A representative fluorescence spectrum during ablation at the core of the fibre is shown in Figure 10-3. From Figure 10-3, the fluorescence band stretches from 357 nm to 875 nm. The peak intensity of the LIF spectrum falls around 500 nm. A representative optical micrograph of cavities ablated through the diameter of an optical fibre at an energy density of 23 x 10^4 Jm^{-2} during in-situ fluorescence monitoring is presented in Figure 10-4.

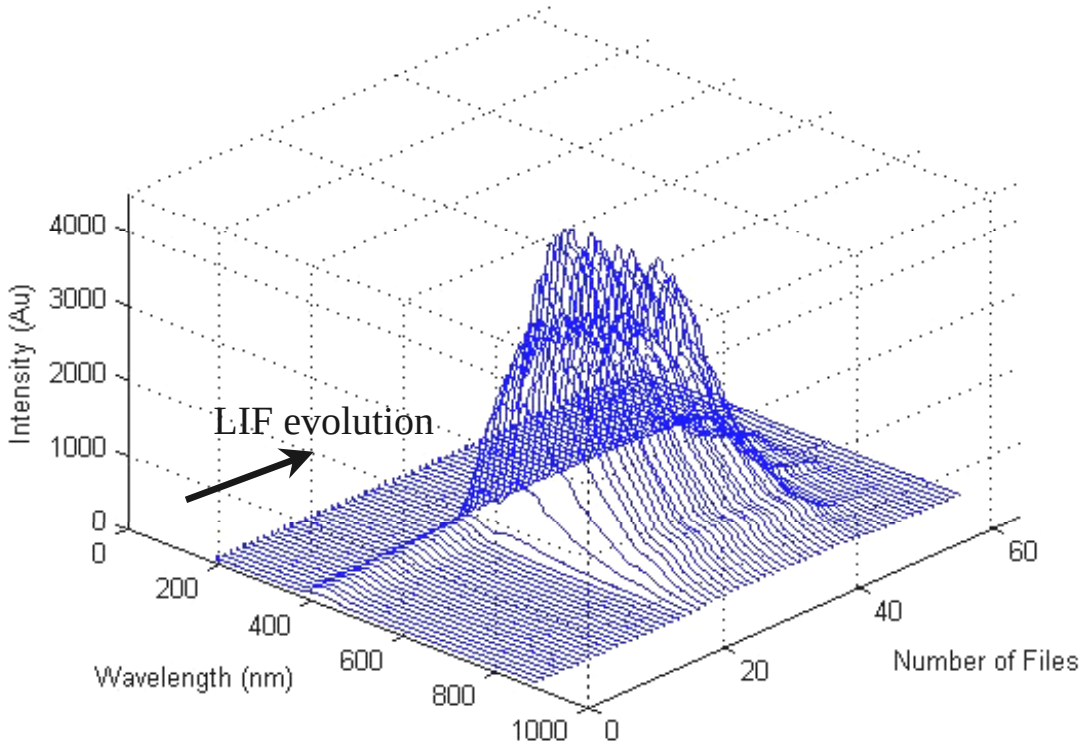

Figure 10-2: Evolution of LIF spectra as the fibre is ablated through its diameter.

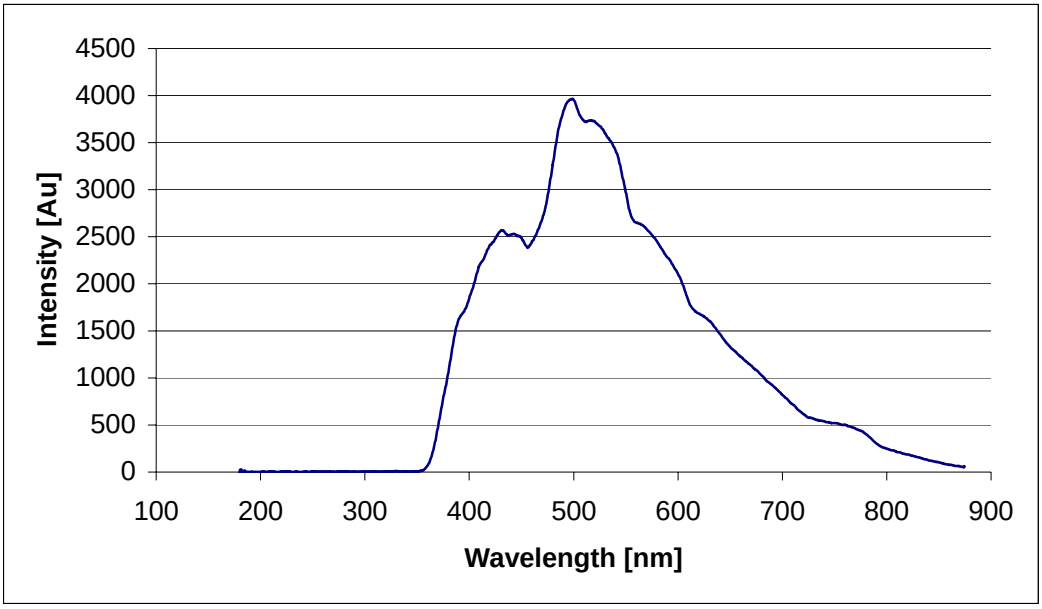

Figure 10-3: LIF spectrum during ablation of core of the fibre.

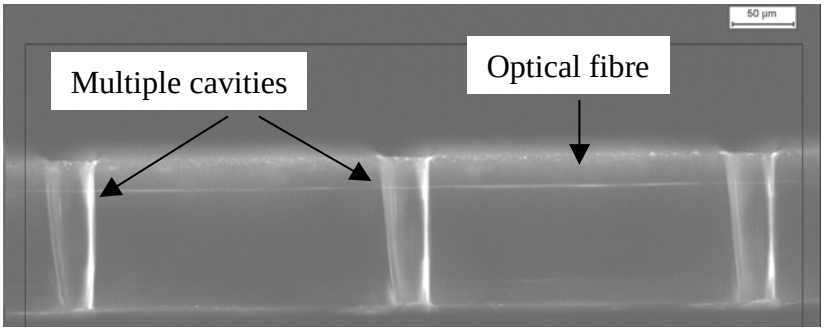

Figure 10-4: Cavities ablated during in-situ LIF monitoring at an energy density of 23 x 10^4 Jm^{-2}.

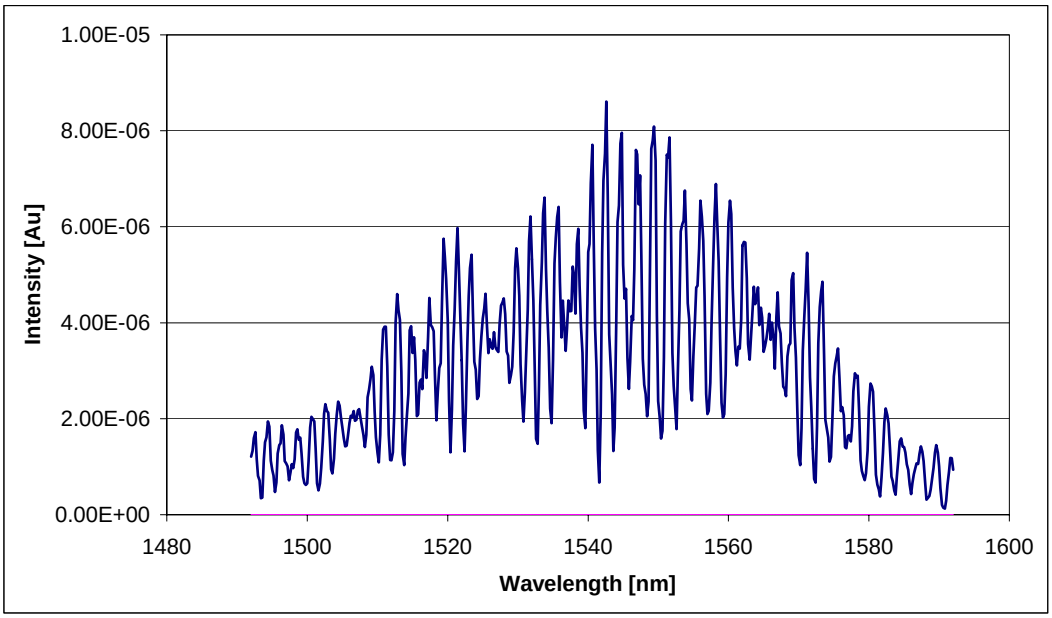

Figure 10-5: Response of multiples cavities micro-machined in SMF 28 fibres.

Once the alignment for machining a cavity across the core of the fibre was determined via fluorescence monitoring, then the fibre was translated along the axis of the fibre to machine multiple cavities. Figure 10-4, shows the repeatability of micro-machining cavities along the diameter of the fibres during fluorescence monitoring. The response of interference of multiple Fresnel reflections from the walls of the multiple cavities ablated in an SMF 28 fibre is presented in Figure 10-5. The Fabry-Perot interference fringes are obvious from Figure 10-5. This demonstrates that multiplexing of intrinsic cavities via 157 nm laser micro-machining is feasible and the author intends to carry out micro-machining of cavities of different cavity lengths along the length of a fibre in the future.

10.1.3 Identifying Cavity Formation across the Core of the Fibre

The aim of micro-machining optical fibres is to produce etalon surfaces across the core of an optical fibre. This is possible when the image plane is aligned along the diameter of the optical fibre. As mentioned in Section 9.1.3, problems were experienced while aligning optical fibres in the image plane. *In-situ* fluorescence monitoring helps to identify whether the cavity has formed across the core of the fibre. During the *in-situ*

fluorescence monitoring, the intensity of fluorescence spectra rapidly increases after a specified duration of irradiation. This rapid increase in fluorescence intensity was not observed during *in-situ* LIF monitoring, when the image plane was not aligned along the diameter of the fibre. This was confirmed by fracturing the ablated fibre followed by examination under an optical microscope. This was repeatedly observed when the image plane was not aligned along the fibre diameter. The evolution of fluorescence spectra during cavity formation, when the fibre was misaligned is presented in Figure 10-6 and a micrograph of a misaligned cavity cross-section is presented in Figure 10-7. From Figure 10-6, it can be observed that the peak intensity of fluorescence was significantly smaller than that shown in Figure 10-2. There was an increase of fluorescence intensity, however, this was insignificant when compared to Figure 10-2. The peak intensity of LIF spectra reached 3000 Au (arbitrary units) when the cavity is formed across the core of the fibre at an energy density of 18.2 x 10^4 Jm^{-2}. Therefore, there is a significant difference between the peak intensities of LIF spectra during cavity formation across the core and misaligned cavity.

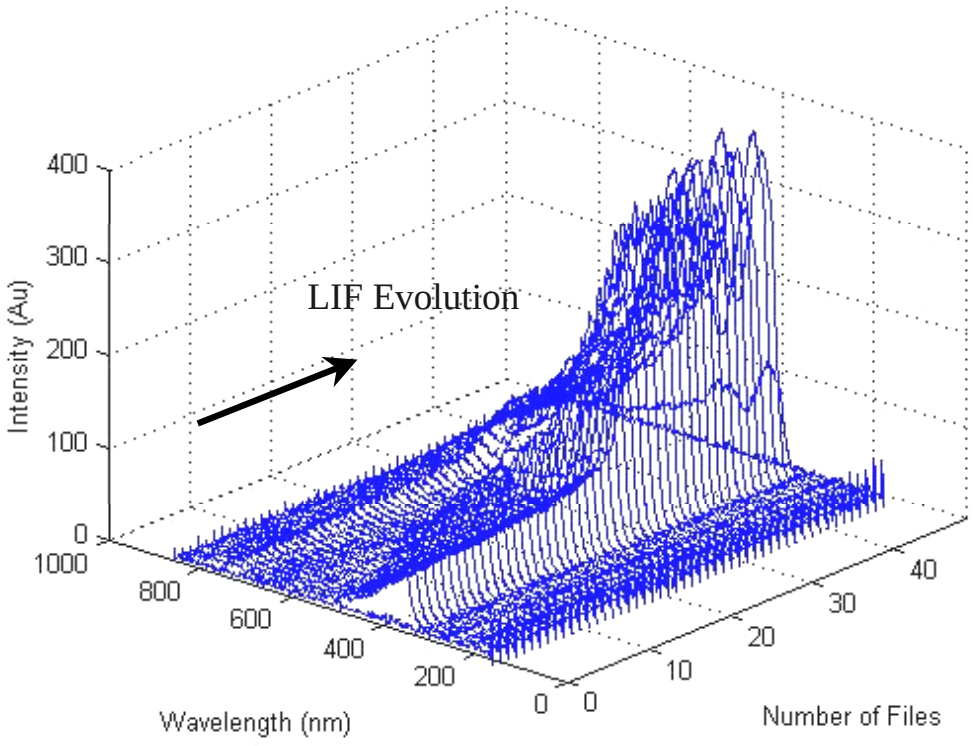

Figure 10-6: LIF evolution during misalignment at an energy density of 18.2 x 10^4 Jm^{-2}.

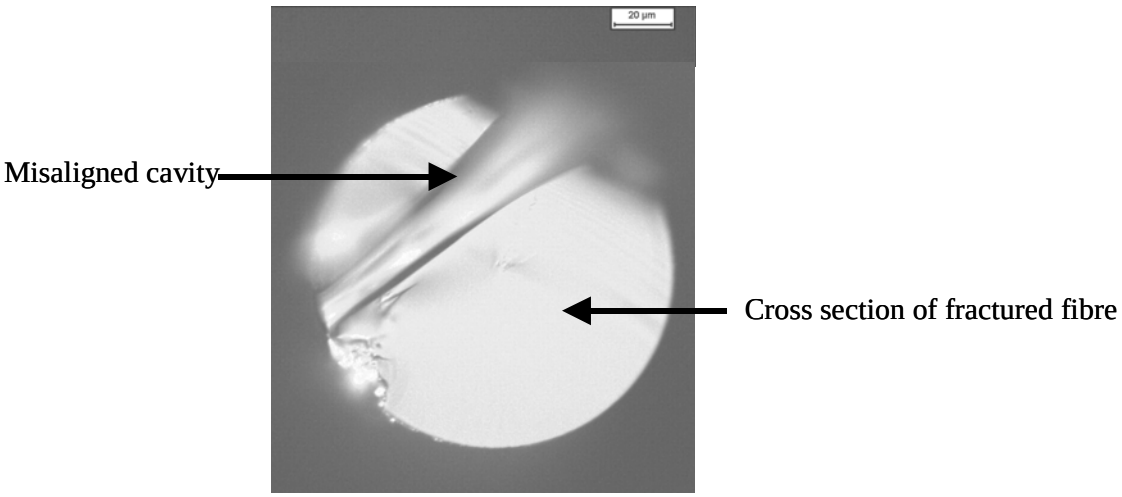

Figure 10-7: A representative micrograph of a misaligned cavity.

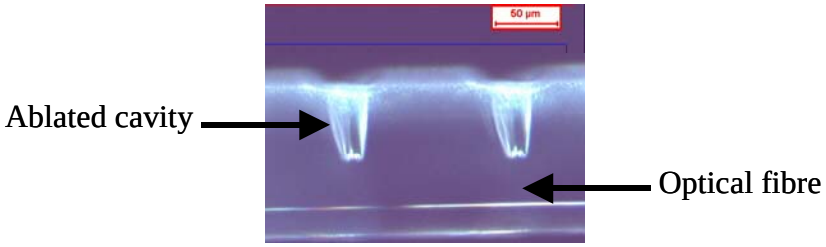

Figure 10-8: Cavities ablated at an energy density of 18.2 x 10^4 Jm^{-2} through the diameter, for 300 pulses.

The reason that the rapid increase of LIF intensity is due to ablation at the core of the fibre is verified by ablating two cavities. The irradiation was stopped immediately after observing the rapid increase of fluorescence. The number of pulses used for machining this cavity is calculated from the recorded time and frequency of the laser and was found to be 300 pulses. Then another cavity was ablated for the same number of pulses and a rapid increase in fluorescence was observed at the end of irradiation. The depth of these cavities was found to be 60 µm using an optical microscope. The corresponding optical micrograph is presented in Figure 10-8. The core of the optical fibre starts at a distance of 58 µm along the diameter from the outer surface of the optical fibre and the depth of the cavities measured using optical microscope is 60 µm, which is just into the core of the optical fibre. Therefore, the start of the rapid increase of fluorescence corresponds to an ablation depth of approximately 58 µm i.e., the surface of the core of the fibre.

Therefore, by in-situ fluorescence monitoring, the alignment of the fibre during ablation and the ablation depth corresponding to the core of the optical fibre can be determined during ablation. The reasons for fluorescence evolution as shown in Figure 10-2 could be the following:

1. The LIF coupled through the fibre gradually increases with increasing ablation depth until the surface of the fibre core.
2. The rapid increase of fluorescence when the ablation depth approaches 58 μm is due to rapid increase in the coupling efficiency of LIF at the core surface.
3. The evolution of LIF spectra from the core to the other end of the diameter of the optical fibre is different from the evolution of LIF spectra up to the core which could be due to the following reasons:

    - The coupling efficiency rapidly increases when the ablation depth reaches the surface of the core and reaches a maximum, which corresponds to maximum coupling efficiency.
    - The rate of ablation of the doped core will be different from that of the cladding due to difference in the absorption of 157 nm radiation. Therefore, the intensity of LIF spectra drops rapidly after reaching a maximum.
    - As the ablation surface moves gradually away from the core due to successive pulses of irradiation, the LIF coupled into the fibre also decreases, however, the beam undergoing multiple reflections from the cavity walls and the reflected light from the crater surface could contribute to the LIF coupled into the fibre.
    - The aspect ratio of the cavity increases with the increasing depth of the cavity. As the ablation surface moves away from the core of the fibre, the plasma emission could also contribute to the measured intensity of fluorescence spectra.

- The LIF coupled into the fibre also decreases as the ablation surface moves away from the core and hence the intensity of the LIF spectra falls. As the cavity is fully formed through the fibre diameter, only a small portion of light undergoing reflections from the cavity walls will contribute to the LIF.

Therefore, a number of factors such as reflection from the crater surface, plasma emission and 157 nm absorption of core could be responsible the evolution of LIF spectra from the core of the optical fibre. The LIF evolution from the surface of the fibre to the core surface is a gradual increase of LIF intensity with an abrupt increase associated with a LIF spectral emission, which is different from the LIF spectrum of fused silica cladding. This technique of identifying cavity ablation depth during fibre ablation had not been previously reported to the best of the knowledge of the author.

10.1.4 Correlating Fluorescence and Ablation Depth

In order to express fluorescence as a function of ablation depth, firstly, the peak intensities of LIF spectra were plotted against the number of pulses at an energy density of 23 x 10^4 Jm^{-2}. A total of 65 LIF spectra were collected during the ablation through the fibre diameter at an energy density of 23 x 10^4 Jm^{-2} for an irradiation of 800 pulses. Then the total pulse number (800 pulses) was divided by the number of LIF spectra (65 spectra). This implies 12.307 pulses per file. Therefore each LIF file corresponds to respective multiples of 12.307. By considering nearest integer of these multiples, it implies that the first LIF spectra recorded corresponds to fluorescence after 12 pulses of irradiation, the second after 25 pulses and so on. Based on these calculations, the plot of evolution of peak intensities of LIF spectra with the number of pulses is presented in Figure 10-9.

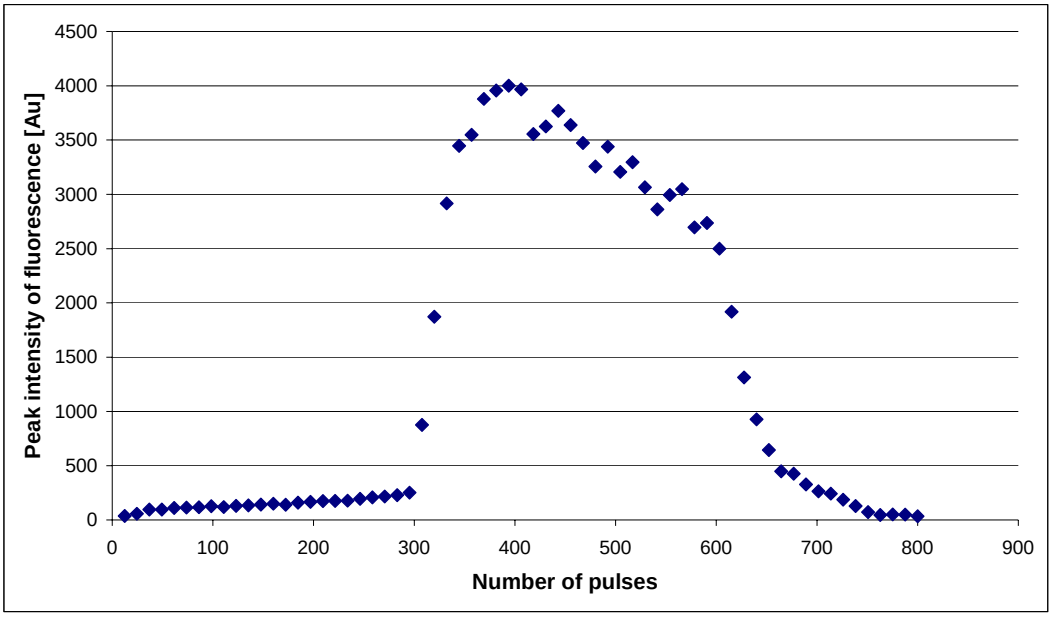

Figure 10-9: Graph showing evolution of peak intensities of LIF spectra with pulse number at an energy density of 23 x 10^4 Jm^{-2}.

From Figure 10-9, it can be clearly observed that the peak intensities of LIF spectra gradually increase up to 300 pulses and increase rapidly up to around 400 pulses and then gradually decrease up to around 600 pulses and thereafter rapidly decrease to zero at around 750 pulses of irradiation. It must be mentioned here that the peak intensities of LIF spectra collected during the ablation through the diameter cannot be plotted against the ablation depth using the same calculations used for plotting Figure 10-9. This is due to the fact that the ablation rate of the cladding will be different from that of the core of the fibre due to the difference in absorption of 157 nm radiation. However, the LIF peak intensities can be expressed as a function of ablation depth when the ablation of the fibre from its surface to the core is considered. This ablation depth corresponds only to the ablation of the fused silica cladding.

From the LIF spectra shown in Figure 10-9, it was identified that the LIF spectral shape started changing and began to increase rapidly from the 23rd spectrum. The evolution of fluorescence spectra up to the core surface is presented in Figure 10-10. From Figure 10-10, it can be observed that the spectral shape of the 23rd file was different from the preceding spectra. It was already proved that the rapid increase of intensity associated

with a change in spectral shape corresponds to ablation at the core of the fibre. Therefore a total of 22 spectra were recorded before the rapid increase of fluorescence and these spectra correspond to a depth of 58 μm. If the ablation depth (58 μm) is divided by the number of spectra (22 spectra), then each spectrum is collected after an ablation depth of 2.636 μm. Therefore, the first spectrum is collected after 2.636 μm, the second after 5.272 μm and the 22nd after 57.992 μm. Based on this calculation, the peak intensities of fluorescence are plotted against ablation depth and a straight line fit was carried out on this data. This is presented in Figure 10-11.

The equation obtained from the straight line fit was used to determine the ablation depth of two cavities ablated at the same energy density for 200 pulses. The number of spectra collected during the ablation of each of these cavities was 17 under the same recording conditions. From the recorded LIF spectra of these cavities, the peak intensities of the fluorescence of the last spectra (17th spectrum) of these two cavities were 173.35 Au and 174.681 Au. The ablation depth of these cavities measured using an optical microscope was found to be 42 μm. Then the ablation depth of these cavities was determined using the straight-line equation mentioned in Figure 10-11 as follows:

$$y = 2.54x + 61.21 \qquad \text{Equation 10-1}$$

'y' represents the peak intensity of the fluorescence and 'x' represents the ablation depth. The ablation depth can be expressed as:

$$x = \frac{y - 61.21}{2.54} \qquad \text{Equation 10-2}$$

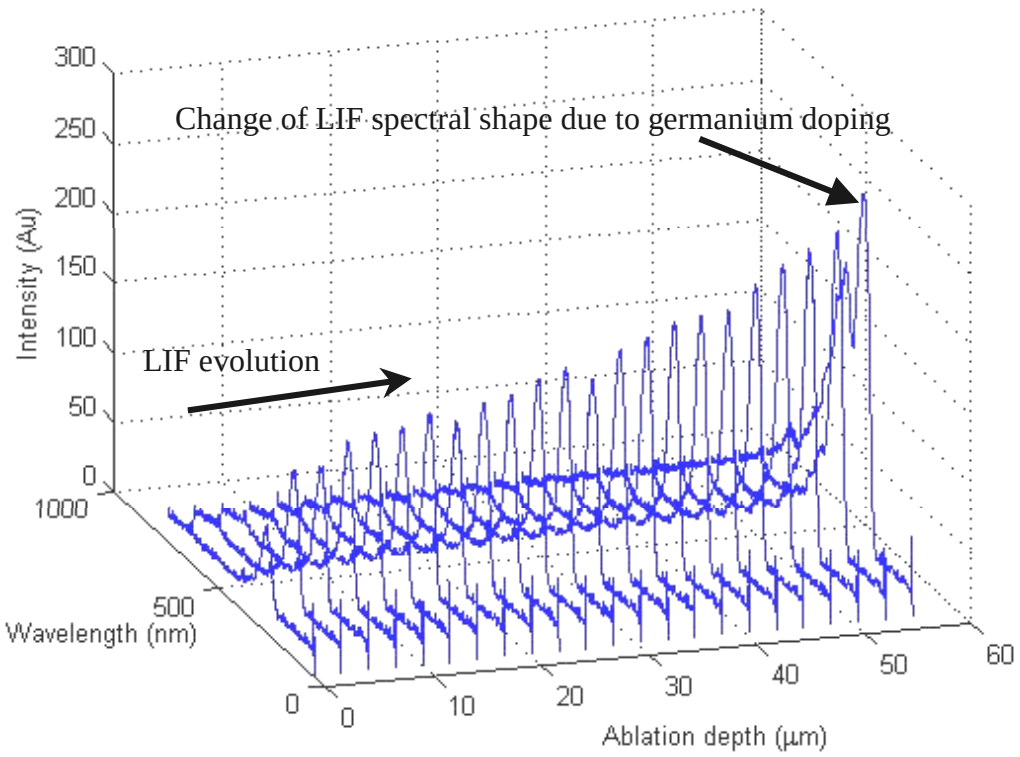

Figure 10-10: Evolution of LIF spectra from the fibre surface to the core.

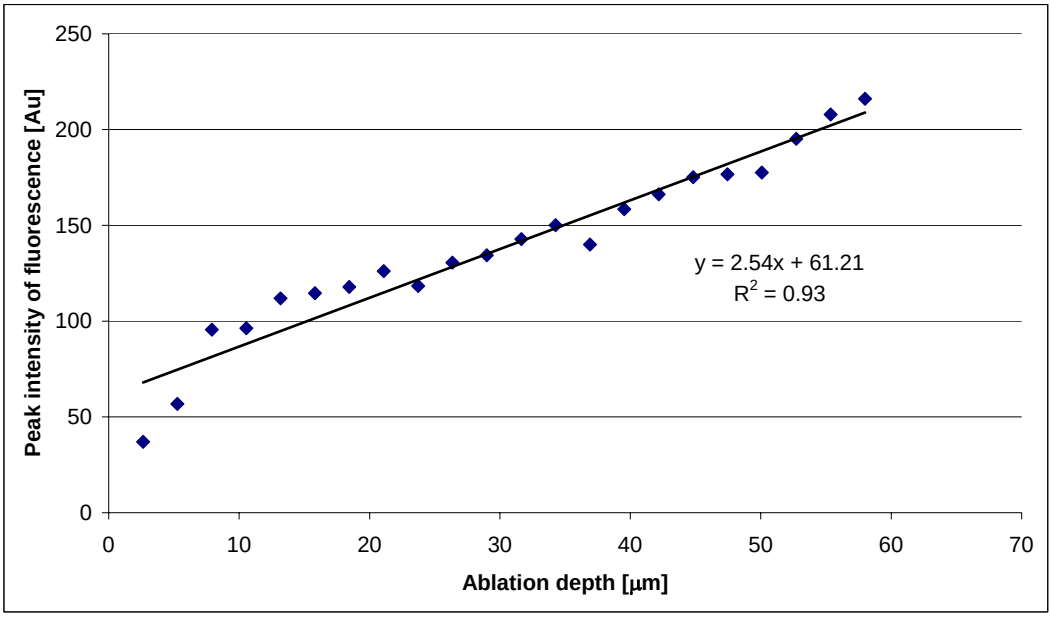

Figure 10-11: Evolution of peak intensities of fluorescence up to the core of the optical fibre.

By substituting the values of peak intensities of the fluorescence in Equation 10-2, the calculated ablation depth was found to be 44.1 and 44.6 μm for 173.35 Au and 174.681 Au respectively. These values of ablation depth are in fairly good agreement with the measured ablation depth of 42 μm.

From these results, it has been proved that the LIF spectral intensities recorded during ablation at the energy density of 23 x 10^4 Jm^{-2} could be used to determine the ablation depth of cavities. By adopting the same procedure, the ablation depth could be determined at other energy densities as well. This procedure can be automated to determine the in-situ ablation depth during micro-machining and hence predetermined cavity depths can be produced. However, this procedure can only determine ablation depths up to the core of the fibre due to the reasons mentioned in Section 10.1.3.

Using this technique, multiple cavities of ablation depth up to the core can be machined in a fibre and can be used as an evanescent sensor for chemical process monitoring. The extent of the evanescent field can be controlled by controlling the ablation depth. Compared to conventional techniques such as polishing plastic clad fibres, this technique of fabrication is relatively easier, repeatable and less time-consuming. The evanescent fused silica sensors that can be produced using this technique will be relatively smaller in size, inert to many industrial chemicals and can be used at higher temperatures than conventional plastic clad fibres.

10.1.5 Summary of Fluorescence Monitoring

In-situ 157 nm LIF monitoring during ablation of an optical fibre through its diameter revealed an abrupt increase of fluorescence associated with a change in spectral shape when the ablation depth corresponded to the core of the fibre. This technique was verified by examining the cross-sections of fibres, which were ablated up to the core. This technique revealed whether the cavity had formed across the core of the fibre. This is a reliable technique for confirming the alignment of optical fibres during the fabrication of

intrinsic FP cavities. The peak intensities of the fluorescence were expressed as a function of ablation depth at an energy density of 23 x 10^4 Jm^{-2}. The ablation depth calculated using this equation for a specified number of pulses was found to be in good agreement with the values of the ablation depth measured using an optical microscope. This procedure could be carried out at other energy densities of ablation as well. The ablation depth can be controlled up to the surface of the core using this technique. Evanescent sensors could be fabricated in fused silica fibres using this technique.

10.1.6 Novelty of this chapter

These experiments were carried out to develop a technique to improve the repeatability of micro-machining cavities along the diameter of the fibres. *In-situ* LIF monitoring during ablation of fibres is based on the evolution of fluorescence emission with the ablation depth. The technique has enabled the author, during fibre ablation, to confirm whether the cavity has formed across the core of the fibre. This technique helped to avoid microscope examination of cavity location on the fibre surface to confirm alignment, after every fibre ablation. Based on this technique, multiple cavities were micro-machined through the fibre diameter along its length. Based on the evolution of peak intensities up to the core of the fibre, the ablation depth of the cavities could be controlled. This technique of controlling ablation depth and cavity formation along the diameter of the fused silica optical fibres has not been reported previously.

11 F_2-Laser Radiation Effects on Fibre Bragg Gratings

11.1 Introduction

The results and the discussion of the results of the experimental methods described in Section 5.8 are presented in this chapter. This study was aimed at investigating the effects of 157 nm laser radiation on fibre Bragg gratings. Firstly, the results and a discussion of the exposure of fibre Bragg gratings to the raw beam of the laser are presented. In these experiments, the temporary and permanent changes of refractive index of the core of the fibre under the influence of a constant incremental exposure dose were investigated with reference to Bragg reflection. Secondly, the results and a discussion of ablation of fibre Bragg gratings is presented. In these experiments, the influence of ablating a cavity through the diameter of a fibre Bragg grating on Bragg reflection was investigated and analysed. The significance of these experiments with respect to the fabrication of FP cavities in optical fibres is also presented.

11.1.1 Exposure of Fibre Bragg Gratings to a 157 nm Beam

As mentioned in the experimental Section 5.8.2, the Bragg grating was exposed to a 157 nm laser beam in increments of 1000 pulses separated by a time of 15 minutes. The Bragg peak reflection before exposure was 1534.023 nm and 1534.082 nm after the experiment at an ambient temperature of 21.4 °C. The plot of shifts in Bragg peak reflection with accumulated fluence is presented in Figure 11-1.

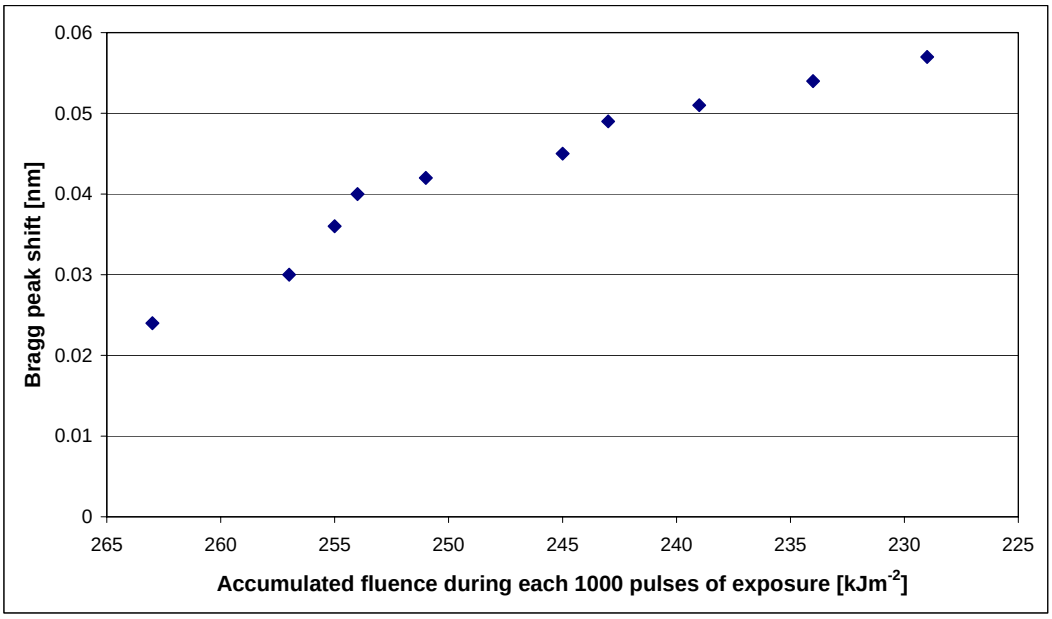

Figure 11-1: Permanent Bragg peak shifts for every 1000 pulses of exposure.

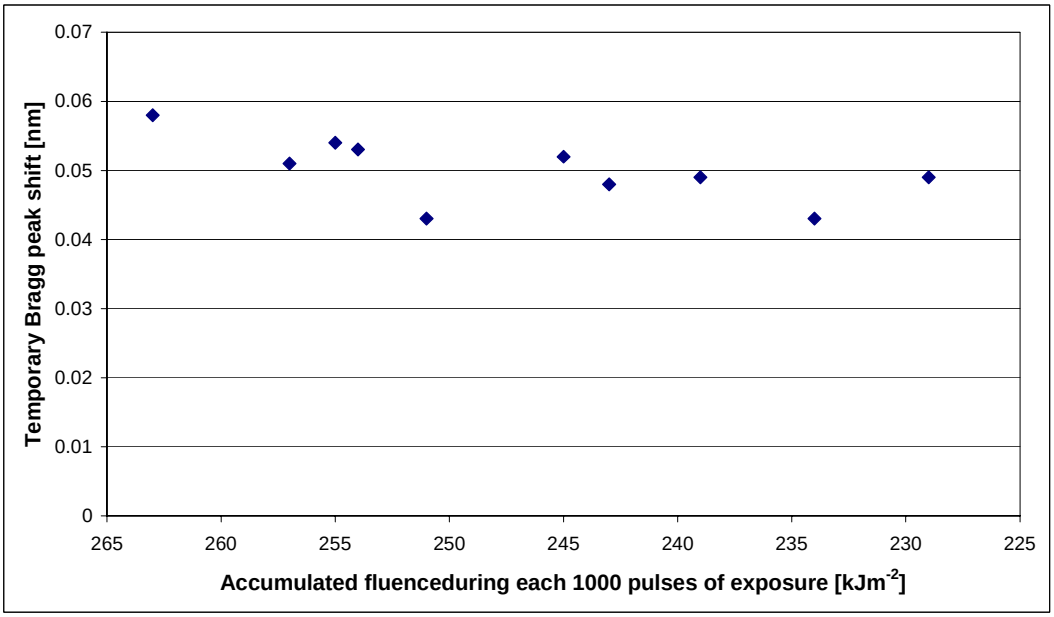

Figure 11-2: Temporary Bragg peak shifts during each 1000 pulses of exposure.

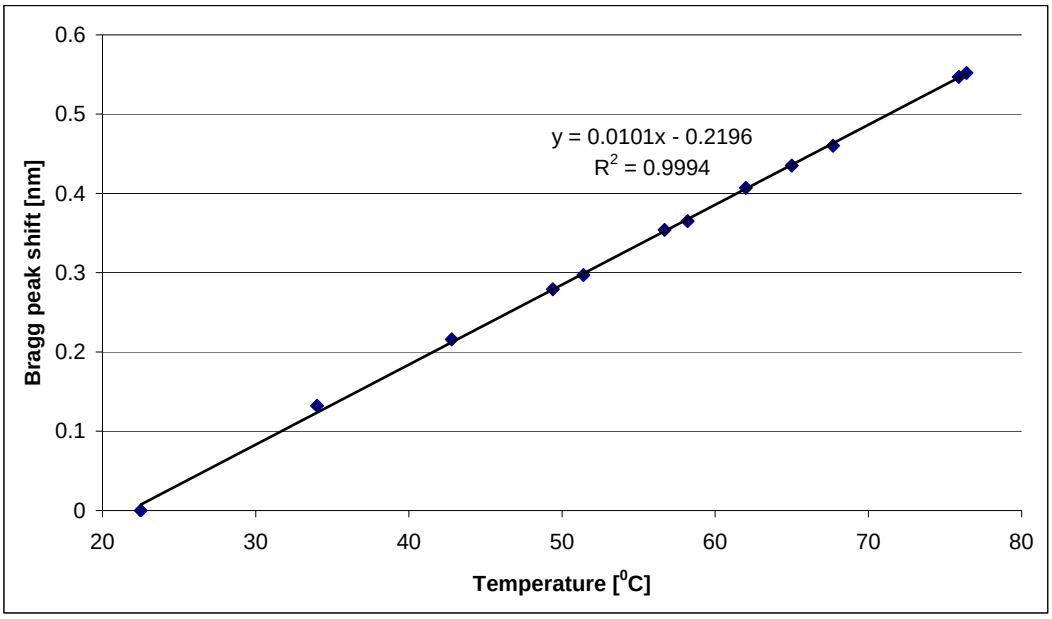

Figure 11-3: Temperature calibration after exposure to radiation.

The accumulated fluence is the product of the average fluence of each pulse and the number of pulses during each exposure. A maximum shift of 0.057 nm was observed after a total accumulated dose of 2470 kJm^{-2}. The temporary peak shift during each 1000 pulses of exposure is presented in Figure 11-2. The temperature calibration of the Bragg grating is presented in Figure 11-3.

From Figure 11-1, it can be observed that each 1000 pulses of irradiation have produced a permanent shift in the Bragg peak reflection towards a longer wavelength. These shifts gradually increased from their preceding shifts and tend to approach a plateau region. During irradiation of each 1000 pulses, temporary shifts in peak reflection occurred and settled at a higher wavelength than that prior to irradiation. For example, from Figure 11-1 and Figure 11-2, there was a permanent shift in the Bragg peak from 1534.023 nm to 1534.047 nm after the first 1000 pulses of irradiation and a temporary shift of 0.058 nm during irradiation. From the Bragg temperature calibration shown in Figure 11-3, a temporary peak shift of 0.058 nm corresponds to a temperature rise of 5.8 °C. The Bragg peak reflections before and after exposure are presented in Figure 11-4. From Figure 11-4 it can be observed that the peak reflection shifted to a longer wavelength and its amplitude decreased.

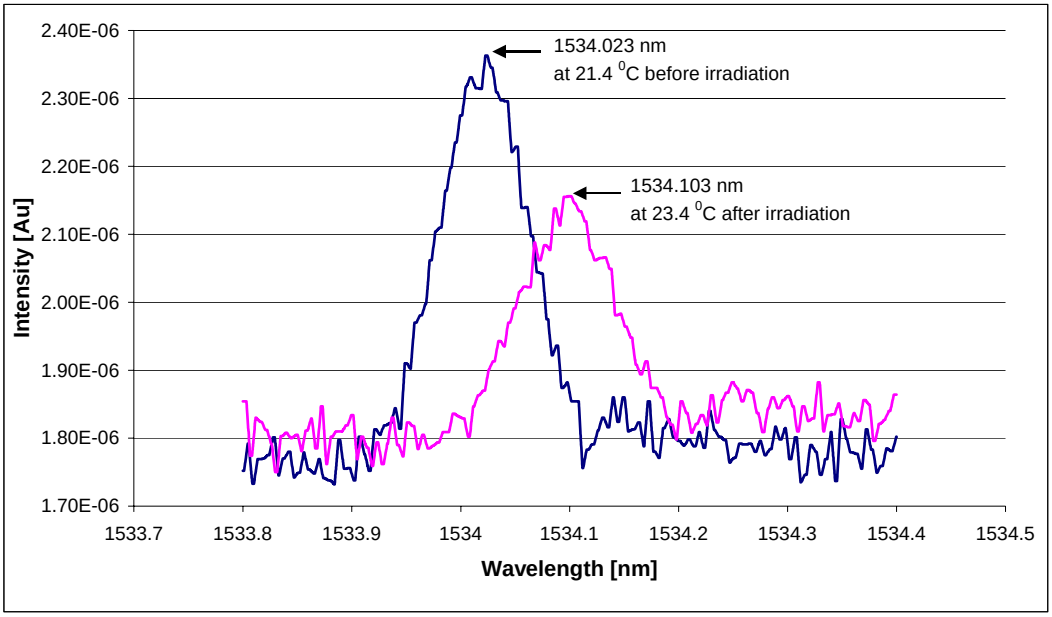

Figure 11-4: Bragg reflection before and after 157 nm exposure.

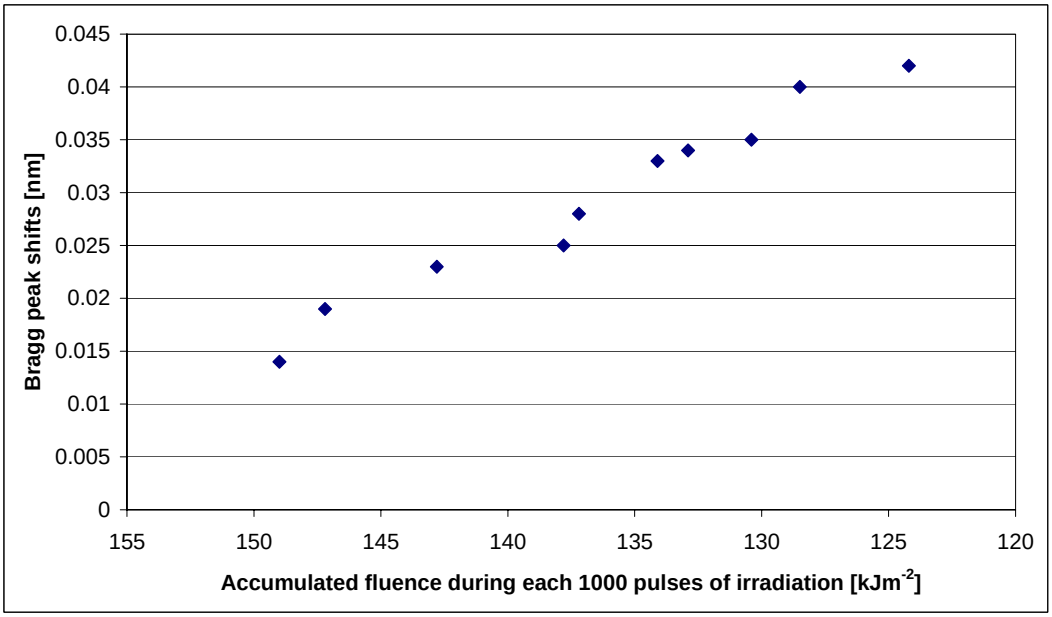

Figure 11-5: Permanent Bragg peak shifts for every thousand pulses of exposure.

Table 11-1: Tabular illustration of permanent and temporary peak shifts due to 157 nm exposure.

Accumulated fluence [kJm^{-2}]	**Permanent shift after each 1000 pulses of irradiation [nm]**	**Temporary shift during each 1000 pulses of irradiation [nm]**
157 nm irradiation of fibre Bragg grating of peak reflection of 1534.023 nm		
263	0.024	0.058
257	0.03	0.051
255	0.036	0.054
254	0.04	0.053
251	0.042	0.043
245	0.045	0.052
243	0.049	0.048
239	0.051	0.049
234	0.054	0.043
229	0.057	0.049
157 nm irradiation of fibre Bragg grating of peak reflection of 1533.935 nm		
149	0.014	0.043
147.2	0.019	0.034
142.8	0.023	0.033
137.8	0.025	0.033
137.2	0.028	0.037
134.1	0.033	0.037
132.9	0.034	0.033
130.4	0.035	0.033
128.5	0.04	0.041
124.2	0.042	0.036

The trend of permanent increase of the Bragg peak reflection towards a longer wavelength for every thousand pulses of irradiation was also observed at a lower accumulated dose. The plot of permanent peak shifts observed at a lower accumulated dose is presented in Figure 11-5. From Figure 11-5, the permanent peak shift for a total accumulated dose of 1364 kJm^{-2} was 0.042 nm. The Bragg peak shifted permanently from 1533.935 nm to 1533.977 nm. This permanent shift is smaller than the total permanent shift of 0.057 nm that was shown in Figure 11-1. Temporary peak shifts during irradiation were also observed. The temperature calibration after exposure showed a 0.01 $nm°C^{-1}$. The permanent and temporary peak shifts due to irradiation of two different Bragg gratings at two accumulated fluence doses is presented in Table 11-1.

11.1.2 Photo-refractive Index Changes

The permanent shifts in the Bragg reflection after every 1000 pulses of 157 nm irradiation is due to a permanent change in effective refractive index of the grating. As mentioned in Section 2.8.6.1 of literature review, 157 nm photons produce strong refractive index changes in fused silica and germanium-doped silica via a variety of induced-colour centres. If it is assumed that the permanent changes in Bragg reflection are caused by a permanent change of the effective index of the grating and then this change in refractive index can be calculated from Equation 2-8 as follows:

The effective index of the Bragg grating with a peak reflection at 1534.023 nm and a grating period of 529.9 nm can be expressed as:

$$n_{eff} = \frac{1534.023}{2(529.9)} = 1.447464616 \qquad \text{Equation 11-1}$$

The effective index after exposure to an accumulated dose of 2470 kJm^{-2} can be expressed as:

$$n_{eff} = \frac{1534.082}{2(529.9)} = 1.447520287 \qquad \text{Equation 11-2}$$

Therefore the effective index of the grating increased by 5.567×10^{-5}. In these calculations, it is assumed that the shift towards a longer wavelength has occurred due to increase of effective index, however, not due to change in grating spacing. By carrying out the same calculation for the Bragg shifts presented in Figure 11-5, the effective index change for a total accumulated dose of 1364 kJm^{-2} was found to be 5.567×10^{-5}. When these index changes are compared to the index changes observed by Chen *et al.* [111], they are significantly smaller. This is due to a much lower accumulated dose. A saturated index change of 1.3×10^{-3} was produced in their experiments due to a total exposure dose

of 25 x 10^4 kJm^{-2}. This dose is much larger than the accumulated dose used in the experiments conducted by the author. They observed weakening of gratings (strong gratings) after exposure to 157 nm radiation [111]. They attributed this reduction in amplitude to erasure of strong index modulation created by 248 nm radiation. As mentioned in the experimental Section 5.8.1, the Bragg gratings used in these experiments were strong gratings written using 248 nm radiation. Therefore, the results obtained from these experiments were in agreement with the findings of Chen *et al.* [111]. Therefore, a much higher refractive index change can be produced by increasing the accumulated dose of 157 nm radiation.

The temporary shifts during irradiation were due to laser-induced heating. A temperature rise during 157 nm exposure was also observed by Dyer *et al.* [110]. However, the rise in temperature was 29 K for an accumulated dose of 0.8 kJm^{-2}, which was much smaller compared to the doses accumulated as shown in Figure 9-29. The discrepancy is due to difference in the ambient atmosphere. The temperature rise was higher in the case of Dyer *et al.* [110] because the experiment was carried out at an ambient pressure $<10^{-2}$ Pa. From the Bragg grating temperature calibration as presented in Figure 11-3, a temporary peak shift of 0.058 nm, as shown in Figure 11-2 during the first 1000 pulses of irradiation, corresponds to a temperature rise of 5.8 K for an accumulated dose of 263 kJm^{-2}. This smaller temperature rise is due to continuous heat transfer to the ambient nitrogen atmosphere by conduction. The transmission ambient for 157 nm radiation was produced by flushing the beam line with dry nitrogen gas. The laser-induced heating did not produce any permanent shifts of Bragg reflection or permanent index changes. However, during ablation of high aspect ratio cavities in fused silica, temperatures as higher than the melting temperature of fibres (1600 °C for fused silica of SMF 28 fibre; mentioned in experimental Section 5.1) will be produced. Conventional fibre Bragg gratings are not suitable for use in harsh ambient environments above 500 ^{0}C [6]. Therefore, besides direct interaction of 157 nm radiation, these high temperatures produced during ablation could have a decaying effect on the effective index of the fibre core. The Bragg grating ablation experiments that were carried out were intended to study

the influence of high temperatures generated during ablation on the effective index of the core.

11.1.3 Ablation of Bragg Gratings

The Bragg grating ablation was carried out at an energy density of 19 x 10^4 Jm^{-2} and 21 x 10^4 Jm^{-2} at a distance approximately 2 mm from the start of the grating along the diameter of the fibre. The Bragg reflections before and after ablation at these two energy densities are presented in Figure 11-6 and Figure 11-7. From Figure 11-6, the slight shift towards a longer wavelength is due to an ambient temperature increase. The Bragg reflections after ablation revealed that there was no permanent shift in peak reflection of the gratings, however a slight reduction in the amplitude of the reflection was observed.

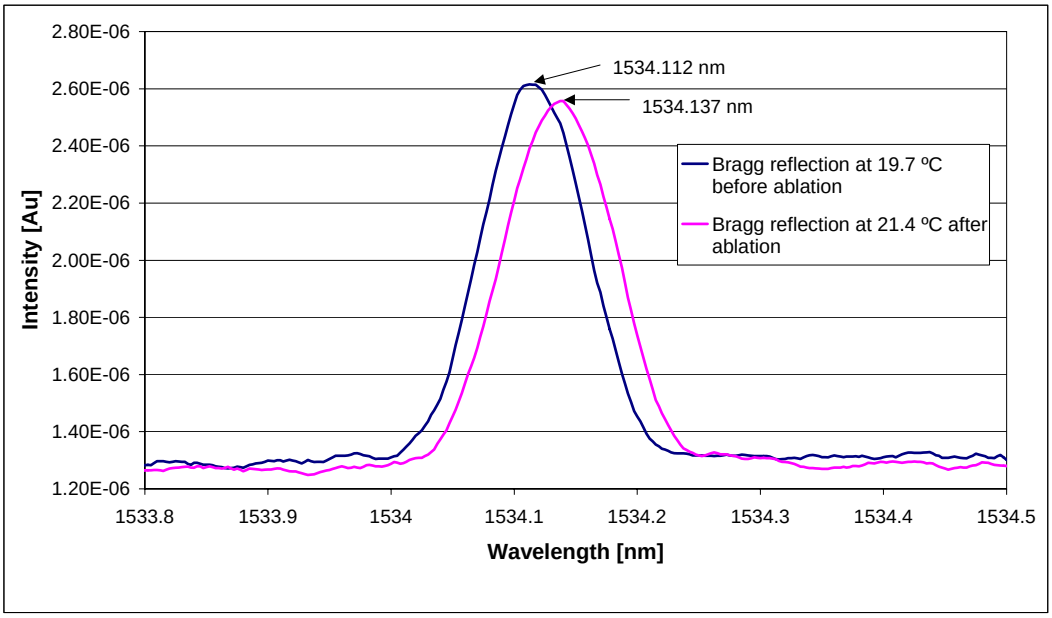

Figure 11-6: Bragg reflections before and after ablation at an energy density of 19 x 10^4 Jm^{-2} through the diameter of the fibre.

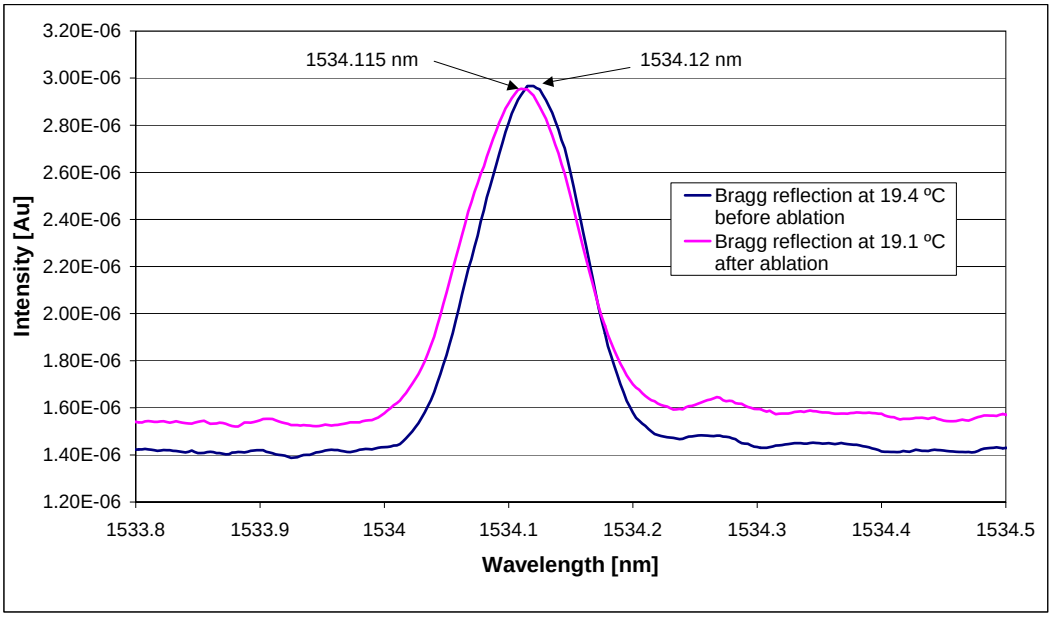

Figure 11-7: Bragg reflections before and after ablation at an energy density of 21 x 10^4 Jm^{-2} through the fibre diameter.

11.1.4 Effect of Ablation on a Bragg Grating

The heat generated during the interaction of a high intensity beam with the material converts it into vapor phase. The response of the grating to the ablation-generated heat will depend on the conduction of heat along the length of the grating from the ablated region. The heat-affected zone during ablation is determined by the thermal properties of the material and the duration of the pulse. This is mentioned in Section 2.8 [42]. The heat-affected zone determines the distance through which the heat generated at the ablation point diffuses into the surrounding material. In the case of SMF 28 fibres, the thermal conductivity, specific heat and density of fused silica are 1.38 $Wm^{-1}K^{-1}$, 770 $Jkg^{-1}K^{-1}$ and 2200 kgm^{-3} respectively as presented in Section 5.1. From these values, the thermal diffusivity can be calculated as follows:

$$Thermal\ diffusivity = \frac{Thermal\ conductivity}{(Specific\ heat)(Density)} \qquad \text{Equation 11-3}$$

$$Thermal\ diffusivity = \frac{1.38 Js^{-1}m^{-1}K^{-1}}{(770 Jkg^{-1}K^{-1})(2200 kgm^{-3})}$$

$$= 0.814 \text{ x } 10^{-6} \text{ m}^2\text{s}^{-1}$$

The heat-affected zone from the ablation site can be calculated by using Equation 2-13 as follows:

$$Heat-affected\ zone = \sqrt{2(thermal\ diffusivity)(duration\ of\ laser\ pulse)} \qquad \text{Equation 11-4}$$

$$Heat-affected\ zone = \sqrt{2(0.814\times10^{-6} m^2 s^{-1})(17\times10^{-9} s)}$$

$$= 0.166\ \mu\text{m}$$

The pulse duration of 157 nm laser radiation is 17 ns FWHM. Therefore, the length of the heat-affected zone is 166 nm. From this calculation, it is obvious that the heat-affected zone is much smaller compared to the length of the grating (10 mm) and the grating period (1000 nm). The initial nanoseconds of the pulse duration ablate the material and the rest of the duration of pulse would be partly attenuated by the plume. The heated plasma expands out of the cavity by transferring a portion of its heat energy to the cavity walls [50]. However, there are several milliseconds of duration between two successive pulses during which the cavity walls lose their heat to the ambient nitrogen atmosphere. Therefore, the conduction of the heat generated during ablation along the length of the grating is not possible. Hence, there is no permanent shift due to ablation along the diameter of the fibre on the length of the grating.

It is well known that the reflectivity of the grating increases with the length of the grating. When the grating was ablated along the length at a distance of approximately 2 mm from one end of the grating, a length of 2mm of the grating was lost. Therefore, this loss of grating length accounts for the loss of Fresnel reflections from the grating planes over a length of 2 mm. This loss of reflection leads to a decrease in the amplitude of the grating reflection after ablation, which is obvious from Figure 11-6 and Figure 11-7. The difference between these two types of irradiation is that the entire length of the grating is

exposed to the 157 nm beam allowing a direct interaction of 7.9 eV with the germanium-doped core of the fibre, whereas during the Bragg grating ablation a 38 μm length of the fibre is ablated along the fibre diameter using a focussed beam, which does not affect the entire length of the grating.

The results of Bragg ablation experiments provide conclusive evidence that during the fabrication of Fabry-Perot cavities along the diameter of the optical fibre, the heat-affected zones do not affect the integrity of the core of the fibre.

11.1.5 Summary of 157 nm Radiation Effects on Bragg Gratings

The exposure of fibre Bragg gratings to 157 nm radiation produced permanent shifts in the peak reflection towards longer wavelengths accompanied by reduced amplitudes of reflection. Transient laser-induced heating during irradiation produced temporary shifts towards a longer wavelength. The observed permanent changes in refractive index were much smaller compared to that produced by other authors due to the much lower accumulated dose of 157 nm radiation used in these experiments. The transient temperature rise was also lower compared to the findings of other authors due to the molecular heat conduction to the nitrogen ambient atmosphere. The heat-generated during the ablation of cavities along the diameter of the fibre Bragg gratings produced no permanent changes in the peak reflectivity. A calculation of heat-affected zone revealed that its length is very small compared to the length of the grating and the grating spacing. The slight decrease of amplitude of reflection is due to the loss of grating planes over a length of 2 mm of the grating from one end of the grating. The Bragg ablation experiments conclusively proved that the heat generated during cavity ablation along the diameter of the fibre does not affect the integrity of the fibre core.

11.1.6 Novelty of this chapter

This novel technique investigated the influence of heat generated during ablation of a cavity through the diameter of a fibre Bragg grating. This work proved that the heat generated during ablation of a microstructure does not cause any shift of Bragg reflection due to submicrometre heat-diffusion zone. The work also proved that there are no detrimental effects on the integrity of the core and cladding of the fibre as there was no significant change in the amplitude of Bragg reflection after ablation. This work demonstrates that this novel technique of fabrication, which involves ablation of FP cavities through the diameter of fused silica optical fibres at relatively high energy densities, inflicts no detrimental affects on the wave guiding properties of the fibres.

12 Applications of Laser Micro-machined Sensors

12.1 Introduction

In this chapter, some applications of laser-ablated sensors are discussed. The results and the discussion are based on the experimental methods described in Section 5.9. This work was aimed at demonstrating the use of laser-ablated fused silica optical fibres for sensing applications. Multiple cavities micro-machined through the diameter of the fibres along their length were used for pH sensing and chemical sensing. In both these applications, the micro-machined cavities were used as miniature transmission cells for detecting spectral changes under the influence of external parameters. An attempt to fabricate a pressure sensor via micro-machining was made.

12.1.1 pH Sensing

As mentioned in Section 5.9.1, the acidified bromocresol solution changes its colour from yellow to blue when the pH of the solution changes from 4 to 5.4. Transmission spectra of a micro-machined fibre with 10 air filled cavities and an acidified bromocresol solution are presented in Figure 12-1. From Figure 12-1, the transfer function of the source spectrum through the air-filled cavities extended from 400 nm to 874 nm, with the peak intensity at 633 nm. When the sensor was immersed in the acidified solution, the transmission spectrum was spread from 470 nm to 874 nm, with a peak intensity at 660 nm. The intensity of the transmission spectrum also increased when the sensor was immersed in the solution. The violet and indigo part of the visible spectrum was absorbed by the solution filling the air cavities. The evolution of transmission spectra with increasing pH is presented in Figure 12-2. The pH of the acidified solution was 2.4.

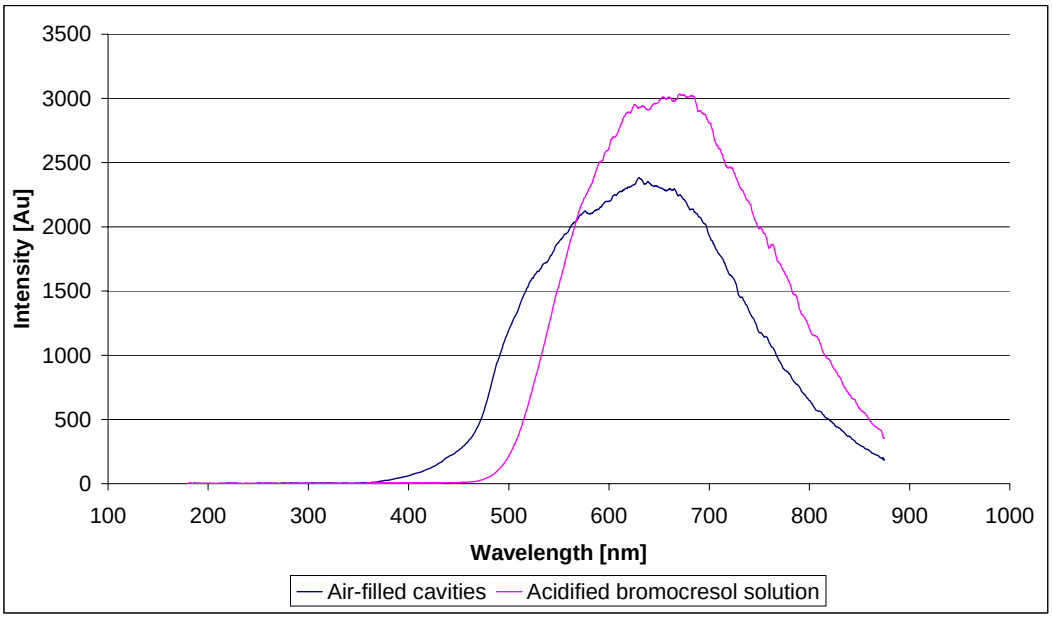

Figure 12-1: Transmission spectra of air-filled cavities and cavities filled with acidified bromocresol solution.

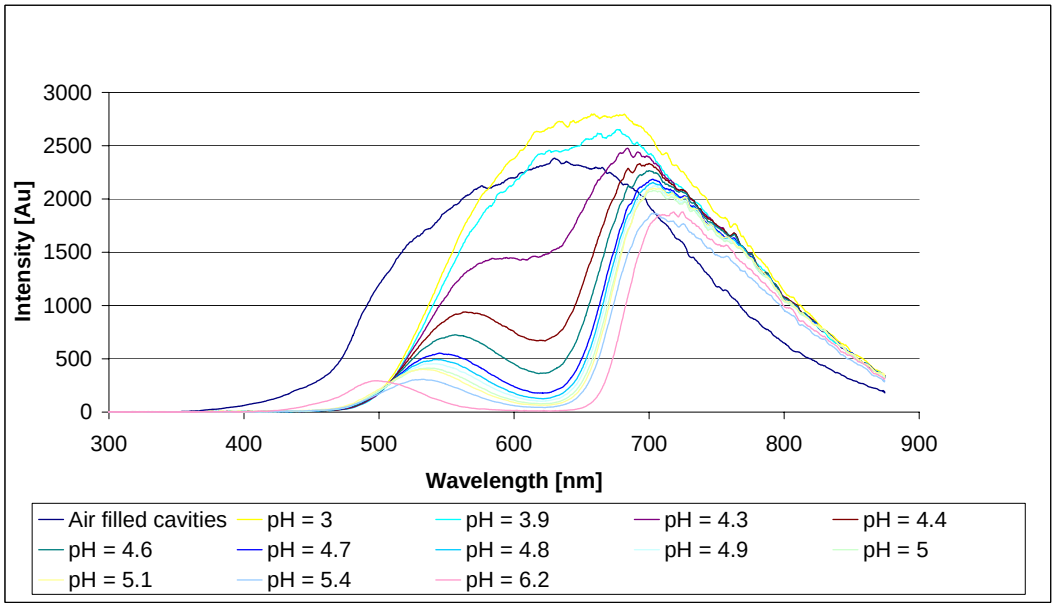

Figure 12-2: Evolution of transmission spectra with increasing pH of the solution.

From Figure 12-2, a dip in transmission spectrum at a wavelength of 620 nm at a pH of 4.3 was obvious and the transmission at this wavelength decreased with increasing pH of the solution. The pH of the solution was increased by adding NaOH solution. When the pH of the solution reached 6.2, a strong absorption in the range of 590 nm to 645 nm was

observed. When the pH was decreased from 6.2 to 2.3 by adding HNO_3 (nitric acid), the transmission in the range of 590 nm to 645 nm gradually increased and the spectrum of acidified bromocresol solution at the start of the experiment was recovered. The evolution of transmission spectra, when the pH was decreased to 2.3 is presented in Figure 12-3. However, the peak intensity of the transmission spectra in acidified bromocresol solution before and after the experiment was not equal, indicating a hysteresis. This could be due to fluctuations in the output of the source intensity.

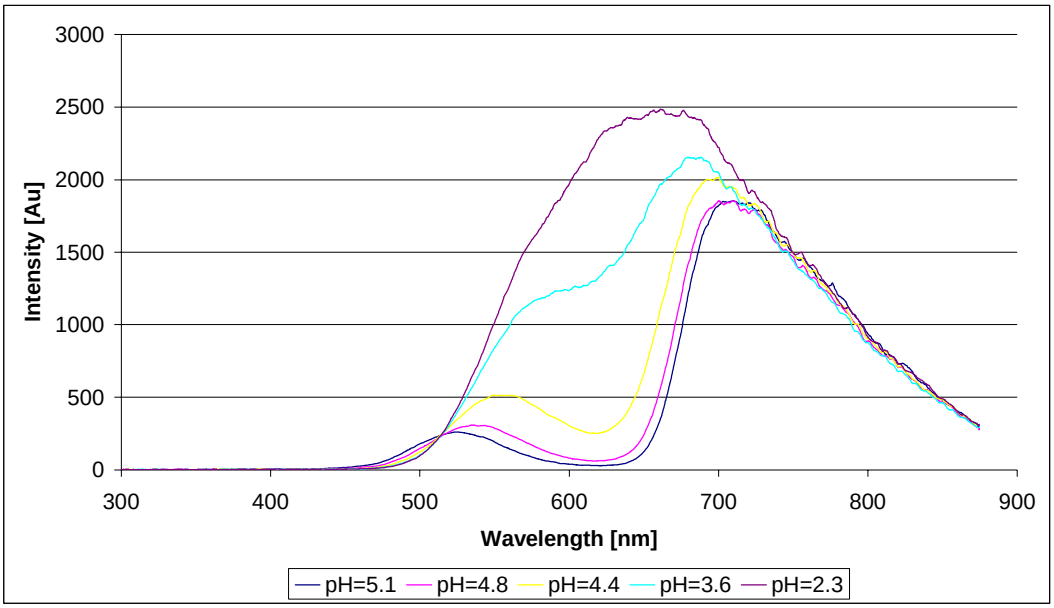

Figure 12-3: Evolution of transmission spectra when the pH was decreased from 6.2 to 2.3.

The reason for the evolution of spectra with a change in pH was due to change of colour of the bromocresol solution. When the pH was increased from 3 to 6.2, the colour of the solution changed from yellow to blue. When the colour of the solution was blue i.e. at pH 6.2 (see Figure 12-2), the transmission band extends from 430 nm to 590 nm with a peak intensity at 490 nm, which is the blue region of the visible spectrum. When the pH was decreased to 2.3 (see Figure 12-3), the colour of the solution again changed to yellow and the transmission spectrum changed to its initial transmission. Therefore, from these results, the changes in the pH can be detected in real time by monitoring the transmission spectrum of the bromocresol solution. The sensor was cleaned with isopropynol after the

Figure 12-4: Multiple cavities micro-machined along the length of the fibre.

The transmission spectrum of polyoxypropylenediamine can be observed in Figure 12-5, which was obtained by taking the ratio of the background to the transmission when the cavities were filled with polyoxypropylenediamine. The background was taken using a MM 800 fibre.

The chemical formula of Polyoxypropylenediamine is expressed as:

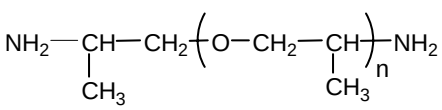

The Fourier transform infrared (FTIR) spectrum of polyoxypropylenediamine has an absorption band in the range of 1.51 μm to 1.57 μm. This is shown in Figure 12-6. This absorption peak is due to the overtone bands of the primary amine ($-NH_2$) symmetric and asymmetric fundamental stretching vibrations. This absorption peak was also observed by using micro-machined optical fibres as shown in the Figure 12-5.

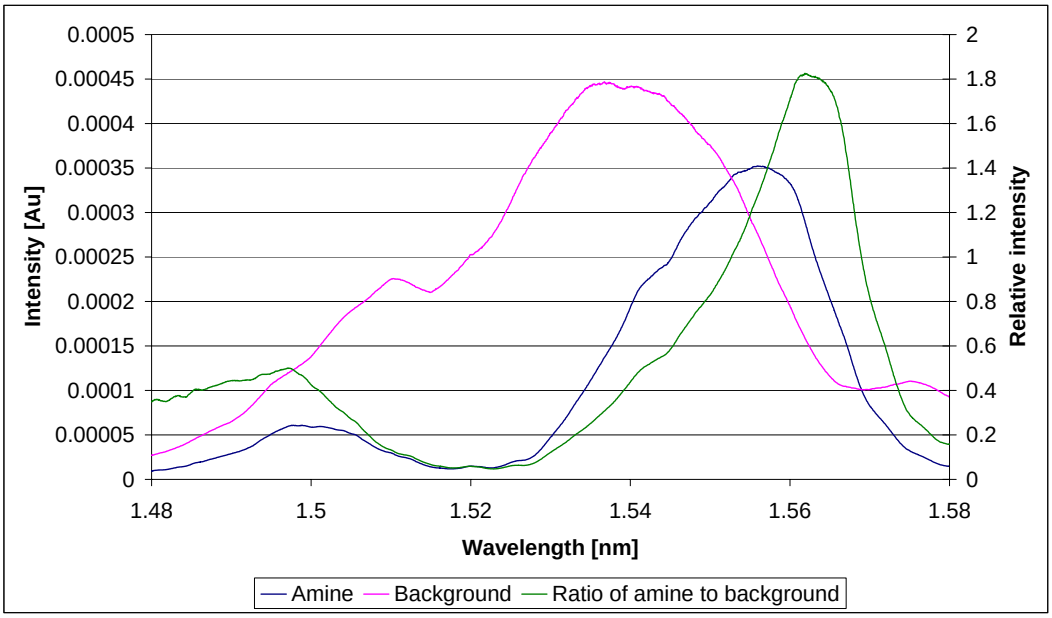

Figure 12-5: Transmission spectrum of polyoxypropylenediamine measured using micro-machined multimode fibre cavities as transmission cells.

The wavelength range shown in Figure 12-6 is relevant because this absorption peak due to the amine gets depleted as the curing reaction of a primary amine and an epoxy progresses and when the curing is finished, the absorption peak disappears. The optical fibres with micro-machined cavities could be embedded in composites to monitor this curing reaction. Therefore, chemical sensing via 157 nm laser micro-machined intrinsic cavities was demonstrated.

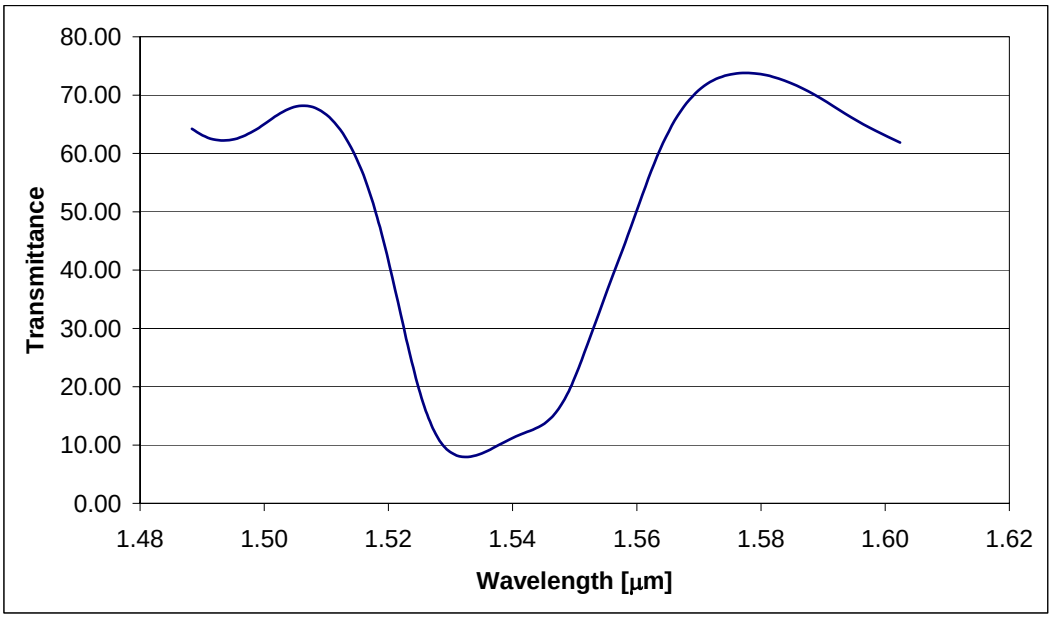

Figure 12-6: FTIR transmission spectrum of polyoxypropylenediamine in the wavelength range of 1.5 μm to 1.6 μm.

12.1.3 Feasibility of Pressure Sensor

An optical micrograph of SM 800 fibre ablated at an energy density of 25 x 10^4 Jm^{-2} is presented in Figure 12-7. The CCD interrogation of this fibre showed excellent Fabry-Perot interference fringes. The response of the ablated fibre is shown in Figure 12-8.

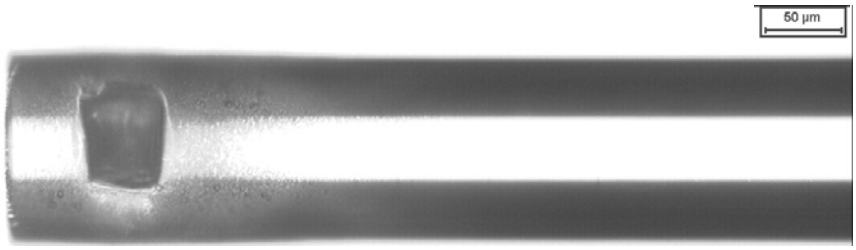

Figure 12-7: Optical micrograph of an SM 800 fibre ablated close to its cleaved-end.

From Figure 12-7, it can be observed that the fibre thickness between the cleaved end-face and the cavity can act like a membrane. However, the entrance and exit of the cavity on the surface of the fibre must be sealed to produce a pressure difference across the diaphragm. Therefore, it is essential to develop techniques to seal the cavity to

demonstrate pressure sensing. Realisation of these techniques could avoid fabrication of a diaphragm. The Fabry-Perot interference fringes of Figure 12-8 are a result of interference of three Fresnel reflections. The third Fresnel reflection occurs from the cleaved end-face of the optical fibre. The third Fresnel reflection could be suppressed using an anti-reflection coating.

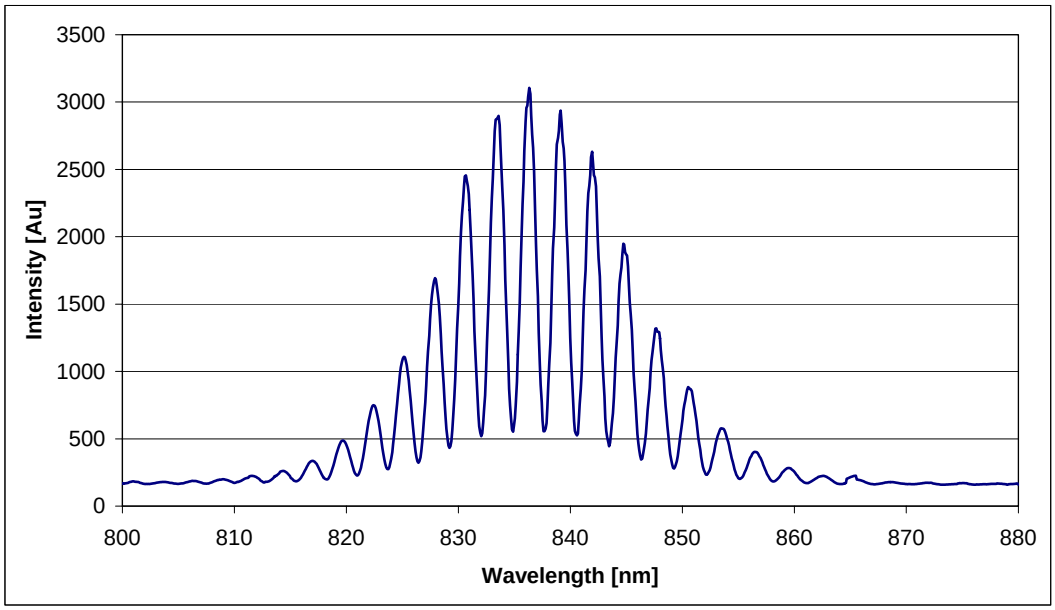

Figure 12-8: FP interference of a cavity ablated close to the cleaved-end of the fibre.

12.1.4 Summary of Sensor Applications

In this chapter, a pH senor and a chemical sensor produced from micro-machined optical fibres are demonstrated. An attempt was made to fabricate pressure sensor. However, the fibre surface must be sealed to produce a pressure difference across the diaphragm. The pH-sensor can be calibrated using a temperature-controlled light source in order to avoid fluctuations in light source intensity. The use of a multimode fibre with multiple micro-machined cavities for chemical detection of the amine in polyoxypropylene diamine was successfully demonstrated. These sensors could be embedded in composites for cure monitoring.

12.1.5 Novelty of this chapter

This chapter demonstrates the potential of F_2-laser based fabrication of intrinsic FP cavities for various sensing applications. The feasibility experiments of pH sensing and amine detection using intrinsic FP cavities as miniature transmission cells demonstrates the potential of this work for developing sensors for remote chemical process monitoring such as curing reactions of composite manufacturing, gas sensing and moisture sensing. These sensing cavities in fused silica fibres can be used in the presence of many industrial chemicals and at relatively high temperature environments, where the use of polymer fibre-based sensors is difficult. This work demonstrates a technique for developing high-pressure sensors by bypassing difficult techniques [3], [36], [37], [131] involved in diaphragm engineering. These feasibility experiments of sensing based on F_2-laser micro-machined intrinsic FP cavities in fused silica optical fibres have not been reported previously.

With respect to the main aims of this PhD research as mentioned in Section 1.1, the first two aims, fabrication and demonstration of strain sensors using HF etching of fused silica single mode optical fibres; and the design and construction of F_2-laser micro-machining station for ablating high aspect ratio cavities in fused silica and sapphire substrates have been fully achieved. The third aim of fabricating intrinsic FP cavities through the diameter has been successfully demonstrated. However, the second part of the third aim, which is the fabrication of intrinsic FP cavities at the cleaved end-face of the optical fibres has not produced the desired results. The main obstacle in realising this design is the alignment of cleaved end-face of the fibres at the focal plane of the objective. Two novel fabrication techniques, which have the potential to overcome problems involved in the design and fabrication of conventional EFFPIs and for the development of new sensor systems, have been successfully demonstrated.

13 Conclusions and Suggestions for Future Work

Two techniques for micro-machining intrinsic Fabry-Perot cavities in fused silica optical fibres were investigated in this thesis. They are hydrofluoric acid etching and F_2-laser micro-machining of optical fibres. Based on the research work reported in the literature, these techniques were believed to produce adequate optical quality and geometry of the designed intrinsic cavity structures in optical fibres to produce Fabry-Perot interference. The conclusions of various investigations involved with techniques were presented as follows:

13.1 HF-Etching of Optical Fibres

Etch-rate of Optical Fibres:

This technique is based on the principle that the germanium doped-core of the fibre undergoes preferential etching compared with the un-doped fused silica cladding during HF-etching. HF-etching of unprotected SM 800 fibres for different times at a controlled acid temperature of 20 ± 0.5 °C produced cavities of different etch-depths and end-face diameters across the core of the fibres. Optical microscope measurements of etched fibre-ends showed that both the end-face diameter decreased and etch-depth increased in a linear fashion respectively with the etch-time. The etch rate of the core and the end-face diameter were found to be 1 μm minute^{-1} and 3 μm minute^{-1} respectively. However, the observed decrease in etch-depth after 22 minutes was due to etching of the cleaved end-face that produced a shift towards the crater.

SEM Investigation of Etched Cavities:

Scanning electron microscope investigations showed a smooth topography of etched end-faces of the fibre with a circular entrance of cavities across the core. The cladding thickness was found to decrease with etch-time. After an etch-time of 35 minutes, no obvious cladding thickness remained at the fibre end-face. The cladding thickness of the etched end-face of the fibre is the most important factor, which determined the fusion splicing of two etched-fibres of equal end-face diameters. The end-face of the fibre was

reduced to a tip after an etch-time of one hour, with the core forming the tip of the fibre. The etching of the cylindrical surface of the immersed-length of the unprotected fibre and the surface tension at the meniscus produced a tapered length of the fibre.

Surface Profile Analysis:

Interferometric surface profile analysis showed that the etching-induced RMS roughness across the core and cladding were in the range 80-160 nm and 20-150 nm respectively over an etch-time of 22 minutes. Due to steepness of the wall surfaces, no reflection was obtained from the cavity surface. However, the roughness data obtained from the cladding thickness could also be attributed to the cavity surfaces as they are made of the same material. A concave curvature across the surface of the etched-core was observed. This was probably due to accumulation of reaction products at the core/cladding interface or due to deviations in the index-profile of the core from the ideal step-profile.

CCD Interrogation:

The CCD interrogation of the evolution of the response of two etched-cavities from their butted position to an 80 μm separation showed that the cavity length that was calculated from the Fabry-Perot interference produced from the etched cavities increased in a linear fashion with an increase in the translated distance. This proved that the etched cavities, in principle, could be used for fabricating FP sensors. The etched fibre-ends of equal diameter were fusion spliced using controlled fusion parameters and intrinsic fibre Fabry-Perot interferometers of different cavity lengths were produced. The intensity of the FP interference fringes slightly increased after fusion splicing. This could be due to improved surface smoothness of cavity surfaces under the influence of high temperatures generated by the fusion arc.

Fabrication of IFFPI and Demonstration of Strain Sensors:

Intrinsic fibre Fabry-Perot interferometers were surface mounted on composite coupons and were subjected to tension-tension fatigue. The CCD interrogation of these sensors showed an excellent linearity of the changes in etched-cavity length with the respective changes in the strain measured by the surface-mounted electrical resistance strain gauges. The sensors of larger cavity length were fabricated using fibres etched for longer periods

of time. These sensors have a smaller contact area at the fusion splice point due to smaller cladding thickness and showed a larger change in cavity length for a specified applied strain.

In comparison to the extrinsic fibre Fabry-Perot sensors, these sensors have a much smaller diameter (similar to that of a 125 μm diameter optical fibre), no abrupt discontinuities of diameter along the length of the sensor, well-defined fusion-splice point and do not involve gauge length and calibration prior to use. The sensor fabrication involves three steps: (i) HF etching of fibres at a controlled temperature, (ii) cleaning of etched fibres and (iii) controlled fusion-splicing of etched fibres of equal end-face diameter. The repeatability of fabrication can be improved by using a higher precision temperature controller and fusion splicer.

13.2 F_2-Laser Ablation of Disks and Optical Fibres

This technique required a custom-designed micro-machining station, which involved the design of illumination optics; design and construction of a purge chamber; a target alignment system and a monitoring system.

Design of Illumination System:

Based on conventional Kohler illumination, the illumination optics was designed so as to produce feature dimensions ranging from 15 μm to 125 μm at the image plane of an objective lens. A low numerical aperture (NA = 0.1) objective lens with a demagnification ratio of 1:40 was used for imaging the projected mask features. These optical parameters were chosen to facilitate the micro-machining of high-aspect ratio cavities according to the design criteria of various intrinsic fibre Fabry-Perot cavities and to facilitate the alignment of optical fibres in the image plane.

Construction of a Target Alignment and a Monitoring System:

A target alignment system comprising motorised translation stages of suitable motion resolution for aligning optical fibres were assembled and suitably modified to comply with the optical beam delivery specifications. The telescope of the CCD camera was modified using plano-concave lenses to enhance the magnification of the optical fibres during on-axis monitoring.

Design and Construction of a Purge Chamber:

An ablation chamber in compliance with the beam delivery system was designed and constructed. Besides the optical beam delivery design and alignment system, the purge chamber design and construction was an essential part of F_2-laser micro-machining station as it determined the transmission of the 157 nm laser beam to the target surface. The chamber was flushed with dry nitrogen gas to establish a transmission ambient for the 157 nm laser beam. The ablation chamber was designed so that the target could be illuminated from outside the chamber and the work piece could be monitored along the axis of the objective. The power-supply-leads of the motorised translation stages were sealed in glands using epoxy resin to ensure a leak-proof chamber.

Evaluation of the Purge Chamber:

The transmission of the beam through the purge chamber was investigated at 25 litre $minute^{-1}$ and 35 litre $minute^{-1}$. At both these flow rates the beam transmission gradually increased and reached at plateau region. At a higher flow rate the transmission reached the plateau region at a faster rate. An average loss of 16.6% of pulse energy per meter was observed with the 3.3 m long beam tunnel. However, using pure inert gases such as argon or N_2 of higher purity than that used in these experiments could reduce the transmission losses. When the flow rate of the purge gas was reduced from 35 litre $minute^{-1}$ to 10 litre $minute^{-1}$, the transmission dropped from the plateau region and stabilised over a period of time. The transmission started to increase again when the flow rate was increased. The higher flow rate of purging not only reduced the contamination concentration at a faster rate but also produced a higher flow velocity of the gas efflux through the vent orifice. The reason for the decrease in transmission after reducing the

flow rate could be that the efflux velocity of gas through the vent orifice was not adequate to exert an equal and opposite drag force on particles infiltrating through the vent orifice. A maximum transmitted energy of 0.38 mJ through a 1.5 mm x 1.5 mm mask feature was obtained. This was only 0.76% of 50 mJ pulse-energy. However, with this transmitted energy through the mask feature, the energy density at the de-magnified image plane would be 25.9 x 10^4 Jm^{-2}, which was well above the ablation threshold of fused silica and sapphire. Therefore the purge chamber designed was capable of transmitting the desired energy densities for carrying out the ablation of fused silica and sapphire.

Evaluation of the Beam Delivery System:

Köhler-based illumination design and the imaging system were used for the projection of mask features. Preliminary studies on 157 nm laser ablation of fused silica showed that the beam delivery system produced the desired demagnification and geometry of the mask features. Edge-ringing, which is a characteristic feature of coherent illumination, was manifested as notches or depressions near the corners of the craters of the ablated structures.

SEM Study of Fused Silica Disk Ablation:

Fused silica and sapphire disk ablation were carried out at energy densities ranging from 7 x 10^4 Jm^{-2} to 26 x 10^4 Jm^{-2}. The general morphology (SEM investigations) of cavities at 7 x 10^4 Jm^{-2} was very rough and no reflectivity was obtained from these surfaces during surface profile measurements. When the energy density was increased to 15.4 x 10^4 Jm^{-2}, a significant improvement in the geometric shape and smoothness of the cavities was observed. The smoothness of craters and cavity walls improved with an increasing number of pulses. However, the deposition of ablation debris was increased with ablation depth. The tapering of cavity walls decreased with an increase in energy density. When the energy density was increased to 24.5 x 10^4 Jm^{-2}, smooth sidewalls and well-defined crater surfaces were obtained. There was no obvious micro-crack formation at all the energy densities used in these experiments. The deposition of ablation debris was also significantly reduced at an energy density of 24.5 x 10^4 Jm^{-2}. The undulations along the

mask edge were clearly replicated along the corresponding wall surfaces of the ablated microstructures. Edge-ringing of the intensity produced a greater ablation around the margins of the crater and largest ablation was observed at the corners of craters. This resulted in higher debris deposition along the cavity wall edges.

Surface Profile Analysis:

Surface profile analysis showed that the optical quality of microstructural craters ablated at an energy density of 24.5 x 10^4 Jm^{-2} was adequate to produce Fabry-Perot interference. The RMS roughness measured on crater surfaces varied over a range of 100 to 500 nm. The rate of ablation of silica at three different energy densities was determined. The flatness of the crater surfaces improved with an increasing number of pulses. The depth of the cavities could be controlled from the ablation rate data obtained at different energy densities. No quantitative data about the roughness of cavity walls were obtained due to a lack of reflection from the steep walls. One major problem identified in these studies was the deposition of ablation debris. This could be due to plume attenuation of the pulse energy and hindered expansion of the plume due to the influence of atmosphere surrounding the ablation site. The study of ablation debris deposition during F_2-laser ablation of fused silica at different ambient pressures of the atmosphere surrounding the ablation site could be a useful future study.

SEM Study of the Ablation of Sapphire Disks:

An SEM study of microstructures ablated on sapphire disks at different energy densities revealed that the thermal effects of ablation deteriorated the quality of machined surface. The entrance of the cavities was dominated by residual un-ablated material. However, the wall formation and craters became more evident with an increasing number of pulses. This indicated an enhanced absorption of the ablated surface, which could be due to colour centre formation. Smooth walls and crater surfaces were produced at energy densities of 23.1 x 10^4 and 24.5x 10^4 Jm^{-2}. Flaking of wall surfaces and micro-cracking were observed at 24 x 10^4 Jm^{-2}. The walls of the cavities were not as flat as those obtained during fused silica ablation. Undulations on the wall surfaces deteriorated the cavity wall definition. Although the crater surfaces were smooth, the deposition of

ablation debris could deteriorate the optical quality of structures. The thermal effects were due to poor absorption, the high melting temperature of sapphire and long pulse duration. These effects were detrimental for the fabrication of Fabry-Perot microstructures.

Surface Profile Analysis:

Surface profile analysis of the cavities ablated at 24 x 10^4 Jm^{-2} revealed that the optical finish of cavity craters was adequate to produce FP interference. The RMS surface roughness of the cavity craters was in the range of 110 to 220 nm. The rate of ablation of sapphire at three different energy densities was determined. The rate of ablation of sapphire was found to be lower than that of fused silica. This could be due to poorer absorption by sapphire at 157 nm than the fused silica used in these experiments. Besides the optical beam delivery, material absorption at a specified wavelength was shown to be a very important factor, which determined the quality of ablation. The data on optical quality of cavity wall surfaces could not be gathered due to the steepness of the walls. The flatness of craters was found to be higher for structures ablated for larger number of pulses. The conclusion of these studies was that high aspect-ratio microstructures of an optical quality sufficient to produce Fabry-Perot interference could be micro-machined in sapphire substrates.

Ablation of Optical Fibres through the Diameter:

Ablation of SM 800 and SMF 28 fibres was investigated. Cavities with entrance dimensions of 38 μm x 38 μm and 50 μm x 50 μm were machined through the diameter of the optical fibres at energy densities in the range of 7 x 10^4 to 26 x 10^4 Jm^{-2} through their diameter. The target monitoring and alignment system designed for this work was found to be suitable during micro-machining fibres through their diameter. When the energy density of ablation increased from 11.2 x 10^4 Jm^{-2} to 25.5 x 10^4 Jm^{-2}, the taper angle of the cavities decreased from 12° to 1.2°. CCD interrogation of the ablated cavities showed that Fabry-Perot interference fringes could be produced in both SM 800 and SMF 28 fibres at an energy density of ablation in the range of 25 x 10^4 to 26 x 10^4 Jm^{-2}. In addition to the energy density of the ablation, the symmetric alignment of optical fibres is

a vital factor, which determined the cavity tapering. The cavity tapering in turn determined the FP interference via ablated cavities. The taper profiles of the ablated cavity walls of the fractured fibres showed that the alignment of the fibres in the image plane determined the wall-angle of the cavities. Different regions of the ablation surface on the optical fibre, experienced unequal image defocusing as the ablation depth increased. This was a difference between the ablation of flat and curved substrates. The image defocusing, which was the main reason for cavity tapering, was larger in the case of optical fibre ablation due to the curvature of the fibres. The problem could be overcome by polishing the fibre surface.

The cavity length calculated from the FP interference fringes obtained from the cavities ablated at 25 x 10^4 Jm^{-2} was not exactly same as the entrance dimensions of the ablated structure. This implied that the FP interference was possible in spite of the departure from parallelism of etalon surfaces to a certain degree. Theoretical calculations based on Snell's laws have shown that there was a possibility of interference of Fresnel reflections to an extent of tapering. This could be the reason for the observed difference in the entrance dimensions of the cavity and the calculated cavity length. The calculation of Fresnel reflection coefficients showed that the tapering reduced the contrast of FP interference fringes. Another probable reason for this discrepancy was that the aerial image evolving from the cladding/core interface to the core/cladding interface could alter the wall-angle across the core of the fibres. As the core of the fibre had a much stronger absorption of 157 nm radiation than the cladding, the influence of the evolving aerial image through the diameter of the core could be different from that of the cladding. However, more in-depth research is required to investigate these factors.

SEM and surface profiler analysis of the ablated cavity wall surfaces showed a smooth surface with little ablation debris and RMS roughness ranging from 400 to 500 nm. However, it was the roughness across the core of that determined the light transmitted to the second wall surface. Micro-cracks were observed on the cavity walls of some of the ablated fibres. Although reasons such as the sudden cooling of wall surfaces after the expansion of the plasma out of the cavity, stress corrosion due to the influence of

atmospheric moisture and influence of fracturing the ablated fibre could be suggested, the exact reason was not established and requires further investigations. The deposition of ablation debris across the wall surface was significantly lower than that observed during fused silica disk ablation. This could be due to higher absorption of fused silica optical fibres, which is due industrial manufacturing-induced defects and colour centres. Therefore, a novel fabrication technique for producing intrinsic fibre Fabry-Perot cavities was demonstrated.

Ablation of Optical Fibres at the Cleaved End-face:

SEM analysis of ablated structures on the cleaved end-face of the SM 800 fibres showed a smooth morphology of cavity walls and craters. However, a difficulty of aligning the cleaved end-faces in the image plane did not produce the desired geometry. Therefore, ablation of cleaved ends requires a higher precision alignment zig and illumination techniques to be developed. Realization of this intrinsic Fabry-Perot design could offer many advantages over acid-etched sensors. For example, the fibre tapering, which is inevitable during acid etching of bare fibres, could be avoided by this technique. Changing the number of pulses of irradiation can produce cavities of the desired and repeatable gap lengths. The strain sensitivity of the intrinsic FP sensors could be tailored by ablating varying feature dimensions on the cleaved end face. Hence, a higher cavity gap length could be produced in a sensor with a smaller contact area for the same applied tensile load due to higher stress. The author has a strong intention to fabricate strain sensors using this technique in the near future.

Ablation of Sapphire Fibres:

The ablation of sapphire fibres was carried out to demonstrate that cavities could be micro-machined through the diameter (150 μm) of the fibres. SEM and surface profile analysis showed that cavity wall surfaces had adequate optical quality to produce FP interference. However, flaking and micro-cracking of wall surfaces and ablation debris around the entrance of the cavity were observed. These observations were in agreement with the results obtained from the sapphire disk ablation. Micro-cracks, flaking and tapering of cavity walls are detrimental to the fabrication of FP micro-cavities. The CCD

interrogation showed FP interference fringes of poor contrast and this demonstrated that F_2-laser-based fabrication of intrinsic FP micro-structures in sapphire fibres was feasible. However, further investigations on micro-machining of sapphire fibres are required to establish the technique. These cavities could also be filled with suitable materials and may be used for high temperature sensing applications.

In-situ Monitoring of Laser-indued Fluorescence during Ablation:

In-situ 157 nm LIF monitoring during ablation of optical fibre through its diameter revealed an abrupt increase of fluorescence associated with a change in spectral shape when the ablation depth corresponded to the core of the fibre. This technique revealed whether the cavity had formed across the core of the fibre. Therefore a reliable technique for confirming the alignment of optical fibres during the fabrication of intrinsic FP cavities was developed. The peak intensities of fluorescence were expressed as a function of ablation depth at an energy density of 23 x 10^4 Jm^{-2}. The ablation depth calculated using this equation for a specified number of pulses was found to be in good agreement with the values of ablation depth measured using an optical microscope. This procedure could be carried out at other energy densities of ablation as well. The ablation depth can be controlled up to the surface of the core using this technique. Evanescent sensors could be fabricated in fused silica fibres using this technique.

Ablation of Fibre Bragg Gratings:

Bragg grating ablation experiments were carried out to investigate the effect of heat-generated inside the cavity on the fibre grating. No change in peak reflection wavelength of the grating was observed during ablation. The calculation of the heat-affected zone revealed that the heat diffusion length during ablation is very small compared to the length of the grating and the grating spacing, and hence the grating was insensitive to the high temperatures generated during ablation. The slight decrease of amplitude of reflection was due to a loss of grating planes over a length of 2 mm of the grating from one end of the grating. The Bragg ablation experiments conclusively proved that the heat generated during cavity ablation along the diameter of the fibre did not affect the integrity of the fibre core.

Applications of Ablated Fibres:

Some applications and feasibilities of ablated fused silica fibres were demonstrated. A pH-sensor based on the colour changes of the bromocresol dye solution was demonstrated. Multiple cavities were ablated through the diameter of a multimode fibre and the transmission was measured using a CCD spectrometer. The sensor showed the changes in transmission, based on the colour of the solution, which indicates the pH of the solution. An attempt was made to calibrate the sensor using an external pH-meter. Due to the fluctuations in the intensity of the light source, hysteresis was observed in the response of the sensor. This problem could be overcome by using a temperature-controlled light source. The transmission spectrum of the multi-cavity fibre was regained after it was cleaned with isopropanol. The sensor can be used as a pH switch.

Multiple cavities micro-machined through the diameter of a fibre along its length were used as transmission cells to detect the amine group in polyoxypropylene diamine. The transmission spectrum of this chemical was measured at near-infrared wavelengths using an optical spectrum analyser. The measured spectrum was in good agreement with the spectrum measured using a Fourier transform infrared spectrometer. This experiment demonstrated that these ablated cavities could be used as chemical sensors. Sensors for detecting a variety of gases and other chemicals could also be developed using these multiple cavities. The author intends to use these sensors for chemical process monitoring of thermosetting resins, which are used in advanced fibre-reinforced composites.

A cavity was ablated through the diameter of an SM 800 fibre at a distance of 50 μm from the cleaved-end of a fibre at an energy density of 25×10^4 Jm^{-2}. The intention was to fabricate a pressure sensor by bypassing the diaphragm engineering. The CCD interrogation of the cavity showed excellent Fabry-Perot interference, which was produced due to the interference of three Fresnel reflections. The 50 μm length of the fibre towards the cleaved-end of the fibre was expected to act as a diaphragm. However, the cavity through the diameter must be sealed on the outer surface of the fibre to investigate its response to the air pressure.

13.3 Future Work

Two micro-fabrication techniques for producing intrinsic fibre Fabry-Perot sensors were successfully demonstrated in the investigations described in this thesis. The author hopes that this research has provided some useful contributions to the development of fibre optic sensor technologies and some fundamental aspects of laser material interactions. This research has also generated some ideas for developing new sensor systems. The author intends to carry out research work on the development of new sensor technologies and fundamental aspects of the science of laser-micromachining. These future investigations are presented as follows.

Influence of Partial Coherence on Micro-structure Wall-angle:

This study is aimed at investigating the influence of partial coherence on the wall-angle of microstructures in fused silica and sapphire substrates. The degree of partial coherence can be altered by varying the extent of entrance pupil fill. This can be achieved using an homogeniser-based Köhler illumination optical system. Increasing the partial coherence leads to a decrease in the edge-ringing and consequently a top-hat spatial intensity profile can be achieved. This profile reduces the non-uniformity of ablation across the image plane and the optical quality of an ablated surface can be improved. This work has two main objectives. The first objective is the calculation of aerial image across a desired depth of focus at different partial coherences. The aerial image has to be calculated at a specified partial coherence for different energy densities. The second objective is to carry out ablation of the materials of interest (strong and weak absorbers of 157 nm radiation) at specified partial coherences and energy densities and to correlate the calculated aerial image with the experimental data of cavity wall angles. This study is believed will produce useful knowledge regarding the control of the geometry of high-aspect-ratio ablated microstructures.

Influence of Aerial Image on the Cavity Wall-Angle at the Interface of Two Different Materials:

The work is aimed at studying the influence of aerial image of a specified optical beam delivery system on the wall-angle of microstructures ablated through the interface of two different materials which significantly differ in their absorption properties at 157 nm. For example, a 30 μm germanium-doped fused silica will be grown on a 30 μm pure fused silica and a microstructure will be machined through the entire thickness of this substrate at different energy densities. The wall-angle of the microstructure is expected to be different in fused silica from that of the doped-silica due to the difference in their absorption properties. The aerial image, taking into account the material absorption properties, will be calculated across the thickness of the substrate and will be compared with the experimental results. The influence of entrance dimensions of the ablated structure on the wall-angle of the cavities will also be studied. It is believed that this research will answer the observed discrepancy in the entrance dimensions of the cavity and the cavity length of micro-machined FP structures through the diameter of optical fibres.

Influence of Aerial Image on the Wall-angle of Cavities Micro-machined in Substrates of Different Curvatures:

It is well known that image defocusing is the main reason for cavity tapering during micro-machining of high-aspect-ratio structures. In this work, microstructures of a specified aspect-ratio will be ablated through the diameter of cylindrical substrates of different curvatures. During ablation of curved substrates, an elemental area of the target surface will be subjected to different portions of the aerial image, which undergo defocusing at different rates. The combined effect of this defocusing at a specified energy density will determine the wall angle of the cavity in the curved substrate. These aspects will be studied from experiments and will be compared with the theoretical calculations.

Effect of Cleave Angle of Fibres on FP Interference:

The intention of this study is to determine how the cleave-angle of fibres affects the resulting FP interference. Fibre cleavers, which can cleave optical fibres to desired cleave-angles are commercially available. Fibres can be cleaved to different cleave angles and the resulting characteristics of the interference pattern that is obtained when these cleaved fibres are separated by suitable distances may be studied. The threshold of cleave-angle of the fibres for producing FP interference can also be determined.

Pressure Sensor Fabrication Technique:

Diaphragm engineering is a challenging aspect in the fabrication of optical fibre pressure sensors. However, diaphragm fabrication can be bypassed by using a combination of acid etching and laser ablation. An acid etched FP sensor will be made using SM 800 fibres and the fibre will be cleaved close to the cavity using an F_2-laser mask projection technique. Other researchers have proved that 157 nm laser cleaving of optical fibres can produce a mirror finish at the cleaved end-face. The length of the fibre between the etched cavity wall and laser-cleaved end-face can act like a diaphragm. Hence, the complex techniques of diaphragm fabrication can be overcome using this technique. This technique is illustrated in Figure 13-1.

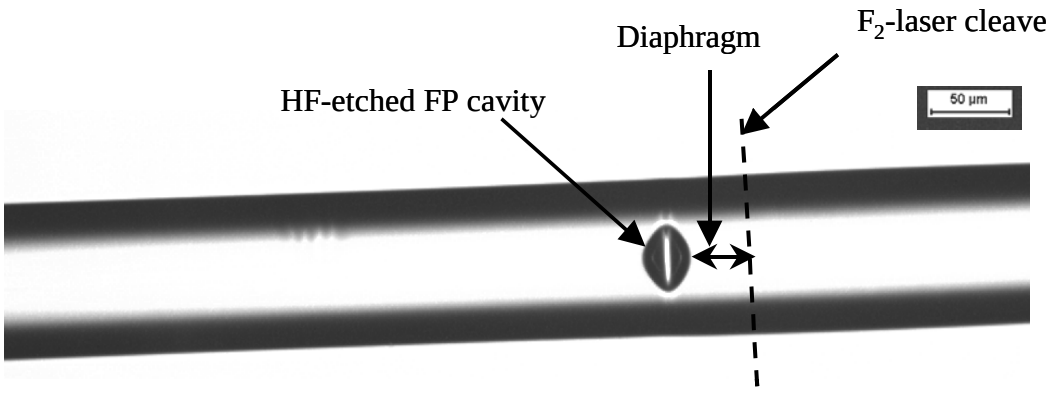

Figure 13-1: Illustration of pressure sensor fabrication.

Vibration Sensors:

This study is aimed at developing vibration and acoustic emission sensors using acid-etched fibres. A vibration sensor configuration that could be produced from an acid-etched fibre and a cleaved fibre illustrated in Figure 13-2. The loss of light due to diminished cladding and loss of transmission through the reference fibre can be reduced by using an etched multimode fibre (until a tip is produced at its end) and a cleaved single mode fibre or an etched single mode fibre (until a tip is produced at its end) and a cleaved multi-mode fibre.

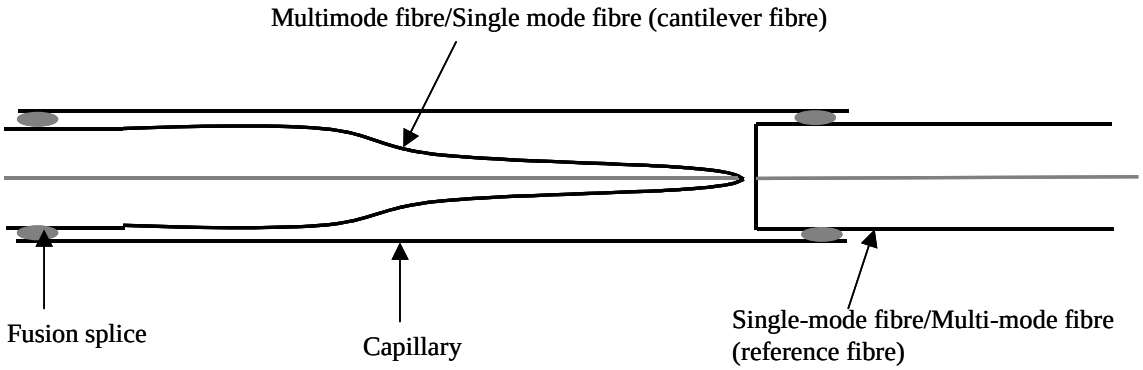

Figure 13-2: Schematic illustration of a vibration sensor configuration.

A vibration sensor could also be produced by controlled fusion splicing of etched multimode fibres. The transmitted light through the multimode etched intrinsic cavity is very sensitive to mechanical motion. This high sensitivity to mechanical perturbations was observed when an attempt was made to fabricate intrinsic FPs using multimode graded index fibres. An optical micrograph of a multimode intrinsic cavity produced via acid etching is shown in Figure 13-3.

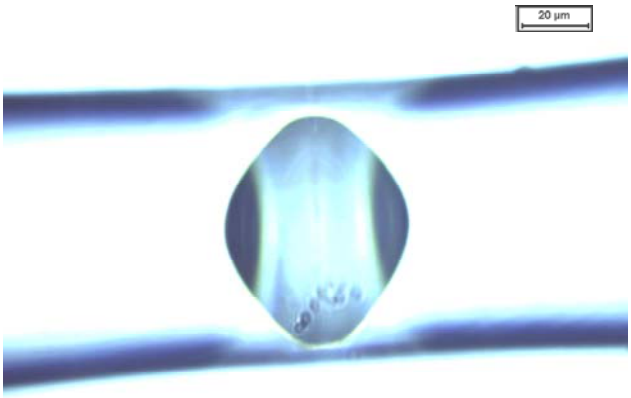

Figure 13-3: Optical micrograph of an intrinsic HF-etched cavity in a multimode fibre.

Fabrication of Holey Fibres:

A feasibility experiment was conducted with an intention to develop techniques for the fabrication of photonic crystal fibres. An acid-etched intrinsic cavity in a single mode fibre was heated and drawn to investigate whether the cavity collapses during this process.

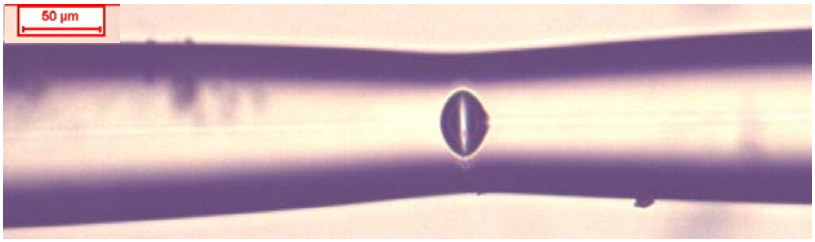

Figure 13-4: Optical micrograph of an intrinsic cavity before stretching.

Figure 13-5: Optical micrograph of the cavity after stretching.

The cavity was gradually stretched. Then the stretched fibre was fractured by applying a longitudinal force and the fractured cross-section was studied using SEM. Pictures of the cavity shape before stretching and after stretching are presented in Figure 13-4 and Figure 13-5 respectively. The fractured cross-sections are presented in Figure 13-6 and Figure 13-7. From Figure 13-6 and Figure 13-7, it is obvious that the cavity has not collapsed even after stretching it by a few hundred micrometres.

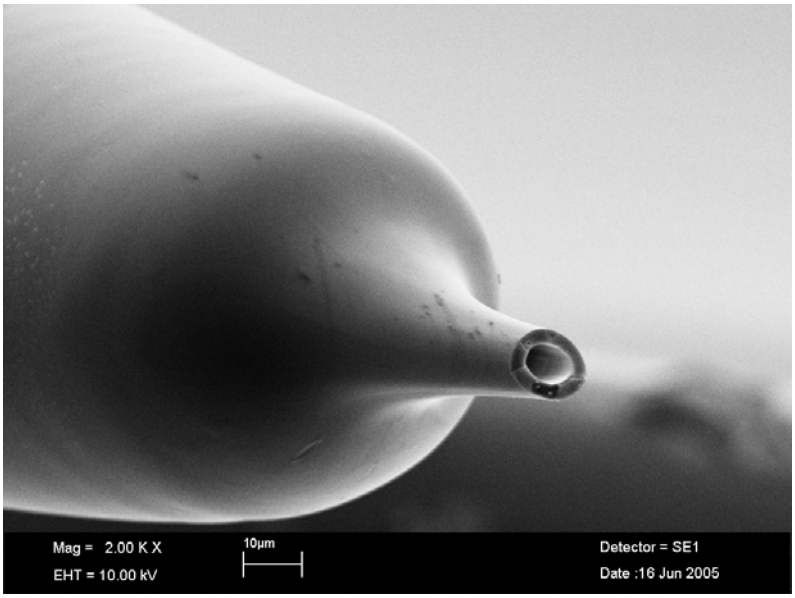

Figure 13-6: SEM micrograph of fractured cross-section of a stretched cavity.

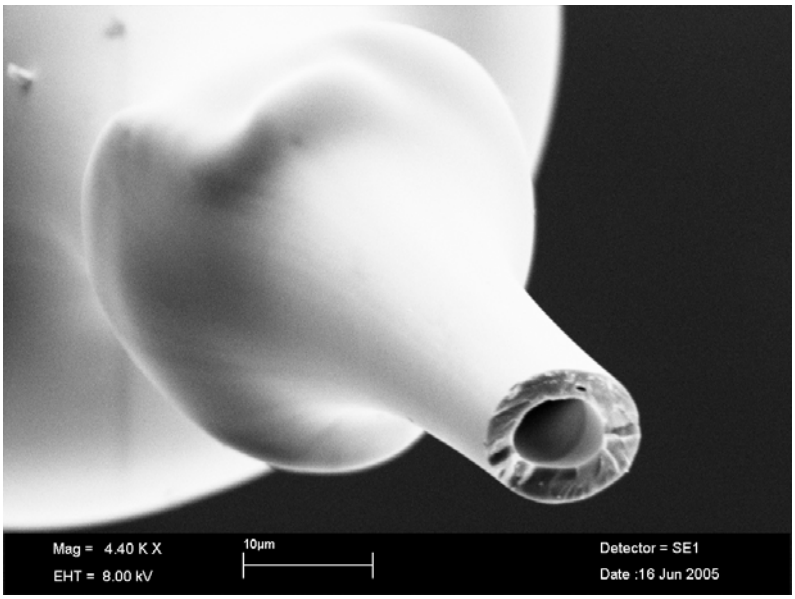

Figure 13-7: SEM micrograph of fractured cross-section of a stretched cavity.

The hydrostatic pressure of air inside the cavity prevented the collapse of cavity walls during heating and simultaneous stretching. Desired patterns of varying dimensions can be micro-machined on a fused silica stub and a similar un-ablated stub may be fused to it and can be heated and drawn to the required dimensions. The technique may be used for the fabrication of holey fibres or holey fibre components.

14 References

1. FERNANDO, G.F., LIU, T., CROSBY, P., DOYLE, C., MARTIN, A., BROOKS, D., RALPH, B., BADCOCK, R., *A multi-purpose optical fibre sensor design for fibre reinforced composite materials.* Measurement Science and Technology, 1997. **8**: p. 1065-1079.
2. LIU, T., FERNANDO, G.F., RAO, Y.J., JACKSON, D.A., ZHANG, L., BENNION, I., *Simultaneous strain and temperature measurements in composites using a multiplexed fibre Bragg grating and an extrinsic Fabry-Perot sensor.* SPIE, 1997. **3042**: p. 203-212.
3. ABEYSINGHE, D.C., DASGUPTA, S., BOYD, J., T., JACKSON, H.E., *A novel MEMS pressure sensor fabricated on an optical fibre.* IEEE photonics technology letters, 2001. **13**(9): p. 993-995.
4. CHEN, R., FERNANDO, G.F., BUTLER, T., BADCOCK, R.A., *A Novel ultrasound Fibre Optic Sensor based on a Fused-Tapered Optical Fibre Coupler.* Measurement Science and Technology, 2004. **15**: p. 1490-1495.
5. LAWRENCE, C.M., NELSON, D.V., *An embedded fibre optic sensor method for determining residual stresses in fibre-reinforced composite materials.* Journal of Intelligent Material Systems and Structures, 1998. **9**: p. 788-799.
6. OTHONOS, A., KALLI, K., *Fibre Bragg Gratings: Fundamentals and applications in telecommunications and sensing*. 1999, Norwood: Artech House, INC. 422.
7. LEE, D.C., LEE, J.J., YUN, S.J., *The mechanical characteristics of smart composite structures with embedded optical fibre sensors.* Composite Structures, 1995. **32**: p. 39-50.
8. TUCK, C., *Novel production techniques for fibre Fabry-Perot sensors*, in *Engineering Systems Department*. 2002, Cranfield university: Swindon. p. 197.
9. CHIARALUCE F., *Single-mode optical fibres and devices*, in *Single -mode optical fibre measurement: Characterization and sensing*, CANCELLIERI G., Editor. 1993, Artech House, INC.: Norwood. p. 17.
10. NING, Y.N., GRATTAN, K.T.V., WANG, W.M., PALMER, A.W., *A systematic classification and identification of optical fibre sensors.* Sensors and Actuators A, 1991. **29**: p. 21-36.
11. JACKSON, D.A., JONES, J.D.C., *Fibre optic sensors.* Optica Acta, 1986. **33**(12): p. 1469-1503.
12. ROGERS, A.J., *Optical-fibre sensors*, in *Sensors: A compresensive survey*, W. GOPEL, HESSE, J., ZEMEL, J.N., Editor. 1992, VCH Verlagsgesellschaft mbH, VCH Inc.: Weinheim. p. 362.
13. NING, Y.N., GRATTAN, K.T.V., PALMER, A.W., *Fibre-optic interferometric systems using low-coherence light sources: Review Paper.* Sensors and Actuators A, 1992. **30**: p. 181-192.
14. MURPHY, K.A., GUNTHER, M.F., VENGSARKAR, A.M., CLAUS, R.O., *Quadrature phase-shifted, extrinsic Fabry-Perot optical fibre sensors.* Optics Letters, 1991. **16**(4): p. 273-275.

15. LIU, T., BROOKS, D., MARTIN, A., BADCOCK, R., RALPH, B., FERNANDO, G.F., *A multi-mode extrinsic Fabry-Perot interferometric strain sensor.* Smart Structures and Materials, 1997. **6**: p. 464-469.
16. LIU, T., BROOKS, D., MARTIN, A., BADCOCK, R., FERNANDO, G.F., *Design, fabrication and evaluation of an optical fibre sensor for tensile and compressive strain measurements via the use of white light interferometry.* SPIE, 1996. **2718**: p. 408-416.
17. JACKSON, D.A., JONES, J.D.C., *Interferometers*, in *Optical fibre sensors*, B. CULSHAW, DAKIN, J., Editor. 1988, Artech House: London. p. 329.
18. CLAUS, R.O., GUNTHER, M.S., WANG, A.B., MURPHY K.A., SUN, D., *Extrinsic Fabry-Perot sensors for structural evaluation*, F. ANSARI, Editor. 1993, ASCE: New York. p. 60-70.
19. BELLEVILLE, C., DUPLAIN, G., *White-light interferometric multimode fibre-optic strain sensor.* Optics Letters, 1993. **18**(1): p. 78-80.
20. JACKSON, D.A., *Recent progress in monomode fibre-optic sensors: Review article.* Measurement Science and Technology, 1994. **5**: p. 621-637.
21. SINGH, M., TUCK, C.J., FERNANDO, G.F., *Multiplexed optical fibre Fabry-Perot sensors for strain metrology.* Smart Materials and Structures, 1999. **8**: p. 549-553.
22. LEE, C.E., GIBLER, W.N., ATKINS, R.A., TAYLOR, H.F., *In-line fibre Fabry-Perot interferometer with high-reflectance internal mirrors.* Journal of Light Wave Technology, 1992. **10**(10): p. 1376-1379.
23. LEE, C.E., TAYLOR, H.F., *Interferometric optical fibre sensors using internal mirrors.* Electronic Letters, 1988. **24**(4): p. 193-194.
24. LEE, C.E., TAYLOR, H.F., MARKUS, A.M., UDD, E., *Optical-fibre Fabry-Perot embedded sensor.* Optics Letters, 1989. **14**(21): p. 1225-1227.
25. INCI, M.N., KIDD, S.R., BARTON, J.S., JONES, J.D.C., *High temperature miniature fibre optic interferometric thermal sensors.* Measurement Science and Technology, 1993. **4**: p. 382-387.
26. MORSE, T.F., HE, Y., LUO, F., *An optical fibre sensor for measurement of elevated temperatures.* IEICE Trans. Electron., 2000. **E83-C**(3): p. 298-302.
27. KADDU, S.C., BOOTH, D.J., GARCHEV, D.D., COLLINS, S.F., *Intrinsic fibre Fabry-Perot sensors based on co-located Bragg gratings.* Optics Communications, 1997. **142**: p. 189-192.
28. PAL, S., MANDAL, J., SUN, T., GRATTAN, K.T.V., FOKINE, M., CARLSSON, F., FONJALLAZ, P.Y., WADE, S.A., COLLINS, S.F., *Characteristics of potential fibre Bragg grating sensor-based devices at elevated temperatures.* Measurement Science and Technology, 2003. **14**: p. 1131-1136.
29. MIZUNAMI, T., TATEHATA, H., KAWASHIMA, H., *High-sensitivity cryogenic fibre-Bragg-grating temperature sensors using teflon substrates.* Measurement Science and Technology, 2001. **12**: p. 914-917.
30. MACPHERSON, W.N., KILPATRICK, J.M., BARTON, J.S., JONES, J.D.C., ZHANG, L., BENNION, I., *Heat-flux measurement using fibre-Bragg-grating Fabry-Perot sensors.* Measurement Science and Technology, 1999. **10**: p. 1300-1304.

31. SIRKIS, J.S., BRENNAN, D.D., PUTMAN, M.A., BERKOFF, T.A., KERSEY, A.D., FRIEBELE, E.J., *In-line fibre etalon for strain measurement.* Optics Letters, 1993. **18**(22): p. 1973-1975.
32. HARAN, F.W., REW, J.K., FOOTE, P.D., *A strain-isolated fibre Bragg grating sensor for temperature compensation of fibre Bragg grating strain sensors.* Measurement Science and Technology, 1998. **9**: p. 1163-66.
33. FRIEBELE, E.J., *Fibre Bragg grating strain sensors: present and future applications in smart structures.* Optics and Photonics News, 1998. **9**: p. 33-37.
34. LEVIN, K., JARLAS, R., *Vulnerability of embedded EFPI-sensors to low-energy impacts.* Smart Materials and Structures, 1997. **6**: p. 369-382.
35. TAY, A.K., WILSON, D.A., WOOD, R.L., *Microdamage and optical signal analysis of impact induced fracture in smart structures.* Proceedings of SPIE, 1999. **1370**: p. 328-343.
36. YU, B., KIM, D.W., DENG, J., XIAO, H., WANG, A., *Fibre Fabry-Perot sensors for detection of partial discharges in power transformers.* Applied Optics, 2003. **42**(16): p. 3241-3250.
37. XU, J., PICKRELL, G., WANG, X., PENG, W., COOPER, K., WANG, A., *A novel temperature-insensitive optical fibre pressure sensor for harsh environments.* IEEE Photonics Technology Letters, 2005. **17**(4): p. 870-872.
38. DEGAMBER, B., *Microwave curing and process monitoring of thermosets*, in *Engineering systems department*. 2003, Cranfield university: Swindon. p. 180.
39. IHLEMANN, J., *Excimer laser ablation of fused silica.* Applied Surface Science, 1992. **54**: p. 193-200.
40. IHLEMANN, J., WOLFF, B., SIMON, P., *Nanosecond and femtosecond excimer laser ablation of fused silica.* Applied Physics A, 1992. **54**: p. 363-368.
41. DYER, P.E., FARLEY, R.J., GIEDL,R., KARNAKIS, D.M., *Excimer laser ablation of polymers and glasses for grating fabrication.* Applied Surface Science, 1996. **96-98**: p. 537-549.
42. IHLEMANN, J., WOLFF-ROTTKE, B., *Excimer laser micro machining of inorganic dielectrics.* Applied Surface Science, 1996. **106**: p. 282-286.
43. IHLEMANN, J., SCHOLL, A., SCHMODT, H., WOLFF-ROTTKE, B., *Nanosecond and femtosecond excimer-laser ablation of oxide ceramics.* Applied Physics A, 1995. **60**: p. 411-417.
44. OLIVEIRA, V., SIMOES, F., VILAR, R., *Column-growth mechanisms during KrF laser micromachining of Al_2O_3-TiC ceramics.* Applied Physics A, 2004. **DOI: 10.1007/s00339-004-3083-2**: p. 1-6.
45. OLIVEIRA, V., CONDE, O., VILAR, R., *UV laser micromachining of ceramic materials: Formation of columnar topographies.* Advanced Engineering Materials, 2001. **3**(1-2): p. 75-81.
46. MENDES, M., VILAR, R., *Influence of the working atmosphere on the excimer laser ablation of Al_2O_3-TiC ceramics.* Applied Surface Science, 2003. **206**: p. 196-208.
47. ZENG, X., MAO, S.S., LIU, C., MAO, X., GREIF, R., RUSSO, R.E., *Laser-induced plasmas in micromachined fused silica cavities.* Applied Physics Letters, 2003. **83**(2): p. 240-242.

48. ZENG, X., MAO, S.S., LIU, C., MAO, X., GREIF, R., RUSSO, R.E., *Plasma diagnostics during laser ablation in a cavity.* Spectrochimica Acta Part B, 2003. **58**: p. 867-877.
49. ZENG, X., MAO, X., MAO, S.S., YOO, J.H., GREIF, R., RUSSO, R.E., Journal of Applied Physics B, 2004. **95**(2004): p. 16-22.
50. ZENG, X., MAO, X., WEN, S., GREIF, R., RUSSO, R.E., *Energy deposition and shock wave propagation during pulsed laser ablation in fused silica cavities.* Journal of Physics D: Applied Physics, 2004. **37**: p. 1132-1136.
51. WOLFF-ROTTKE, B., IHLEMANN, J., SCHMIDT, H., SCHOLL,A., *Influence of the laser-spot diameter on photo-ablation rates.* Applied Physics A, 1995. **60**: p. 13-17.
52. BURGHARDT, B., SCHEEDE, S., SENCZUK, R., KAHLERT, H.J., *Ablation plume effects on high precision excimer laser-based micromachining.* Applied Physics A, 1999. **69**: p. S137-S140.
53. SCHAFFER, C.B., BRODEUR, A., MAZUR, E., *Laser-induced breakdown and damage in bulk transparent materials induced by tightly focussed femtosecond laser pulses.* Measurement Science and Technology, 2001. **12**: p. 1784-1794.
54. LIU, X., DU, D., MOUROU, G., *Laser ablation and micromachining with ultrashort laser pulses.* IEEE Journal of Quantum Electronics, 1997. **33**(10): p. 1706-1716.
55. KRUGER, J., KAUTEK, W., *Ultrashort pulse laser interaction with dielectrics and polymers.* Advances in Polymer Science, 2004. **168**: p. 247-289.
56. KRUGER, J., KAUTEK, W., *Femtosecond-pulse visible laser processing of transparent materials.* Applies Surface Science, 1996. **96-98**: p. 430-438.
57. LENZNER, M., KRUGER, J., KAUTEK, W., KRAUSZ, F., *Presicion laser ablation of dielectrics in the 10-fs regime.* Applied Physics A, 1999. **68**: p. 369-371.
58. WANG, X.C., LIM, G.C., ZHENG, H.Y., NG, F.L., LIU, W., CHUA, S.J., *Femtosecond pulse laser ablation of sapphire in ambient air.* Applied Surface Science, 2004. **228**: p. 221-226.
59. ALLMEN, M.V., *Laser-beam interactions with materials*, ed. A. MOORADIAN. Vol. 2. 1987, Berlin Heidelberg: Springer-Verlag. 232.
60. SPROULL, R.L., PHILLIPS, W.A., *Modern physics-The quantum physics of atoms, solids and nuclei*. 3rd Edition ed. 1980, Canada: John Wiley & Sons, Inc.
61. KITTEL, C., *Introduction to solid state physics*. 6th Edition ed. 1986, Toronto, Canada: John Wiley & Sons, Inc. 646.
62. ELLIOTT, S.R., *Physics of amorphous materials*. Second ed. 1990, Hong Kong: Longman Scientific & Technical. 481.
63. NISHIKAWA, H., *Structures and properties of amorphous silicon dioxide-Issues on the reliability and novel applications*, in *Silicon-Based Materials and Devices*, H.S. Nalwa, Editor. 2001, Academic Press: San Diego. p. 93.
64. KAJIHARA, K., IKUTA, Y., OTO, M., HIRANO, M., SKUJA, L., HOSONO, H., *UV-VUV laser induced phenomena in SiO_2 glass.* Nuclear Instruments and Methods in Physics Research B, 2004. **218**: p. 323-331.

65. IMAI, H., ARAI, K., IMAGAWA, H., HOSONO, H., ABE, Y., *Two types of oxygen-deficient centres in synthetic silica glass.* Physical Review B, 1988. **38**(17): p. 12772-12775.
66. LOU, V., SATO, R., TOMOZAWA, M., *Hydrogen diffusion in fused silica at high temperatures.* Journal of Non-Crystalline Solids, 2003. **315**: p. 13-19.
67. MUHLIG, C., TRIEBEL, W., BARK-ZOLLMANN, GREBNER, D., *In situ diagnostics of pulse laser-induced defects in DUV transparent fused silica glasses.* Nuclear Instruments and Methods in Physics Research B, 2000. **166-167**: p. 698-703.
68. IKUTA, Y., KIKUGAWA, S., HIRANO, M., HOSONO, H., *Defect formation and structural alteration in modified SiO_2 glasses by irradiation with F_2 laser or ArF excimer laser.* Journal of Vacuum Science and Technology: B, 2000. **18**(6): p. 2891-2895.
69. NEUSTRUEV, V.B., *Colour centres in germanosilicate glass and optical fibres.* Journal of Physics: Condensed Matter, 1994. **6**: p. 6901-6936.
70. STEVENS-KALCEFF, M.A., STESMANS, A., WONG, J., *Defects induced in fused silica by high fluence ultraviolet laser pulses at 355 nm.* Applied Physics Letters, 2002. **80**(5): p. 758-760.
71. KUHNLENZ, F., BARK-ZOLLMANN, S., STAFAST, H., TRIEBEL, W., *VUV absorption tail changes of fused silica during ArF laser irradiation.* Journal of Non-Crystalline Solids, 2000. **278**: p. 115-118.
72. LIBERMAN, V., ROTHSCHILD, M., SEDLACEK, J.H.C., UTTARO, R.S., GRENVILLE, A., *Excimer-laser-induced densification of fused silica: laser-fluence and material-grade effects on the scaling law.* Journal of Non-Crystalline Solids, 1999. **244**: p. 159-171.
73. SEWARD, T.P., SMITH, C., BORRELLI, N.F., ALLAN, D.C., *Densification of synthetic fused silica under ultraviolet irradiation.* Journal of Non-Crystalline Solids, 1997. **222**: p. 407-414.
74. ZHENG, L., LAMBROPOULOS, J.C., SCHMID, A.W., *UV-laser-induced densification of fused silica: a molecular dynamics study.* Journal of Non-Crystalline Solids, 2004. **347**: p. 144-152.
75. IKUTA, Y., KAJIHARA, K., HIRANO, M., HOSONO, H., *Correlation between oxygen-deficient centre formation and volume compaction in synthetic SiO_2 glass upton ArF or F_2 excimer-laser irradiation.* Applied Optics, 2004. **43**(11): p. 2332-2336.
76. SCHMIDTH, H., IHLEMANN, J., WOLF-ROTTKE, B., *Excimer laser micro-machining based on dielectric masks.* SPIE: Laser Materials Processing and Machining, 1994. **2246**: p. 67-73.
77. GOODMAN, J.W., *Introduction to Fourier optics*. Second ed, ed. W. STEPHEN. 1996, Singapore: McGraw-Hill. 441.
78. POL, V., BENNEWITZ, J.H., JEWELL, T.E., PETERS, D.W., *Excimer laser based lithography: a deep-ultraviolet wafer stepper for VLSi processing.* Optical Engineering, 1987. **26**(4): p. 311-318.
79. HOPKINS, H.H., *The concept of partial coherence in optics.* Proceedings of Royal Society. London Ser. A, 1951. **208**: p. 263-277.

80. HOPKINS, H.H., *On the diffraction theory of optical images.* Proceedings of Royal Society. London Ser. A, 1953. **217**: p. 408-432.
81. ROTHSCHILD, M., EHRLICH, D.J., *A review of excimer laser projection lithography.* Journal of Vacuum Science and Technology: B, 1988. **6**(1): p. 1-17.
82. INDEBETOUW, G., *Image formation in partially coherent light: Some quantitative remarks.* European Journal of Physics, 1980. **1**: p. 102-105.
83. WATANABE, H., *Analytical description of partially coherent optical systems for optimisation of numerical aperture and degree of coherence.* Japanese Journal of Applied Physics, 1994. **33**: p. 6549-6556.
84. KINTNER, E.C., SILLITTO, R.M., *Edge-ringing in partially coherent imaging.* Optica Acta, 1977. **24**(5): p. 591-605.
85. TABAT, M., O'KEEFFE, T.R., HO, W., *Profile characteristics of excimer laser micromachined features.* SPIE, 1992. **1835**: p. 144-157.
86. WALKER, A.C., *Laser resonators and Gaussian beams*, in *The Physics and Technology of Laser Resonators*, D.R. HALL, JACKSON, P.E., Editor. 1989, IOP Publishing Ltd: Bristol. p. 13-14.
87. SHAW, M.J., *Excimer laser resonators*, in *The Physics and Technology of Laser Resonators*, D.R. HALL, JACKSON, P.E., Editor. 1989, IOP publishing Ltd: Bristol. p. 237.
88. DYER, P.E., *Unstable resonators*, in *The Physics and Technology of Laser Resonators*, D.R. HALL, JACKSON, P.E., Editor. 1989, IOP Publishing Ltd: Bristol. p. 23.
89. HERMAN, P.R., MAROWSKY, SIMON, P., *Introduction to laser physics and excimer laser sources*, in *Excimer Laser Technology*, D. BASTING, Editor. 2001, Lambda Physik AG: Gottingen. p. 53.
90. NIKOLAJEFF, F., HARD, S., CURTIS, B., *Diffractive microlenses replicated in fused silica for excimer laser-beam homogenizing.* Applied Optics, 1997. **36**(32): p. 8481-8489.
91. HERMAN, P.R., CHEN, K.P., WEI, M., ZHANG, J., IHLEMANN, J., SCHAFER, D., MAROWSKY, G., OESTERLIN, P., BURGHARDT, B., *F_2-lasers: High-resolution optical processing system for shaping photonic components.* Proceedings of SPIE, 2001. **4274**: p. 149-157.
92. PATERSON, C., HOLMES, A.S., SMITH, R.W., *Excimer laser ablation of microstructures: A numerical model.* Journal of Applied Physics, 1999. **86**(11): p. 6538-6546.
93. HERMAN, P.R., IHLEMANN, J., KORBER, K., *Ablation at 157 nm*, in *Excimer Laser Technology*, D. BASTING, Editor. 2001, Lambda Physik AG: Gottingen. p. 170.
94. FIEBIG, M., KAUF, M., FAIR, J., ENDERT, H., RAHA, M., BASTING, D., *New aspects of micromachining and microlithography using 157-nm excimer laser.* Applied Physics A, 1999. **69**: p. S305-S307.
95. SCHAFER, D., IHLEMANN, J., MAROWSKY, G., HERMAN, P.R., *F_2-laser ablation patterning of dielectric layers.* Applied Physics A, 2001. **72**: p. 377-379.
96. KAHLERT, H.J., *UV optics systems for excimer lasers*, in *Excimer Laser Technology*, D. BASTING, Editor. 2001, Lambda Physik: Gottingen. p. 78.

97. HERMAN, P.R., MARJORIBANKS, R.S., OETTL, A., CHEN, K., KONOVALOV, I., NESS, S., *Laser shaping of phtonic materials: deep-ultraviolet and ultrafast lasers.* Applied Surface Science, 2000. **154-155**: p. 577-586.
98. HERMAN, P.R., YICK, A., LI, J., MUMCE, N., LILGE, L., JERVIS, E., KRYLOV, S., *F_2-laser micromachining of microfluidic channels and vias for biophtonic chip applications.* Conference on Lasers and Electro-optics Technology Digest (OSA, Wahington DC), 2003. **CFL5**: p. 1-3.
99. SNELLING, H.V., WALTON, C.D., WHITEHEAD, D.J., *Polymer jacket stripping of optical fibres by laser irradiation.* Applied Physics A, 2004. **79**: p. 937-940.
100. DYER, P.E., MASWADI, S.M., WALTON, C.D., ERSOZ, M., FLETCHER, P.D.I., PAUNOV, V.N., *157-nm laser micromachining of N-BK7 glass and replication for microcontact printing.* Applied Physics A, 2003. **77**: p. 391-394.
101. DYER, P.E., WALTON, C.D., *VUV laser ablation of insulators.* Applied Physics A, 2004. **79**: p. 721-727.
102. LI, J., HERMAN, P.R., WEI, M., CHEN, K.P., IHLEMANN, J., MAROWSKY, G., OESTERLIN, P., BURGHARDT, B., *High-resolution F_2-laser machining of micro-optic components.* Laser Applications in Microelectronics & Optoelectronics manufacturing; SPIE, 2002. **4637**: p. 228-234.
103. OBATA, K., SUGIOKA, K., AKANE, T., AOKI, N., TOYODA, K., MIDORIKAWA, K., *Influence of laser fluence and irradiation timing of F_2 laser on ablation properties of fused silica in F_2-KrF excimer laser multi-wavelength excitation process.* Applied Physics A, 2001. **73**: p. 755-759.
104. OBATA, K., SUGIOKA, K., AKANE, T., MIDORIKAWA, K., AKOI, N., TOYODA, K., *Efficient refractive-index modification of fused silica by a resonance-photoionization-like prosess using F_2 and KrF excimer lasers.* Optics Letters, 2002. **27**(5): p. 330-332.
105. KONOVALOV, I.A., HERMAN, P.R., *Ablation-induced stresses in fused silica by 157-nm F_2-laser irradiation.* Materials research Society Symposium, 2000. **617**: p. J3.3.1-J3.3.7.
106. ZHANG, J., HERMAN, P.R., LAUER, C., CHEN, K.P., WEI, M., *157-nm laser-induced modofication of fused silica glasses.* Proceedings of SPIE, 2001. **4272**: p. 125-132.
107. HERMAN, P.R., CHEN, K.P., NG, S., ZHANG, J., CORIC, D., CORKUM, P., MEHENDALE, M., NAUMOV, A., RAYNER, D., *Photosensitivity in glasses: comparing ultrafast lasers with vacuum-ultraviolet lasers.* Conference on Lasers and Electro-optics Technology Digest (OSA, Wahington DC), 2001. **56**: p. 490-491.
108. DYER, P.E., JOHNSON, A.M., SNELLING, H.V., WALTON, C.D., *Pulsed 157 nm VUV induced refractive index modification of optical fibres and planar fused silica.* Applied Surface Science, 2002. **186**: p. 583-587.
109. CHEN, K.P., HERMAN, P.R., TAM, R., ZHANG, J., *Rapid long-period grating formation in hydrogen-loaded fibre with 157 nm F_2-laser radiation.* Electronics Letters, 2000. **36**(24): p. 2000-2001.

110. DYER, P.E., JOHNSON, A.M., SNELLING, H.V., WALTON, C.D., *Measurement of 157 nm F_2 laser heating of silica fibre using an in situ fibre Bragg grating.* Journal of Physics D: Applied Physics, 2001. **34**: p. L109-L112.
111. CHEN, K.P., HERMAN, P.R., TAYLOR, R., HNATOVSKY, C., *Vacuum-ultraviolet laser-induced refractive-index changes and birefringence in standard optical fibres.* Journal of Light Wave Technology, 2003. **21**(9): p. 1969-1977.
112. ROTHSCHILD, M., BLOOMSTEIN, T.M., CURTIN, J.E., DOWNS, D.K., FEDYNYSHYN, T.H., HARDY, D.E., KUNZ, R.R., LIBERMAN, V., SEDLACEK, J.H.C., UTTARO, R.S., *157 nm: Deepest deep-ultraviolet yet.* Journal of Vacuum Science and Technology: B, 1999. **17**(6): p. 3262-3266.
113. BLOOMSTEIN, T.M., HORN, M.W., ROTHSCHILD, M., KUNZ, R.R., PALMACCI, S.T., GOODMAN, R.B., *Lithography with 157 nm lasers.* Journal of Vacuum Science and Technology: B, 1997. **15**(6): p. 2112-2116.
114. BLOOMSTEIN, T.M., ROTHSCHILD, M., KUNZ, R.R., HARDY, D.E., GOODMAN, R.B., PALMACCI, S.T., *Critical issues in 157 nm lithography.* Journal of Vacuum Science and Technology: B, 1998. **16**(6): p. 3154-3157.
115. LIBERMAN, V., BLOOMSTEIN, T.M., ROTHSCHILD, M., SEDLACEK, J.H.C., UTTARO, R.S., BATES, A.K., VAN PESKI, C., ORVEK, K., *Materials issues for optical components and photomasks in 157 nm lithography.* Journal of Vacuum Science and Technology: B, 1999. **17**(6): p. 3273-3279.
116. HOSONO, H., IKUTA, Y., *Interaction of F_2 excimer laser with SiO_2 glasses: Towards the third generation of synthetic SiO_2 glasses.* Nuclear Instruments and Methods in Physics Research B, 2000. **166-167**: p. 691-697.
117. BATES, A.K., ROTHSCHILD, M., BLOOMSTEIN, T.M., FEDYNYSHYN, T.H., KUNZ, R.R., LIBERMAN, V., SWITKES, M., *Review of technology for 157-nm lithography.* IBM Journal of Research and development, 2001. **45**(5): p. 605-614.
118. GRUENEWALD, P., CASHMORE, J., FIERET, J., GOWER, M., *High-resolution 157 nm laser micromachining of polymers*. 2003, Excitech Ltd., Hanborough Park, Long Hanborough, Oxford OX8 8LH, United Kingdom; http://www.exitech.co.uk.
119. GSC-14241, N.T.B., *Designing purging flows of clean, dry gases*, National Aeronautics and Space Administration; http://www.sti.nasa.gov: Greenbelt, Maryland 20771. p. 1-11.
120. BUHLER, J., STEINER, F.P., BALTES, H., *Silicon dioxide sacrificial layer etching in surface micromachining.* Journal of Micromechanics and Microengineering, 1997. **7**: p. R1-R13.
121. OKU, T., HATTORI, R., KAZUHIKO, S., *Mechanisms for breakage of Si-O networks of SiO2 films in HF solutions.* Materials Research Society Symposium Proceedings., 1998. **492**: p. 213-218.
122. WEAST, *Hand book of chemistry and physics*. 62 nd ed: CRC Press. 1981-1982.
123. GREENWOOD, N.N., EARNSHAW, A., *Chemistry of the elements*. 2 nd ed, ed. B. HEINEMANN. 2001. 382.
124. STOCKLE, R., FOKAS, C., DECKERT, V., ZENOBI, R., SICK, B., HECHT, B., WILD, U.P., *High-quality near-field optical probes by tube etching.* Applied physics letters, 1999. **75**(2): p. 160-162.

125. WONG, P.K., WANG, T.H., HO, C.M., *Optical fibre tip fabricated by surface tension controlled etching.* Solid-state sensor, Actuator and microsystems workshop; Hilton head Island, South Carolina, 2002.
126. CHUANG, Y.H., SUN, K.G., WANG, C.J., HUANG, J.Y., PAN, C.L., *A simple chemical etching technique for reproducible fabrication of robust scanning near-field fibre probes.* Review of scientific instruments, 1998. **69**(2): p. 437-439.
127. Wong, P., K., Wang, T., H., Ho, C., M. *Optical fibre tip fabricated by surface tension controlled etching*. in *Solid-state sensor, Actuator and microsystems workshop*. 2002. Hilton head Island, South carolina.
128. BURRUS, C.A., STANDLEY, R.A.,, *Viewing refractive index profiles and small scale inhomogenities in glass optical fibres: some techniques.* Applied Optics, 1974. **13**: p. 2365-2369.
129. ZHONG, Q., INNISS, D.,, *Characterisation of the light guiding structure of optical fibres by atomic force microscopy.* Journal of lightwave technology, 1994. **12**: p. 1517-1523.
130. MURPHY, V., MACCRAITH, B.D., BUTLER, T., MCDONAGH, C., LAWLESS, B., *Quasi-distributed fibre-optic chemical sensing using telecom optical fibre.* Electronic Letters, 1997. **33**: p. C-21-C-22.
131. ZHU, Y., WANG, A., *Miniature Fibre-optic pressure sensor.* IEEE Photonics Technology Letters, 2005. **17**(2): p. 447-449.
132. VAZIRI, M., CHEN, C.L.,, *Etched fibres as strain gauges.* Journal of Light Wave Technology, 1992. **10**(6): p. 836-841.
133. TUCK, C.J., FERNANDO, G.F., *New Techniques for manufacturing optical fibre-based Fabry-Perot sensors.* SPIE Smart Materials and Structure Conference, San Diego, 2002. **4694**.

Appendices

Appendix A

Calculation of the location of incidence of the second Fresnel reflection in a tapered cavity

Calculation of location of incidence of the second Fresnel reflection for a cavity taper angle (θ_t) of 2.75° with reference to the Figure 9-10 is presented as follows:

From ΔAHB, AH = 59.7 μm; θ_t = 2.75°;

$$HB = \tan 2.75^0 (59.7) = (0.0480)(59.7) = 2.8656\,\mu m \qquad \text{Equation A-1}$$

$$AB = \frac{AH}{\cos 2.75^0} = \frac{59.7}{0.9988} = 59.7717\,\mu m \qquad \text{Equation A-2}$$

From ΔBCK, BC = 2.8 μm; θ_t = 2.75°;

$$BK = \frac{BC}{\cos 2.75^0} = \frac{2.8}{0.9988} = 2.8033\,\mu m \qquad \text{Equation A-3}$$

$$CK = \tan 2.75^0 (BC) = (0.0480)(2.8) = 0.1344\,\mu m \qquad \text{Equation A-4}$$

From ΔBED, BE = 5.6 μm; θ_t = 2.75°;

$$ED = \tan 2.75^0 (BE) = (0.0480)(5.6) = 0.2688\,\mu m \qquad \text{Equation A-5}$$

$$BD = \frac{BE}{\cos 2.75^0} = \frac{5.6}{0.9988} = 5.6067\,\mu m \qquad \text{Equation A-6}$$

From Figure 9-10, HB = JC = IE = 2.8 μm

DK = BD – BK= 5.5.6067 – 2.8033 = 2.8034 μm Equation A-7

From ΔAWX, AW = 125 μm; θ_t = 2.75°;

$$XW = \tan 2.75^0 (AW) = (0.0480)(125) = 6\,\mu m \qquad \text{Equation A-8}$$

From Δ BYX, YB = 65.3 μm; θ_t = 2.75°;

$$XY = \tan 2.75^0 (YB) = (0.0480)(65.3) = 3.1344\,\mu m \qquad \text{Equation A-9}$$

From Figure 9-10,

WZ = WY (= IE) + YX + XZ′ + Z′Z′′(= XY) + Z′′Z (IE) Equation A-10

$\Rightarrow 40 = 2.8656 + 3.1344 + XZ' + 3.1344 + 2.8656$

$\Rightarrow XZ' = 28\ \mu m$

$YX = CV' = CK + KV + VV'$ Equation A-11

$\Rightarrow 3.1344 = 0.1344 + 0.1344 + VV'$

$\Rightarrow VV' = 2.8656\ \mu m$

$KQ = KV + VV' + V'V'' (= XZ') + V''R (= VV') + RQ (= KV)$ Equation A-12

$\Rightarrow KQ = 0.1344 + 2.8656 + 28 + 2.8656 + 0.1344$

$\Rightarrow KQ = 34\ \mu m$

From ΔKGQ, and Figure 9-10,

$\angle QKG = \theta_{1r} - \theta_t (=\theta_{1i}) = 4.0139 - 2.75 = 1.2639°$ Equation A-13

$\angle KQG = 90 - \theta_t = 90° - 2.75° = 87.25°$ Equation A-14

$\angle QGK = 90 + 2\theta_t - \theta_{1r} = 90° + 5.5° - 4.0139° = 91.4861°$ Equation A-15

By applying the sine rule of triangles to ΔKGQ,

$$\frac{\sin\angle QKG}{QG} = \frac{\sin\angle KGQ}{KQ} = \frac{\sin\angle KQG}{KG}$$ Equation A-16

$$\frac{\sin\angle KGQ}{KQ} = \frac{\sin\angle KQG}{KG}$$ Equation A-17

$$\Rightarrow \frac{\sin 91.4861^0}{34} = \frac{\sin 87.25^0}{KG}$$

$\Rightarrow KG = 33.9727\ \mu m$

From ΔKGF, and Figure 9-10,

$\angle KGF = 2(2\theta_t - \theta_{1r}) = 4(2.75°) - 2(4.0139°) = 2.9722°$ Equation A-18

$\angle GFK = 90 - 4\theta_t + \theta_{1r} = 90° - 11° + 4.0139° = 83.0139°$ Equation A-19

$\angle FKG = 90 + \theta_{1r} = 90° + 4.0139° = 94.0139°$ Equation A-20

By applying the sine rule to ΔKGF,

$$\frac{\sin\angle KGF}{KF} = \frac{\sin\angle GFK}{KG} = \frac{\sin\angle FKG}{FG}$$ Equation A-21

$$\frac{\sin\angle KGF}{KF} = \frac{\sin\angle GFK}{KG}$$ Equation A-22

$$\Rightarrow \frac{\sin 2.9722^0}{KF} = \frac{\sin 83.0139^0}{33.9727}$$

$$\Rightarrow \text{KF} = 1.7730\ \mu\text{m}$$

$\therefore$ KF = 1.7730 μm; BD = 5.6067 μm; and DK = 2.8034 μm.

DK + KF =2.8034 μm + 1.7730 μm = 4.5764 μm < BD (= 5.6067 μm) Equation A-23

Therefore according to these calculations, for $\theta_t = 2.75°$ and an entrance dimension of 40 μm, the second Fresnel reflection will be incident on the core across the first wall.

Appendix B

Invited paper presented at the proceedings of SPIE conference on ‘Microelectronics, MEMS and Nanotechnology’, which was held 11-14 December 2005 in Brisbane, Australia.